

*Wydział Chemii Uniwersytetu Gdańskiego*

mgr inż. Onur Cavdar

Synthesis, characterization, and application of  $\text{ZnIn}_2\text{S}_4$ - based  
photocatalyst for photocatalytic hydrogen evolution  
under the visible light spectrum

Promotor:  
prof. dr hab. inż. Adriana Zaleska-Medynska

Promotor pomocniczy:  
dr inż. Anna Malankowska

*Praca doktorska wykonana w  
Katedrze Technologii Środowiska*

**Gdańsk 2023**



N A R O D O W E C E N T R U M N A U K I



**Fundusze Europejskie**  
Wiedza Edukacja Rozwój



**Unia Europejska**  
Europejski Fundusz Społeczny

## Acknowledgment

I would like to thank my advisor prof. dr hab. inż. Adriana Zaleska-Medynska, for her endless support, advice and providing an opportunity to work on this topic. Professor Zaleska-Medynska inspired me with the many ways how she approaches the scientific questions.

I would like to express my great gratitude to my co-advisor dr inż. Anna Malankowska. Dr. Malankowska was always with me with encouragement and her expertise in photocatalysis that helped me to gain indefinable perspective. Ponieważ często na co dzień mówimy po polsku, chciałbym kontynuować po polsku. Byłaś też moim nauczycielem w nauczaniu języka polskiego. Brakuje mi słów aby to wyrazić.

I appreciate the financial support provided by National Science Centre, Poland (*Narodowe Centrum Nauki*) (SONATA-2016/23/D/ST8/02682 and PRELUDIUM-2016/23/D/ST8/02682) and Interfaculty and Interdisciplinary doctoral studies Chemistry with Physics (CHEMFIZ) which was conducted jointly by the Faculty of Chemistry and the Faculty of Mathematics, Physics and Computer Science at the University of Gdańsk as the part of a project co-financed by the European Union under the European Social Fund - Operational Program Knowledge Education Development (WND-POWR.03.02.00-00-I059/16).

Special thanks to all the co-authors of the scientific articles helping me to write this thesis.

Big thanks to employees of the Faculty of Chemistry at the University of Gdańsk and all my colleagues in the Department of Environmental Technology especially to my office mate mgr Jakub Sowik, for all our brainstorming and being always supportive and motivating colleague.

I love my beloved wife Monika Jurkiewicz-Çavdar (Kocham cię Monia) and our cat Wenus (aka Pimpuś).

Many thanks to my mother, Jurkiewicz family and all the friends.



## Contents

1	Introduction .....	1
1.1	Short introduction to photocatalytic hydrogen evolution .....	3
1.2	Visible light induced photocatalytic hydrogen evolution over TiO <sub>2</sub> and other metal oxides .....	4
1.3	Metal sulfides for visible light induced photocatalytic hydrogen evolution .....	7
1.3.1	Cocatalyst for photocatalytic hydrogen evolution.....	13
1.3.2	Sacrificial reagent for photocatalytic hydrogen evolution .....	15
1.4	ZnIn <sub>2</sub> S <sub>4</sub> based photocatalytic systems for photocatalytic hydrogen evolution.....	18
1.5	Details of experimental parts used in publication P1, P2 and P3 .....	27
1.5.1	Synthesis.....	27
1.5.2	Characterization .....	28
2	Literature used in the introduction .....	30
3	Aim of the dissertation .....	56
4	Summary of the publications.....	56
4.1	P1: “Remarkable visible-light induced hydrogen generation with ZnIn <sub>2</sub> S <sub>4</sub> microspheres/CuInS <sub>2</sub> quantum dots photocatalytic system” .....	57
4.2	P2: “Capping ligand initiated CuInS <sub>2</sub> quantum dots decoration on, ZnIn <sub>2</sub> S <sub>4</sub> microspheres surface under different alkalinity levels resulting in different hydrogen evolution performance” .....	60
4.3	P3: “Photocatalytic hydrogen evolution from glycerol-water mixture under visible light over zinc indium sulfide (ZnIn <sub>2</sub> S <sub>4</sub> ) nanosheets grown on bismuth oxychloride (BiOCl) microplates” .....	63
4.4	Summary.....	68

5	Publications .....	69
6	Scientific achievements .....	154

## Table of Figures

Figure 1	The gravimetric and volumetric density values of several fuels. The measure is based on lower heating values. JP-8 and E-10 mean “Jet Propellant 8” and petrol with 10% ethanol content, respectively (Taken from U.S. Department of Energy) [5] .....	1
Figure 2	A basic representation of a polymer membrane electrolyser and half reactions occurring on the cathode and anode .....	2
Figure 3	Schematic representation of overall photocatalytic water splitting over single photocatalyst. Ideal photocatalyst for water splitting purposes should have more negative than redox potential of $H^+/H_2$ (0 V vs NHE, pH = 0) and more positive than oxidation potential of $O_2/H_2O$ (1.23 V vs NHE, pH = 0) .....	4
Figure 4	Doping strategy for visible light induced photocatalytic hydrogen evolution purposes where a) dopants can create donor level above the valence band or b) acceptor level below the conduction band in the target doped photocatalytic material.....	5
Figure 5	Simplified representation of visible light induced photocatalytic hydrogen evolution mechanisms over a) gold nanoparticle sensitized $TiO_2$ through hot electron injection originated from SPR effect in gold nanoparticles and b) $CdS/TiO_2$ heterostructure in which photogenerated electrons are produced over $CdS$ and transferred on $TiO_2$ surface (Note: The presence of cocatalyst is not shown). .....	6
Figure 6	Comparison of the energy levels of metal-oxide and metal sulfide based photocatalysts (inspired from Kudo and Miseki [93]) .....	8
Figure 7	The most common metals used for metal sulfide photocatalysts shown in periodic table with their electron configuration (inspired from Zhang et al. [89]) .....	9
Figure 8	Two main functions of the cocatalyst in the photocatalytic system: (I) cocatalyst is an electron sink which is highly related with the work function that is the difference between the	

Fermi level (electrochemical potential) and vacuum level (inspired from Beasley et. al [126]). Cocatalyst should provide an active site for (II) proton reduction for hydrogen evolution in accordance with Volmer, Heyrovsky and Tafel reactions depending on the pH of the PHE medium (Volcano curve was taken from Guo et al. [127])...... 13

Figure 9 Number of publications from the beginning of the first photocatalytic application of ZnIn<sub>2</sub>S<sub>4</sub> in 2003 to 2022. Data was accessed from Scopus (Elsevier) on December 14, 2022 19

Figure 10 a) Cubic, b) hexagonal and c) trigonal structures of ZnIn<sub>2</sub>S<sub>4</sub> with d) their XRD patterns. Reproduced with the permission of Ref. [169]. Copyright (2021) Elsevier..... 20

Figure 11 Mechanisms of different heterojunctions for PHE applications a) Type-I, b) Type-II, c) p-n junction and d) Z-scheme where SC and S are semiconductor and sacrificial reagent, respectively..... 22

## Abstract

Hydrogen energy has become very attractive since it has remarkably high energy density in comparison to diesel or gasoline and more importantly it is a zero-emission fuel. Although it can be provided from several sources, the key point is that hydrogen production method should have low-environmental impact. Unfortunately, the hydrogen fuel market heavily relies on steam reforming which requires fossil fuel processing under high pressure and temperature conditions where a greenhouse gas, carbon dioxide, is produced largely. Electrolysis can be considered as an alternative method since it uses electricity to split water to oxygen and hydrogen fuel. However, the same criteria apply to this method for the source of the electricity. In other words, depending on the source of the electricity production such as hydropower, wind, or solar energy input, electrolysis process can be sustainable.

The idea of developing a system that converts solar energy directly to hydrogen fuel could be another way to produce hydrogen fuel from water. Photocatalytic hydrogen evolution permits direct solar conversion on account of the photocatalytically active semiconductor materials. Among various of studied photocatalysts,  $\text{TiO}_2$  is prominent owing to its suitable band alignment for photocatalytic hydrogen evolution. Nevertheless, the biggest obstacle is that  $\text{TiO}_2$  can be activated only via UV part of the solar spectrum. Thus, there is a massive effort that must be taken to develop a photocatalytic system that can initiate PHE process under wider range of the solar spectrum, specifically visible light spectrum. The candidate photocatalyst also should be cheap and require as low as possible amount of noble metal (usually Pt) or have promising Pt-free photocatalytic hydrogen evolution performance.

In my doctoral dissertation, I investigated the several ways to improve the performance of zinc indium sulfide ( $\text{ZnIn}_2\text{S}_4$ ) which is one of the most popular photocatalyst in the literature especially for the photocatalytic hydrogen evolution applications under visible light spectrum ( $\lambda > 420 \text{ nm}$ ). Two different types of  $\text{ZnIn}_2\text{S}_4$  based photocatalytic system were investigated in detail:  $\text{ZnIn}_2\text{S}_4/\text{CuInS}_2$  and  $\text{BiOCl}@\text{ZnIn}_2\text{S}_4$ . For  $\text{ZnIn}_2\text{S}_4/\text{CuInS}_2$  photocatalytic systems, the first part was related with the development of  $\text{ZnIn}_2\text{S}_4/\text{CuInS}_2$  photocatalytic system via hydrothermal method in the presence of pre-prepared  $\text{CuInS}_2$  quantum dots. While the second part was on a specific question related with the effect of the aggregation properties on PHE performance of  $\text{ZnIn}_2\text{S}_4$ . Lastly, the photocatalytic glycerol reforming for photocatalytic hydrogen evolution was examined over  $\text{BiOCl}@\text{ZnIn}_2\text{S}_4$ .

This thesis begins with the short information about the published works constituting the thesis which are mentioned in the whole thesis as **P1**, **P2** and **P3**. In the introduction part, The Reader can find concise information about the photocatalytic hydrogen evolution providing a strong background which is useful to understand the published works. After implying the aim of the thesis, the publications (**P1**, **P2** and **P3**) are summarized defining the most important points of each published works followed by the summary of the whole thesis highlighting the suggested outcomes of the thesis and propositions for the further studies. Finally, the publications are given with their supplementary information followed by the scientific achievements at the end of the thesis.

## Streszczenie

Energia w postaci wodoru stała się bardzo atrakcyjna, ponieważ wodór ma większą gęstość energii w porównaniu z olejem napędowym czy benzyną, a co ważniejsze jest paliwem zero-emisyjnym. Wodór może być dostarczany z kilku źródeł, jednakże kluczową kwestią jest jego metoda produkcji, która powinna mieć niewielki wpływ na środowisko. Niestety rynek paliw wodorowych opiera się na reformingu, który wymaga przetwarzania paliw kopalnych pod wysokim ciśnieniem i w wysokiej temperaturze, gdzie w dużej mierze wytwarzany jest gaz cieplarniany- dwutlenek węgla. Elektrolizę można uznać za metodę alternatywną produkcji wodoru, ponieważ wykorzystuje ona energię elektryczną do rozkładu wody na tlen i paliwo wodorowe. Jednak te same kryteria mają zastosowanie do tej metody, gdy bierze się pod uwagę źródło energii elektrycznej. Innymi słowy, w zależności od źródła produkcji energii elektrycznej, takiej jak energia wodna, wiatrowa lub słoneczna, proces elektrolizy może być procesem zrównoważonym.

Pomysł na opracowanie systemu, który przekształca energię słoneczną bezpośrednio w paliwo wodorowe, może być kolejnym sposobem na produkcję paliwa wodorowego z wody. Fotokatalityczne generowanie wodoru (PHE) umożliwia bezpośrednią konwersję słoneczną dzięki fotokatalitycznie aktywnym materiałom półprzewodnikowym. Wśród badanych fotokatalizatorów,  $\text{TiO}_2$  wyróżnia się tym, że posiada odpowiednie położenie pasm do fotokatalitycznego procesu wydzielania wodoru. Jednak największym ograniczeniem  $\text{TiO}_2$  jest to, że może być on aktywowany tylko pod wpływem promieniowania UV, które stanowi tylko część promieniowania słonecznego. Dlatego należy podjąć badania w celu opracowania fotokatalizatora, który może zainicjować proces PHE w szerszym zakresie widma słonecznego, a konkretnie promieniowania widzialnego. Proponowany fotokatalizator powinien być także tani i wymagać jak najmniejszej ilości metalu szlachetnego (zwykle Pt) lub powinien wykazywać znaczną wydajność fotokatalitycznego generowania wodoru bez obecności Pt.

W mojej rozprawie doktorskiej zbadałem kilka metod zwiększenia efektywności siarczku cynkowo-indowego ( $\text{ZnIn}_2\text{S}_4$ ), który jest jednym z najpopularniejszych fotokatalizatorów w literaturze, zwłaszcza w procesie fotokatalitycznego generowania wodoru pod wpływem promieniowania widzialnego ( $\lambda > 420 \text{ nm}$ ). Szczegółowo zbadano dwa typy układów fotokatalitycznych opartych na  $\text{ZnIn}_2\text{S}_4$ :  $\text{ZnIn}_2\text{S}_4/\text{CuInS}_2$  oraz  $\text{BiOCl}@\text{ZnIn}_2\text{S}_4$ . W przypadku układu  $\text{ZnIn}_2\text{S}_4/\text{CuInS}_2$ , pierwsza część badań dotyczyła otrzymywania kompozytu  $\text{ZnIn}_2\text{S}_4/\text{CuInS}_2$  metodą hydrotermalną, gdzie  $\text{ZnIn}_2\text{S}_4$  był syntezowany w obecności wcześniej

przygotowanych kropek kwantowych typu  $\text{CuInS}_2$ . Natomiast druga część badań związana z kompozytami  $\text{ZnIn}_2\text{S}_4/\text{CuInS}_2$  dotyczyła badania wpływu agregacji kropek kwantowych na wydajność generowania wodoru. W kolejnej części badawczej pracy zbadano efektywność generowania wodoru w procesie fotokatalitycznego reformingu glicerolu w obecności kompozytów  $\text{BiOCl}@ZnIn_2S_4$ .

Niniejszą pracę rozpoczyna krótka informacja na temat publikacji naukowych składających się na rozprawę doktorską, które w całej pracy zostały oznaczone jako **P1**, **P2** i **P3**. We wstępie Czytelnik może znaleźć informacje, które mogą być przydatne do zrozumienia publikowanych prac. Po przedstawieniu celu pracy, streszczono publikacje (**P1**, **P2** i **P3**) opisując najważniejsze osiągnięcia każdej z prac. Na końcu przedstawiono podsumowanie całej rozprawy oraz propozycję dalszych badań, Do rozprawy doktorskiej dołączono opisywane publikacje wraz z informacjami uzupełniającymi oraz dorobek naukowy.

## **List of publications**

### **P1. Remarkable visible-light induced hydrogen generation with ZnIn<sub>2</sub>S<sub>4</sub> microspheres/CuInS<sub>2</sub> quantum dots photocatalytic system**

**O.Cavdar**, A. Malankowska, D. Amgar, P. Mazierski, J. Łuczak, W. Lisowski, A. Zaleska-Medynska

International Journal of Hydrogen Energy, 46, 2021, 486-498

IF<sub>2021</sub> = 7.139, Ministerial Points<sub>2021</sub> = 140

---

### **P2. Capping ligand initiated CuInS<sub>2</sub> quantum dots decoration on, ZnIn<sub>2</sub>S<sub>4</sub> microspheres surface under different alkalinity levels resulting in different hydrogen evolution performance**

**O.Cavdar**, A. Malankowska, J. Łuczak, A. Żak, W. Lisowski, T. Klimczuk,

A. Zaleska-Medynska

Colloids and Surfaces A: Physicochemical and Engineering Aspects, 652, 2022, 129760

IF<sub>2021</sub> = 5.518, Ministerial Points<sub>2021</sub> = 70

---

### **P3. Photocatalytic hydrogen evolution from glycerol-water mixture under visible light over zinc indium sulfide (ZnIn<sub>2</sub>S<sub>4</sub>) nanosheets grown on bismuth oxychloride (BiOCl) microplates**

**O.Cavdar**, M. Baluk, A. Malankowska, A. Żak, W. Lisowski, T. Klimczuk, A. Zaleska-Medynska

Journal of Colloids and Interface Science, 640 (2023) 578–587

IF<sub>2021</sub> = 9.965, Ministerial Points<sub>2021</sub> = 100



# 1 Introduction

Seeking an alternative energy source to fossil fuels has been a hot topic since the first oil crisis in 1973 [1]. Indeed, those attempts escalated due to the concerns about global warming leading this effort with decarbonization to cut the greenhouse gasses emission by 2030 as depicted in Paris Agreement [2] and have spiked especially after Russian invasion of Ukraine on 22 February 2022 concerning the energy security [1]. Clearly, there is a dire need for swift a transition to a reliable, secure, and green energy source that is necessary ever than before [3].

If the storage problem is set aside [4], hydrogen energy seems very attractive due to its high gravimetric energy density which is the highest compared to other fossil-based fuels (Figure 1) [5]. The most importantly it releases only water after its combustion. However, since a negligible amount of hydrogen molecules exist naturally, they must be derived from some other sources. Luckily, hydrogen atom is the most abundant in the universe and third in the Earth in the form of hydrocarbons, water, or other compounds. Converting hydrogen atoms to molecular hydrogen requires different strategies depending on the hydrogen atom sources and it needs an energy input regardless of a source. The most common method in the market is steam methane

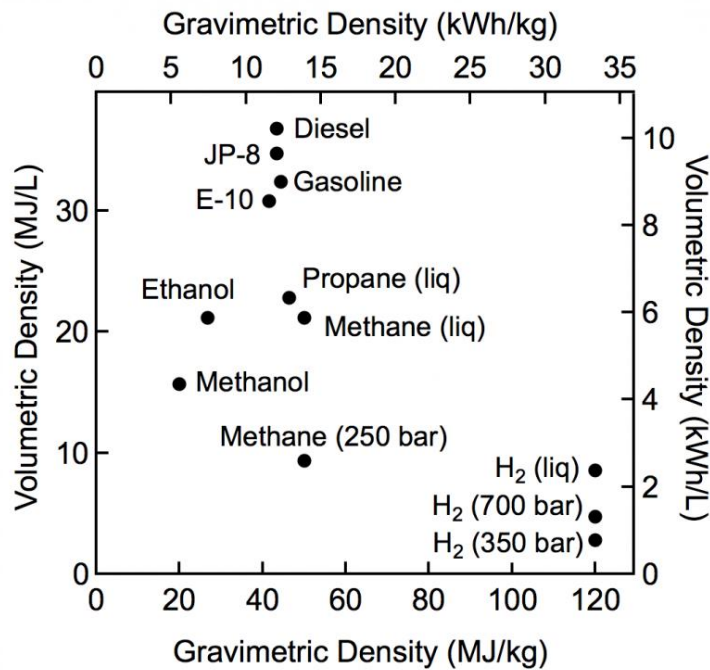


Figure 1 The gravimetric and volumetric density values of several fuels. The measure is based on lower heating values. JP-8 and E-10 mean “Jet Propellant 8” and petrol with 10% ethanol content, respectively (Taken from U.S. Department of Energy) [5]

reforming (STM) that is basically a utilization of natural gas with the steam under high temperature releasing CO (Eq. 1) and CO<sub>2</sub> (Eq. 2) resulting in an overall reaction of STM (Eq.3) [6].



Through a greener path, hydrogen fuel can be produced by water splitting via process called water electrolysis that requires electrical current input facilitating the water splitting reaction in an electrolyser unit consisting of cathode and anode in an alkali electrolyte (alkaline water electrolyser) or a proton exchange membrane between located between electrodes (polymer membrane electrolyser) (Figure 2). Depending on the source of the electricity production such as hydropower, wind, or solar energy input, this process can be sustainable [7] as the predictions for renewable energy share in global electricity production will increase from 18% to around 31% between 2018 to 2050 [8,9]. Thus, surplus electricity production from those sources can be utilized to produce hydrogen to store this electricity in the form of stable chemical bonds [10]. This seems to be promising solution and especially huge efforts have been made in the

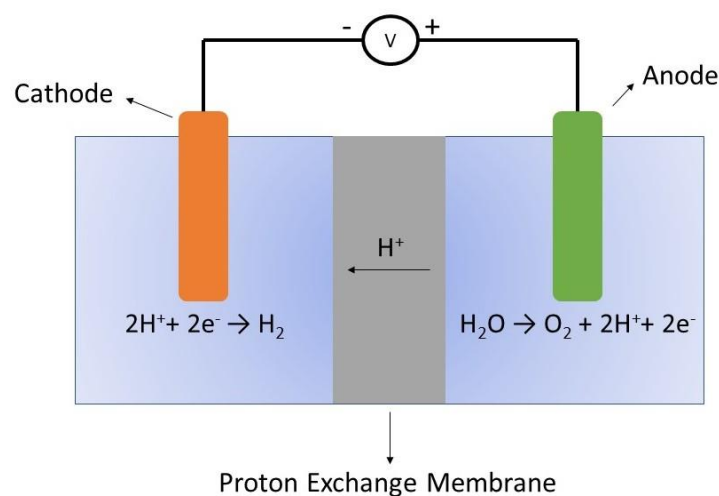


Figure 2 A basic representation of a polymer membrane electrolyser and half reactions occurring on the cathode and anode

market to lower the cost of hydrogen production via electrolyser yet to be soon lower than steam reforming-produced hydrogen by 2030 [11].

## 1.1 Short introduction to photocatalytic hydrogen evolution

The idea of developing a system which can convert solar energy to hydrogen fuel could be another way with the aim of simpleness and cost-effectiveness [12]. Suchlike system was firstly reported by Honda-Fujishima in 1974 from a installation with UV irradiated semiconductor TiO<sub>2</sub> photoanodes connected to the Pt plate where hydrogen ions are reduced to hydrogen fuel [13]. The process occurred over the TiO<sub>2</sub> layer is called Honda-Fujishima effect that is accepted by the photocatalysis community as a pioneer of photocatalysis research for hydrogen production. Since then, many efforts have been devoted to development of TiO<sub>2</sub>-based photocatalytic systems for photocatalytic hydrogen evolution (PHE) applications as it is one of the most widely studied photocatalyst in this discipline [14]. The fact of the popularity of TiO<sub>2</sub> is not surprising since it fulfills the one of the most important fundamental requirements of a photocatalyst for PHE that is suitable band alignment for PHE [15]. Location of conduction band (CB) and valence band (VB) in a photocatalyst with suitable band alignment for PHE should have more negative than redox potential of H<sup>+</sup>/H<sub>2</sub> (0 V vs NHE, pH = 0) and more positive than oxidation potential of O<sub>2</sub>/H<sub>2</sub>O (1.23 V vs NHE, pH = 0), respectively (Figure 3). In the typical PHE evolution process, a charge carrier generation occurs (Route II in Figure 3) where electrons and holes over CB and VB upon light irradiation (Route I in Figure 3) with the sufficient photon energy ( $h\nu$ ) that is higher than band gap ( $E_g$ ) resulting in proton reduction and water oxidation over CB and VB (Route III in Figure 3). Overall water splitting is a challenging goal because the number of both holes and electrons should be 4 [16] which makes this reaction complex. In other words, both proton reduction and water oxidation should occur over a photocatalyst (Figure 2). However, in this thesis, the two main objectives are:

- to achieve a visible light induced ( $\lambda > 420$  nm) PHE. One of the biggest barriers for PHE over TiO<sub>2</sub> is harvesting the visible light to start PHE reactions. This requires a design strategy to overcome this problem. After-mentioned reported strategies for TiO<sub>2</sub> will be focused on only the examples around the light excitation wavelength above 400 nm.
- to initiate half water splitting for PHE. This requires the use of sacrificial reagents (that will be explained in detail in the next section) to scavenge the photogenerated holes whose VB potential should be higher than that of the sacrificial reagent's oxidation

potential to fasten the proton reduction kinetics. On the contrary electron scavengers are required for oxygen evolution reactions which is not part of this thesis.

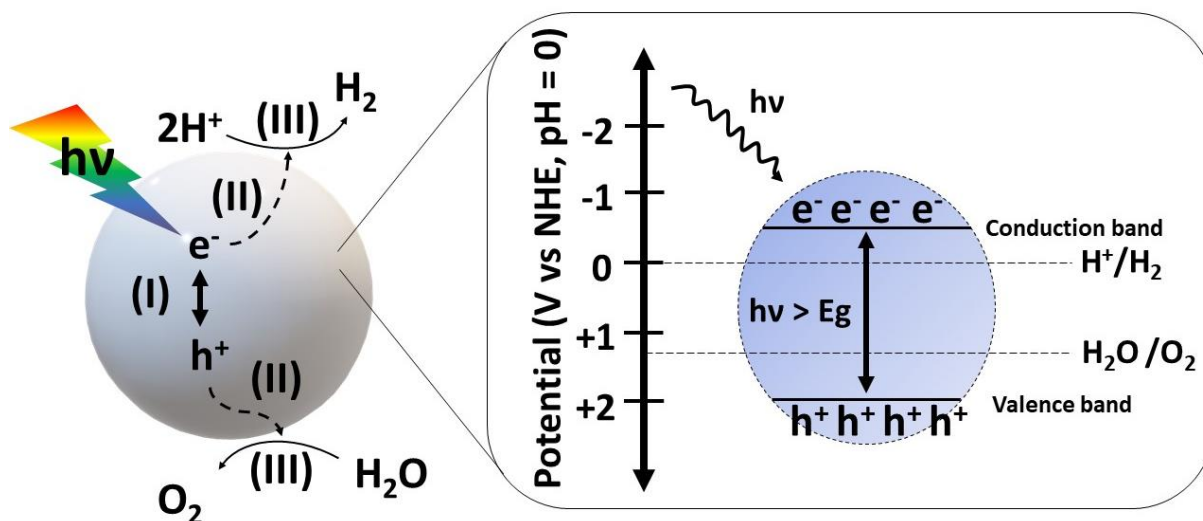


Figure 3 Schematic representation of overall photocatalytic water splitting over single photocatalyst. Ideal photocatalyst for water splitting purposes should have more negative than redox potential of  $\text{H}^+/\text{H}_2$  (0 V vs NHE, pH = 0) and more positive than oxidation potential of  $\text{O}_2/\text{H}_2\text{O}$  (1.23 V vs NHE, pH = 0)

## 1.2 Visible light induced photocatalytic hydrogen evolution over $\text{TiO}_2$ and other metal oxides

The justification for the goal of the visible light application of photocatalysts originates from the one of the biggest limitations of the  $\text{TiO}_2$ -based photocatalytic system that it can be only activated by UV light due to its wide band gap more than  $E_g > 3.0$  eV. As the solar spectrum consists of only 3-5% UV light lower than 400 nm [17], it is crucial to build photocatalytic system that benefits the visible light spectrum that is around 43% of solar spectrum [18]. Indeed, this problem has been tried to be overcome by applying various strategies that can be categorized into two main methods: doping and surface modification. The significant distinction between the surface modification or doping definitions should be considered which was described by Kowalska et al [19]. In short, the doping is introducing of metal atoms [14] such as Ag [20] Fe[21], V [22], Cr [23], Bi [24], Co [25], Ru [26] or nonmetal atoms [27,28] (N [29], C [30], B [31], S [32], P [33], F [34]) in a target material during the synthesis causing intrinsic changes due to the emerged intragap localized states narrowing the band gap (Figure 4) or even completely forming a different material lower band gap than that of  $\text{TiO}_2$  [35] while

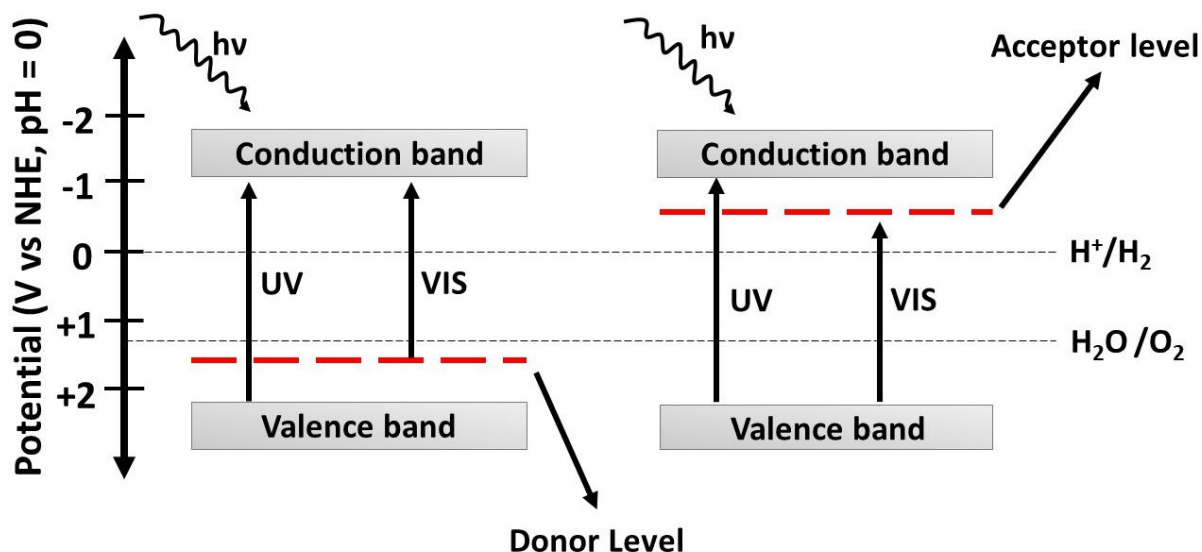


Figure 4 Doping strategy for visible light induced photocatalytic hydrogen evolution purposes where a) dopants can create donor level above the valence band or b) acceptor level below the conduction band in the target doped photocatalytic material

surface modification is the treatment of the pre-prepared bulk material that is further processed in another step. For example, nano-sized Au can significantly improve the visible light response and PHE performance of TiO<sub>2</sub> owing to the surface plasmon resonance (SPR) [36–39] effect. It was suggested that the SPR excited electrons over Au nanoparticles under visible light are transferred to CB of TiO<sub>2</sub> and finally can reach the metal cocatalyst where the H<sup>+</sup> to H<sub>2</sub> reduction occurs (Figure 5a) [39]. As well as for Ag nanoparticles deposited TiO<sub>2</sub>, similar SPR phenomenon over was observed [40,41]. Besides, Cu based nanoparticle deposition in the form of Cu<sub>2</sub>O, CuO and Cu were proven to have capability to cause red-shift TiO<sub>2</sub> thus improved PHE activity under visible light [42–44]. Graphene oxide was responsible for visible light activation of graphene oxide-TiO<sub>2</sub> composite due its sensitization effect [45]. Same effect was reported for synthesized TiO<sub>2</sub> with graphitic carbon material [46] and carbon quantum dots [47] Beyond the sensitization effect, structural changes established by reduced graphene oxide derived from graphene oxide via hydrothermal treatment were reported, where oxygen vacancies and crystal disorders on the surface of TiO<sub>2</sub> promote the visible light activity [48]. Dye-sensitization are another widely proven technique in which dye molecules such as eosin Y, Ru-bipyridyl complexes [49], merbromine, 2',7'-dichlorofluorescein, rhodamine 6G, rhodamine B are anchored on TiO<sub>2</sub> through chemical fixation [50] and as well as metal-based dye molecules like copper phthalocyanine (CuPc) [51] and zin phthalocyanine based (ZnPc) [52] exhibited good sensitization performance on TiO<sub>2</sub>. Lastly, coupling TiO<sub>2</sub> with another semiconductor photocatalyst can effectively improve the visible light induced PHE

performance [53,54]. The main criterion in this strategy is the selection of the proper semiconductor with a higher level of conduction band than  $\text{TiO}_2$  and the ability to utilize the visible light spectrum [55].  $\text{TiO}_2/\text{CdS}$  heterostructure is one of the most remarkable example [56–61] for PHE where  $\text{H}^+$  reduction occurs directly on  $\text{TiO}_2$  surface or over a cocatalyst through injected electron from  $\text{TiO}_2$  (Figure 5b). Additionally,  $\text{WS}_2$  [55],  $\text{CaFe}_2\text{O}_4$  [62] and black phosphorus [63], graphitic carbon nitride ( $\text{g-C}_3\text{N}_4$ ) [64] were investigated for sensitization of  $\text{TiO}_2$  as an alternative to CdS. Above-mentioned strategies for enhancing the visible light activity of  $\text{TiO}_2$  are also applicable to other extensively discussed wide-band-gap metal oxide photocatalysts such as  $\text{ZnO}$  [65,66],  $\text{SrTiO}_3$  [67–70],  $\text{NaTaO}_3$  [71,72] and other UV active materials [54,73]. In addition to those attempts, single crystal metal oxides were also

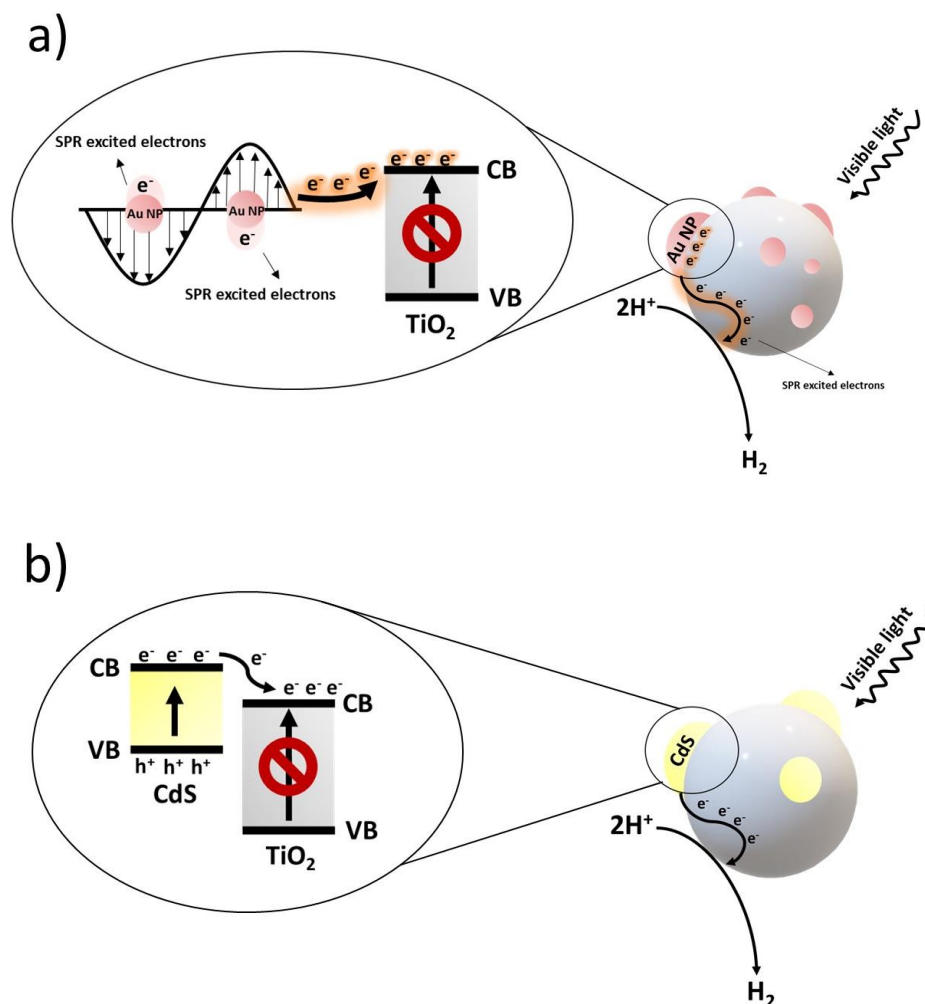


Figure 5 Simplified representation of visible light induced photocatalytic hydrogen evolution mechanisms over a) gold nanoparticle sensitized  $\text{TiO}_2$  through hot electron injection originated from SPR effect in gold nanoparticles and b)  $\text{CdS}/\text{TiO}_2$  heterostructure in which photogenerated electrons are produced over CdS and transferred on  $\text{TiO}_2$  surface (Note: The presence of cocatalyst is not shown).

reported for visible light induced PHE [74] including  $\text{NiM}_2\text{O}_6$  ( $\text{M} = \text{Nb}; \text{Ta}$ ) [75],  $\text{InVO}_4$  [76],  $\text{MCrO}_4$  ( $\text{M} = \text{Sr}, \text{Ba}$ ) [77],  $\text{LaFeO}_3$  [78],  $\text{ZnFe}_2\text{O}_4$  [79],  $\text{Fe}_2\text{O}_3$  [80],  $\text{Fe}_3\text{O}_4$  [81].

Clearly, all those attempts show that continuing valiant efforts are high for the application of  $\text{TiO}_2$  for visible light induced PHE. Nevertheless, the motivation is more than a suitable band alignment. Low-cost, stability, corrosion resistance and environmental safety [82] are another key measures which promotes  $\text{TiO}_2$  as a desirable photocatalyst for PHE in larger scale than laboratory scale [83–85]. What's more,  $\text{TiO}_2$  is very quickly emerged material last 20 years [86] thus the information regarding  $\text{TiO}_2$  has been soaring and likely it will continue to do so in the next years more than any other photocatalysts. Alternatively, as discussed above, researchers have been making effort to find an alternative to  $\text{TiO}_2$  either wide-band-gap metal oxide based photocatalysts by employing the similar strategies as for visible light induced PHE or designing narrow-band-gap metal oxide single crystals. However, one should consider while designing a photocatalytic system that if the full water splitting is not desired but particularly the half-reaction, then the reducing capability of the target photocatalyst should be the main interest along with the visible light spectrum harvesting capability.

In the next title, the reasons why the metal sulfides fulfill those specifications will be widely discussed followed by the main interest of this thesis  $\text{ZnIn}_2\text{S}_4$  based photocatalytic systems.

### **1.3 Metal sulfides for visible light induced photocatalytic hydrogen evolution**

Before going into the detail of metal sulfide based photocatalytic system, the two very similar and in the same time drastically different oxygen and sulfur elements will be introduced as is clearly explained by Ao [87]. In short, the similarity between oxygen and sulfur bonding with metals arises from their similar valence electron configuration ( $\text{O}: [\text{He}] 2s^2 2p^4$  and  $\text{S}: [\text{Ne}] 3s^2 3p^4$ ). That's why almost all the metal oxides have analogues of metal sulfides. However, the distinctions between those two elements are even observable in our surroundings as in the case of the direct evidence of the formation of S-S bonding in elemental sulfur which is a solid ( $\text{S}_8$ ) while elemental oxygen ( $\text{O}_2$ ) is a gas. Also, the oxidation and reduction of sulfur are heavily influenced by the surroundings. Because sulfur can hold more than 10 to even 12 electrons in its valence shell by expanding to d orbital as d orbital in sulfur element is available due to its quantum number ( $n = 3$ ) [88]. Therefore, the oxidation number of sulfur can range from -2 to +6. It was suggested by Ao that in consideration of those factors, the bonding characteristics of metal sulfides are more complicated than that of metal oxides [87].

Metal sulfide based photocatalysts are usually composed of metals with  $d^{10}$  configuration which hybridize with  $S^{2-}$  [89]. The VB in metal sulfides is formed by the S 3p orbitals that is located higher valence band position than O 2p (Figure 6) due to its higher located atomic orbital energy than O [90]. Also, when an anion and a cation interact to form metal oxide crystals, the electrostatic potential is reduced as same as with metal sulfides. However, the higher electron affinity for sulfide anions than oxides cause narrower energy separation that is leading lower energy gap [90,91]. As a result, both conduction and valence band energies of the metal sulfides usually have higher energy than that of their oxide counterparts. Thus, metal sulfides are better candidates for visible light induced reduction applications (such as PHE), but poor oxidizer and non-stable compared to metal-oxide counterparts [92].

Metals used for metal sulfide are usually d block element can be categorized into transition and nontransition metals. Examples of metal sulfide semiconductor photocatalysts in this section

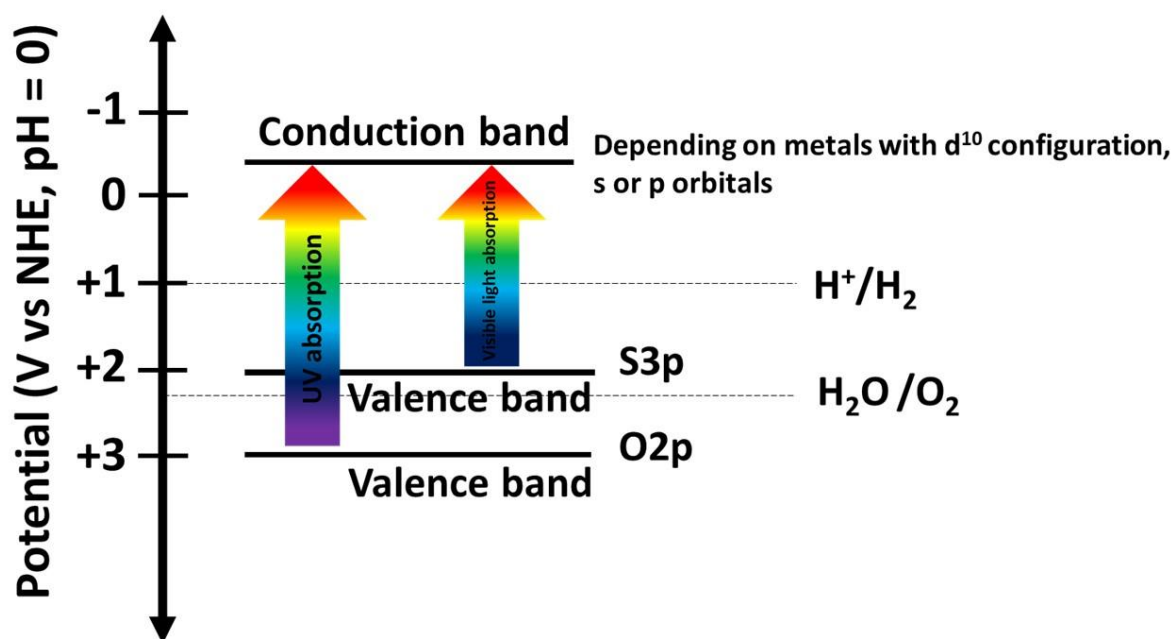
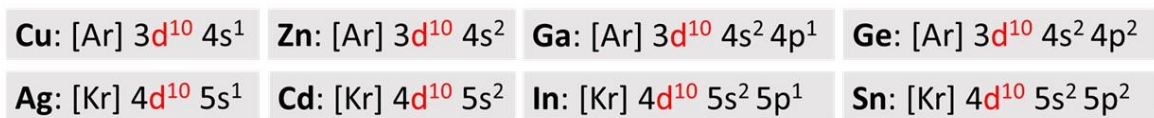


Figure 6 Comparison of the energy levels of metal-oxide and metal sulfide based photocatalysts (inspired from Kudo and Miseki [93])

are on nontransition metal (a metal that can form stable ions with filled d orbitals) (Figure 6). Therefore, nontransition metals sulfides' conduction band are formed usually s or p orbitals. In transient metal sulfides as expected, the participation of metal d states can be observed within s/p orbitals or S 3p orbital that can be hybridized to the CB or VB [93]





The figure shows a periodic table with a red box highlighting the transition metals Cu, Zn, Ga, Ge, Ag, Cd, In, and Sn. A red line connects the top of this box to the electron configurations listed above. The configurations are: Cu: [Ar] 3d<sup>10</sup> 4s<sup>1</sup>; Zn: [Ar] 3d<sup>10</sup> 4s<sup>2</sup>; Ga: [Ar] 3d<sup>10</sup> 4s<sup>2</sup> 4p<sup>1</sup>; Ge: [Ar] 3d<sup>10</sup> 4s<sup>2</sup> 4p<sup>2</sup>; Ag: [Kr] 4d<sup>10</sup> 5s<sup>1</sup>; Cd: [Kr] 4d<sup>10</sup> 5s<sup>2</sup>; In: [Kr] 4d<sup>10</sup> 5s<sup>2</sup> 5p<sup>1</sup>; Sn: [Kr] 4d<sup>10</sup> 5s<sup>2</sup> 5p<sup>2</sup>.

Figure 7 The most common metals used for metal sulfide photocatalysts shown in periodic table with their electron configuration (inspired from Zhang et al. [89])

CdS maybe one of the most popular metal sulfides photocatalyst for visible light induced PHE. Detailed reviews about CdS for PHE applications have been made previously [16,94]. The two main structural properties of CdS can be found as wurtzite and zinc blende whose band gap values is around 2.4 eV and 2.3 eV, respectively [16]. Both polytypes have a suitable band alignment for hydrogen evolution reaction. Variety of morphologies were devoted for PHE such as 0-dimensional shapes (quantum dots), 1-dimensional (nanorods, nanowires), 3-dimensional (hierarchical structures) and 2-dimensional (nanosheets) [94]. Xian et al reported CdS quantum dots (QDs) which exhibited 1.61 mmol g<sup>-1</sup> h<sup>-1</sup> PHE rate in presence of Sn<sup>2+</sup> as a cocatalyst and glycerol under visible light ( $\lambda > 420$  nm) [95]. Similarly, Shi et al. obtained Se doped CdS quantum dots which showed 29.12 mmol h<sup>-1</sup> g<sup>-1</sup> PHE rate from Na<sub>2</sub>S/Na<sub>2</sub>SO<sub>3</sub> aqueous solution under simulated solar irradiation (320–780 nm) without any cocatalyst [96]. Both reports have drawn attention to quantum dots' high light-harvesting capability and large surface-to-volume ratio. Nanorods or nanowires were also another investigated morphology of CdS due the possibility to study migration of charges through long axis thanks to its geometry by placing the cocatalyst on the most prominent location on the nanorods to achieve the highest activity [97–99]. For example, Chen et al. produced nanorods whose tips were selectively decorated by IrSe<sub>2</sub> coated with a MoSe<sub>2</sub> shell. The heterostructure exhibited outstanding PHE rate (137 mmol h<sup>-1</sup> g<sup>-1</sup>) from lactic acid-water solution (20% v/v) under 405 LED irradiation (250 mW). Another remarkable visible light ( $\lambda > 420$  nm) induced PHE rate was reported by Y. Chen in

which NiSe<sub>2</sub> in-situ growth over CdS nanorods performed 167.1 mmol g<sup>-1</sup> h<sup>-1</sup> from Na<sub>2</sub>S/Na<sub>2</sub>SO<sub>3</sub> aqueous solution. Lu proved that MoS<sub>2</sub> tipped CdS nanorods resulted in higher PHE rate (31.46 mmol h<sup>-1</sup> g<sup>-1</sup>) than the MoS<sub>2</sub> coated CdS (7.32 mmol h<sup>-1</sup> g<sup>-1</sup>) from 10% lactic acid-water solution under visible light ( $\lambda > 420$  nm) [100]. Look-alike morphology to nanorods, CdS nanowires coated with g-C<sub>3</sub>N<sub>4</sub> performed 4152  $\mu$ mol h<sup>-1</sup> g<sup>-1</sup> PHE rate from Na<sub>2</sub>S/Na<sub>2</sub>SO<sub>3</sub> aqueous solution where Pt in-situ cocatalyst deposition (0.6 wt.%) was implemented [101]. 95.7 mmol h<sup>-1</sup> g<sup>-1</sup> PHE rate from 20% lactic acid aqueous solution was reported by He et al. where the ultra-thin g-C<sub>3</sub>N<sub>4</sub> covered CdS nanowires was used. Accordingly, previously mentioned g-C<sub>3</sub>N<sub>4</sub> coating strategy was applied by Yin et al. where they investigated the effect of coating amount on CdS nanospheres. Optimum amount of g-C<sub>3</sub>N<sub>4</sub> resulted 4.39 mmol h<sup>-1</sup> g<sup>-1</sup> PHE rate under visible light ( $\lambda > 420$  nm) [102]. Analogous 3D morphology of CdS photocatalyst were also reported by Kadam et al. They synthesized CdS microparticles with MoS<sub>2</sub> shell which had PHE rate around 4 mmol g<sup>-1</sup> h<sup>-1</sup> from Na<sub>2</sub>S/Na<sub>2</sub>SO<sub>3</sub> aqueous solution under simulated sunlight [103]. Li et al. studied thermal assisted Pt cocatalyst loading on CdS nanoparticles surface. 10.25 mmol h<sup>-1</sup> g<sup>-1</sup> PHE rate from lactic acid aqueous solution was observed under visible light ( $\lambda > 420$  nm). Lastly, the report by Xu et al. can be given as a noticeable example for CdS nanosheets. CdS nanosheets was stabilized by L-cysteine. The resulted nanosheets performed 41.1 mmol h<sup>-1</sup> g<sup>-1</sup> PHE rate from Na<sub>2</sub>S/Na<sub>2</sub>SO<sub>3</sub> aqueous solution under visible light without any cocatalyst [104].

Obviously, CdS is very promising material for visible light induced PHE. However, one of the main problems cannot be overlooked: Cd leaching. Highly toxic Cd leaching [105] whose origin is a self-oxidation of CdS that is caused by photogenerated holes (Eq. 4) [106] can be considered an obstacle for its use in biological and aqueous systems. For this reason, many other metal-sulfide based photocatalytic systems [107] like ZnS, Cd<sub>1-x</sub>Zn<sub>x</sub>S solid solutions and ZnIn<sub>2</sub>S<sub>4</sub> emerge as a substitute for CdS.



Either cubic (sphalerite) or hexagonal (wurtzite), ZnS has the coordination geometry where Zn and S are of tetrahedral of crystal system with the band gap values of 3.72 eV and 3.77 eV, respectively [108]. Although its wide bandgap that limits its use for visible light induced PHE, ZnS is an attractive option for that kind of application by applying the strategies as in TiO<sub>2</sub>. For instance, 280  $\mu\text{mol h}^{-1} \text{g}^{-1}$  PHE rate was obtained from 1% mol Ni doped ZnS under visible light ( $\lambda > 420 \text{ nm}$ ) without cocatalyst from aqueous solutions containing K<sub>2</sub>SO<sub>3</sub> and Na<sub>2</sub>S [109]. Likewise, Cu doping effect on visible light induced PHE performance of ZnS was studied by Lee where the tuning of band gap was controlled by Cu<sup>2+</sup> ions in which 2% mol Cu<sup>2+</sup> ion doping was the optimum for the highest PHE rate of 973.1  $\mu\text{mol h}^{-1} \text{g}^{-1}$  under visible light ( $\lambda > 400 \text{ nm}$ ) from Na<sub>2</sub>S/Na<sub>2</sub>SO<sub>3</sub> aqueous solution without any cocatalyst [110]. Huang et al. investigated the effect of carbon group elements (C, Si, Ge, Sn, Pb) doping in ZnS using the first-principals of density functional theory concluding the absorptions of the doped structures in the visible light range are significantly enhanced while keeping their band alignment of doped ZnS still suitable for water splitting to generate hydrogen [111]. Efficient N-doped ZnS was outlined as a way to improve its stability and visible light activity by rising its VB level leading to decreased oxidation ability and bandgap where Zhou et al. reported relatively low PHE rate of 30  $\mu\text{mol h}^{-1} \text{g}^{-1}$  without Pt cocatalysts deposition from an aqueous solution containing methanol (10 % v/v) was used as a PHE medium [112]. The sensitization is among the other strategies that has been applied to ZnS. Wang et al. showed the notable effect of graphene as sensitizer where they reported 7.42  $\mu\text{mol h}^{-1} \text{g}^{-1}$  PHE rate from cocatalyst free ZnS from aqueous Na<sub>2</sub>S/Na<sub>2</sub>SO<sub>3</sub> solution. The sensitization effect of graphene was also proven by Zhang et al [113]. Despite their focus was not hydrogen evolution but visible light induced selective oxidation of alcohols and alkenes under ambient conditions. It was suggested that the role of the reduced graphene oxide was not an electron reservoir but photosensitizer acting like an organic molecule. Meantime, one can expect that SPR effect of Au NPs on ZnS might be also a successful strategy as for TiO<sub>2</sub>. However, Zhang et al. have proven that it is not the case because of the highly located CB level of the ZnS which prevents the excited energetic electrons in the SPR state from injecting into the CB of ZnS [114]. Intrinsic property engineering is another sufficient method as widely applied one is Zn vacancies. Those defects can form another energy level resulting in narrower bandgap and accelerate the charge carrier dynamics reducing the recombination of photogenerated holes and electrons [115,116]. Hao et al. reported 337.71  $\mu\text{mol h}^{-1} \text{g}^{-1}$  PHE rate from ZnS with Zn vacancies under visible light ( $\lambda > 420 \text{ nm}$ ) from Na<sub>2</sub>S/Na<sub>2</sub>SO<sub>3</sub> aqueous solution [116]. Then in their another study, they growth Zn vacancy ZnS on g-C<sub>3</sub>N<sub>4</sub> that exhibited 713.68  $\mu\text{mol h}^{-1} \text{g}^{-1}$  [115]. Combination with the other metal

sulfides can be mentioned as last example for visible light induced PHE from ZnS. Composition-controlled CdS/ZnS heterostructure generated hydrogen with the PHE rate 830.95  $\mu\text{mol g}^{-1} \text{h}^{-1}$  under visible light ( $\lambda > 420 \text{ nm}$ ) without any cocatalyst addition from  $\text{Na}_2\text{S}/\text{Na}_2\text{SO}_3$  aqueous solution.

The strategy to mix ZnS and CdS that is known as  $\text{Cd}_{1-x}\text{Zn}_x\text{S}$  solid solution whose band structure can be controlled by adjusting Cd/Zn ratio will be mentioned lastly.  $\text{Cd}_{1-x}\text{Zn}_x\text{S}$  solid solutions are preferable for visible light induced PHE due to their lower toxicity compared to CdS and increased visible light harvesting property higher than ZnS. An impressive PHE performance from two different crystal phase junctions of  $\text{Cd}_{1-x}\text{Zn}_x\text{S}$  was reported by Guo et al. without cocatalyst with the PHE rate of 282.14  $\text{mmol h}^{-1} \text{mg}^{-1}$  under visible light ( $\lambda > 420 \text{ nm}$ ) from  $\text{Na}_2\text{S}/\text{Na}_2\text{SO}_3$  aqueous solution [117]. Noble metal free  $\text{Ni}(\text{OH})_2$  cocatalyst deposited  $\text{Cd}_{0.3}\text{Zn}_{0.7}\text{S}$  material obtained by Lv et al. even resulted in higher rate 58.9  $\text{mmol h}^{-1} \text{g}^{-1}$  from the same conditions [118] as previously-mentioned report. From 20% v/v lactic acid aqueous solution, amorphous  $\text{MoS}_2$  decorated  $\text{Cd}_{0.8}\text{Zn}_{0.2}\text{S}$  performed PHE rate of 12.39  $\text{mmol g}^{-1} \text{h}^{-1}$  under visible light ( $\lambda > 420 \text{ nm}$ ) [119]. 2128  $\mu\text{mol h}^{-1} \text{g}^{-1}$  PHE rate was reported by Yu et al. in which CdS quantum dots-sensitization was achieved over  $\text{Zn}_{1-x}\text{Cd}_x\text{S}$  solid solution [120]. Additionally,  $\text{Cd}_{1-x}\text{Zn}_x\text{S}$  solid solutions can be doped by metals [89]. Closely, Luo et al. investigated the effect of Ni doping where noble metal free 5 wt % Ni-doped  $\text{Zn}_{0.8}\text{Cd}_{0.2}\text{S}$  showed 33.81  $\text{mmol g}^{-1} \text{h}^{-1}$  PHE rate under visible light from  $\text{Na}_2\text{S}/\text{Na}_2\text{SO}_3$  based sacrificial reagent solution [121]. Remarkable example for non-metal doping, P-doped  $\text{Cd}_{1-x}\text{Zn}_x\text{S}$  porous nano-spheres decorated with  $\text{Ni}_2\text{P}$  and reduced graphene oxide was studied by Sun et al. that produced hydrogen with the very high rate compared to the other reported metal sulfide based photocatalytic systems which was 616.8  $\text{mmol g}^{-1} \text{h}^{-1}$  [122].

Apparently, two terms “cocatalyst” and “sacrificial reagent” have been mentioned very frequently. Those are undoubtedly essential elements for photocatalytic systems for PHE applications. Shortly, alcohols such as methanol, isopropanol and ethanol are widely studied sacrificial reagents for PHE from metal-oxide based photocatalytic systems for scavenging photogenerated holes while cocatalysts are needed for several purposes such as electron capturer. Moreover, the sacrificial reagents which are effective for metal-oxide is not always a good fit for metal-sulfide based photocatalytic systems [123]. Thus, it is worth to clarify role of those terms in PHE mechanism before giving details about  $\text{ZnIn}_2\text{S}_4$  photocatalytic systems.

### 1.3.1 Cocatalyst for photocatalytic hydrogen evolution

Usually, the photocatalytic systems require a noble metal based cocatalyst to boost their PHE performance as the surface reaction that is necessary for PHE along with photogenerated charge transfer is inhibited by the charge carrier recombination [124,125]. At this juncture, one of the affirmed functions of the cocatalysts can be defined as an “electron sink”. The accumulation of the photogenerated electrons to the electron sink reduces the photogenerated electron-hole recombination. Basically, this is related with the work function of the cocatalyst where higher working function provides better capturing ability of electrons (Figure 8, route I). This is one the reason why Pt is one of the most widely used cocatalyst due its high work function (5.93 eV) compared to other metals such as Pd (5.60 eV), Cu (5.10 eV), Ru (4.71 eV), and Ag (4.26 eV) [126]. Moreover, cocatalysts facilitate the proton reduction providing active sites for H adsorption in accordance with the Volmer reaction (Figure 8, route II). Then the reaction route might go into two ways one Heyrovsky step or Tafel step in which an adsorbed hydrogen intermediate ( $H^*$ ) reacts with a second hydrogen ion (or water molecule in the case of alkaline condition) or another  $H^*$ , respectively (Figure 8) [127–130]. As expected, a molecular hydrogen desorption occurs in both cases. On the assumption that Sabatier’s principle is the only factor affecting the surface reactions initiating the hydrogen evolution from cocatalyst surface, the

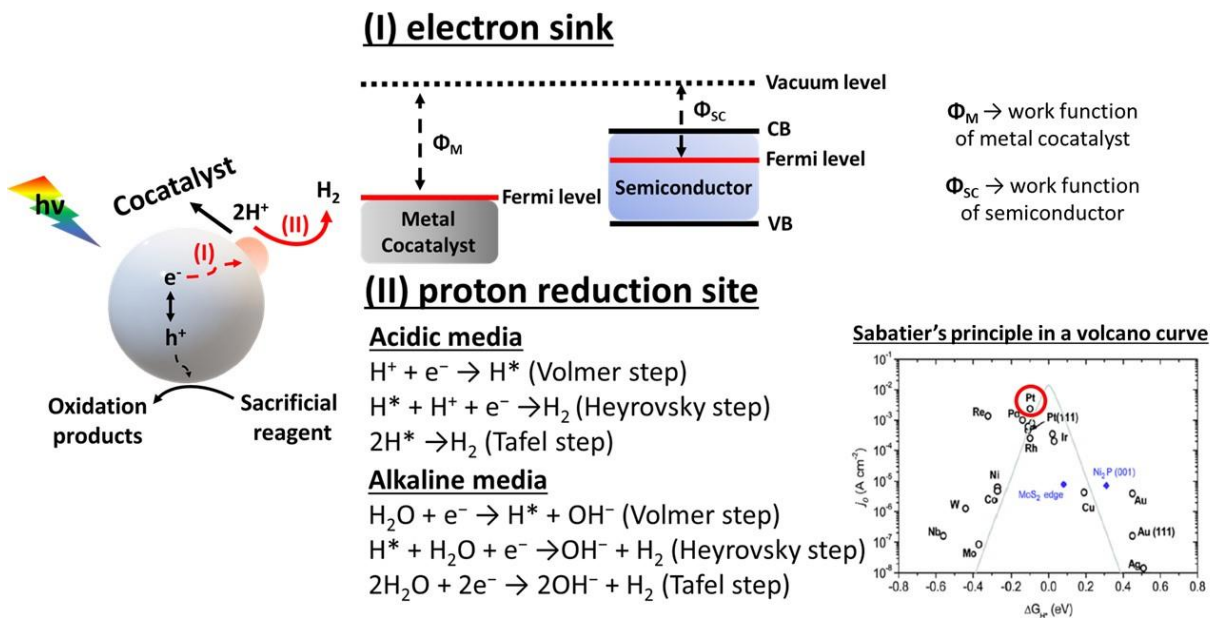


Figure 8 Two main functions of the cocatalyst in the photocatalytic system: (I) cocatalyst is an electron sink which is highly related with the work function that is the difference between the Fermi level (electrochemical potential) and vacuum level (inspired from Beasley et. al [126]). Cocatalyst should provide an active site for (II) proton reduction for hydrogen evolution in accordance with Volmer, Heyrovsky and Tafel reactions depending on the pH of the PHE medium (Volcano curve was taken

ideal cocatalyst should bind to  $H^*$  moderately, not too weak and too strong [127,131]. Thus, when viewed from this perspective, Pt seems as one of the closes to the ideal cocatalyst since its hydrogen adsorption energy is the nearest the zero (Figure 8, Volcano curve) [127].

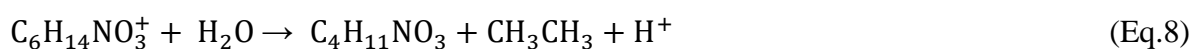
The methods for Pt cocatalyst deposition over the surface of the target photocatalytic system can be divided into *ex situ* and *in situ* deposition. The *ex situ* deposition technique is the method where the cocatalyst loading is achieved by chemical or photochemical methods in the designated conditions followed by the PHE test of cocatalyst deposited photocatalytic system. Chemical and photochemical *ex situ* methods both begin with addition of the Pt cocatalyst precursor solution to the dispersion of the photocatalyst. Then the reduction of the Pt complex ions is accomplished using reducing reagents (such as  $NaBH_4$ ) in the chemical deposition while in the photochemical deposition (mostly called photodeposition), the reduction of the precursor is achieved by the photogenerated electrons over the conduction band of the photocatalytic system. On the other hand, *in situ* deposition method requires the photoreduction of the precursor salt by adding the precursor solution to the PHE reactor just prior to PHE test. This technique leads to the photodeposition of the Pt cocatalyst while simultaneous generation of hydrogen fuel. As in this thesis, the applied method for cocatalyst loading was *ex situ* and *in situ* photodeposition. The condition of the cocatalyst deposition (dissolved oxygen in PHE medium and pH) can drastically change the state of Pt cocatalyst thus PHE rate [P1, P2]. Moreover, the oxidation state of Pt in the Pt precursor salt is another determining factor of PHE performance of the photocatalytic system [P3]. It is worth noting that Pt photodeposition in all the works [P1-P3] resulted in different Pt species, such as  $PtS_x$ ,  $Pt(OH)_2$  and  $PtO_x$  due to the different conditions of the photodeposition, respectively.  $PtS_x$  species are readily formed under neutral conditions as anhydrous ethanol was used as a *ex situ* photodeposition media [P1] while  $Pt(OH)_2$  was the dominant specie of *in situ* Pt deposition due to the highly alkaline PHE media originating from the sacrificial reagents [P2]. Glycerol-water mixture (5% v/v,  $pH \approx 7$ ) in the last study, the resultant Pt specie was  $PtO_x$ . The effect of the cocatalyst depending on the deposition methods, oxidation number of Pt, pH of photodeposition media (the role of sacrificial reagent) were deeply discussed in the review by Wenderich and Mul [132] and also in Section 1.5.

Not surprisingly, a noble metal free cocatalyst design have attracted a lot of interest due to the high cost of Pt.  $MoS_2$  [133], Ni-based ( $NiO_x$ ,  $Ni(OH)_2$ ,  $NiS$ ,  $Ni_2P$ ) [134], Co-based (Co, oxides, hydroxides, sulfides) [135], metal-organic framework (MOF) based [136] or even hydrogenase enzyme [137] cocatalysts are some of reported alternatives to Pt. Besides, ultra-low Pt loading

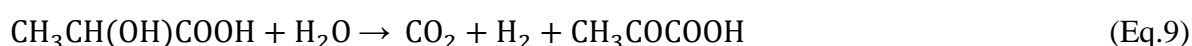
can increase the PHE rate better than higher Pt loading [P3] depending on the deposition technique [138] or in some cases forming single-atom Pt cocatalyst over the matrix surface therefore the lower concentration results superior PHE rate than higher Pt loading [139].

### 1.3.2 Sacrificial reagent for photocatalytic hydrogen evolution

Sacrificial reagents are crucial factor for PHE applications since the photogenerated holes must be scavenged to improve the charge separation. Otherwise, the pure water splitting through PHE application is almost not feasible because PHE rate without them is too low [140]. The metal sulfide based photocatalytic systems have been studied with usually three different types of sacrificial reagent. Among them triethanolamine (TEOA) is an organic electron donor which is tertiary aliphatic amine whose degradation pathway during its oxidation through photocatalytic processes was very detailed discussed elsewhere [141,142]. Briefly, the oxidation pathway of TEOA starts with the electron transfer forming the positively charged radical followed by the deprotonation and lastly formation of secondary amine and ethanal (Eq.5-8) [123].

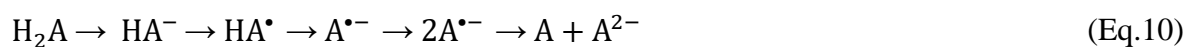


Other widely used sacrificial reagent is lactic acid whose degradation way ends up with usually a formation of pyruvic acid with CO<sub>2</sub> and H<sub>2</sub> release [123,143]. Ascorbic acid is another encountered sacrificial reagent



Ascorbic acid is another encountered sacrificial reagent whose degradation pathway by photogenerated holes were described in detail by Pellegrin and Odobel as seen in Eq. 10 where

H<sub>2</sub>A (ascorbic acid) forms ion (HA<sup>-</sup>) that is oxidized to HA<sup>•</sup> radical and finally forms A<sup>•-</sup> to A (dehydroascorbic acid) and A<sup>2-</sup> (ascorbate) [141,144]



Na<sub>2</sub>S/Na<sub>2</sub>SO<sub>3</sub> sacrificial reagent, maybe the most popular inorganic scavenger, is especially favored for the metal sulfides due its several benefits. Firstly, Na<sub>2</sub>S/Na<sub>2</sub>SO<sub>3</sub> sacrificial reagent are more readily to be oxidized compared to TEOA and alcohols [145]. Moreover, Na<sub>2</sub>S/Na<sub>2</sub>SO<sub>3</sub> sacrificial reagent inhibits the corrosion of metal sulfides through self-repairing mechanism as in the case of CdS based photocatalytic system where Cd<sup>2+</sup> ions react with S<sup>2-</sup> and form CdS. Same mechanism can be also expected such as ZnS and other metal-sulfide based photocatalytic systems. Finally, Na<sub>2</sub>S/Na<sub>2</sub>SO<sub>3</sub> aqueous solution forms highly alkaline PHE condition [P2] (Eq. 13-14) facilitating the hydroxylation of the metal sulfide photocatalyst surface which decrease the aggregation of the photocatalyst that might be favorable for PHE.



The mechanism of hole scavenging through the oxidation of Na<sub>2</sub>S/Na<sub>2</sub>SO<sub>3</sub> sacrificial reagent can be given as follows. Briefly, both sulfite and sulfide ions are oxidized by the photogenerated holes on the VB level. Sulfite can transform into two different ions after the oxidation which are dithionate or sulfate. Dithionate occurs through bonding of the sulfite radicals that requires only photogenerated holes (Eq.13) while sulfate ions are produced via holes and hydroxyl ion (Eq. 14). The formation of dithionate is thermodynamically less favorable [140] than that of sulfate ions so one can assume that the dominant oxidation product of sulfate in the PHE media is sulfate.





On the other hand, sulfide ions are oxidized to disulfide ions (Eq. 15) that can be reduced by photogenerated electron which compete with the  $H^+$  ions [140]. Moreover, they act as a light filter in the PHE media [145]. However, the excess formation of disulfide ions is blocked because disulfide and sulfide ions undergo the formation of thiosulfate ion (Eq. 16) [146]. Thus, the presence of the sulfide ions is crucial to prevent the undesired effects of sulfide ions that inhibits the performance of photocatalytic system.



The formation of the thiosulfate ion is even beneficial for the PHE performance of the overall photocatalytic system because it can act also as a sacrificial reagent (Eq. 17) resulting tetrathionate [147].



$Na_2S/Na_2SO_3$  with the concentration of 0.35 M/0.25 M is somehow popularly selected for PHE studies in the literature. However, the motivation in this thesis was the work done by Guo et al. where 0.35 M/0.25 M  $Na_2S/Na_2SO_3$  was used [148].

Lastly, in the last work [**P3**], glycerol has been preferred for the first time in the literature for the purpose of its photocatalytic glycerol reforming to achieve PHE, unconventionally. The degradation by-products are numerous during PHE but apart from the mechanism, the reaction pathway follows as in Eq. 18 [149,150]. Qualitative analysis of by-products of glycerol from the designed photocatalytic system in the work will be discussed further.



#### 1.4 ZnIn<sub>2</sub>S<sub>4</sub> based photocatalytic systems for photocatalytic hydrogen evolution

As three different types of metal sulfide based photocatalyst materials have been shortly summarized so far, ZnIn<sub>2</sub>S<sub>4</sub>, the main topic of the thesis, will be discussed in this section.

The first reports on ZnIn<sub>2</sub>S<sub>4</sub> which is a ternary type chalcogenide (AB<sub>2</sub>X<sub>4</sub>) material started with Lappe et al. in 1962 [151] followed by the study by Shionoya and Tamoto in 1964 [152] on the photoluminescence and photoconductivity of ZnIn<sub>2</sub>S<sub>4</sub> produced via the chemical transport reaction. Yet again in the same year, Shionoya and Ebina studied the refractive index, fundamental absorption, and infrared lattice absorption properties of ZnIn<sub>2</sub>S<sub>4</sub> [153]. Physiochemical characteristics of ZnIn<sub>2</sub>S<sub>4</sub> like photoconductivity, photoluminescence, thermoluminescence, optical absorption were some of the research subjects on ZnIn<sub>2</sub>S<sub>4</sub> [151,154–160] along with its application in solar cells in which its reported n-type character was combined with p-type CuInSe<sub>2</sub> creating p-n junction [151] from 1970 to early 2000.

The pioneering research on PHE from aqueous solution mixture of Na<sub>2</sub>S/Na<sub>2</sub>SO<sub>3</sub> and ZnIn<sub>2</sub>S<sub>4</sub> photocatalyst was conducted by Lei et al. in 2003 (Figure 9) where the relatively mild hydrothermal synthesis method was implemented to obtain ZnIn<sub>2</sub>S<sub>4</sub> photocatalyst compared to its counterpart, chemical transport method, to overcome limitations originating from the need of high temperature and vacuum and carrier reagent such as iodine. 333 μmol h<sup>-1</sup> g<sup>-1</sup> PHE rate was reported in the presence of *in situ* Pt deposition (2 wt.%) showing the stability up to 150 hours under visible light irradiation ( $\lambda > 420$  nm) [161]. In 2006, Gou et. al proved that the morphology-controlled synthesis methods of ZnIn<sub>2</sub>S<sub>4</sub> using solvothermal method or surfactant assisted hydrothermal method initiating the formation of different morphologies. Solvothermal method with pyridine as a solvent produced nanoribbons while surfactant, polyethylene glycol or CTAB, assisted hydrothermal method resulted in microspheres [162]. This work has been followed by the three significant works by Guo et al. in 2008 where the effect of the concentration of CTAB in the hydrothermal synthesis medium [163], Cu-doping in CTAB assisted ZnIn<sub>2</sub>S<sub>4</sub> [148] and aqueous-, methanol- and ethylene glycol-mediated conditions via a solvothermal/hydrothermal method on PHE performance [164] under visible light irradiation ( $\lambda > 430$  nm or  $> 420$  nm) from Na<sub>2</sub>S/Na<sub>2</sub>SO<sub>3</sub> (0.35 M/0.25M) with *in situ* deposited Pt cocatalyst.

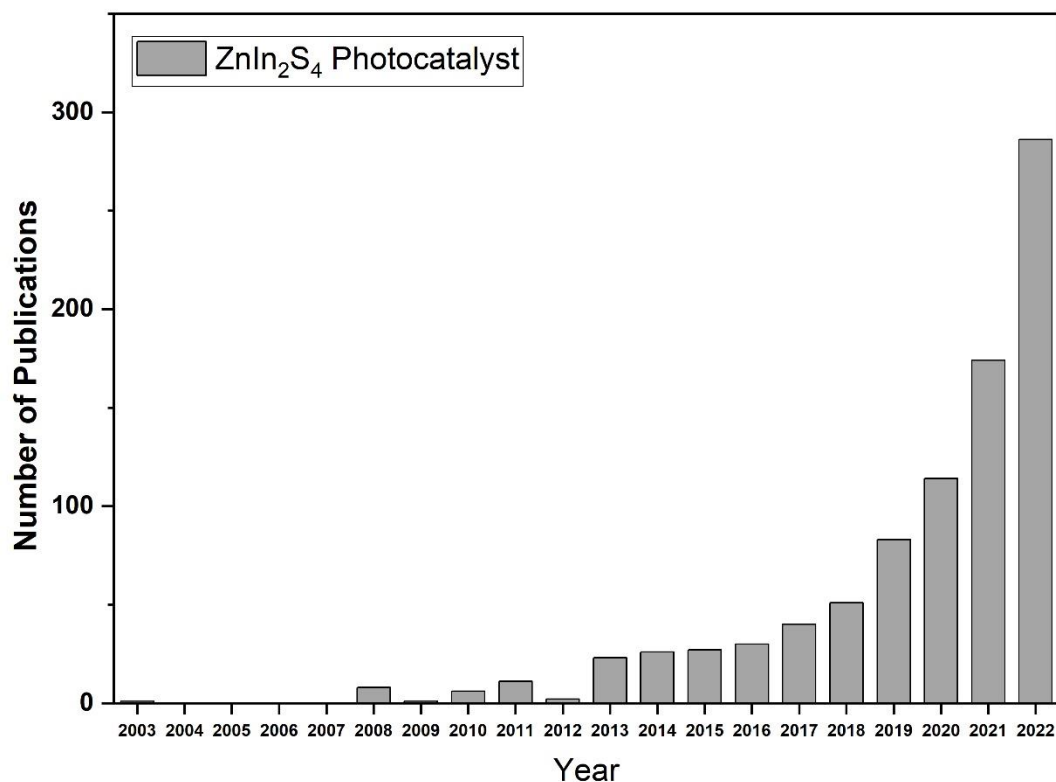


Figure 9 Number of publications from the beginning of the first photocatalytic application of  $ZnIn_2S_4$  in 2003 to 2022. Data was accessed from Scopus (Elsevier) on December 14, 2022

The crystal structure of  $ZnIn_2S_4$  in Lei's work [161] was hexagonal, but  $ZnIn_2S_4$  has three different polymorphs in total including hexagonal, cubic, and trigonal. All the polymorphs have visible light absorption (band gap ranges between 2.06-2.85 eV) [165] however their photocatalytic performances differ. Probably the least studied polymorph is trigonal structured  $ZnIn_2S_4$  whose PHE activity was reported only in two studies. Hodjamberdiev et al. [166] have treated ZnS from industrial waste with different fluxes containing indium salts using flux method to obtain  $ZnIn_2S_4$  photocatalyst in which the resultant polymorph was trigonal. Another trigonal structured  $ZnIn_2S_4$  synthesis has been accomplished by Liao et al. where a solid reaction method under 700 °C was utilized [167]. The unpopularity of the trigonal structured  $ZnIn_2S_4$  is possibly related with its high temperature synthesis conditions even its crystal structure is like the hexagonal polymorphed  $ZnIn_2S_4$ . Hexagonal polymorph of  $ZnIn_2S_4$  is the most popular for PHE among all polymorphs where Zn atoms and the half of the In atoms have tetrahedral coordination with S atoms whereas the other half of In atoms have octahedral coordination with S atoms which has ABAB stacking [165,168]. This configuration is likely identical to trigonal polymorph however it was suggested that main difference is the sulfur arrangement and metal site occupancy where the stronger Zn-S or In-S bonds exist compared

to hexagonal while S-S bonds are weaker [169]. On the other hand, the cubic structured  $\text{ZnIn}_2\text{S}_4$  is much more studied polymorph than that of trigonal but lesser focused than hexagonal. In atoms and Zn atoms have coordination with S octahedrally and tetrahedrally respectively [169]. Beyond the thermal transformation under the extreme conditions from hexagonal to cubic and trigonal [169], mild synthesis methods can be also applied for the structure control by changing precursor for  $\text{ZnIn}_2\text{S}_4$  synthesis [170,171]. In this thesis, mostly hexagonal phase will be discussed, as the synthesis method in the experimental part was adopted from the previously mentioned work by Guo [148].

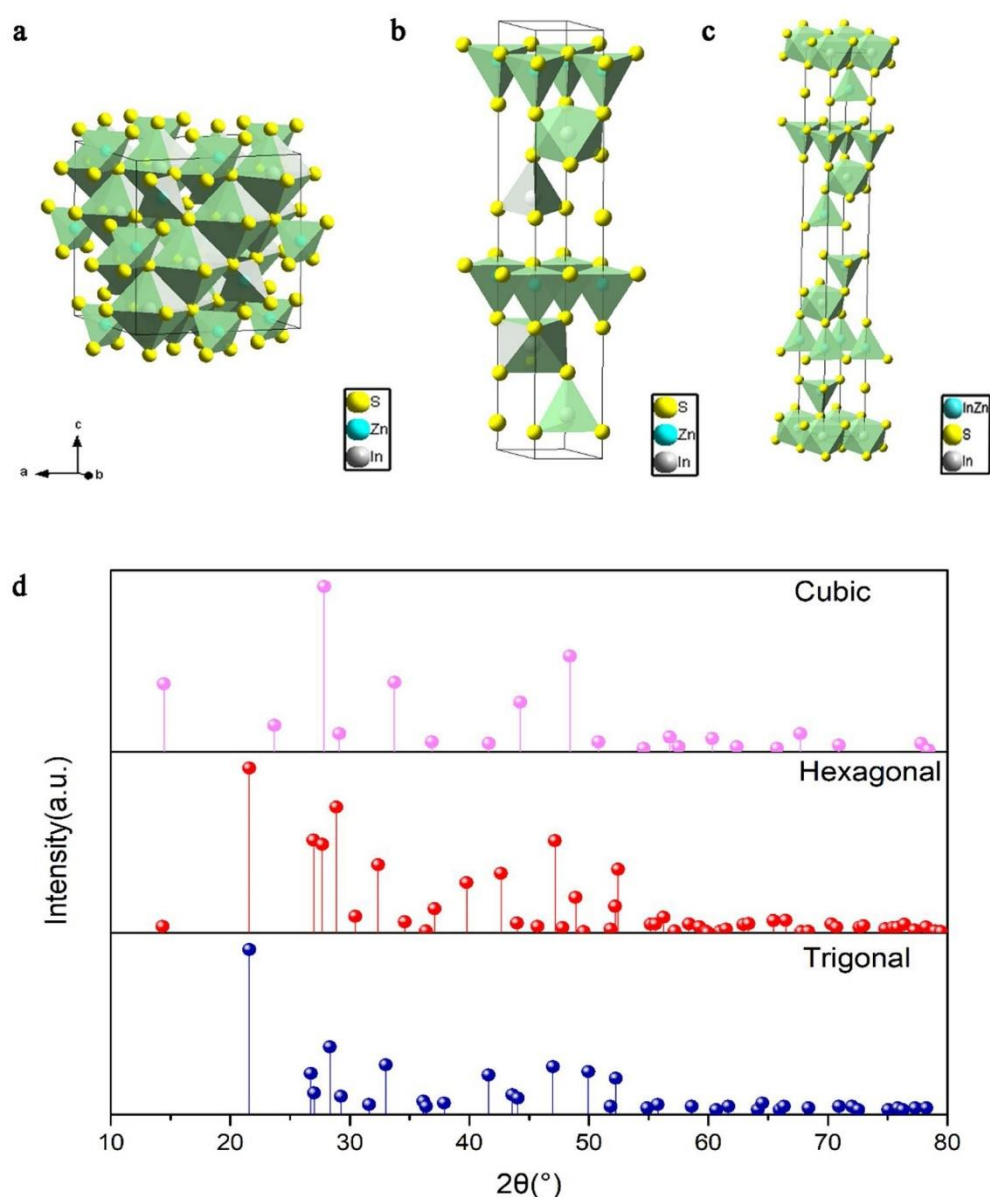


Figure 10 a) Cubic, b) hexagonal and c) trigonal structures of  $\text{ZnIn}_2\text{S}_4$  with d) their XRD patterns. Reproduced with the permission of Ref. [169]. Copyright (2021) Elsevier.

It can be seen from the early examples of  $\text{ZnIn}_2\text{S}_4$  (ZIS) on PHE that it has all the positive sides of CdS such as reduction ability for PHE applications and suitable bandgap for visible light harvesting without owning the worst characteristic problem of CdS: the toxicity. However, the recombination is one of the main addressed troubles along with the stability due to the lack of active catalytic sites and low Brunauer–Emmett–Teller (BET) area around  $20 \text{ m}^2 \text{ g}^{-1}$  [P1] [172]. Indeed, doping techniques and vacancy engineering as reported in other metal sulfides are valid for ZIS to overcome those obstacles. For example, Zhang et al. reported that 5 mol % Cu doping created S-vacancies in ZIS forming nanosheet morphology which exhibited PHE rate without noble metal cocatalyst loading with PHE rate of  $9.8647 \text{ mmol g}^{-1} \text{ h}^{-1}$  from 0.2 M ascorbic acid aqueous solution under visible light [173]. This significant performance without cocatalyst was attributed to the synergetic effect between atomic Cu and S-vacancy regulating the charge separation in the ZIS lattice. Another work on Cu-doped ZIS by Wang et al. has proven that 0.5 wt.% Cu doping substituted Zn atoms in ZIS lattice causing the creation of electron acceptor level close to the VB of ZIS leading efficient charge carrier transport with  $26.2 \text{ mmol g}^{-1} \text{ h}^{-1}$  PHE rate under simulated sun with 1 wt.% Pt *in situ* loading from 0.75 M ascorbic acid aqueous solution [174]. More example can be given such as noble metal cocatalysts-free Co-doped ZIS nanotubes [175], Ni- [176], Mo [177]-doped nanosheets and Mo-[178], Cr[179]-doped ZIS microspheres are other examples of metal doping while N-, and O-doped ZIS can be given as an example of nonmetal doping strategy. For instance, Du et al. obtained N-doped ZIS by adjusting the dosage of *N,N*-dimethylformamide in solvothermal reaction medium resulting in not only efficient charge separation but elevated conduction band where optimum N-doping performed  $11086 \text{ } \mu\text{mol g}^{-1} \text{ h}^{-1}$  under visible light irradiation ( $\lambda > 400 \text{ nm}$ ) from 10% v/v triethanolamine aqueous solution without cocatalyst loading [180]. O-doping was applied Yang et al. where O-doped ZIS nanosheets that generated hydrogen from  $\text{Na}_2\text{S}/\text{Na}_2\text{SO}_3$  aqueous solution under visible light with the PHE rate of  $2120 \text{ } \mu\text{mol h}^{-1} \text{ g}^{-1}$ . without cocatalyst deposition [181].

Introducing of vacancy can be either anionic, S vacancies, or cationic which is mostly Zn vacancies in the literature. However, S vacancy is broadly investigated strategy for PHE application while Zn vacancy was mostly examined for  $\text{CO}_2$  reduction and only one report was found in the literature for PHE. S vacancy in ZIS can trap the photo-generated electrons to inhibit the recombination of photogenerated charge carrier as reported by Du et al. [182]. They reported ZIS nanosheets with sulfur vacancies exhibiting  $13.478 \text{ mmol g}^{-1} \text{ h}^{-1}$  under the visible light irradiation ( $\lambda > 400 \text{ nm}$ ) from 10% v/v triethanolamine aqueous solution without

cocatalyst loading. S vacancies can be also used as a site for effective MoS<sub>2</sub> cocatalyst loading on ZIS nanosheets surface to favor the direct electron transfer to cocatalyst to prevent vertical electron migration as shown by Zhang et al. where 6.884 mmol g<sup>-1</sup> h<sup>-1</sup> PHE rate was achieved from 10% v/v lactic acid aqueous solution under simulated solar irradiation [183].

Combining another semiconductor photocatalyst with ZnIn<sub>2</sub>S<sub>4</sub> forming heterojunctions is broadly applied strategy to enhance the PHE performance. Heterojunction strategies were categorized in this thesis into four types: Type I, Type II, p-n junction, and Z-scheme. The schematic description of those mechanisms in Figure 11 to simplify to follow the literature review given below.

In Type I heterojunction systems, the electron and hole transfer are initiated from the one photocatalyst to the second semiconductor (SC 2) photocatalyst where both oxidation and reduction reactions take place. This is due to the SC 1 has higher CB level and lower VB than that of SC 2. Ji et al. obtained ZIS/ultra-thin-g-C<sub>3</sub>N<sub>4</sub> photocatalytic system with the PHE rate of 5.02 mmol g<sup>-1</sup> h<sup>-1</sup> under Xe lamp irradiation (full spectrum) from 20% triethanolamine aqueous solution with *ex situ* NiS deposition where g-C<sub>3</sub>N<sub>4</sub> and ZIS acted as SC 1 and SC 2,

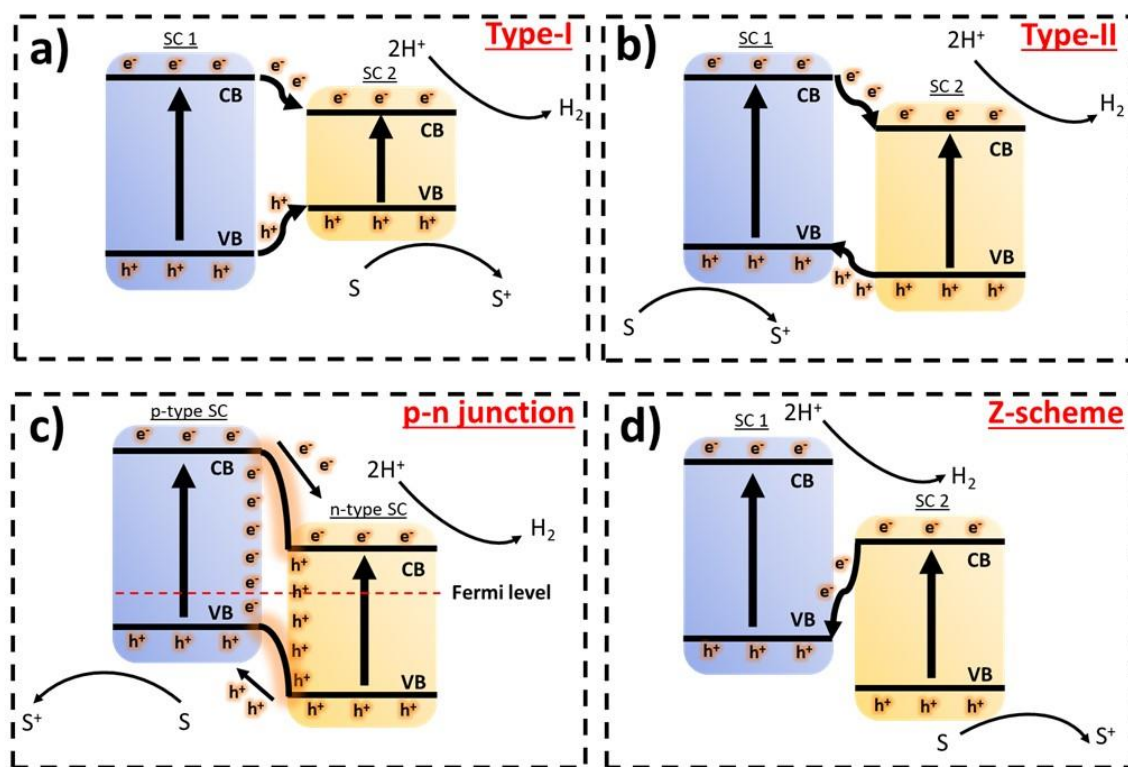


Figure 11 Mechanisms of different heterojunctions for PHE applications a) Type-I, b) Type-II, c) p-n junction and d) Z-scheme where SC and S are semiconductor and sacrificial reagent, respectively.

respectively. However, it was shown that the NiS deposition was also on the g-C<sub>3</sub>N<sub>4</sub> surface therefore hydrogen evolution process occurred on SC 1 either [184]. ZIS performed the function as a SC 1 in the work by Xiao in the 1D/2D core/shell Sb<sub>2</sub>S<sub>3</sub>-ZIS photocatalytic system which exhibited 1685.14  $\mu\text{mol g}^{-1} \text{h}^{-1}$  PHE rate 3 wt% Pt *in-situ* loading under the same irradiation and PHE media condition as Ji used [185]. ZIS as a SC1 can be seen also from SnS@ZIS heterostructure which was synthesized by Gunjal et al. [186]. The SnS@ZIS photocatalytic system performed 650  $\mu\text{mol h}^{-1} \text{g}^{-1}$  from methanol aqueous solution (20% v/v) and 6429  $\mu\text{mol h}^{-1} \text{g}^{-1}$  from H<sub>2</sub>S under sunlight where SnS acted as a cocatalyst. Cheng et al. demonstrated integration of ReS<sub>2</sub> (SC2) on ZIS (SC1) microspheres which has obeyed the Type I heterojunction mechanism. Without a noble metal loading, the photocatalytic system generated hydrogen fuel with the PHE rate of 3092.9  $\mu\text{mol h}^{-1} \text{g}^{-1}$  as a result of oxidation of furfural alcohols under visible light ( $\lambda > 420 \text{ nm}$ ) [187].

In comparison with Type I mechanism, the main difference in Type II is that the oxidation and the reduction occur separately over SC1 and SC2, respectively. Basically, SC1 has higher CB level than SC2 while both having sufficient level of CB for proton reduction for hydrogen evolution but appears over SC2 whereas photogenerated hole transfer is towards the SC1 from SC2 as SC2 has lower level of VB than that of SC1. The advantage of Type II mechanism over Type I might be related with the staggered charge carrier distribution in Type II favors the efficient charge separation (the electron and hole accumulation to SC2 and SC1, respectively) while straddling path of charge carriers in Type I initiates all photogenerated electrons and holes over SC2 which is more like to have tendency to recombine [188]. CdS/ZIS Type II heterojunction has shown 2260  $\mu\text{mol h}^{-1} \text{g}^{-1}$  PHE rate under visible light ( $\lambda > 420 \text{ nm}$ ) from triethanolamine aqueous solution (9% v/v) in the presence of Pt *in situ* deposition (the amount of the Pt loading was not given) where ZIS functioned as SC2 while CdS SC1 [189]. The reverse role of ZIS as SC1 can be seen in the work by Chen et al. where they obtained hierarchical hollow tubular g-C<sub>3</sub>N<sub>4</sub>/ZIS nanosheets with the Type II construction energy level alignment. The photocatalytic system exhibited 20738  $\mu\text{mol h}^{-1} \text{g}^{-1}$  PHE rate under visible light ( $\lambda > 420 \text{ nm}$ ) with the aid of *in situ* 1 wt.% deposited Pt from 10% (v/v) triethanolamine aqueous solution [190]. Wang et al. proposed opposite role in the identical photocatalytic system as in Chen's work where ZIS was SC2. The system exhibited 1.63 mmol  $\text{g}^{-1} \text{h}^{-1}$  under visible light ( $\lambda > 420 \text{ nm}$ ) from triethanolamine aqueous solution (9% v/v) with Pt *in situ* deposition (the amount was not described) [191]. Pudkon et al. synthesized ZIS/WS<sub>2</sub> composites which

achieved  $76.6 \mu\text{mol h}^{-1} \text{g}^{-1}$  PHE rate under visible light from  $\text{Na}_2\text{S}/\text{Na}_2\text{SO}_3$  (0.35 M/0.25 M) without noble metal deposition [192].

On the other hand, the p-n junctions, the configuration is identical to Type II, however the internal electric field is additionally created thanks to the combination of p-type and n-type semiconductors where the Fermi level located closer to VB maximum and the CB minimum in p- and n-type semiconductor, respectively. The origin of the electric field between the interface of the p- and n-type semiconductor (p- and n-type SC) photocatalyst is due to the contact initiating the electron flow from p-type to n-type whereas holes from n-type to p-type. After Fermi levels of both semiconductor reaches equilibrium, the charge flow is terminated that creates inner electric field [168,193,194]. Thus, it has been argued that p-n junctions are more suitable for charge separation than that of Type II [168]. Multidimensional hierarchical hollow  $\text{Co}_3\text{O}_4/\text{ZIS}$  tubular core-shell heterostructures where growth of ZIS nanosheets (n-type SC) was carried out over  $\text{Co}_3\text{O}_4$  tubular structure (p-type SC) was achieved by Zhang et al [195]. It was proposed that the p-n junction originated internal electric field was the main factor of the synergetic effect in which the heterostructure exhibited  $3844.12 \mu\text{mol h}^{-1} \text{g}^{-1}$ , which was 4.67 times higher than that of pristine ZIS from triethanolamine aqueous solution (9:1 vol ratio) under visible light ( $\lambda > 400 \text{ nm}$ ) irradiation without noble metal cocatalyst [195]. Another noble metal cocatalyst-free photocatalytic system was investigated by Zhang et al [196]. The combination of ZIS with sulfur vacancies (VZIS) and  $\text{NiWO}_4$  where p-n junction was achieved after the contact from Type-I alignment.  $\text{NiWO}_4$  (p-type SC) was grown on the pre-prepared VZIS (n-type SC) using ion-precipitation method and the final VZIS/ $\text{NiWO}_4$  composite generated hydrogen with the PHE rate of  $1.781 \text{ mmol g}^{-1} \text{h}^{-1}$ , around 10 times higher than pure ZIS. The pre-prepared ZIS microspheres (n-type SC) and  $\text{AgFeO}_2$  (p-type SC) nanoparticles were combined using ultrasound-calcination process by Kong et al [197]. The ZIS (n-type SC)/ $\text{AgFeO}_2$  (p-type SC) composite performed PHE rate of  $9.14 \text{ mmol h}^{-1} \text{g}^{-1}$  from  $\text{Na}_2\text{S}/\text{Na}_2\text{SO}_3$  which was 30 folds higher than that of pristine ZIS. Noble metal-free ZIS nanosheets on  $\text{FeWO}_4$  flowers was obtained by again Kong [198] to create p-n junction that produced hydrogen from  $\text{Na}_2\text{S}/\text{Na}_2\text{SO}_3$  aqueous solution with the PHE rate of  $3531.2 \mu\text{mol h}^{-1} \text{g}^{-1}$  under Xenon lamp irradiation (full spectrum).



Combining metal sulfide based with p-type characteristics with n-type ZIS photocatalyst is other encountered example in the literature for p-n junction photocatalytic systems. Broadly investigated MoS<sub>2</sub> as an alternative cocatalyst is literally a low-bandgap p-type semiconductor and some of the reported examples of the ZIS/MoS<sub>2</sub> photocatalytic systems were proposed as a p-n junction. Swain et al. showed very high PHE rate from Au-nanodot-promoted MoS<sub>2</sub>/ZIS with p-n junction between ZIS and MoS<sub>2</sub> that displayed around 28 mmol g<sup>-1</sup> h<sup>-1</sup> PHE rate under visible light ( $\lambda > 400$  nm) from Na<sub>2</sub>S/Na<sub>2</sub>SO<sub>3</sub> aqueous solution. Sun et al. synthesized hierarchical 3D carbon nanofibers (CNFs)/MoS<sub>2</sub>/ZIS composites with p-n heterojunctions. The photocatalytic system generated relatively high hydrogen with 151.42 mmol h<sup>-1</sup> g<sup>-1</sup> PHE rate among all reported examples in this thesis [199]. Similar function can be seen from the report by Fan et al. where 3D CuS@ZIS hierarchical nanocages with 2D/2D nanosheet morphology with p-n junction were studied. It was discussed that thanks to the proper band structure of CuS and its cocatalyst function matching with n-type semiconductor ZIS to form p-n heterojunction, the composite exhibited enhanced 7910  $\mu\text{mol h}^{-1} \text{g}^{-1}$  PHE rate from Na<sub>2</sub>S/Na<sub>2</sub>SO<sub>3</sub> aqueous solution [200].

CuInS<sub>2</sub> (CIS) is another p-type metal sulfide based semiconductor that has been investigated to increase PHE performance of ZIS. The first study on CIS/ZIS photocatalytic system for PHE application was reported by Guan et al. in 2019. In their method, ZIS microspheres were prepared via hydrothermal method followed by the solvothermal growth of CIS on the ZIS surface. To achieve the strong contact between ZIS and CIS, the product was calcined at 200 °C under N<sub>2</sub> atmosphere. 5 wt.% CIS loading was the optimum for the highest PHE rate of 3430.2  $\mu\text{mol g}^{-1} \text{h}^{-1}$  from Na<sub>2</sub>S/Na<sub>2</sub>SO<sub>3</sub> (0.35 M/0.25 M) with *in situ* Pt deposition (2 wt.%) under visible light irradiation ( $\lambda > 420$  nm) [201]. Likewise, the second report regarding CIS/ZIS photocatalytic system was published in 2020 by Guo et al. where the function of CIS as a p-type match for forming p-n junction and cocatalyst were investigated. CIS growth over ZIS created core-shell structure where the optimum CIS loading (5 atom%) without Pt deposition even exhibited higher performance (292  $\mu\text{mol g}^{-1} \text{h}^{-1}$ ) than that of Pt photodeposited (0.05 wt.%) ZIS (237  $\mu\text{mol g}^{-1} \text{h}^{-1}$ ) [202]. Additionally, **P1** and **P2** can be considered as detailed studies contributing to those achievements which proves CIS loading as a promising improvement method of ZIS photocatalyst that will be discussed in detail further (Section 1.5, Summary of the publications). Briefly, on the contrary, ZIS growth was achieved hydrothermally with the addition of pre-prepared CIS quantum dots (QDs) to achieve the contact between ZIS and CIS [**P1**] while in **P2**, comparatively mild method was preferred to

achieve the contact between ZIS and CIS QDs where both pre-prepared ZIS and CIS QDs were combined in aqueous solution by adjusting the pH level, to investigate the capping ligand initiated aggregation effect of CIS QDs on PHE rate of ZIS/CIS photocatalytic system. According to the given examples by Guan and Guo, the expected mechanism was p-n junction.

Lastly, Z-scheme mechanism is the combination of two semiconductor photocatalysts with strong reduction (SC1 in Figure 11) and oxidation (SC2 in Figure 11) capability. The photogenerated electrons in CB of SC2 migrates to VB of SC1. This type of charge transfer mechanism extends the life span of charges and conserve the higher reducing ability of CB electrons of SC-II and the oxidizing ability of holes in VB of SC-I [203]. In fact, there are 3 kinds of Z-scheme mechanisms. However, as-explained mechanism applies to direct Z-scheme mechanism in addition to traditional Z-scheme and all-solid-state Z-scheme where photocatalytic systems require shuttle redox ion pairs and solid-state mediator respectively.  $H_xMoO_3@ZIS$  hierarchical direct Z-scheme heterojunction was obtained by Xing et al. 5.9 mmol  $g^{-1} h^{-1}$  PHE was achieved from 10% (v/v) triethanolamine aqueous solution without noble metal cocatalyst under visible light where electrons in the conduction band of ZIS (SC 1) and holes in the valence band of  $H_xMoO_3$  (SC 2) efficiently involve in the  $H^+$  reduction and sacrificial agent oxidation reaction, respectively [204]. Z-scheme  $CeO_2/ZIS$  photocatalytic system for PHE via oxidation of aromatic alcohols was obtained ZIS nanosheets growth on  $CeO_2$  nanorods. It was proposed that Z-scheme was achieved in  $CeO_2/ZIS$  thanks to the contact at the interface of  $CeO_2$  and ZIS that induced charge separation and transfer. The system performed 1496.6  $\mu mol g^{-1} h^{-1}$  PHE rate under solar simulation with no noble metal cocatalyst addition to the photocatalytic system [205]. ZIS (SC 1)/ $BiVO_4$  (SC 2) heterojunction with Z-scheme mechanism was achieved by Hu et al. by simple oil-bath growth of ZIS nanosheets on micro-sized decahedron  $BiVO_4$ . 5.944 mmol  $g^{-1} h^{-1}$  PHE rate was reported which is about five times higher than that of pure  $ZnIn_2S_4$  in the presence 3 wt.% *in situ* photodeposited Pt [206].

Bi-based photocatalysts seem a good match for a template-like structure as seen from Hu et al. [206]. Comparably, in **P3**, Z-scheme mechanism in  $BiOCl@ZIS$  was suggested not due to the interaction between  $BiOCl$  and ZIS but to the *in situ* growth of  $Bi_2S_3$  in the interface between  $BiOCl$  template-like structure and ZIS nanosheets where ZIS and  $Bi_2S_3$  acted as SC 1 and SC 2, respectively. The Z-scheme reported in the photocatalytic system  $BiOCl@ZIS$ , which was literally a multicomponent photocatalytic system due to unignorable presence of  $Bi_2S_3$ , used for photocatalytic glycerol reforming for PHE under visible light ultralow Pt *in situ* deposition

(0.0675 wt.%) was proven the highest PHE rate among the sample series with optimum BiOCl (Section 2, Summary of the publications).

## 1.5 Details of experimental parts used in publication P1, P2 and P3

All the details regarding the synthesis and characterization can be seen in the experimental parts of P1, P2 and P3. Here, the summary of the experimental parts will be given.

### 1.5.1 Synthesis

The hydrothermal method used for ZIS microsphere and heating-up method for CIS QDs synthesis in **P1** and **P2** were adopted from Shen et al. [148] and Booth's doctoral dissertation [207], respectively. In **P1**, the pre-prepared CIS QDs were added to hydrothermal reaction medium of ZIS microspheres while in **P2** pre-prepared ZIS microspheres were decorated with CIS QDs in the aqueous media with different alkalinities to obtain ZIS/CIS photocatalytic system. CIS QDs were prepared using heating-up method where all CIS precursors and long alkyl chain mercaptocarboxylic acid ligand as given above (Table 1) were added to the three-necked flask and heated up controllably in the silica-oil-bath [**P1**].

Table 1 Reagents used in **P1** and **P2**

ZIS microsphere precursors for hydrothermal synthesis		CIS QDs precursors for heating-up method	
ZnSO <sub>4</sub> ·7H <sub>2</sub> O	Zn source	CuI	Cu source
In(NO <sub>3</sub> ) <sub>3</sub> ·H <sub>2</sub> O	In source	Indium acetate	In source
Thioacetamide	S source	Thiourea	S source
Cetrimonium bromide (CTAB)	Surfactant	11-mercaptoundecanoic acid (MUA)	Surface ligand

In **P3**, Zhang [208] and Shao [209] et al.'s methods were used for hydrothermal synthesis of BiOCl microplates and oil-bath assisted method for ZIS nanosheets, respectively. BiOCl@ZIS composite synthesis was conducted as in Shao's method in addition with the different amount of BiOCl microplates in ZIS nanosheets reaction media [**P3**].

Table 2 Reagents used in **P3**

<b>ZIS nanosheet precursors for oil-bath method</b>		<b>BiOCl microplates precursors for hydrothermal method</b>	
ZnCl <sub>2</sub>	Zn source	Bi(NO <sub>3</sub> ) <sub>3</sub> ·5H <sub>2</sub> O	Bi source
Indium acetate	In source	H <sub>2</sub> O	O source
Thioacetamide	S source	KCl	Cl source

### 1.5.2 Characterization

- **Morphological investigation** of the photocatalytic systems was conducted using scanning electron microscope images (SEM) which were recorded by JEOL JSM-7610F in **P1**, **P2** and **P3**. The high resolution transmission electron microscope (HRTEM) images with energy dispersive spectrometry (EDS) in **P1** (ZIS/CIS samples without Pt) were recorded in a double aberration-corrected Themis Z microscope (Thermo Fisher Scientific Electron Microscopy Solutions, Hillsboro, USA) equipped with a high-brightness field emission gun (FEG) at an accelerating voltage of 200 kV. Also, high-angle annular dark field (HAADF) scanning TEM images were recorded with a Fishione Model 3000 detector (E.A. Fischione Instruments Inc., Export, PA, USA) with a semi-convergence angle of 30 mrad, a probe current of 50 pA and SEM (JEOL JSM-7001F and JEOL JSM-7610F operating at 15 kV). The Pt deposition over the most active sample (ZIS/CIS\_100-Pt) in **P1** was studied using Hitachi H-800 microscope (Hitachi High-Technologies), operating at 150 kV as well as in **P2** and **P3**.
- **Crystalline structure** was analyzed by X-ray diffraction (XRD) method. In **P1**, X-ray diffractometer, Rigaku MiniFlex 600 with Cu Ka irradiation was used while a Bruker

D8 Focus diffractometer with Cu K $\alpha$  ( $\lambda = 1.54 \text{ \AA}$ ) radiation and a LynxEye XE-T detector was used in **P2** and **P3**.

- **Chemical composition of the surface** of photocatalytic systems were determined in all studies in this thesis (**P1**, **P2** and **P3**) by X-ray photoelectron spectroscopy (XPS) using a PHI 5000 VersaProbe<sup>TM</sup> spectrometer (ULVAC-PHI, Chigasaki, Japan) with monochromatic Al K $\alpha$  irradiation ( $h\nu = 1486.6 \text{ eV}$ ) and the high-resolution (HR) XPS spectra were recorded with the hemispherical analyzer at the pass energy of 23.5 eV and the energy step size of 0.1 eV. Fourier transform infrared (FTIR) spectroscopy (Bruker, IFS66) measurements were also conducted in addition to XPS in **P2**.
- **Amount of metal loading** were analyzed in **P1** (Cu and Pt) and **P2** (Pt) inductively coupled plasma-optical emission spectrometry (ICP-OES) using Agilent 5100 spectrometer, according to PN-EN ISO 11885:2009 standard.
- **Optical properties** were studied based on absorbance and photoluminescence of the obtained photocatalytic system in **P1**, **P2** and **P3** using ultraviolet-visible (UV-vis) and photoluminescence (PL) spectroscopy.
- **Photocatalytic hydrogen evolution performances** were tested using an artificial light source. In detail, in **P1**, Oriel, 66021 (1000 W) Xe lamp was used while in **P2** and **P3** Quantum Design, LSH 602 (1000 W). In all the works, cut-off filter (Optel,  $\lambda > 420 \text{ nm}$ ) was attached to the light source in addition with the water filter to remove the infrared light (no transmittance above 1.2  $\mu\text{m}$ ). The evolved hydrogen was determined using the data collected from gas chromatography (Thermo Scientific TRACE 1300-GC, N<sub>2</sub> carrier) coupled with thermal conductivity detector (GC-TCD). The gas samples with the volume of 200  $\mu\text{L}$  were collected manually from the headspace of the photoreactors using airtight syringe (Hamilton). The photoreactor used in **P1** and **P2** was in the form of cylinder shape with another cylinder attached inside where PHE reaction took place (Volume = 110 ml). The space between the main body and the PHE reaction container acted as a cooling jacket. For the irradiation part of the reactor, a quartz glass with 3 mm thickness was attached to the mentioned main glass body of the photoreactor as an irradiation area. The cooling was provided by thermostat in both **P1** and **P2**. On the other hand, in **P3** quartz made tube reactor with 12.5 ml volume and 1.5 mm thickness was used for PHE experiments. For the calibration in the works of **P1** and **P2**, the

different volumes of pure hydrogen (99.99%) were introduced using air-tight syringes (Hamilton) to the reactor with digital manometer attached (SIKA) to monitor the partial pressure of hydrogen. Then, the amount of hydrogen in moles was calculated using calibration curve which was based on a collected data from GC-TCD after sampling 200  $\mu\text{L}$  from the head space of the reactor and the partial pressure value in accordance with the ideal gas equation. But in **P3**, the manually prepared gas mixture ( $\text{N}_2/\text{H}_2$ ) prepared with different volumes of  $\text{H}_2$  was introduced to GC-TCD and based on the data, amount of the evolved hydrogen in moles was calculated in accordance with the ideal gas equation. In **P1** and **P2**, the sacrificial reagent used was  $\text{Na}_2\text{S}/\text{Na}_2\text{SO}_3$  (0.35 M/0.25 M) aqueous solution while in **P3**, 5% (v/v) glycerol aqueous mixture was used. In **P2** and **P3**, Pt cocatalyst was introduced via in situ method whereas in **P1** *ex situ*. The photoreactor configuration in **P1** and **P2** was a glass reactor with a quartz glass and a cooling jacket where the cooling water circulation was initiated by a thermostat while in **P3**, the quartz glass test tube was implemented as a reactor. The apparent quantum yield (AQE) was calculated only in P1. The details can be found in Section 2 (Summary of the publications).

- **Plus**, to reveal the reduction power of the photocatalytic systems in which methyl viologen was used. This experiment has been conducted in **P2** and **P3** under monochromatic light ( $\lambda > 420 \text{ nm}$ ) to have tractable methyl viologen radical formation.

## 2 Literature used in the introduction

- [1] J. Osička, F. Černoch, European energy politics after Ukraine: The road ahead, Energy Res. Soc. Sci. 91 (2022) 102757. <https://doi.org/10.1016/j.erss.2022.102757>.
- [2] X. Yuan, C.W. Su, M. Umar, X. Shao, O.R. LOBONTȚ, The race to zero emissions: Can renewable energy be the path to carbon neutrality?, J. Environ. Manage. 308 (2022). <https://doi.org/10.1016/j.jenvman.2022.114648>.
- [3] S.E. Hosseini, M.A. Wahid, Hydrogen from solar energy, a clean energy carrier from a sustainable source of energy, Int. J. Energy Res. 44 (2020) 4110–4131. <https://doi.org/10.1002/er.4930>.
- [4] M.R. Usman, Hydrogen storage methods: Review and current status, Renew. Sustain. Energy Rev. 167 (2022) 112743. <https://doi.org/10.1016/j.rser.2022.112743>.

- [5] U.S. Department of Energy, Hydrogen Storage | Department of Energy, U.S. Dep. Energy. (2012) n/a. <http://energy.gov/eere/fuelcells/hydrogen-storage>.
- [6] T.L. Levalley, A.R. Richard, M. Fan, The progress in water gas shift and steam reforming hydrogen production technologies - A review, *Int. J. Hydrogen Energy*. 39 (2014) 16983–17000. <https://doi.org/10.1016/j.ijhydene.2014.08.041>.
- [7] A. Coskun Avci, E. Toklu, A new analysis of two phase flow on hydrogen production from water electrolysis, *Int. J. Hydrogen Energy*. 47 (2022) 6986–6995. <https://doi.org/10.1016/j.ijhydene.2021.03.180>.
- [8] U.S. EIA, Annual Energy Outlook 2019 with projections to 2050, 2019. <https://www.eia.gov/outlooks/aeo/pdf/aeo2019.pdf>.
- [9] D.J. Singh Aulakh, K.G. Boulama, J.G. Pharoah, On the reduction of electric energy consumption in electrolysis: A thermodynamic study, *Int. J. Hydrogen Energy*. 46 (2021) 17084–17096. <https://doi.org/10.1016/j.ijhydene.2021.02.161>.
- [10] Z. Yan, J.L. Hitt, J.A. Turner, T.E. Mallouk, Renewable electricity storage using electrolysis, *Proc. Natl. Acad. Sci. U. S. A.* 117 (2020) 12558–12563. <https://doi.org/10.1073/pnas.1821686116>.
- [11] N. Chestney, High gas prices spur green hydrogen investment-report, Reuters. (2022). <https://www.reuters.com/business/energy/high-gas-prices-spur-green-hydrogen-investment-report-2022-10-19/> (accessed October 25, 2022).
- [12] K. Takanabe, Photocatalytic Water Splitting: Quantitative Approaches toward Photocatalyst by Design, *ACS Catal.* 7 (2017) 8006–8022. <https://doi.org/10.1021/acscatal.7b02662>.
- [13] A. FUJISHIMA, K. HONDA, Electrochemical Photolysis of Water at a Semiconductor Electrode, *Nature*. 238 (1972) 37–38. <https://doi.org/10.1038/238037a0>.
- [14] V. Kumaravel, S. Mathew, J. Bartlett, S.C. Pillai, Photocatalytic hydrogen production using metal doped TiO<sub>2</sub>: A review of recent advances, *Appl. Catal. B Environ.* 244 (2019) 1021–1064. <https://doi.org/10.1016/j.apcatb.2018.11.080>.
- [15] A.K. Singh, K. Mathew, H.L. Zhuang, R.G. Hennig, Computational screening of 2D

- materials for photocatalysis, *J. Phys. Chem. Lett.* 6 (2015) 1087–1098. <https://doi.org/10.1021/jz502646d>.
- [16] Y.J. Yuan, D. Chen, Z.T. Yu, Z.G. Zou, Cadmium sulfide-based nanomaterials for photocatalytic hydrogen production, *J. Mater. Chem. A.* 6 (2018) 11606–11630. <https://doi.org/10.1039/c8ta00671g>.
- [17] B. Ohtani, Preparing Articles on Photocatalysis—Beyond the Illusions, Misconceptions, and Speculation, *Chem. Lett.* 37 (2008) 216–229. <https://doi.org/10.1246/cl.2008.216>.
- [18] M. Reza Gholipour, C.T. Dinh, F. Béland, T.O. Do, Nanocomposite heterojunctions as sunlight-driven photocatalysts for hydrogen production from water splitting, *Nanoscale.* 7 (2015) 8187–8208. <https://doi.org/10.1039/c4nr07224c>.
- [19] S. Ghosh, E. Kowalska, Z. Wei, M. Janczarek, Band-gap Engineering of Photocatalysts: Surface Modification versus Doping S. Ghosh (Ed.), in: *Visible Light. Photocatal.*, John Wiley&Sons,Ltd,2018:pp.447–484. <https://doi.org/https://doi.org/10.1002/9783527808175.ch16>.
- [20] Y.K. Park, B.J. Kim, S. Jeong, K.J. Jeon, K.H. Chung, S.C. Jung, Characteristics of hydrogen production by photocatalytic water splitting using liquid phase plasma over Ag-doped TiO<sub>2</sub> photocatalysts, *Environ. Res.* 188 (2020) 109630. <https://doi.org/10.1016/j.envres.2020.109630>.
- [21] M. Ismael, Enhanced photocatalytic hydrogen production and degradation of organic pollutants from Fe (III) doped TiO<sub>2</sub> nanoparticles, *J. Environ. Chem. Eng.* 8 (2020) 103676. <https://doi.org/10.1016/j.jece.2020.103676>.
- [22] A.K. Agegnehu, C.J. Pan, M.C. Tsai, J. Rick, W.N. Su, J.F. Lee, B.J. Hwang, Visible light responsive noble metal-free nanocomposite of V-doped TiO<sub>2</sub> nanorod with highly reduced graphene oxide for enhanced solar H<sub>2</sub> production, *Int. J. Hydrogen Energy.* 41 (2016) 6752–6762. <https://doi.org/10.1016/j.ijhydene.2016.03.025>.
- [23] R. Dholam, N. Patel, M. Adami, A. Miotello, Hydrogen production by photocatalytic water-splitting using Cr- or Fe-doped TiO<sub>2</sub> composite thin films photocatalyst, *Int. J. HydrogenEnergy.* 34 (2009) 5337–5346. <https://doi.org/10.1016/j.ijhydene.2009.05.011>.



- [24] W. Zhao, X. Wang, H. Sang, K. Wang, Synthesis of Bi-doped TiO<sub>2</sub> Nanotubes and Enhanced Photocatalytic Activity for Hydrogen Evolution from Glycerol Solution, *Chinese J. Chem.* 31(2013)415–420.  
<https://doi.org/https://doi.org/10.1002/cjoc.201201151>.
- [25] G. Sadanandam, K. Lalitha, V.D. Kumari, M. V. Shankar, M. Subrahmanyam, Cobalt doped TiO<sub>2</sub>: A stable and efficient photocatalyst for continuous hydrogen production from glycerol: Water mixtures under solar light irradiation, *Int. J. Hydrogen Energy.* 38 (2013) 9655–9664. <https://doi.org/10.1016/j.ijhydene.2013.05.116>.
- [26] M. Ismael, Highly effective ruthenium-doped TiO<sub>2</sub> nanoparticles photocatalyst for visible-light-driven photocatalytic hydrogen production, *New J. Chem.* 43 (2019) 9596–9605. <https://doi.org/10.1039/c9nj02226k>.
- [27] S.B. Patil, P.S. Basavarajappa, N. Ganganagappa, M.S. Jyothi, A. V. Raghu, K.R. Reddy, Recent advances in non-metals-doped TiO<sub>2</sub> nanostructured photocatalysts for visible-light driven hydrogen production, CO<sub>2</sub> reduction and air purification, *Int. J. Hydrogen Energy.* 44 (2019) 13022–13039. <https://doi.org/10.1016/j.ijhydene.2019.03.164>.
- [28] Y.Y. Wang, Y.X. Chen, T. Barakat, Y.J. Zeng, J. Liu, S. Siffert, B.L. Su, Recent advances in non-metal doped titania for solar-driven photocatalytic/photoelectrochemical water-splitting, *J. Energy Chem.* 66 (2022) 529–559. <https://doi.org/10.1016/j.jechem.2021.08.038>.
- [29] F.N. Sayed, O.D. Jayakumar, R. Sasikala, R.M. Kadam, S.R. Bharadwaj, L. Kienle, U. Schürmann, S. Kaps, R. Adelung, J.P. Mittal, A.K. Tyagi, Photochemical hydrogen generation using nitrogen-doped TiO<sub>2</sub>-Pd nanoparticles: Facile synthesis and effect of Ti<sup>3+</sup>-incorporation, *J. Phys. Chem. C.* 116(2012)12462–12467.  
<https://doi.org/10.1021/jp3029962>.
- [30] G. Jia, Y. Wang, X. Cui, W. Zheng, Highly Carbon-Doped TiO<sub>2</sub> Derived from MXene Boosting the Photocatalytic Hydrogen Evolution, *ACS Sustain. Chem. Eng.* 6 (2018) 13480–13486. <https://doi.org/10.1021/acssuschemeng.8b03406>.
- [31] K.C. Christoforidis, T. Montini, M. Fittipaldi, J.J.D. Jaén, P. Fornasiero, Photocatalytic Hydrogen Production by Boron Modified TiO<sub>2</sub>/Carbon Nitride Heterojunctions, *ChemCatChem.* 11 (2019) 6408–6416. <https://doi.org/10.1002/cctc.201901703>.

- [32] Z. Xing, Z. Li, X. Wu, G. Wang, W. Zhou, In-situ S-doped porous anatase TiO<sub>2</sub> nanopillars for high-efficient visible-light photocatalytic hydrogen evolution, *Int. J. Hydrogen Energy*. 41 (2016) 1535–1541. <https://doi.org/10.1016/j.ijhydene.2015.12.033>.
- [33] S. Zhou, H. Jang, Q. Qin, L. Hou, M.G. Kim, S. Liu, X. Liu, J. Cho, Boosting Hydrogen Evolution Reaction by Phase Engineering and Phosphorus Doping on Ru/P-TiO<sub>2</sub>, *Angew. Chemie Int. Ed.* 784 (2022). <https://doi.org/10.1002/anie.202212196>.
- [34] Q. Gao, F. Si, S. Zhang, Y. Fang, X. Chen, S. Yang, Hydrogenated F-doped TiO<sub>2</sub> for photocatalytic hydrogen evolution and pollutant degradation, *Int. J. Hydrogen Energy*. 44 (2019) 8011–8019. <https://doi.org/10.1016/j.ijhydene.2019.01.233>.
- [35] N. Serpone, Is the Band Gap of Pristine TiO<sub>2</sub> Narrowed by Anion- and Cation-Doping of Titanium Dioxide in Second-Generation Photocatalysts?, *J. Phys. Chem. B.* 110 (2006) 24287–24293. <https://doi.org/10.1021/jp065659r>.
- [36] B. Gupta, A.A. Melvin, T. Matthews, S. Dash, A.K. Tyagi, TiO<sub>2</sub> modification by gold (Au) for photocatalytic hydrogen (H<sub>2</sub>) production, *Renew. Sustain. Energy Rev.* 58 (2016) 1366–1375. <https://doi.org/10.1016/j.rser.2015.12.236>.
- [37] M.G. Méndez-Medrano, E. Kowalska, A. Lehoux, A. Herissan, B. Ohtani, S. Rau, C. Colbeau-Justin, J.L. Rodríguez-López, H. Remita, Surface Modification of TiO<sub>2</sub> with Au Nanoclusters for Efficient Water Treatment and Hydrogen Generation under Visible Light, *J. Phys. Chem. C*. 120(2016)25010–25022. <https://doi.org/10.1021/acs.jpcc.6b06854>.
- [38] Z.W. Seh, S. Liu, M. Low, S.-Y. Zhang, Z. Liu, A. Mlayah, M.-Y. Han, Janus Au-TiO<sub>2</sub> Photocatalysts with Strong Localization of Plasmonic Near-Fields for Efficient Visible-Light Hydrogen Generation, *Adv. Mater.* 24 (2012) 2310–2314. <https://doi.org/https://doi.org/10.1002/adma.201104241>.
- [39] A. Tanaka, S. Sakaguchi, K. Hashimoto, H. Kominami, Preparation of Au/TiO<sub>2</sub> with metal cocatalysts exhibiting strong surface plasmon resonance effective for photoinduced hydrogen formation under irradiation of visible light, *ACS Catal.* 3 (2013) 79–85. <https://doi.org/10.1021/cs3006499>.
- [40] F. Wu, X. Hu, J. Fan, E. Liu, T. Sun, L. Kang, W. Hou, C. Zhu, H. Liu, Photocatalytic

- Activity of Ag/TiO<sub>2</sub> Nanotube Arrays Enhanced by Surface Plasmon Resonance and Application in Hydrogen Evolution by Water Splitting, *Plasmonics*. 8 (2013) 501–508. <https://doi.org/10.1007/s11468-012-9418-5>.
- [41] D. Gogoi, A. Namdeo, A.K. Golder, N.R. Peela, Ag-doped TiO<sub>2</sub> photocatalysts with effective charge transfer for highly efficient hydrogen production through water splitting, *Int.J.HydrogenEnergy*.45(2020)2729–2744. <https://doi.org/10.1016/j.ijhydene.2019.11.127>.
- [42] L. Clarizia, D. Spasiano, I. Di Somma, R. Marotta, R. Andreozzi, D.D. Dionysiou, Copper modified-TiO<sub>2</sub> catalysts for hydrogen generation through photoreforming of organics. A short review, *Int. J. Hydrogen Energy*. 39 (2014) 16812–16831. <https://doi.org/10.1016/j.ijhydene.2014.08.037>.
- [43] A.J. Simamora, T.L. Hsiung, F.C. Chang, T.C. Yang, C.Y. Liao, H.P. Wang, Photocatalytic splitting of seawater and degradation of methylene blue on CuO/nano TiO<sub>2</sub>, *Int.J.HydrogenEnergy*.37(2012)13855–13858. <https://doi.org/10.1016/j.ijhydene.2012.04.091>.
- [44] J. Bandara, C.P.K. Udawatta, C.S.K. Rajapakse, Highly stable CuO incorporated TiO<sub>2</sub> catalyst for photocatalytic hydrogen production from H<sub>2</sub>O, *Photochem. Photobiol. Sci.* 4 (2005) 857–861. <https://doi.org/10.1039/b507816d>.
- [45] P. Zeng, Q. Zhang, X. Zhang, T. Peng, Graphite oxide-TiO<sub>2</sub> nanocomposite and its efficient visible-light-driven photocatalytic hydrogen production, *J. Alloys Compd.* 516 (2012) 85–90. <https://doi.org/10.1016/j.jallcom.2011.11.140>.
- [46] C. Chen, M. Long, H. Zeng, W. Cai, B. Zhou, J. Zhang, Y. Wu, D. Ding, D. Wu, Preparation, characterization and visible-light activity of carbon modified TiO<sub>2</sub> with two kinds of carbonaceous species, *J. Mol. Catal. A Chem.* 314 (2009) 35–41. <https://doi.org/10.1016/j.molcata.2009.08.014>.
- [47] I. Sargin, G. Yanalak, G. Arslan, I.H. Patir, Green synthesized carbon quantum dots as TiO<sub>2</sub> sensitizers for photocatalytic hydrogen evolution, *Int. J. Hydrogen Energy*. 44 (2019) 21781–21789. <https://doi.org/10.1016/j.ijhydene.2019.06.168>.
- [48] M. Long, Y. Qin, C. Chen, X. Guo, B. Tan, W. Cai, Origin of visible light photoactivity

- of reduced graphene oxide/TiO<sub>2</sub> by in situ hydrothermal growth of undergrown TiO<sub>2</sub> with graphene oxide, *J. Phys. Chem. C.* 117 (2013) 16734–16741. <https://doi.org/10.1021/jp4058109>.
- [49] E. Bae, W. Choi, Effect of the anchoring group (carboxylate vs phosphonate) in Ru-complex-sensitized TiO<sub>2</sub> on hydrogen production under visible light, *J. Phys. Chem. B.* 110 (2006) 14792–14799. <https://doi.org/10.1021/jp062540+>.
- [50] R. Abe, K. Hara, K. Sayama, K. Domen, H. Arakawa, Steady hydrogen evolution from water on Eosin Y-fixed TiO<sub>2</sub> photocatalyst using a silane-coupling reagent under visible light irradiation, *J. Photochem. Photobiol. A Chem.* 137 (2000) 63–69. [https://doi.org/10.1016/S1010-6030\(00\)00351-8](https://doi.org/10.1016/S1010-6030(00)00351-8).
- [51] H.S. Moon, K. Yong, Noble-metal free photocatalytic hydrogen generation of CuPc/TiO<sub>2</sub> nanoparticles under visible-light irradiation, *Appl. Surf. Sci.* 530 (2020) 147215. <https://doi.org/10.1016/j.apsusc.2020.147215>.
- [52] E. Genc Acar, A.C. Yüzer, G. Kurtay, G. Yanalak, E. Harputlu, E. Aslan, K. Ocakoglu, M. Güllü, M. Ince, I.H. Patir, Improving the Photocatalytic Hydrogen Generation Using Nonaggregated Zinc Phthalocyanines, *ACS Appl. Energy Mater.* 4 (2021) 10222–10233. <https://doi.org/10.1021/acsaem.1c02102>.
- [53] A. Truppi, F. Petronella, T. Placido, M. Striccoli, A. Agostiano, M.L. Curri, R. Comparelli, Visible-light-active TiO<sub>2</sub>-based hybrid nanocatalysts for environmental applications, *Catalysts.* 7 (2017). <https://doi.org/10.3390/catal7040100>.
- [54] X. Chen, S. Shen, L. Guo, S.S. Mao, Semiconductor-based photocatalytic hydrogen generation, *Chem. Rev.* 110 (2010) 6503–6570. <https://doi.org/10.1021/cr1001645>.
- [55] D. Jing, L. Guo, WS<sub>2</sub> sensitized mesoporous TiO<sub>2</sub> for efficient photocatalytic hydrogen production from water under visible light irradiation, *Catal. Commun.* 8 (2007) 795–799. <https://doi.org/10.1016/j.catcom.2006.09.009>.
- [56] X. Yao, T. Liu, X. Liu, L. Lu, Loading of CdS nanoparticles on the (101) surface of elongated TiO<sub>2</sub> nanocrystals for efficient visible-light photocatalytic hydrogen evolution from watersplitting, *Chem. Eng. J.* 255 (2014) 28–39. <https://doi.org/10.1016/j.cej.2014.06.055>.

- [57] C. Li, J. Yuan, B. Han, L. Jiang, W. Shangguan, TiO<sub>2</sub> nanotubes incorporated with CdS for photocatalytic hydrogen production from splitting water under visible light irradiation, *Int. J. Hydrogen Energy*. 35 (2010) 7073–7079. <https://doi.org/10.1016/j.ijhydene.2010.01.008>.
- [58] J. Bai, J. Li, Y. Liu, B. Zhou, W. Cai, A new glass substrate photoelectrocatalytic electrode for efficient visible-light hydrogen production: CdS sensitized TiO<sub>2</sub> nanotube arrays, *Appl. Catal. B Environ.* 95 (2010) 408–413. <https://doi.org/10.1016/j.apcatb.2010.01.020>.
- [59] Y. Lu, X. Cheng, G. Tian, H. Zhao, L. He, J. Hu, S.M. Wu, Y. Dong, G.G. Chang, S. Lenaerts, S. Siffert, G. Van Tendeloo, Z.F. Li, L.L. Xu, X.Y. Yang, B.L. Su, Hierarchical CdS/m-TiO<sub>2</sub>/G ternary photocatalyst for highly active visible light-induced hydrogen production from water splitting with high stability, *Nano Energy*. 47 (2018) 8–17. <https://doi.org/10.1016/j.nanoen.2018.02.021>.
- [60] J.S. Jang, S.M. Ji, S.W. Bae, H.C. Son, J.S. Lee, Optimization of CdS/TiO<sub>2</sub> nano-bulk composite photocatalysts for hydrogen production from Na<sub>2</sub>S/Na<sub>2</sub>SO<sub>3</sub> aqueous electrolyte solution under visible light ( $\lambda \geq 420$  nm), *J. Photochem. Photobiol. A Chem.* 188 (2007) 112–119. <https://doi.org/10.1016/j.jphotochem.2006.11.027>.
- [61] M. Khatamian, M. Saket Oskoui, M. Haghghi, M. Darbandi, Visible-light response photocatalytic water splitting over CdS/TiO<sub>2</sub> and CdS–TiO<sub>2</sub>/metasilicate composites, *Int. J. Energy Res.* 38 (2014) 1712–1726. <https://doi.org/https://doi.org/10.1002/er.3186>.
- [62] A.K.R. Police, S. Basavaraju, D.K. Valluri, S. Muthukonda V., S. Machiraju, J.S. Lee, CaFe<sub>2</sub>O<sub>4</sub> sensitized hierarchical TiO<sub>2</sub> photo composite for hydrogen production under solar light irradiation, *Chem. Eng. J.* 247 (2014) 152–160. <https://doi.org/10.1016/j.cej.2014.02.076>.
- [63] O. Elbanna, M. Zhu, M. Fujitsuka, T. Majima, Black Phosphorus Sensitized TiO<sub>2</sub> Mesocrystal Photocatalyst for Hydrogen Evolution with Visible and Near-Infrared Light Irradiation, *ACS Catal.* 9 (2019) 3618–3626. <https://doi.org/10.1021/acscatal.8b05081>.
- [64] J. Ma, X. Tan, F. Jiang, T. Yu, Graphitic C<sub>3</sub>N<sub>4</sub> nanosheet-sensitized brookite TiO<sub>2</sub> to achieve photocatalytic hydrogen evolution under visible light, *Catal. Sci. Technol.* 7 (2017) 3275–3282. <https://doi.org/10.1039/c7cy00788d>.

- [65] D. Barpuzary, Z. Khan, N. Vinothkumar, M. De, M. Qureshi, Hierarchically grown urchinlike CdS@ZnO and CdS@Al<sub>2</sub>O<sub>3</sub> heteroarrays for efficient visible-light-driven photocatalytic hydrogen generation, *J. Phys. Chem. C.* 116 (2012) 150–156. <https://doi.org/10.1021/jp207452c>.
- [66] K.G. Kanade, B.B. Kale, J.O. Baeg, S.M. Lee, C.W. Lee, S.J. Moon, H. Chang, Self-assembled aligned Cu doped ZnO nanoparticles for photocatalytic hydrogen production under visible light irradiation, *Mater. Chem. Phys.* 102 (2007) 98–104. <https://doi.org/10.1016/j.matchemphys.2006.11.012>.
- [67] G. Zhang, S. Sun, W. Jiang, X. Miao, Z. Zhao, X. Zhang, D. Qu, D. Zhang, D. Li, Z. Sun, A Novel Perovskite SrTiO<sub>3</sub>-Ba<sub>2</sub>FeNbO<sub>6</sub> Solid Solution for Visible Light Photocatalytic Hydrogen Production, *Adv. Energy Mater.* 7 (2017) 1600932. <https://doi.org/https://doi.org/10.1002/aenm.201600932>.
- [68] K. Han, W. Li, C. Ren, H. Li, X. Liu, X. Li, X. Ma, H. Liu, A. Khan, Dye-sensitized SrTiO<sub>3</sub>-based photocatalysts for highly efficient photocatalytic hydrogen evolution under visible light, *J. Taiwan Inst. Chem. Eng.* 112 (2020) 4–14. <https://doi.org/10.1016/j.jtice.2020.07.014>.
- [69] S. Boumaza, A. Boudjemaa, A. Bouguelia, R. Bouarab, M. Trari, Visible light induced hydrogen evolution on new hetero-system ZnFe<sub>2</sub>O<sub>4</sub>/SrTiO<sub>3</sub>, *Appl. Energy.* 87 (2010) 2230–2236. <https://doi.org/10.1016/j.apenergy.2009.12.016>.
- [70] D. Jiang, X. Sun, X. Wu, L. Shi, F. Du, Hydrothermal synthesis of single-crystal Cr-doped SrTiO<sub>3</sub> for efficient visible-light responsive photocatalytic hydrogen evolution, *Mater. Res. Express.* 7 (2020). <https://doi.org/10.1088/2053-1591/ab660d>.
- [71] P. Kanhere, J. Zheng, Z. Chen, Visible light driven photocatalytic hydrogen evolution and photophysical properties of Bi<sup>3+</sup> doped NaTaO<sub>3</sub>, *Int. J. Hydrogen Energy.* 37 (2012) 4889–4896. <https://doi.org/10.1016/j.ijhydene.2011.12.056>.
- [72] A. Malankowska, M.P. Kobylański, A. Mikolajczyk, O. Cavdar, G. Nowaczyk, M. Jarek, W. Lisowski, M. Michalska, E. Kowalska, B. Ohtani, A. Zaleska-Medynska, TiO<sub>2</sub> and NaTaO<sub>3</sub> Decorated by Trimetallic Au/Pd/Pt Core-Shell Nanoparticles as Efficient Photocatalysts: Experimental and Computational Studies, *ACS Sustain. Chem. Eng.* 6 (2018) 16665–16682. <https://doi.org/10.1021/acssuschemeng.8b03919>.

- [73] B. Bajorowicz, M.P. Kobylański, A. Malankowska, P. Mazierski, J. Nadolna, A. Pieczyńska, A. Zaleska-Medynska, 4 - Application of metal oxide-based photocatalysis, in: A.B.T.-M.O.-B.P. Zaleska-Medynska (Ed.), *Met. Oxides*, Elsevier, 2018: pp. 211–340. <https://doi.org/10.1016/B978-0-12-811634-0.00004-4>.
- [74] S. Martha, P. Chandra Sahoo, K.M. Parida, An overview on visible light responsive metal oxide based photocatalysts for hydrogen energy production, *RSC Adv.* 5 (2015) 61535–61553. <https://doi.org/10.1039/c5ra11682a>.
- [75] D. Wang, Z. Zou, J. Ye, A novel series of photocatalysts  $M_{2.5}VMoO_8$  (M = Mg, Zn) for  $O_2$  evolution under visible light irradiation, *Catal. Today.* 93–95 (2004) 891–894. <https://doi.org/10.1016/j.cattod.2004.06.090>.
- [76] J. Ye, Z. Zou, M. Oshikiri, A. Matsushita, M. Shimoda, M. Imai, T. Shishido, A novel hydrogen-evolving photocatalyst  $InVO_4$  active under visible light irradiation, *Chem. Phys. Lett.* 356 (2002) 221–226. [https://doi.org/10.1016/S0009-2614\(02\)00254-3](https://doi.org/10.1016/S0009-2614(02)00254-3).
- [77] J. Yin, Z. Zou, J. Ye, Photophysical and photocatalytic properties of new photocatalysts  $MCrO_4$  (M=Sr, Ba), *Chem. Phys. Lett.* 378 (2003) 24–28. [https://doi.org/10.1016/S0009-2614\(03\)01238-7](https://doi.org/10.1016/S0009-2614(03)01238-7).
- [78] K.M. Parida, K.H. Reddy, S. Martha, D.P. Das, N. Biswal, Fabrication of nanocrystalline  $LaFeO_3$ : An efficient sol-gel auto-combustion assisted visible light responsive photocatalyst for water decomposition, *Int. J. Hydrogen Energy.* 35 (2010) 12161–12168. <https://doi.org/10.1016/j.ijhydene.2010.08.029>.
- [79] X. Xu, A.K. Azad, J.T.S. Irvine, Photocatalytic  $H_2$  generation from spinels  $ZnFe_2O_4$ ,  $ZnFeGaO_4$  and  $ZnGa_2O_4$ , *Catal. Today.* 199 (2013) 22–26. <https://doi.org/10.1016/j.cattod.2012.03.013>.
- [80] G. Carraro, C. MacCato, A. Gasparotto, T. Montini, S. Turner, O.I. Lebedev, V. Gombac, G. Adami, G. Van Tendeloo, D. Barreca, P. Fornasiero, Enhanced hydrogen production by photoreforming of renewable oxygenates through nanostructured  $Fe_2O_3$  polymorphs, *Adv. Funct. Mater.* 24 (2014) 372–378. <https://doi.org/10.1002/adfm.201302043>.
- [81] P.A. Mangrulkar, V. Polshettiwar, N.K. Labhsetwar, R.S. Varma, S.S. Rayalu, Nanoferrites for water splitting: Unprecedented high photocatalytic hydrogen production

- under visible light, *Nanoscale*. 4 (2012) 5202–5209. <https://doi.org/10.1039/c2nr30819c>.
- [82] J. Cai, J. Shen, X. Zhang, Y.H. Ng, J. Huang, W. Guo, C. Lin, Y. Lai, Light-Driven Sustainable Hydrogen Production Utilizing TiO<sub>2</sub> Nanostructures: A Review, *Small Methods*. 3 (2019) 1800184. <https://doi.org/https://doi.org/10.1002/smtd.201800184>.
- [83] A. Ruiz-Aguirre, J.G. Villachica-Llamosas, M.I. Polo-López, A. Cabrera-Reina, G. Colón, J. Peral, S. Malato, Assessment of pilot-plant scale solar photocatalytic hydrogen generation with multiple approaches: Valorization, water decontamination and disinfection, *Energy*. 260 (2022). <https://doi.org/10.1016/j.energy.2022.125199>.
- [84] M.I. Maldonado, E. Saggiaro, J. Peral, E. Rodríguez-Castellón, J. Jiménez-Jiménez, S. Malato, Hydrogen generation by irradiation of commercial CuO + TiO<sub>2</sub> mixtures at solar pilot plant scale and in presence of organic electron donors, *Appl. Catal. B Environ.* 257 (2019) 117890. <https://doi.org/10.1016/j.apcatb.2019.117890>.
- [85] P. Ribao, M. Alexandra Esteves, V.R. Fernandes, M.J. Rivero, C.M. Rangel, I. Ortiz, Challenges arising from the use of TiO<sub>2</sub>/rGO/Pt photocatalysts to produce hydrogen from crude glycerol compared to synthetic glycerol, *Int. J. Hydrogen Energy*. 44 (2019) 28494–28506. <https://doi.org/10.1016/j.ijhydene.2018.09.148>.
- [86] S. Kreft, D. Wei, H. Junge, M. Beller, Recent advances on TiO<sub>2</sub>-based photocatalytic CO<sub>2</sub> reduction, *EnergyChem*. 2 (2020). <https://doi.org/10.1016/j.enchem.2020.100044>.
- [87] B. Ao, Quantum-mechanical oxidation states of metal ions in the solid-state binary sulfides, *Acta Mater.* 186 (2020) 597–608. <https://doi.org/10.1016/j.actamat.2020.01.036>.
- [88] Saylor Academy, General Chemistry: Principles, Patterns, and Applications, Saylor Acad. (2012) 1–7. [https://saylordotorg.github.io/text\\_general-chemistry-principles-patterns-and-applications-v1.0/s12-06-exceptions-to-the-octet-rule.html](https://saylordotorg.github.io/text_general-chemistry-principles-patterns-and-applications-v1.0/s12-06-exceptions-to-the-octet-rule.html)(accessed November 22, 2022).
- [89] K. Zhang, L. Guo, Metal sulphide semiconductors for photocatalytic hydrogen production, *Catal. Sci. Technol.* 3(2013)1672–1690. <https://doi.org/10.1039/c3cy00018d>.
- [90] X. Wu, S. Xie, H. Zhang, Q. Zhang, B.F. Sels, Y. Wang, Metal Sulfide Photocatalysts for Lignocellulose Valorization, *Adv. Mater.* 33(2021).



<https://doi.org/10.1002/adma.202007129>.

- [91] M.R. Harrison, M.G. Francesconi, Mixed-metal one-dimensional sulfides-A class of materials with differences and similarities to oxides, *Coord. Chem. Rev.* 255 (2011) 451–458. <https://doi.org/10.1016/j.ccr.2010.10.008>.
- [92] X. Yong, M.A.A. Schoonen, The absolute energy positions of conduction and valence bands of selected semiconducting minerals, *Am. Mineral.* 85 (2000) 543–556. <https://doi.org/10.2138/am-2000-0416>.
- [93] A. Kudo, Y. Miseki, Heterogeneous photocatalyst materials for water splitting, *Chem. Soc. Rev.* 38 (2009) 253–278. <https://doi.org/10.1039/b800489g>.
- [94] L. Cheng, Q. Xiang, Y. Liao, H. Zhang, CdS-Based photocatalysts, *Energy Environ. Sci.* 11 (2018) 1362–1391. <https://doi.org/10.1039/c7ee03640j>.
- [95] X. Xiang, B. Zhu, B. Cheng, J. Yu, H. Lv, Enhanced Photocatalytic H<sub>2</sub>-Production Activity of CdS Quantum Dots Using Sn<sup>2+</sup> as Cocatalyst under Visible Light Irradiation, *Small.* 16 (2020) 2001024. <https://doi.org/https://doi.org/10.1002/sml.202001024>.
- [96] J.W. Shi, D. Sun, Y. Zou, D. Ma, C. He, X. Ji, C. Niu, Trap-level-tunable Se doped CdS quantum dots with excellent hydrogen evolution performance without co-catalyst, *Chem. Eng. J.* 364 (2019) 11–19. <https://doi.org/10.1016/j.cej.2019.01.147>.
- [97] L. Amirav, A.P. Alivisatos, Photocatalytic hydrogen production with tunable nanorod heterostructures, *J. Phys. Chem. Lett.* 1 (2010) 1051–1054. <https://doi.org/10.1021/jz100075c>.
- [98] Y. Chen, K. Dong, L. Amirav, Ternary Dumbbell Nanowires for Photocatalytic Hydrogen Production, *Chem. Mater.* (2022). <https://doi.org/10.1021/acs.chemmater.2c01242>.
- [99] K. Wu, H. Zhu, T. Lian, Ultrafast Exciton Dynamics and Light-Driven H<sub>2</sub> Evolution in Colloidal Semiconductor Nanorods and Pt-Tipped Nanorods, *Acc. Chem. Res.* 48 (2015) 851–859. <https://doi.org/10.1021/ar500398g>.
- [100] X. Lu, W. Chen, Y. Yao, X. Wen, J.N. Hart, C. Tsounis, C. Ying Toe, J. Scott, Y.H. Ng, Photogenerated charge dynamics of CdS nanorods with spatially distributed MoS<sub>2</sub> for

- photocatalytic hydrogen generation, *Chem. Eng. J.* 420 (2021) 127709. <https://doi.org/10.1016/j.cej.2020.127709>.
- [101] J. Zhang, Y. Wang, J. Jin, J. Zhang, Z. Lin, F. Huang, J. Yu, Efficient Visible-Light Photocatalytic Hydrogen Evolution and Enhanced Photostability of Core/Shell CdS/g-C<sub>3</sub>N<sub>4</sub> Nanowires, *ACS Appl. Mater. Interfaces.* 5 (2013) 10317–10324. <https://doi.org/10.1021/am403327g>.
- [102] C. Yin, L. Cui, T. Pu, X. Fang, H. Shi, S. Kang, X. Zhang, Facile fabrication of nano-sized hollow-CdS@g-C<sub>3</sub>N<sub>4</sub> Core-shell spheres for efficient visible-light-driven hydrogen evolution, *Appl. Surf. Sci.* 456 (2018) 464–472. <https://doi.org/10.1016/j.apsusc.2018.06.137>.
- [103] S.R. Kadam, S.W. Gosavi, B.B. Kale, N. Suzuki, C. Terashima, A. Fujishima, Unique CdS@MoS<sub>2</sub> Core Shell Heterostructure for Efficient Hydrogen Generation Under Natural Sunlight, *Sci. Rep.* 9 (2019) 1–10. <https://doi.org/10.1038/s41598-019-48532-3>.
- [104] Y. Xu, W. Zhao, R. Xu, Y. Shi, B. Zhang, Synthesis of ultrathin CdS nanosheets as efficient visible-light-driven water splitting photocatalysts for hydrogen evolution, *Chem. Commun.* 49 (2013) 9803–9805. <https://doi.org/10.1039/c3cc46342g>.
- [105] X. Yu, N. Ren, J. Qiu, D. Sun, L. Li, H. Liu, Killing two birds with one stone: To eliminate the toxicity and enhance the photocatalytic property of CdS nanobelts by assembling ultrafine TiO<sub>2</sub> nanowires on them, *Sol. Energy Mater. Sol. Cells.* 183 (2018) 41–47. <https://doi.org/10.1016/j.solmat.2018.04.003>.
- [106] M. Solakidou, A. Giannakas, Y. Georgiou, N. Boukos, M. Louloui, Y. Deligiannakis, Efficient photocatalytic water-splitting performance by ternary CdS/Pt-N-TiO<sub>2</sub> and CdS/Pt-N,F-TiO<sub>2</sub>: Interplay between CdS photo corrosion and TiO<sub>2</sub>-doping, *Appl. Catal. B Environ.* 254 (2019) 194–205. <https://doi.org/10.1016/j.apcatb.2019.04.091>.
- [107] S. Zhang, X. Ou, Q. Xiang, S.A.C. Carabineiro, J. Fan, K. Lv, Research progress in metal sulfides for photocatalysis: From activity to stability, *Chemosphere.* 303 (2022). <https://doi.org/10.1016/j.chemosphere.2022.135085>.
- [108] G.J. Lee, J.J. Wu, Recent developments in ZnS photocatalysts from synthesis to photocatalytic applications — A review, *Powder Technol.* 318 (2017) 8–22.

<https://doi.org/10.1016/j.powtec.2017.05.022>.

- [109] A. Kudo, M. Sekizawa, Photocatalytic H<sub>2</sub> evolution under visible light irradiation on Ni-doped ZnS photocatalyst, *Chem. Commun.* (2000) 1371–1372. <https://doi.org/10.1039/b003297m>.
- [110] G.J. Lee, S. Anandan, S.J. Masten, J.J. Wu, Photocatalytic hydrogen evolution from water splitting using Cu doped ZnS microspheres under visible light irradiation, *Renew. Energy*. 89 (2016) 18–26. <https://doi.org/10.1016/j.renene.2015.11.083>.
- [111] H.C. Huang, C.L. Yang, M.S. Wang, X.G. Ma, Enhancement of the optical absorption of carbon group elements doped ZnS in the visible light range, *Renew. Energy*. 117 (2018) 22–27. <https://doi.org/10.1016/j.renene.2017.10.038>.
- [112] Y. Zhou, G. Chen, Y. Yu, Y. Feng, Y. Zheng, F. He, Z. Han, An efficient method to enhance the stability of sulphide semiconductor photocatalysts: A case study of N-doped ZnS, *Phys. Chem. Chem. Phys.* 17 (2015) 1870–1876. <https://doi.org/10.1039/c4cp03736g>.
- [113] F. Wang, M. Zheng, C. Zhu, B. Zhang, W. Chen, L. Ma, W. Shen, Visible light photocatalytic H<sub>2</sub>-production activity of wide band gap ZnS nanoparticles based on the photosensitization of graphene, *Nanotechnology*. 26 (2015). <https://doi.org/10.1088/0957-4484/26/34/345402>.
- [114] J. Zhang, Y. Wang, J. Zhang, Z. Lin, F. Huang, J. Yu, Enhanced Photocatalytic Hydrogen Production Activities of Au-Loaded ZnS Flowers, *ACS Appl. Mater. Interfaces*. 5 (2013) 1031–1037. <https://doi.org/10.1021/am302726y>.
- [115] X. Hao, J. Zhou, Z. Cui, Y. Wang, Y. Wang, Z. Zou, Zn-vacancy mediated electron-hole separation in ZnS/g-C<sub>3</sub>N<sub>4</sub> heterojunction for efficient visible-light photocatalytic hydrogen production, *Appl. Catal. B Environ.* 229 (2018) 41–51. <https://doi.org/10.1016/j.apcatb.2018.02.006>.
- [116] X. Hao, Y. Wang, J. Zhou, Z. Cui, Y. Wang, Z. Zou, Zinc vacancy-promoted photocatalytic activity and photostability of ZnS for efficient visible-light-driven hydrogen evolution, *Appl. Catal. B Environ.* 221 (2018) 302–311. <https://doi.org/10.1016/j.apcatb.2017.09.006>.

- [117] X. Guo, C. Cheng, F. Xing, C. Huang, Engineering highly active  $\text{Cd}_{1-x}\text{Zn}_x\text{S}$  nanopopcorns via zinc blende/wurtzite phase junctions for enhanced photocatalytic  $\text{H}_2$  evolution without a co-catalyst, *J. Mater. Chem. A.* 9 (2021) 7913–7923. <https://doi.org/10.1039/d0ta12600d>.
- [118] B. Lv, X. Feng, X. Xi, X. Feng, Z. Yuan, Y. Yang, F. Zhang, Noble-metal-free  $\text{Cd}_{0.3}\text{Zn}_{0.7}\text{S-Ni(OH)}_2$  for high efficiency visible light photocatalytic hydrogen production, *J. Colloid Interface Sci.* 601 (2021) 177–185. <https://doi.org/10.1016/j.jcis.2021.05.130>.
- [119] B. Chai, J. Yan, G. Fan, G. Song, C. Wang, Amorphous  $\text{MoS}_2$  decorated on uniform  $\text{Cd}_{0.8}\text{Zn}_{0.2}\text{S}$  microspheres with dramatically improved photocatalytic hydrogen evolution performance, *New J. Chem.* 43 (2019) 7846–7854. <https://doi.org/10.1039/c9nj01196j>.
- [120] J. Yu, J. Zhang, M. Jaroniec, Preparation and enhanced visible-light photocatalytic  $\text{H}_2$ -production activity of  $\text{CdS}$  quantum dots-sensitized  $\text{Zn}_{1-x}\text{Cd}_x\text{S}$  solid solution, *Green Chem.* 12 (2010) 1611–1614. <https://doi.org/10.1039/c0gc00236d>.
- [121] Y. Luo, X. Zhang, C. Huang, X. Han, Q. Jiang, T. Zhou, H. Yang, J. Hu,  $\text{Zn}_{0.8}\text{Cd}_{0.2}\text{S}$  Hollow Spheres with a Highly Dispersed Ni Dopant for Boosting Photocatalytic Hydrogen Generation, *ACS Omega.* 6 (2021) 13544–13553. <https://doi.org/10.1021/acsomega.0c06038>.
- [122] B. Sun, J. Wu, W. Wang, H. Wang, Y. Li, Z. Guo, Y. Geng, H. Lin, L. Wang, Efficient visible-light-driven  $\text{H}_2$  evolution induced by P-doped  $\text{Cd}_{1-x}\text{Zn}_x\text{S}$  porous nano-spheres decorated with  $\text{Ni}_2\text{P}$  and reduced graphene oxide, Elsevier B.V., 2021. <https://doi.org/10.1016/j.apsusc.2020.148542>.
- [123] V. Kumaravel, M.D. Imam, A. Badreldin, R.K. Chava, J.Y. Do, M. Kang, A. Abdel-Wahab, Photocatalytic hydrogen production: Role of sacrificial reagents on the activity of oxide, carbon, and sulfide catalysts, *Catalysts.* 9 (2019). <https://doi.org/10.3390/catal9030276>.
- [124] N. Xiao, S. Li, X. Li, L. Ge, Y. Gao, N. Li, The roles and mechanism of cocatalysts in photocatalytic water splitting to produce hydrogen, *Chinese J. Catal.* 41 (2020) 642–671. [https://doi.org/10.1016/S1872-2067\(19\)63469-8](https://doi.org/10.1016/S1872-2067(19)63469-8).

- [125] J. Yang, D. Wang, H. Han, C. Li, Roles of cocatalysts in photocatalysis and photoelectrocatalysis, *Acc. Chem. Res.* 46 (2013) 1900–1909. <https://doi.org/10.1021/ar300227e>.
- [126] C. Beasley, M. Kumaran Gnanamani, E. Santillan-Jimenez, M. Martinelli, W.D. Shafer, S.D. Hopps, N. Wanninayake, D.Y. Kim, Effect of Metal Work Function on Hydrogen Production from Photocatalytic Water Splitting with MTiO<sub>2</sub> Catalysts, *ChemistrySelect*. 5 (2020) 1013–1019. <https://doi.org/10.1002/slct.201904151>.
- [127] L. Guo, Y. Chen, J. Su, M. Liu, Y. Liu, Obstacles of solar-powered photocatalytic water splitting for hydrogen production: A perspective from energy flow and mass flow, *Energy*. 172 (2019) 1079–1086. <https://doi.org/10.1016/j.energy.2019.02.050>.
- [128] P.K. Sahoo, S.R. Bisoi, Y.J. Huang, D.S. Tsai, C.P. Lee, 2d-layered non-precious electrocatalysts for hydrogen evolution reaction: Fundamentals to applications, *Catalysts*. 11 (2021) 1–24. <https://doi.org/10.3390/catal11060689>.
- [129] C. Walter, P.W. Menezes, M. Driess, Perspective on intermetallics towards efficient electrocatalytic water-splitting, *Chem. Sci.* 12 (2021) 8603–8631. <https://doi.org/10.1039/d1sc01901e>.
- [130] B.E. Conway, B. V. Tilak, Interfacial processes involving electrocatalytic evolution and oxidation of H<sub>2</sub>, and the role of chemisorbed H, *Electrochim. Acta*. 47 (2002) 3571–3594. [https://doi.org/10.1016/S0013-4686\(02\)00329-8](https://doi.org/10.1016/S0013-4686(02)00329-8).
- [131] P. Quaino, F. Juarez, E. Santos, W. Schmickler, Volcano plots in hydrogen electrocatalysis – uses and abuses, (2014) 846–854. <https://doi.org/10.3762/bjnano.5.96>.
- [132] K. Wenderich, G. Mul, Methods, Mechanism, and Applications of Photodeposition in Photocatalysis: A Review, *Chem. Rev.* 116 (2016) 14587–14619. <https://doi.org/10.1021/acs.chemrev.6b00327>.
- [133] Z. Liang, R. Shen, Y.H. Ng, P. Zhang, Q. Xiang, X. Li, A review on 2D MoS<sub>2</sub> cocatalysts in photocatalytic H<sub>2</sub> production, *J. Mater. Sci. Technol.* 56 (2020) 89–121. <https://doi.org/10.1016/j.jmst.2020.04.032>.
- [134] X. Liu, H. Zhuang, Recent progresses in photocatalytic hydrogen production: design and

- construction of Ni-based cocatalysts, *Int. J. Energy Res.* 45 (2021) 1480–1495. <https://doi.org/10.1002/er.5970>.
- [135] W. Wang, T. Li, S. Komarneni, X. Lu, B. Liu, Recent advances in Co-based co-catalysts for efficient photocatalytic hydrogen generation, *J. Colloid Interface Sci.* 608 (2022) 1553–1575. <https://doi.org/10.1016/j.jcis.2021.10.051>.
- [136] J. Guan, T. Pal, K. Kamiya, N. Fukui, H. Maeda, T. Sato, H. Suzuki, O. Tomita, H. Nishihara, R. Abe, R. Sakamoto, Two-Dimensional Metal-Organic Framework Acts as a Hydrogen Evolution Cocatalyst for Overall Photocatalytic Water Splitting, *ACS Catal.* 12 (2022) 3881–3889. <https://doi.org/10.1021/acscatal.1c05889>.
- [137] N. Kosem, Y. Honda, M. Watanabe, A. Takagaki, Z.P. Tehrani, F. Haydous, T. Lippert, T. Ishihara, Photobiocatalytic H<sub>2</sub> evolution of GaN:ZnO and [FeFe]-hydrogenase recombinant: *Escherichia coli*, *Catal. Sci. Technol.* 10 (2020) 4042–4052. <https://doi.org/10.1039/d0cy00128g>.
- [138] L. Zhang, X. Fu, S. Meng, X. Jiang, J. Wang, S. Chen, Ultra-low content of Pt modified CdS nanorods: One-pot synthesis and high photocatalytic activity for H<sub>2</sub> production under visible light, *J. Mater. Chem. A.* 3 (2015) 23732–23742. <https://doi.org/10.1039/c5ta07459b>.
- [139] X. Li, W. Bi, L. Zhang, S. Tao, W. Chu, Q. Zhang, Y. Luo, C. Wu, Y. Xie, Single-Atom Pt as Co-Catalyst for Enhanced Photocatalytic H<sub>2</sub> Evolution, *Adv. Mater.* 28 (2016) 2427–2431. <https://doi.org/https://doi.org/10.1002/adma.201505281>.
- [140] J. Schneider, D.W. Bahnemann, Undesired role of sacrificial reagents in photocatalysis, *J. Phys. Chem. Lett.* 4 (2013) 3479–3483. <https://doi.org/10.1021/jz4018199>.
- [141] Y. Pellegrin, F. Odobel, Les donneurs d'électron sacrificiels pour la production de combustible solaire, *Comptes Rendus Chim.* 20 (2017) 283–295. <https://doi.org/10.1016/j.crci.2015.11.026>.
- [142] A.J. Esswein, D.G. Nocera, Hydrogen Production by Molecular Photocatalysis, *Chem. Rev.* 107 (2007) 4022–4047. <https://doi.org/10.1021/cr050193e>.
- [143] M. Gopannagari, D.P. Kumar, D.A. Reddy, S. Hong, M.I. Song, T.K. Kim, In situ

- preparation of few-layered WS<sub>2</sub> nanosheets and exfoliation into bilayers on CdS nanorods for ultrafast charge carrier migrations toward enhanced photocatalytic hydrogen production, *J. Catal.* 351 (2017) 153–160. <https://doi.org/https://doi.org/10.1016/j.jcat.2017.04.016>.
- [144] F. Wen, X. Wang, L. Huang, G. Ma, J. Yang, C. Li, A Hybrid Photocatalytic System Comprising ZnS as Light Harvester and an [Fe<sub>2</sub>S<sub>2</sub>] Hydrogenase Mimic as Hydrogen Evolution Catalyst, *ChemSusChem.* 5 (2012) 849–853. <https://doi.org/https://doi.org/10.1002/cssc.201200190>.
- [145] Y. Wang, C. Yang, Y. Zhang, L. Guo, Y. Wang, G. Gao, F. Fu, B. Xu, D. Wang, Nanoarchitectonics of CdS/ZnSnO<sub>3</sub> heterostructures for Z-Scheme mediated directional transfer of photo-generated charges with enhanced photocatalytic performance, *Int. J. Hydrogen Energy.* 47 (2022) 9566–9578. <https://doi.org/10.1016/j.ijhydene.2022.01.015>.
- [146] J.F. Reber, K. Meier, Photochemical production of hydrogen with zinc sulfide suspensions, *J. Phys. Chem.* 88 (1984) 5903–5913. <https://doi.org/10.1021/j150668a032>.
- [147] T. Lange, S. Reichenberger, S. Ristig, M. Rohe, J. Strunk, S. Barcikowski, R. Schlögl, Zinc sulfide for photocatalysis: White angel or black sheep?, *Prog. Mater. Sci.* 124 (2022). <https://doi.org/10.1016/j.pmatsci.2021.100865>.
- [148] S. Shen, L. Zhao, Z. Zhou, L. Guo, Enhanced photocatalytic hydrogen evolution over Cu-doped ZnIn<sub>2</sub>S<sub>4</sub> under visible light irradiation, *J. Phys. Chem. C.* 112 (2008) 16148–16155. <https://doi.org/10.1021/jp804525q>.
- [149] M.R. Karimi Estahbanati, M. Feilizadeh, F. Attar, M.C. Iliuta, Current developments and future trends in photocatalytic glycerol valorization: Process analysis, *React. Chem. Eng.* 6 (2021) 197–219. <https://doi.org/10.1039/d0re00382d>.
- [150] A. V. Puga, Photocatalytic production of hydrogen from biomass-derived feedstocks, *Coord. Chem. Rev.* 315 (2016) 1–66. <https://doi.org/10.1016/j.ccr.2015.12.009>.
- [151] N. Berand, K.-J. Range, A redetermination of the crystal structure of the (III)a-polytypic form of diindium zinc tetrasulfide, ZnIn<sub>2</sub>S<sub>4</sub>, *J. Alloys Compd.* 205 (1994) 295–301.

[https://doi.org/https://doi.org/10.1016/0925-8388\(94\)90805-2](https://doi.org/https://doi.org/10.1016/0925-8388(94)90805-2).

- [152] S. Shionoya, Y. Tamoto, Luminescence of ZnIn<sub>2</sub>S<sub>4</sub> and ZnIn<sub>2</sub>S<sub>4</sub>:Cu Single Crystals, *J. Phys. Soc. Japan.* 19 (1964) 1142–1149. <https://doi.org/10.1143/JPSJ.19.1142>.
- [153] S. Shionoya, A. Ebina, Fundamental Optical Properties of ZnIn<sub>2</sub>S<sub>4</sub> Single Crystals, *J. Phys. Soc. Japan.* 19 (1964) 1150–1156. <https://doi.org/10.1143/JPSJ.19.1150>.
- [154] A. Serpi, Trap distribution in ZnIn<sub>2</sub>S<sub>4</sub> from photoconductivity analysis, *J. Phys. D. Appl. Phys.* 9 (1976) 1881–1892. <https://doi.org/10.1088/0022-3727/9/13/008>.
- [155] A. Cingolani, M. Ferrara, A. Minafra, F. Adduci, P. Tantalò, Photoelectronic properties of ZnIn<sub>2</sub>S<sub>4</sub>, *Phys. Status Solidi.* 23 (1974) 367–371. <https://doi.org/https://doi.org/10.1002/pssa.2210230204>.
- [156] A. Bosacchi, B. Bosacchi, S. Franchi, L. Hernandez, Optical properties of a ‘quasi-disordered’ semiconductor: ZnIn<sub>2</sub>S<sub>4</sub>, *Solid State Commun.* 13 (1973) 1805–1809. [https://doi.org/https://doi.org/10.1016/0038-1098\(73\)90734-5](https://doi.org/https://doi.org/10.1016/0038-1098(73)90734-5).
- [157] M. Guzzi, G. Baldini, Recombination centres and traps in ZnIn<sub>2</sub>S<sub>4</sub>, *J. Lumin.* 9 (1975) 514–522. [https://doi.org/https://doi.org/10.1016/0022-2313\(75\)90065-4](https://doi.org/https://doi.org/10.1016/0022-2313(75)90065-4).
- [158] E. Grilli, M. Guzzi, E. Camerlenghi, F. Pio, On the radiative recombination in ZnIn<sub>2</sub>S<sub>4</sub>, *Phys. Status Solidi.* 90(1985)691–701. <https://doi.org/https://doi.org/10.1002/pssa.2210900235>.
- [159] N. Romeo, O. Vigil, Electric field variation of photoconductivity quenching due to hot electron capture in ZnIn<sub>2</sub>S<sub>4</sub>, *Phys. Status Solidi.* 10 (1972) 447–453. <https://doi.org/https://doi.org/10.1002/pssa.2210100213>.
- [160] T. Toyoda, M. Sorazawa, H. Nakanishi, S. Endo, T. Irie, Hydrostatic Pressure Dependence of the Fundamental Absorption Edges of CdInCaS<sub>4</sub> and ZnIn<sub>2</sub>S<sub>4</sub>, *Jpn. J. Appl. Phys.* 32 (1993) 291. <https://doi.org/10.7567/JJAPS.32S1.291>.
- [161] Z. Lei, W. You, M. Liu, G. Zhou, T. Takata, M. Hara, K. Domen, C. Li, Photocatalytic water reduction under visible light on a novel ZnIn<sub>2</sub>S<sub>4</sub> catalyst synthesized by hydrothermal method, *Chem. Commun.* 3 (2003) 2142–2143. <https://doi.org/10.1039/b306813g>.



- [162] X. Gou, F. Cheng, Y. Shi, L. Zhang, S. Peng, J. Chen, P. Shen, Shape-controlled synthesis of ternary chalcogenide  $\text{ZnIn}_2\text{S}_4$  and  $\text{CuIn}(\text{S,Se})_2$  nano-/microstructures via facile solution route, *J. Am. Chem. Soc.* 128 (2006) 7222–7229. <https://doi.org/10.1021/ja0580845>.
- [163] S. Shen, L. Zhao, L. Guo, Cetyltrimethylammoniumbromide (CTAB)-assisted hydrothermal synthesis of  $\text{ZnIn}_2\text{S}_4$  as an efficient visible-light-driven photocatalyst for hydrogen production, *Int. J. Hydrogen Energy.* 33 (2008) 4501–4510. <https://doi.org/https://doi.org/10.1016/j.ijhydene.2008.05.043>.
- [164] S. Shen, L. Zhao, L. Guo, Morphology, structure and photocatalytic performance of  $\text{ZnIn}_2\text{S}_4$  synthesized via a solvothermal/hydrothermal route in different solvents, *J. Phys. Chem. Solids.* 69(2008)2426–2432. <https://doi.org/https://doi.org/10.1016/j.jpcs.2008.04.035>.
- [165] Y. Song, J. Zhang, X. Dong, H. Li, A Review and Recent Developments in Full-Spectrum Photocatalysis using  $\text{ZnIn}_2\text{S}_4$ -Based Photocatalysts, *Energy Technol.* 9 (2021) 1–29. <https://doi.org/10.1002/ente.202100033>.
- [166] M. Hojamberdiev, Y. Cai, J.J.M. Vequizo, M.M. Khan, R. Vargas, K. Yubuta, A. Yamakata, K. Teshima, M. Hasegawa, Binary flux-promoted formation of trigonal  $\text{ZnIn}_2\text{S}_4$  layered crystals using ZnS-containing industrial waste and their photocatalytic performance for  $\text{H}_2$  production, *Green Chem.* 20 (2018) 3845–3856. <https://doi.org/10.1039/c8gc01746h>.
- [167] C. Liao, J. Li, Y. Zhang, Y. Qu, P. Jiang, R. Cong, T. Yang, Visible light driven photocatalytic  $\text{H}_2$  generation property of trigonal  $\text{ZnIn}_2\text{S}_4$  prepared by high temperature solid state reaction, *Mater. Lett.* 248 (2019) 52–54. <https://doi.org/10.1016/j.matlet.2019.03.144>.
- [168] X. Zheng, Y. Song, Y. Liu, Y. Yang, D. Wu, Y. Yang, S. Feng, J. Li, W. Liu, Y. Shen, X. Tian,  $\text{ZnIn}_2\text{S}_4$ -based photocatalysts for photocatalytic hydrogen evolution via water splitting, *Coord. Chem. Rev.* 475 (2023) 214898. <https://doi.org/10.1016/j.ccr.2022.214898>.
- [169] J. Wang, S. Sun, R. Zhou, Y. Li, Z. He, H. Ding, D. Chen, W. Ao, A review: Synthesis, modification and photocatalytic applications of  $\text{ZnIn}_2\text{S}_4$ , *J. Mater. Sci. Technol.* 78

- (2021) 1–19. <https://doi.org/10.1016/j.jmst.2020.09.045>.
- [170] Y. Chen, R. Huang, D. Chen, Y. Wang, W. Liu, X. Li, Z. Li, Exploring the different photocatalytic performance for dye degradations over hexagonal  $\text{ZnIn}_2\text{S}_4$  microspheres and cubic  $\text{ZnIn}_2\text{S}_4$  nanoparticles, *ACS Appl. Mater. Interfaces*. 4 (2012) 2273–2279. <https://doi.org/10.1021/am300272f>.
- [171] Y. Chen, S. Hu, W. Liu, X. Chen, L. Wu, X. Wang, P. Liu, Z. Li, Controlled syntheses of cubic and hexagonal  $\text{ZnIn}_2\text{S}_4$  nanostructures with different visible-light photocatalytic performance, *Dalt. Trans.* 40 (2011) 2607–2613. <https://doi.org/10.1039/c0dt01435d>.
- [172] V.B.Y. Oh, S.F. Ng, W.J. Ong, Shining light on  $\text{ZnIn}_2\text{S}_4$  photocatalysts: Promotional effects of surface and heterostructure engineering toward artificial photosynthesis, *EcoMat*. 4 (2022) 1–49. <https://doi.org/10.1002/eom2.12204>.
- [173] S. Zhang, Z. Zhang, Y. Si, B. Li, F. Deng, L. Yang, X. Liu, W. Dai, S. Luo, Gradient Hydrogen Migration Modulated with Self-Adapting S Vacancy in Copper-Doped  $\text{ZnIn}_2\text{S}_4$  Nanosheet for Photocatalytic Hydrogen Evolution, *ACS Nano*. 15 (2021) 15238–15248. <https://doi.org/10.1021/acsnano.1c05834>.
- [174] P. Wang, Z. Shen, Y. Xia, H. Wang, L. Zheng, W. Xi, S. Zhan, Atomic Insights for Optimum and Excess Doping in Photocatalysis: A Case Study of Few-Layer  $\text{Cu-ZnIn}_2\text{S}_4$ , *Adv. Funct. Mater.* 29 (2019) 1–9. <https://doi.org/10.1002/adfm.201807013>.
- [175] J. Xue, H. Liu, S. Zeng, Y. Feng, Y. Zhang, Y. Zhu, M. Cheng, H. Zhang, L. Shi, G. Zhang, Bifunctional Cobalt-Doped  $\text{ZnIn}_2\text{S}_4$  Hierarchical Nanotubes Endow Noble-Metal Cocatalyst-Free Photocatalytic  $\text{H}_2$  Production Coupled with Benzyl Alcohol Oxidation, *Sol. RRL*. 6 (2022) 2101042. <https://doi.org/https://doi.org/10.1002/solr.202101042>.
- [176] W. Liu, J. Chen, X. Pan, T. Wang, Y. Li, Ultrathin Nickel-doped  $\text{ZnIn}_2\text{S}_4$  Nanosheets with Sulfur Vacancies for Efficient Photocatalytic Hydrogen Evolution, *ChemCatChem*. 13 (2021) 5148–5155. <https://doi.org/https://doi.org/10.1002/cctc.202101267>.
- [177] W. Guan, L. Zhang, P. Wang, Y. Wang, H. Wang, X. Dong, M. Meng, L. Sui, Z. Gan, L. Dong, L. Yu, Highly Efficient Photocatalytic Hydrogen Evolution over Mo-Doped  $\text{ZnIn}_2\text{S}_4$  with Sulfur Vacancies, *Nanomaterials*. 12 (2022) 3980. <https://doi.org/10.3390/nano12223980>.

- [178] F. Xing, Q. Liu, C. Huang, Mo-Doped ZnIn<sub>2</sub>S<sub>4</sub> Flower-Like Hollow Microspheres for Improved Visible Light-Driven Hydrogen Evolution, *Sol. RRL*. 4 (2020) 1900483. <https://doi.org/https://doi.org/10.1002/solr.201900483>.
- [179] S. Shen, J. Chen, X. Wang, L. Zhao, L. Guo, Microwave-assisted hydrothermal synthesis of transition-metal doped ZnIn<sub>2</sub>S<sub>4</sub> and its photocatalytic activity for hydrogen evolution under visible light, *J. Power Sources*. 196 (2011) 10112–10119. <https://doi.org/10.1016/j.jpowsour.2011.08.103>.
- [180] C. Du, B. Yan, Z. Lin, G. Yang, Enhanced carrier separation and increased electron density in 2D heavily N-doped ZnIn<sub>2</sub>S<sub>4</sub> for photocatalytic hydrogen production, *J. Mater. Chem. A*. 8 (2020) 207–217. <https://doi.org/10.1039/C9TA11318E>.
- [181] W. Yang, L. Zhang, J. Xie, X. Zhang, Q. Liu, T. Yao, S. Wei, Q. Zhang, Y. Xie, Enhanced Photoexcited Carrier Separation in Oxygen-Doped ZnIn<sub>2</sub>S<sub>4</sub> Nanosheets for Hydrogen Evolution, *Angew. Chemie Int. Ed.* 55 (2016) 6716–6720. <https://doi.org/https://doi.org/10.1002/anie.201602543>.
- [182] C. Du, Q. Zhang, Z. Lin, B. Yan, C. Xia, G. Yang, Half-unit-cell ZnIn<sub>2</sub>S<sub>4</sub> monolayer with sulfur vacancies for photocatalytic hydrogen evolution, *Appl. Catal. B Environ.* 248 (2019) 193–201. <https://doi.org/10.1016/j.apcatb.2019.02.027>.
- [183] S. Zhang, X. Liu, C. Liu, S. Luo, L. Wang, T. Cai, Y. Zeng, J. Yuan, W. Dong, Y. Pei, Y. Liu, MoS<sub>2</sub> Quantum Dot Growth Induced by S Vacancies in a ZnIn<sub>2</sub>S<sub>4</sub> Monolayer: Atomic-Level Heterostructure for Photocatalytic Hydrogen Production, *ACS Nano*. 12 (2018) 751–758. <https://doi.org/10.1021/acsnano.7b07974>.
- [184] X. Ji, R. Guo, J. Tang, Z. Lin, Y. Yuan, L. Hong, W. Pan, Fabrication of a ternary NiS/ZnIn<sub>2</sub>S<sub>4</sub>/g-C<sub>3</sub>N<sub>4</sub> photocatalyst with dual charge transfer channels towards efficient H<sub>2</sub> evolution, *J. Colloid Interface Sci.* 618 (2022) 300–310. <https://doi.org/https://doi.org/10.1016/j.jcis.2022.03.099>.
- [185] Y. Xiao, H. Wang, Y. Jiang, W. Zhang, J. Zhang, X. Wu, Z. Liu, W. Deng, Hierarchical Sb<sub>2</sub>S<sub>3</sub>/ZnIn<sub>2</sub>S<sub>4</sub> core-shell heterostructure for highly efficient photocatalytic hydrogen production and pollutant degradation, *J. Colloid Interface Sci.* 623 (2022) 109–123. <https://doi.org/https://doi.org/10.1016/j.jcis.2022.04.137>.

- [186] A.R. Gunjal, A.R. Gunjal, A.K. Kulkarni, U. V. Kawade, Y.A. Sethi, R.S. Sonawane, J. Ook-Baeg, A. V. Nagawade, B.B. Kale, A hierarchical SnS@ZnIn<sub>2</sub>S<sub>4</sub> marigold flower-like 2D nano-heterostructure as an efficient photocatalyst for sunlight-driven hydrogen generation, *Nanoscale Adv.* 2 (2020) 2577–2586. <https://doi.org/10.1039/d0na00175a>.
- [187] Y.-S. Cheng, Z.-Y. Xing, X. Zheng, X.-D. Xu, Y.-S. Kang, D. Yu, K.-L. Wu, F.-H. Wu, G. Yuan, X.-W. Wei, Integration of ReS<sub>2</sub> on ZnIn<sub>2</sub>S<sub>4</sub> for boosting the hydrogen evolution coupled with selective oxidation of biomass intermediate under visible light, *Int. J. Hydrogen Energy.* (2022). <https://doi.org/https://doi.org/10.1016/j.ijhydene.2022.11.047>.
- [188] C. Wang, H. Ni, J. Dai, T. Liu, Z. Wu, X. Chen, Z. Dong, J. Qian, Z. Wu, Comparison of highly active Type-I and Type-II heterojunction photocatalytic composites synthesized by electrospinning for humic acid degradation, *Chem. Phys. Lett.* 803 (2022) 139815. <https://doi.org/https://doi.org/10.1016/j.cplett.2022.139815>.
- [189] Y. Wang, J. Li, S. Chen, Y. Xie, Y. Ma, Y. Luo, Y. Ling, J. Ye, CdS/ZnIn<sub>2</sub>S<sub>4</sub> type II heterojunctions improve photocatalytic hydrogen production: faster electron-hole separation and wider visible light utilization, *Sustain. Energy Fuels.* (2022) 4893–4902. <https://doi.org/10.1039/d2se01142e>.
- [190] Z. Chen, F. Guo, H. Sun, Y. Shi, W. Shi, Well-designed three-dimensional hierarchical hollow tubular g-C<sub>3</sub>N<sub>4</sub>/ZnIn<sub>2</sub>S<sub>4</sub> nanosheets heterostructure for achieving efficient visible-light photocatalytic hydrogen evolution, *J. Colloid Interface Sci.* 607 (2022) 1391–1401. <https://doi.org/https://doi.org/10.1016/j.jcis.2021.09.095>.
- [191] Y. Wang, J. Li, S. Chen, Y. Xie, Y. Ma, Y. Luo, J. Huang, Y. Ling, J. Ye, Y. Liang, J. Du, In situ loading of ZnIn<sub>2</sub>S<sub>4</sub> nanosheets onto S doped g-C<sub>3</sub>N<sub>4</sub> nanosheets to construct type II heterojunctions for improving photocatalytic hydrogen production, *J. Alloys Compd.* 924(2022)166569. <https://doi.org/https://doi.org/10.1016/j.jallcom.2022.166569>.
- [192] W. Pudkon, S. Kaowphong, S. Pattison, P.J. Miedziak, H. Bahruji, T.E. Davies, D.J. Morgan, G.J. Hutchings, Microwave synthesis of ZnIn<sub>2</sub>S<sub>4</sub>/WS<sub>2</sub> composites for photocatalytic hydrogen production and hexavalent chromium reduction, *Catal. Sci. Technol.* 9 (2019) 5698–5711. <https://doi.org/10.1039/c9cy01553a>.
- [193] G. Zhang, H. Wu, D. Chen, N. Li, Q. Xu, H. Li, J. He, J. Lu, A mini-review on ZnIn<sub>2</sub>S<sub>4</sub>-

- Based photocatalysts for energy and environmental application, *Green Energy Environ.* 7 (2022) 176–204. <https://doi.org/10.1016/j.gee.2020.12.015>.
- [194] A. Sherryana, M. Tahir, W. Nabgan, Recent advancements of layered double hydroxide heterojunction composites with engineering approach towards photocatalytic hydrogen production: A review, *Int. J. Hydrogen Energy.* 47 (2022) 862–901. <https://doi.org/10.1016/j.ijhydene.2021.10.099>.
- [195] Y. Zhang, D. Chen, N. Li, Q. Xu, H. Li, J. Lu, Fabricating 1D/2D  $\text{Co}_3\text{O}_4/\text{ZnIn}_2\text{S}_4$  core–shell heterostructures with boosted charge transfer for photocatalytic hydrogen production, *Appl. Surf. Sci.* 610 (2023) 155272. <https://doi.org/https://doi.org/10.1016/j.apsusc.2022.155272>.
- [196] M. Zhang, P. Tan, L. Yang, H. Zhai, H. Liu, J. Chen, R. Ren, X. Tan, J. Pan, Sulfur Vacancy and p-n junction Synergistically Boosting Interfacial Charge Transfer and Separation in  $\text{ZnIn}_2\text{S}_4/\text{NiWO}_4$  Heterostructure for Enhanced Photocatalytic Hydrogen Evolution, *J. Colloid Interface Sci.* (2022). <https://doi.org/https://doi.org/10.1016/j.jcis.2022.12.051>.
- [197] D. Kong, H. Fan, D. Yin, D. Zhang, X. Pu, S. Yao, C. Su,  $\text{AgFeO}_2$  Nanoparticle/ $\text{ZnIn}_2\text{S}_4$  Microsphere p–n Heterojunctions with Hierarchical Nanostructures for Efficient Visible-Light-Driven  $\text{H}_2$  Evolution, *ACS Sustain. Chem. Eng.* 9 (2021) 2673–2683. <https://doi.org/10.1021/acssuschemeng.0c07638>.
- [198] D. Kong, X. Hu, J. Geng, Y. Zhao, D. Fan, Y. Lu, W. Geng, D. Zhang, J. Liu, H. Li, X. Pu, Growing  $\text{ZnIn}_2\text{S}_4$  nanosheets on  $\text{FeWO}_4$  flowers with p-n heterojunction structure for efficient photocatalytic  $\text{H}_2$  production, *Appl. Surf. Sci.* 591 (2022) 153256. <https://doi.org/https://doi.org/10.1016/j.apsusc.2022.153256>.
- [199] Y. Sun, C. Xue, L. Chen, Y. Li, S. Guo, Y. Shen, F. Dong, G. Shao, P. Zhang, Enhancement of Interfacial Charge Transportation Through Construction of 2D–2D p–n Heterojunctions in Hierarchical 3D CNFs/ $\text{MoS}_2/\text{ZnIn}_2\text{S}_4$  Composites to Enable High-Efficiency Photocatalytic Hydrogen Evolution, *Sol. RRL.* 5 (2021) 2000722. <https://doi.org/https://doi.org/10.1002/solr.202000722>.
- [200] H.-T. Fan, Z. Wu, K.-C. Liu, W.-S. Liu, Fabrication of 3D  $\text{CuS}@\text{ZnIn}_2\text{S}_4$  hierarchical nanocages with 2D/2D nanosheet subunits p-n heterojunctions for improved

- photocatalytic hydrogen evolution, *Chem. Eng. J.* 433 (2022) 134474. <https://doi.org/https://doi.org/10.1016/j.cej.2021.134474>.
- [201] Z. Guan, J. Pan, Q. Li, G. Li, J. Yang, Boosting Visible-Light Photocatalytic Hydrogen Evolution with an Efficient CuInS<sub>2</sub>/ZnIn<sub>2</sub>S<sub>4</sub> 2D/2D Heterojunction, *ACS Sustain. Chem. Eng.* 7 (2019) 7736–7742. <https://doi.org/10.1021/acssuschemeng.8b06587>.
- [202] X. Guo, Y. Peng, G. Liu, G. Xie, Y. Guo, Y. Zhang, J. Yu, An Efficient ZnIn<sub>2</sub>S<sub>4</sub>@CuInS<sub>2</sub> Core–Shell p–n Heterojunction to Boost Visible-Light Photocatalytic Hydrogen Evolution, *J. Phys. Chem. C.* 124 (2020) 5934–5943. <https://doi.org/10.1021/acs.jpcc.9b11623>.
- [203] Y. Kumar, R. Kumar, P. Raizada, A.A.P. Khan, Q. Van Le, P. Singh, V.H. Nguyen, Novel Z-Scheme ZnIn<sub>2</sub>S<sub>4</sub>-based photocatalysts for solar-driven environmental and energy applications: Progress and perspectives, *J. Mater. Sci. Technol.* 87 (2021) 234–257. <https://doi.org/10.1016/j.jmst.2021.01.051>.
- [204] F. Xing, C. Cheng, J. Zhang, Q. Liu, C. Chen, C. Huang, Tunable charge transfer efficiency in HxMoO<sub>3</sub>@ZnIn<sub>2</sub>S<sub>4</sub> hierarchical direct Z-scheme heterojunction toward efficient visible-light-driven hydrogen evolution, *Appl. Catal. B Environ.* 285 (2021) 119818. <https://doi.org/10.1016/j.apcatb.2020.119818>.
- [205] C. Jiang, H. Wang, Y. Wang, H. Ji, All solid-state Z-scheme CeO<sub>2</sub>/ZnIn<sub>2</sub>S<sub>4</sub> hybrid for the photocatalytic selective oxidation of aromatic alcohols coupled with hydrogen evolution, *Appl. Catal. B Environ.* 277 (2020) 119235. <https://doi.org/https://doi.org/10.1016/j.apcatb.2020.119235>.
- [206] J. Hu, C. Chen, Y. Zheng, G. Zhang, C. Guo, C.M. Li, Spatially Separating Redox Centers on Z-Scheme ZnIn<sub>2</sub>S<sub>4</sub>/BiVO<sub>4</sub> Hierarchical Heterostructure for Highly Efficient Photocatalytic Hydrogen Evolution, *Small.* 16 (2020) 2002988. <https://doi.org/https://doi.org/10.1002/sml.202002988>.
- [207] M. Booth, Synthesis and Characterisation of CuInS<sub>2</sub> Quantum Dots, The University of Leeds School of Physics & Astronomy, 2014. <https://doi.org/uk.bl.ethos.640628>.
- [208] L. Zhang, W. Wang, S. Sun, D. Jiang, E. Gao, Selective transport of electron and hole among {001} and {110} facets of BiOCl for pure water splitting, *Appl. Catal. B Environ.*

162 (2015) 470–474. <https://doi.org/10.1016/j.apcatb.2014.07.024>.

- [209] B. Shao, J. Wang, Y. Zhang, X. Tan, W. Zhou, Y. Chen, T. Xie, T. Yu, Construction of a 3D/2D g-C<sub>3</sub>N<sub>4</sub>/ZnIn<sub>2</sub>S<sub>4</sub> hollow spherical heterostructure for efficient CO<sub>2</sub> photoreduction under visible light, *Catal. Sci. Technol.* 11 (2021) 1282–1291. <https://doi.org/10.1039/d0cy01890b>.

### 3 Aim of the dissertation

The aim of this dissertation is to examine several the ways for the enhancement of the PHE activity of very promising metal-sulfide photocatalyst,  $\text{ZnIn}_2\text{S}_4$  under visible light spectrum ( $\lambda > 420$  nm). As will be seen in the summary of the publications section, the first goal of the dissertation [**P1**] was to obtain  $\text{CuInS}_2$  quantum dots through a heating-up method which can be used as a support during hydrothermal synthesis of  $\text{ZnIn}_2\text{S}_4$  matrix where a coupling between quantum dots and the matrix can be achieved and thus improved PHE performance can be acquired in the presence of the *ex-situ* photodeposition of Pt cocatalyst. This study [**P1**] led me to investigate a particular question related with the dispersibility of  $\text{CuInS}_2$  quantum dots which was actual the scope of the **P2**: the effect of the  $\text{CuInS}_2$  quantum dots aggregates on PHE performance of  $\text{ZnIn}_2\text{S}_4/\text{CuInS}_2$  photocatalytic systems constituting same amount of quantum dots and *in-situ* Pt deposition. The purpose of this study [**P2**] was to test pH dependent aggregation properties of the  $\text{CuInS}_2$  quantum dots in an aqueous media where  $\text{ZnIn}_2\text{S}_4/\text{CuInS}_2$  photocatalytic systems can be produced. Lastly, in **P3**, the insights into a specific and almost non-debated composite  $\text{BiOCl}@ZnIn_2S_4$  were the main goal.  $\text{BiOCl}$  is a wide bandgap semiconductor that is broadly investigated but rarely studied in the literature in the form of  $\text{BiOCl}@ZnIn_2S_4$  composite. But although  $\text{BiOCl}$  cannot be activated under visible light due to the large bandgap, is it possible to use it as a support for  $\text{ZnIn}_2\text{S}_4$  to boost PHE performance? In **P3**, this was the main objective in the thesis. Unlike  $\text{Na}_2\text{S}/\text{Na}_2\text{SO}_3$  sacrificial reagents as in **P1** and **P2**, the photocatalytic glycerol reforming was the purpose of the study to investigate PHE performances to examine  $\text{BiOCl}$ 's effect on PHE from  $\text{BiOCl}@ZnIn_2S_4$  composites.

### 4 Summary of the publications

The background information on the photocatalytic hydrogen evolution applications under visible light of  $\text{ZnIn}_2\text{S}_4$  based photocatalytic systems were discussed along with the referring the definition of cocatalyst and sacrificial reagents followed by the brief details on the experimental details in the publications **P1**, **P2** and **P3** in the previous sections.

Herein, the summary for each publication **P1**, **P2** and **P3** will be given briefly by emphasizing the most important points.



#### 4.1 P1: “Remarkable visible-light induced hydrogen generation with ZnIn<sub>2</sub>S<sub>4</sub> microspheres/CuInS<sub>2</sub> quantum dots photocatalytic system”

Usually, the pre-prepared matrix photocatalyst is introduced in the hydrothermal media for the growth of the quantum dots to form a heterojunction. However, in this work, the opposite approach has been applied where the pre-prepared CIS QDs was introduced to ZIS microsphere precursor solution for hydrothermal treatment. In the introduction part of the **P1**, the “quantum dot” definition was mentioned. In short, QDs are nanoparticles whose size vary between 2-10 nm. This particular range of size is lower than the nanoparticles’ Bohr Radius, thus quantum confinement effect can be observed. QDs are considered as a beneficial support for enhancing photocatalytic activity of selected photocatalyst matrix due to their high volume-to-surface ratio. In addition, CIS is a p-type semiconductor that is good match for n-type ZIS for the effective charge separation and its high light adsorption edge (Fig. S4 in Supplementary data of **P1**) to improve the PHE rate under visible light irradiation of ZIS microspheres. As a result, those critical traits for the improvement of PHE performance of ZIS microspheres can be achieved by CIS in QD size.

Accordingly, CIS QDs were synthesized through the “heating-up” method which was adopted from Booth’s doctoral dissertation. The critical factor was the presence of MUA during the synthesis (Fig. S1 in Supplementary data of **P1**), which is called “surface ligand” that was responsible for the stabilization of the nuclei of CIS during the synthesis, thus quantum-sized nanoparticles was obtainable. Indeed, the size of CIS QDs was proven by HAADF-STEM image of CIS (Fig. S2a, b in Supplementary data of **P1**) where the size of CIS QDs ranged between 1.8 and 2.4 nm. PL spectra of CIS QDs (Fig. S2c in Supplementary data of **P1**) gave two distinguishable peaks at around 420 and 660 nm which were attributed nonradiative transition of excited electrons on conduction band bottom to sub-bands due to the surface defects or sulfur vacancies on CIS and radiative transition of the electrons to the valence band of CIS, respectively. The comparison of the FTIR spectra of CIS QDs and MUA (Fig. S2d in Supplementary data of **P1**) was shown to reveal the fate of MUA on CIS QDs. The evanescent peak attributing S-H bonds in the FTIR spectra of CIS QDs demonstrated that the thiol group in MUA was bound to the surface of CIS QDs. Additionally, the pH initiated aggregation induced emission of CIS QDs (Fig. S3 in Supplementary data of **P1**), which was the main motivation of the next study in the section for **P2**, was mentioned briefly. Lastly, XRD analysis showed that CIS was in tetragonal crystal system (Fig. S5b in Supplementary data of **P1**).

After explanation of the characteristics of CIS QDs in **P1**, the synthesis of ZIS and ZIS/CIS photocatalytic system was given. The hydrothermal synthesis method for the synthesis of ZIS/CIS photocatalytic systems was described where the pre-prepared CIS QDs was introduced into the ZIS precursor solution. The investigation of the optimum amount of CIS QDs over ZIS to achieve the best PHE performance from ZIS/CIS photocatalytic system was conducted by introducing 50, 100, 150 and 200 mg CIS QDs into the ZIS hydrothermal medium (ZIS/CIS\_50, ZIS/CIS\_100, ZIS/CIS\_150 and ZIS/CIS\_200) (Fig. 1 in **P1**). For comparison, ZIS microspheres were obtained in the same way without CIS QDs. XRD proved that all ZIS and ZIS/CIS sample had the same crystalline structure while there was no diffraction originating from CIS QDs because of the weak diffraction (Fig. S5a in Supplementary data of **P1**). The morphological investigation by SEM and TEM showed that CIS was attached to the ZIS microspheres' (the size of all ZIS and ZIS/CIS range between 3 and 5  $\mu\text{m}$  while the thickness of the petals forming microspheres were between 20 and 50 nm) surface in the form of aggregates nonuniformly and but also uniform distribution can be seen from EDS mapping (Fig. 2 in **P1**). *Ex situ* Pt cocatalyst deposition over the ZIS and ZIS/CIS samples was applied in an anhydrous ethanol photochemical deposition media (Xe lamp, UV-vis). XPS analysis has shown that all ZIS and ZIS/CIS photocatalytic systems have the chemical nature of elements of Zn, In, Cu, S determined by analysis of the high-resolution (HR) XPS spectra of Zn 2p, In 3d, Cu 2p, S 2p as well as the well-controlled CIS QDs decoration over ZIS microspheres was proven (Table S1, 2 in Supplementary data of **P1**). This was also confirmed by ICP-OES analysis of Cu amount in ZIS/CIS photocatalytic systems (Table S4 in Supplementary data of **P1**). It is worth to mention that the Cu oxidation state in CIS sample (CIS-MUA) before the hydrothermal treatment was +2 then to reduced +1 after the hydrothermal ZIS/CIS synthesis (Fig. 4c in **P1**). The Pt deposition was proven also in detail as the Pt oxidation was +4 or +2 indicating that Pt species were arisen in the form of  $\text{PtS}_x$  ( $\text{PtS}$  or  $\text{PtS}_2$ ) or  $\text{PtO}_x$  ( $\text{PtO}$  or  $\text{PtO}_2$ ) (Fig S7 and Table S3 in Supplementary data of **P1**). The Pt deposition can be seen also from TEM images of ZIS/CIS\_100 and Pt deposited ZIS/CIS\_100 (ZIS/CIS\_100-Pt). Comparably, both ZIS/CIS\_100 and ZIS/CIS\_100-Pt had identical morphology expect visible dots in ZIS/CIS\_100-Pt sample which was identified as "Pt species" (Fig. 3 in **P1**). Around 1.26 wt.% Pt loading in all tested sample series (ZIS-Pt, ZIS/CIS\_50-Pt, ZIS/CIS\_100-Pt, ZIS/CIS\_150-Pt and ZIS/CIS\_200-Pt) via ICP-OES (Table S4 in Supplementary data of **P1**).

Investigation into the optical properties of the samples were mentioned in **P1** to give details regarding the light absorption (UV-vis) and recombination property (PL). CIS had the highest

photoabsorption with the edge around 800 nm while ZIS and ZIS/CIS samples had around 630 nm to 660 nm (Fig. S4a in Supplementary data of **P1**). The Pt deposition radically enhanced the absorption properties of the samples and among all the samples, ZIS/CIS\_100-Pt had the highest absorption (Fig. S4b in Supplementary data of **P1**). Meanwhile, ZIS/CIS\_100-Pt had the lowest electron-hole recombination in comparison to all photocatalysts with and without Pt (Fig. S4c, d in Supplementary data of **P1**). Excess amount of CIS in ZIS/CIS photocatalytic system led to the higher recombination due to the narrow energy gap of CIS.

ZIS/CIS-Pt photocatalytic systems had higher PHE performance than of ZIS-Pt (Fig. 5b in **P1**). The highest PHE rate of  $1041 \mu\text{mol h}^{-1} \text{g}^{-1}$  was performed by ZIS/CIS\_100-Pt which is about 2.5 times higher than that of ZIS-Pt ( $411.17 \mu\text{mol h}^{-1} \text{g}^{-1}$ ). ZIS/CIS\_100-Pt sample was also considerably active when the PHE experiment was conducted with higher range spectrum cut-off filter ( $\lambda > 455 \text{ nm}$ ).  $1025.26 \mu\text{mol g}^{-1}$  and  $2745.32 \mu\text{mol g}^{-1}$  hydrogen evolution was exhibited by ZIS-Pt and ZIS/CIS\_100-Pt after 4 hours of PHE test, respectively. When the samples were assessed in the 2<sup>nd</sup> run under the same conditions both samples show a boosted hydrogen evolution. Especially ZIS-Pt produced around 1.7 times higher hydrogen ( $1760 \mu\text{mol g}^{-1}$ ) than in 1<sup>st</sup> run. After the 2<sup>nd</sup> run, the loss in PHE performance of both ZIS-Pt and ZIS/CIS\_100-Pt PHE was observed and in the end of the 4<sup>th</sup> run ZIS-Pt was more stable than that of ZIS/CIS\_100-Pt whose hydrogen evolution amount decrease around 25%. around 35% reduction in the rate of hydrogen evolution was noted in the both ZIS-Pt and ZIS/CIS\_100-Pt as the cut-off filter is changed from the conventional ( $\lambda > 420$ ) nm to higher range spectrum one ( $\lambda > 455 \text{ nm}$ ).

Lastly, the mechanism was explained in terms of the estimated valance and conduction band levels according to the bandgap calculated using Kubelka-Munk function which was  $E_{\text{gZIS}} = 2.49 \text{ eV}$  and  $E_{\text{gCIS}} = 1.87 \text{ eV}$  (Fig. S9 in Supplementary data of **P1**), and valance band maximum were estimated from XPS spectra where  $1.5 \text{ eV}$  and  $0.6 \text{ eV}$  (V vs NHE) (Fig. S8 in Supplementary data of **P1**). Thus, the CB of ZIS and CIS QDs were estimated around  $-0.99$  and  $-1.27 \text{ eV}$  (V vs NHE), respectively. Not surprisingly, both ZIS and CIS were thermodynamically suitable for the proton reduction. Upon the visible light irradiation, both CIS and ZIS in the photocatalytic system were excited and photogenerated electron flow from the CB of CIS through that of ZIS took place while photogenerated holes transfer were expected from ZIS to CIS leading the oxidation of the sacrificial reagent (Fig 6a in **P1**). On the other hand, the action spectra analysis showed that the ZIS/CIS\_100-Pt was active up to the wavelength 540 nm and the highest AQE was at 420 nm (30.6%) (Fig 6b in **P1**). The effect of

the oxidation state of Pt on PHE of ZIS/CIS\_100 photocatalytic system was discussed based on the literature along with the XPS data on Pt oxidation states in ZIS/CIS\_100-Pt sample. It was suggested that revealed Pt oxidation state  $Pt^{4+}$  and  $Pt^{2+}$  by XPS could both be an effective in PHE and however the detailed investigation was necessary. Moreover, the reason behind the decrease in the PHE performance of ZIS/CIS\_150-Pt and ZIS/CIS\_200-Pt was explained. The exceeding presence of CIS over ZIS microspheres blocked the active sites in ZIS for PHE leading diminished PHE performance. The drop in the PHE performance after 2<sup>nd</sup> cycle was clarified by XPS measurement where self-oxidation was observed as XPS analysis of the both ZIS/CIS\_100-Pt and ZIS-Pt samples revealed the noteworthy drop of  $S^{2-}$  fraction (Table S3 in Supplementary data of **P1**) as well as in Zn and In contents (Fig. S7 and Table S1 and S3 in Supplementary data of **P1**).

In conclusion, for the first time pre-prepared CIS QDs introduction into a hydrothermal synthesis media of ZIS microspheres forming ZIS/CIS photocatalytic system was reported. The amount of the CIS QDs was optimized for the best PHE performance. The samples were needed to be loaded with Pt cocatalyst in which the dominating specie of Pt was not elemental Pt but  $PtO_x$  or  $PtS_x$  species. The broad visible range photoactivity up to 540 nm was observed with remarkable AQE at 420 nm (30.6%).

#### **4.2 P2: “Capping ligand initiated $CuInS_2$ quantum dots decoration on, $ZnIn_2S_4$ microspheres surface under different alkalinity levels resulting in different hydrogen evolution performance”**

The main question in this work was “how does the aggregation of CIS QDs effect the PHE performance of ZIS/CIS photocatalytic system?”. This question emerged from the fact that aggregation induced by alkalinity due to the presence of surface ligand (or capping ligand as mentioned in the title of **P2**) ,MUA, bounded over CIS surface. Thus, in this work, ZIS/CIS photocatalytic systems prepared in the aqueous decoration medium with various alkalinity levels resulting in the different size of aggregates over ZIS microspheres surface. Despite all ZIS/CIS photocatalytic systems prepared in different alkalinity levels had the same amount of CIS QDs, their PHE rate differed.

In the beginning of **P2**, the pH dependent aggregation of mercaptocarboxylic acids was briefly introduced which has been well-known for bioimaging applications however there have been

very limited reports on the links between PHE and the aggregation of QDs. This was followed by the details on the synthesis of ZIS/CIS photocatalytic systems prepared under different alkaline pH levels. Optical properties of CIS QDs aggregate firstly was shown by UV-vis and PL spectrums of the samples (Fig. 1 in **P2**). From pH = 7 to pH = 11.5, the aggregates exhibited red-shifted absorption edge and at pH = 12.5, noticeable peak at 250 nm appeared (Fig. 1a in **P2**). To highlight more this behavior, only MUA was tested where the same peak at 250 nm was seen (Fig. S1 in Supplementary data of **P2**). However, the red shifting in CIS QDs was more visible than that of only MUA under pH = 7 and 10.5 proving the coupling between MUA and CIS in CIS QDs. Moreover, the aggregation induced emission was shown by PL spectra of CIS QDs aggregates under different alkalinity levels (Fig. 1b in **P2**). The intensity of the emission intensity was the highest at pH = 7 followed by significant drop as the pH level was raised to 12.5 and the quenched PL emission at pH = 12.5 was observed where the clear and red-colored dispersion was obtained. Then size of the CIS QDs' aggregates under the same conditions were investigated using DLS. Polydisperse aggregates were observed even with macro-sizes at pH = 9.5 and 10.5. However, sizes of CIS QDs expectedly dropped lower as two peaks in DLS formed around 5 nm and 100 nm at pH = 12.5 and 12.9 (Fig. 2 in **P2**). The origin of the macro-sized aggregates was discussed, and it was implied that the non-ionized carboxylic acid group in MUA ligand on CIS surface caused the inter-nanoparticle H-bonds through the hydrophilic groups resulting in the CIS QDs aggregation under the weak basic environment. This could be overcome with the high pH that was necessary for the deprotonation of carboxylic acid groups in MUA leading electrostatic repulsive force between the CIS QDs thus reduced aggregation was achievable.

After providing the aggregation characteristics of CIS QDs, the information regarding the morphology of ZIS/CIS photocatalytic systems were given. Three critical sample was chosen among all the samples (ZIS/CIS-7, ZIS/CIS-10.5 and ZIS/CIS-12.5). Both TEM and SEM images (Fig. 3 in **P2**) revealed that the surface of ZIS/CIS-12.5 had the least irregularity and the coating-like CIS on ZIS have formed (Fig. 3c, f in **P2**). While on the contrary, at pH 7, non-uniform shape of ZIS/CIS-7 with the rough surface was observed and CIS aggregates overwhelmingly covered the ZIS surface (Fig. 3a, d in **P2**). At pH 10.5, both smooth and rigid surface was discovered in ZIS/CIS-10.5 photocatalytic system, in other words, the surface morphology resembled between the ZIS/CIS-7 and ZIS/CIS-12.5 (Fig. 3b, e in **P2**). Significantly, the red-shifting can be seen especially in ZIS/CIS-12.5 and ZIS/CIS-12.9 samples' UV-vis spectra compared to the other samples as the smooth distribution of CIS on

ZIS surface promoted the higher light harvesting due to the increase in surface-to-volume ratio (Fig 4a in **P2**). XRD patterns of all the samples proved that the crystalline structure of the samples was stable during the preparation of ZIS/CIS photocatalytic systems, except ZIS/CIS-12.9 where additional diffraction peaks were detected corresponding to  $\text{In}(\text{OH})_3$  formation was discovered (Fig. 5 in **P2**).

PHE rates of all ZIS/CIS photocatalytic systems were higher than that of ZIS. Firstly, PHE performances of the sample without Pt deposition (0.5 wt.% Pt *in situ* deposition) were clarified where the highest PHE rate was exhibited by ZIS/CIS-12.9 ( $105.31 \mu\text{mol h}^{-1}\text{g}^{-1}$ ) (Fig. 6b in **P2**) as it was the only sample containing  $\text{In}(\text{OH})_3$  crystals which acted as a cocatalyst. Then, ZIS/CIS photocatalytic PHE performances (PHE rate and the amount of the hydrogen evolved after 3 hours) (Fig. 6a, b in **P2**) in the presence of Pt deposition were shown. ZIS/CIS-7/Pt and then ZIS/CIS-9.5/Pt exhibited  $1180.46 \mu\text{mol g}^{-1} \text{h}^{-1}$  (the lowest among ZIS/CIS photocatalytic systems) and  $1300.46 \mu\text{mol g}^{-1} \text{h}^{-1}$ , respectively. While ZIS/CIS-10.5/Pt generated the highest amount of hydrogen with the PHE rate of  $1753.79 \mu\text{mol g}^{-1} \text{h}^{-1}$  signifying that the pH = 10.5 was the optimum pH level for the ZIS/CIS synthesis aqueous decoration medium. Then, the drop in PHE rate from ZIS/CIS-11.5/Pt ( $1450.76 \mu\text{mol g}^{-1} \text{h}^{-1}$ ) but followed by the rise from ZIS/CIS-12.5/Pt ( $1670.16 \mu\text{mol g}^{-1} \text{h}^{-1}$ ). The optimum pH level for the aqueous decoration media was reported as pH = 10.5 for the highest PHE in the presence of in-situ Pt deposition. For the confirmation of the results of ZIS/CIS-7/Pt, ZIS/CIS-10.5/Pt and ZIS/CIS-12.5/Pt, PHE experiments were repeated (Fig.S7 in Supplementary data of **P2**). The stability tests of the selected samples as for the repetition of PHE tests were conducted (Fig. 6c in **P2**). The highest stability was reported from ZIS/CIS-7/Pt comparing to ZIS/CIS-10.5/Pt and ZIS/CIS-12.5/Pt. On the other hand, ZIS/CIS-12.5/Pt had higher stability than that of ZIS/CIS-10.5/Pt indicating that stronger contact between two semiconductors in the photocatalytic system favored the stability. To prove the reduction ability of the three key samples, methyl viologen reduction experiments under monochromatic light ( $\lambda = 420 \text{ nm}$ ) were studied (Fig. 7 in **P2**). Methyl viologen radical formation was the highest from ZIS/CIS-10.5 after 9 minutes of irradiation which was detected by the characteristic peak at 605 nm corresponding to methyl viologen radical (Fig. 7b in **P2**).

Later, the Pt species were detected by XPS (Table 1 in **P2** and Table S1 in Supplementary data of **P2**). But before, ICP-OES characterization of three selected samples were conducted to show the equal amount of Pt and CIS (Cu) was loaded in three selected samples (Table 1 in **P2**). HRXPS spectra of those selected samples were discussed as Pt 4f and O1s HR spectra were

attributed (Table 1 in **P2**) to  $\text{Pt}(\text{OH})_2$  due to the highly alkaline PHE media giving rise to the formation of  $\text{Pt}(\text{OH})_2$  even before the light irradiation (Eq. 3 in **P2**). Then upon the light irradiation, the simultaneous formation of elemental Pt was expectable (Eq 4, 5 in **P2**). However, it was mentioned that the proximity in binding energies of  $\text{Pt}^0$  and Pt with Cu, CO and  $\text{C}_x\text{H}_x$  was difficult to predict the exact oxidation state. The  $\zeta$ -potential of the samples which was reputed to be influential on  $\text{PtCl}_4^{2-}$  adsorption on the surface were debated as it might have no distinct role because the difference was little (Fig. S8 in Supplementary data of **P2**).

The mechanism was shown in which the same was proposed as in P1 (Fig. 6a in **P1**) however the steps in the mechanism were divided into four. (1) In the dark, the hydrolysis of the sacrificial reagent ( $\text{Na}_2\text{S}/\text{Na}_2\text{SO}_3$ ) initiated the formation of  $\text{OH}^-$  which was adsorbed by the ZIS/CIS surface and the displacement of chloride in  $\text{PtCl}_4^{2-}$  forming (2)  $\text{Pt}(\text{OH})_2$  over ZIS/CIS photocatalytic system. Then light initiated processes, (3) generation of holes and electrons, occurred resulting in (4) PHE.

As a result, it was suggested that at this amount of CIS (5 wt.%) in the ZIS/CIS photocatalytic system acted as a recombination center hindering the PHE performance. Nevertheless, due to the relatively lower contact in ZIS/CIS-10.5 compared to ZIS/CIS-12.5, the recombination was higher in ZIS/CIS-12.5 while the light harvesting property was much higher. Thus, the balance between the charge recombination, light harvesting, and Pt species factors, the most suitable for PHE was reported in ZIS/CIS-10.5/Pt.

#### **4.3 P3: “Photocatalytic hydrogen evolution from glycerol-water mixture under visible light over zinc indium sulfide ( $\text{ZnIn}_2\text{S}_4$ ) nanosheets grown on bismuth oxychloride ( $\text{BiOCl}$ ) microplates”**

$\text{BiOCl}$ , as a wide-bandgap (3.35 eV) semiconductor like P25, is widely studied material especially for photodegradation but also have gained attention for half or overall water splitting applications due to its suitable band alignment. Several reports also showed that coupling  $\text{BiOCl}$  with ZIS in which  $\text{BiOCl}$  microparticles has a role as a template-like (the “template-like” definition is used instead of template only, because  $\text{BiOCl}$  is not stable during ZIS growth as will be mentioned further). In this work [**P3**],  $\text{BiOCl}$  microplates’ effect on ZIS was investigated for the first time to be used for photocatalytic glycerol reforming for PHE under visible light ( $\lambda > 420$  nm). The optimization of the amount of  $\text{BiOCl}$  in  $\text{BiOCl@ZIS}$  photocatalytic system showed that the highest PHE rate was achieved from 4%  $\text{BiOCl@ZIS}$  composite in the presence

of *in-situ* ultra-low Pt deposition (0.0625 wt.%). Briefly, this was attributed to the formation of Bi<sub>2</sub>S<sub>3</sub> which was formed during ZIS growth on BiOCl. In other words, template-like BiOCl was as a platform for the Bi<sub>2</sub>S<sub>3</sub> formation in the composite whose role cannot be overlooked as it is a low bandgap semiconductor.

**P3** starts with the short introduction to the several common utilization methods of glycerol which require high temperature ranging around 300-900 °C. As already mentioned through the thesis, photocatalysis also enables the photocatalytic glycerol reforming under relatively mild condition in comparison to the conventional ones. TiO<sub>2</sub>, indeed, is one of the most widely studied material for photocatalytic glycerol reforming for PHE applications but suffers from large bandgap that is considered as one of the biggest obstacles for visible light induced PHE. Investigated metal sulfide based photocatalytic systems for photocatalytic glycerol reforming for PHE were summarized emphasizing the fact that ZIS has been never reported for glycerol reforming. Then, BiOCl@ZIS composites for different photocatalytic applications than PHE such as N<sub>2</sub> fixation, Cr(VI) reduction, rhodamine B and antibiotics degradation were mentioned. BiOCl@ZIS composite is almost undebated in the literature which is discussed only in four different works in the literature for different applications than PHE hydrogen evolution from glycerol photoreforming.

In the experimental part of **P3**, firstly the synthesis method of BiOCl@ZIS was specified in which a simple oil-bath method was used for ZIS growth over different amount of hydrothermally pre-prepared BiOCl (Fig. 1 in **P3**). PHE tests conditions were given in detail along with the H<sub>2</sub> detection and additionally qualitative analysis of the liquid phase before and after PHE process to reveal the by-products using GC-MS head-space analysis where samples were prepared by derivatization (the detailed procedure is given in the description for Fig. S6 in the Supplementary data of **P3**). It is worth mention that in **P3**, the Pt photodeposition technique was *in-situ*.

The morphological investigation of BiOCl, ZIS and 4% BiOCl@ZIS composite were given via SEM images (Fig. 2a, b, c in **P3**) while TEM characterization was conducted only over 4%BiOCl@ZIS composite (Fig. 2e, f, g in **P3**). Two main observations have been made in this part. (i) ZIS suffered from the aggregation but the nanosheet formation was visible and (ii) the cluster formation which can be related with the Bi<sub>2</sub>S<sub>3</sub> formation during the composite synthesis but no obvious. XRD patterns (Fig. 3 in **P3**) showed the indexed hexagonal and tetragonal structure of ZIS and BiOCl, respectively. Although the BiOCl in all the studied composite was



not high, the presence of BiOCl in the composite were clear from the XRD patterns due to the high crystallinity of BiOCl. Following the morphological and the crystal structure analysis, detailed XPS study was given (Fig. 4 in **P3**). Firstly,  $\text{Zn}^{2+}$ ,  $\text{In}^{3+}$  and  $\text{S}^{2-}$  were confirmed in ZIS and BiOCl@ZIS composite from the Zn 2p<sub>3/2</sub>, In 3d<sub>5/2</sub>, S 2p<sub>3/2</sub> and S 2s peaks while Bi 4f spectrum was observed in two different states, Bi(3+) and Bi(+3-x) from Bi 4f<sub>7/2</sub> signals. One of the important observations in the XPS analysis in **P3** was that the 4%BiOCl@ZIS composite had binding energy shift in the main Bi 4f<sub>7/2</sub> signals to the lower energy level which can be attributed to the existence of Bi<sub>2</sub>S<sub>3</sub> in the 4%BiOCl@ZIS composite. The state of the *in-situ* Pt deposited composites after 4 hours (4%BiOCl@ZIS/0.0625 wt.% Pt\_4h) and 16 hours (4%BiOCl@ZIS/0.0625 wt.% Pt\_16h) PHE process were identified via 4f spectra which were assigned to the metallic Pt<sup>0</sup> and PtO<sub>2</sub> species, respectively.

DRS patterns of the samples confirmed that BiOCl cannot be activated by the visible light irradiation ( $\lambda > 420$  nm) (Fig. 5 in **P3**). Also, a noteworthy elevation around 550 nm in the DRS spectra of 4%BiOCl@ZIS and 8%BiOCl@ZIS were assigned to the formation of narrow bandgap Bi<sub>2</sub>S<sub>3</sub>. This elevation accelerated as BiOCl@ZIS samples constituted more BiOCl content that is to say the highest amount of Bi<sub>2</sub>S<sub>3</sub> should exist in 8%BiOCl@ZIS composite.

PHE performances of the samples were conducted in the presence of 1 wt.% Pt deposition (precursor: K<sub>2</sub>PtCl<sub>4</sub>) to evaluate the most active composite (Fig. 6a in **P3**). Amount of hydrogen evolved from ZIS (1945.4  $\mu\text{mol g}^{-1}$ ) and 4%BiOCl@ZIS (1992.2  $\mu\text{mol g}^{-1}$ ) were proximate to refer any synergetic effect in 4%BiOCl@ZIS composite in this case. Moreover, PHE performances of ZIS (260  $\mu\text{mol g}^{-1}$ ) and 4%BiOCl@ZIS (165  $\mu\text{mol g}^{-1}$ ) without any Pt deposition, yet again, were almost the same (Fig. S3 in the Supplementary data of **P3**). Then, the Pt optimization study was conducted over 4%BiOCl@ZIS composite which exhibited the highest PHE rate in the presence of 1 wt.% Pt deposition. For this purpose, a wide range of Pt deposition amount from 0.0625 wt.% to 3 wt.% was selected (Fig. 6a in **P3**). The PHE rate dependent on the amount of Pt deposition can be divided into three regions in the 4%BiOCl@ZIS sample. As can be seen from Fig. 6c in **P3**, 3 wt.% Pt deposition resulted in the lowest PHE rate of 174  $\mu\text{mol g}^{-1} \text{h}^{-1}$  while PHE rate increased as Pt loading reached to 2 wt.%, 1 wt.% and 0.5 wt.% where PHE rates of 511  $\mu\text{mol g}^{-1} \text{h}^{-1}$ , 498  $\mu\text{mol g}^{-1} \text{h}^{-1}$  and 503  $\mu\text{mol g}^{-1} \text{h}^{-1}$  were observed, respectively. Lastly, the highest Pt deposition region was observed from 0.0625 wt.%, 0.125 wt.% and 0.25 wt.% Pt deposition. The best PHE rate was achieved from 4%BiOCl@ZIS 0.0625 wt.% sample with 674  $\mu\text{mol g}^{-1} \text{h}^{-1}$  followed by 4%BiOCl@ZIS 0.125 wt.% (625.5  $\mu\text{mol g}^{-1} \text{h}^{-1}$ ) and 4%BiOCl@ZIS 0.25 wt.% (637  $\mu\text{mol g}^{-1} \text{h}^{-1}$ ). Meanwhile, 0.0625

wt.% deposition over pristine ZIS sample exhibited around  $384 \mu\text{mol g}^{-1} \text{h}^{-1}$  PHE rate (Fig. 6c in **P3**). Lastly, the reproducibility of the results was shown in Fig. 6e in **P3** in which mean evolved hydrogen from ZIS and 4%BiOCl@ZIS samples displayed small standard errors under the same conditions confirming the good reproducibility.

Above-mentioned PHE performances were compared with the other studies where glycerol photoreforming for PHE were tested over other metal sulfide based photocatalytic systems. (Table S2 in the Supplementary data of **P3**). The performance of 4%BiOCl@ZIS/0.0625 wt.% sample was significant, however, not the best considering the PHE rate of  $74600 \mu\text{mol g}^{-1} \text{h}^{-1}$  in one of the studies mentioned in the given Table S2 in the supplementary data of **P3**. It should be noted that in the literature, amount of the glycerol in water-glycerol mixtures vary drastically from 5% (v/v) to 90% (v/v).

As the stability factor for photocatalytic system is one of the essential requirements from the perspective of the large scale application of PHE, the stability of the best performing 4%BiOCl@ZIS/0.0625 wt.% sample was also tested (Fig. 6d in **P3**). 8 h continuous test showed that during the first 4 h, the PHE kinetic was remarkable however a drastic drop in the kinetic was observed thereafter. In the 2<sup>nd</sup> cycle the fresh glycerol-water mixture replacement was not helpful to recover the same level of the kinetic as during the first 4 h where the evolved hydrogen dropped to around  $677 \mu\text{mol g}^{-1}$ . It can be suggested that the obtained 4%BiOCl@ZIS was not stable but somehow expected as metal sulfides are widely known with their stability problem. The cause of the instability was investigated from XPS, XRD and TEM analysis of 4%BiOCl@ZIS/0.0625 wt.% after 16 h PHE test (4%BiOCl@ZIS/0.0625 wt.%\_16h). There was no significant change in morphology and crystal structure of the sample after 16 h of PHE test (Fig. S4 in the Supplementary data of **P3**). However, XPS spectra of 4%BiOCl@ZIS/0.0625 wt.%\_16h showed two emerging peaks (Bi 4f<sub>7/2</sub> and Bi 4f<sub>5/2</sub>) corresponding to Bi<sup>(+3-x)</sup>. This can be a proof of the BiOCl was reduced not because of the self-reduction but photoexcited electrons from ZIS transferred to BiOCl. Moreover, the acidification of the of the PHE medium during the PHE due to the intermediate formation might be another factor causing the instability of the sample.

Speaking of the intermediate formation, the qualitative analysis of the by-products as a result of the photocatalytic glycerol reforming of the glycerol was studied in **P3**. For that purpose, GC chromatogram of the PHE medium before and after the PHE experiments were compared. As the derivatization method was used for the identification of the by-products, only diethyl ether

formation was observed from the PHE medium before the PHE experiment. After 8 h of PHE test, the mass spectra analysis of GC chromatogram showed 5 different peaks in comparison to the chromatogram from before PHE experiments corresponding to by-products such as acetaldehyde, propanal, formic acid, acrolein and acetic acid (Fig S6 in the Supplementary data of **P3**). This was the direct proof of the contribution of glycerol as a  $H^+$  to be reduced by the photogenerated electron over the composite after photogenerated hole mediated glycerol oxidation.

More details were given to explain the mechanism over the composite during PHE by firstly estimating the band gaps of ZIS ( $E_g \approx 2.20$  eV) and BiOCl ( $E_g \approx 3.35$  eV). Then based on the valance band values approximated from XPS spectra  $VB_{ZIS} \approx 1.3$  eV and  $VB_{BiOCl} \approx 2.5$  eV (Fig S6 in the Supplementary data of **P3**). Thus, the estimated conduction band level of the samples for ZIS and BiOCl was around -0.90 eV and 0.85 eV, respectively. Also, methyl viologen reduction experiments showed that BiOCl, ZIS and 4%BiOCl@ZIS samples were able to produce methyl viologen experiments upon the light irradiation (Fig S7 in the Supplementary data of **P3**). Additionally, 4%BiOCl@ZIS generated more radical than that of ZIS which confirmed the same trend as in PHE experiments with ultra-low Pt loading (Fig S7b in the Supplementary data of **P3**).

The effect of the formation of  $Bi_2S_3$  must be considered for the proposed mechanism (Fig. 7 in **P3**) over the composites. Therefore, it was concluded that the photoexcited charge carriers were produced only over ZIS and  $Bi_2S_3$  in BiOCl@ZIS composites where photoexcited electrons from ZIS followed two paths where (i)  $H^+$  ions were reduced to hydrogen gas as the Pt precursor transforming to Pt nanoparticles simultaneously whereas (ii) some part of the electrons should have been captured by BiOCl prompting reduction of BiOCl. Photogenerated electrons from  $Bi_2S_3$  transferred to the CB of ZIS creating a Z-scheme mechanism. Meantime, (iii) the photogenerated hole over the composite oxidized the water molecules directing the formation of by-products and  $H^+$  through hydroxyl radicals.

To sum up, a wide-bandgap semiconductor enhanced PHE performance of ZIS by acting as a template-like structure in the BiOCl@ZIS composite. In other words, template-like BiOCl was as a platform for the  $Bi_2S_3$  formation in the composite. As mentioned in **P3**,  $Bi_2S_3$  is a low bandgap semiconductor whose role cannot be overlooked. The excess loading of low bandgap metal-sulfide semiconductor on a matrix surface can inhibit the light penetration leading lower photocatalytic activity. Those negative effects should be even higher when a noble metal

precursor is introduced to the composite. In this case, the amount of formed  $\text{Bi}_2\text{S}_3$  in 4%  $\text{BiOCl}@ZIS$  composite should have been already high for the efficient PHE. Thus, 1 wt.% in-situ loading of Pt co-catalyst might decrease the performance. Furthermore, the stronger contact between ZIS and  $\text{Bi}_2\text{S}_3$  was achievable in comparison to the other methods (*i.e.* coupling pre-prepared  $\text{Bi}_2\text{S}_3$  and ZIS) which is considered as one of the determining factor for photocatalytic applications of composites. It should be also noted that the method used in **P3** can be considered as an alternative method to the other  $\text{Bi}_2\text{S}_3$  growth methods where the contact is expected to be stronger in which pre-prepared ZIS is introduced to  $\text{Bi}_2\text{S}_3$  precursor solution for solvothermal assisted growth on ZIS surface.

#### 4.4 Summary

The thesis has a strong introduction followed by the 3 publications that brought novelty and unique perspective to the current literature regarding photocatalytic hydrogen evolution from  $\text{ZnIn}_2\text{S}_4$  based photocatalytic systems which can be also applicable with other type of photocatalytic system such as different types of metal sulfide or metal oxide based photocatalytic systems.

Monodisperse  $\text{CuInS}_2$  quantum dots synthesis somehow could have been carried out by the treatment of prepared  $\text{CuInS}_2$  (sintering the quantum dots to remove the capping ligand) or sintering the whole photocatalytic systems after the wet preparation could have been investigated. The concentration of the photocatalytic system in the photocatalytic hydrogen evolution media might have been determined either that could have led to even higher hydrogen evolution than that of reported in the publications constituting the thesis. Beyond  $\text{BiOCl}$  as a template-like structure and support for the improvement of the photocatalytic hydrogen performance of  $\text{ZnIn}_2\text{S}_4$ , I think  $\text{BiOBr}$  and  $\text{Bi}_2\text{WO}_6$  are some other Bi-based semiconductors which are worth to try to form heterojunction for hydrogen evolution from milder conditions as investigated in the last work published [**P3**]. Also, I confirmed the previously mentioned two reports on  $\text{BiOCl}@ZnIn_2S_4$  in the literature where the  $\text{BiOCl}$  based materials can be considered as a alternative method to load  $\text{Bi}_2\text{S}_3$  low-band-gap photocatalyst over  $\text{ZnIn}_2\text{S}_4$ . Especially, controllable  $\text{Bi}_2\text{S}_3$  loading using this technique is compelling and amenable topic.

To sum up, I believe this thesis constitutes valuable information for those who would like to explore photocatalytic hydrogen evolution for  $\text{ZnIn}_2\text{S}_4$  based photocatalytic systems as  $\text{ZnIn}_2\text{S}_4$

based photocatalytic systems have an enormous potential for solar hydrogen production if the stability issue in the metal sulfides will be resolved.

## **5 Publications**

The publications with their supporting information will be given in this section.

---

---

**P1. Remarkable visible-light induced hydrogen generation with ZnIn<sub>2</sub>S<sub>4</sub> microspheres/CuInS<sub>2</sub> quantum dots photocatalytic system**

---

---

Available online at [www.sciencedirect.com](http://www.sciencedirect.com)

ScienceDirect

journal homepage: [www.elsevier.com/locate/hydro](http://www.elsevier.com/locate/hydro)

## Remarkable visible-light induced hydrogen generation with ZnIn<sub>2</sub>S<sub>4</sub> microspheres/CuInS<sub>2</sub> quantum dots photocatalytic system

Onur Cavdar<sup>a</sup>, Anna Malankowska<sup>a</sup>, Daniel Amgar<sup>b</sup>, Paweł Mazierski<sup>a</sup>, Justyna Łuczak<sup>c</sup>, Wojciech Lisowski<sup>d</sup>, Adriana Zaleska-Medynska<sup>a,\*</sup>

<sup>a</sup> Department of Environmental Technology, Faculty of Chemistry, University of Gdansk, Gdansk, 80-308, Poland

<sup>b</sup> Department of Physics of Complex Systems, Faculty of Physics, Weizmann Institute of Science, Rehovot, 761000, Israel

<sup>c</sup> Department of Process Engineering and Chemical Technology, Faculty of Chemistry, Gdansk University of Technology, Gdansk, 80-233, Poland

<sup>d</sup> Institute of Physical Chemistry, Polish Academy of Sciences, Warsaw, 01-224, Poland

### HIGHLIGHTS

- ZnIn<sub>2</sub>S<sub>4</sub> microspheres/CuInS<sub>2</sub> quantum dots photocatalytic system was synthesized.
- Photocatalytic system loaded by Pt NPs are able to generate H<sub>2</sub> under visible light.
- Visible light activity range reaches up to a wavelength of 540 nm.
- Light harvesting property of the system was enhanced by CuInS<sub>2</sub> quantum dots.

### ARTICLE INFO

Article history:

Received 27 July 2020

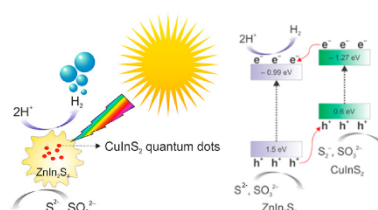
Received in revised form

17 September 2020

Accepted 24 September 2020

Available online 21 October 2020

### GRAPHICAL ABSTRACT



### ABSTRACT

A new and active material in the form of ZnIn<sub>2</sub>S<sub>4</sub> microspheres decorated by CuInS<sub>2</sub> quantum dots have been obtained by hydrothermal method for the first time. The optimum amount of CuInS<sub>2</sub> quantum dots (1.13 wt.%) introduced into reaction medium during ZnIn<sub>2</sub>S<sub>4</sub> microspheres synthesis increased the photocatalytic H<sub>2</sub> generation rate by 2.5 times than that of bare ZnIn<sub>2</sub>S<sub>4</sub> photocatalysis under visible light irradiation. This sample exhibited strong photoactivity in the extended visible range up to 540 nm with 30.6% apparent quantum efficiency ( $\lambda = 420$  nm).

© 2020 The Authors. Published by Elsevier Ltd on behalf of Hydrogen Energy Publications LLC. This is an open access article under the CC BY-NC-ND license (<http://creativecommons.org/licenses/by-nc-nd/4.0/>).

\* Corresponding author.

E-mail addresses: [adriana.zaleska@ug.edu.pl](mailto:adriana.zaleska@ug.edu.pl), [adriana.zaleska-medynska@ug.edu.pl](mailto:adriana.zaleska-medynska@ug.edu.pl) (A. Zaleska-Medynska).

<https://doi.org/10.1016/j.ijhydene.2020.09.212>

0360-3199/© 2020 The Authors. Published by Elsevier Ltd on behalf of Hydrogen Energy Publications LLC. This is an open access article under the CC BY-NC-ND license (<http://creativecommons.org/licenses/by-nc-nd/4.0/>).

## Introduction

As many efforts have been devoted to find the most promising green energy source, H<sub>2</sub> is one of the most conspicuous fuel due to its high specific energy value (33 kWh/kg) and clean by-products relatively to conventional fossil fuels [1,2]. However, the current H<sub>2</sub> market relies on mostly steam reforming of natural gas which requires high energy input and releases greenhouse gas emission while another well-known method, electrolysis requires an external circuit to split water to O<sub>2</sub> and H<sub>2</sub> fuel [3]. After the work by Fujishima and Honda [4], photo-generated H<sub>2</sub> evolution (PHE) by splitting water using TiO<sub>2</sub> semiconductor photocatalysis via irradiation of semiconductors by a light source has been ranked as another green way to generate H<sub>2</sub> fuel. Beyond TiO<sub>2</sub>, many other semiconductors have been studied also such as ZnS [5], ZnO [6], SrTiO<sub>3</sub> [7], Co<sub>3</sub>O<sub>4</sub> [8], LaFeO<sub>3</sub> [9], Ba<sub>5</sub>Ta<sub>4</sub>O<sub>15</sub> [10], BaZrO<sub>3</sub> [11] and CaTiO<sub>3</sub> [12]. Nevertheless, one of the limitations of those materials is wide bandgap which make them active only under UV light that comprise 4% of solar spectrum on the earth surface [13]. Therefore, seeking for new materials which are active under visible light spectrum is crucial to produce H<sub>2</sub> fuel by PHE in terms of green technology.

One of the types of AB<sub>2</sub>X<sub>4</sub> family, ZnIn<sub>2</sub>S<sub>4</sub>, is considered a promising candidate for PHE under visible light due its suitable band gap (2.3 eV) and stability [14]. Several synthesis methods have been proposed that allowed to obtain various shapes of that semiconductor photocatalyst such as microspheres, nanotubes, nanoribbons, monolayers [15,16]. In order to increase performance of ZnIn<sub>2</sub>S<sub>4</sub> under visible light, it is pivotal to inhibit the photo-generated hole and electron recombination that leads to better charge separation on ZnIn<sub>2</sub>S<sub>4</sub> surface or narrow the band gap of ZnIn<sub>2</sub>S<sub>4</sub>. Various methods have been studied to achieve these goals. For instance, visible light induced ZnIn<sub>2</sub>S<sub>4</sub> has been reached by Cu doping [17] whereas combination with different carbon-based analogs [18] or formation of heterostructures using other semiconductors BiVO<sub>4</sub> [19], MoSe<sub>2</sub> [20], g-C<sub>3</sub>N<sub>4</sub> [21], WO<sub>3</sub> [22] have been investigated for better charge separation on ZnIn<sub>2</sub>S<sub>4</sub> or boosting photogenerated electron transfer to the catalytically active sites of heterostructures which is required for better PHE performance. Another alternative for the formation of heterostructures, using quantum dots have also been studied to decorate larger semiconductor matrix materials and this approach has been widely studied for ZnO [23,24], TiO<sub>2</sub> [25,26] and g-C<sub>3</sub>N<sub>4</sub> [27,28]. Quantum dots are basically type of material that exhibits unique properties which arises with particle size lower than the bulk-exciton Bohr radius due to changes in the surface-to-volume ratio and quantum confinement effect [29,30]. Generally saying, a presence of quantum dots on a larger semiconductor matrix induces the activity more than of larger size of nanoparticles due to the relatively higher surface to volume ratio of quantum dots that creates more active site for PHE and high capability of light-harvesting [31]. Among them, CdS [32], MoS<sub>2</sub> [15,33] and carbon [13,18] dots have been used to decorate ZnIn<sub>2</sub>S<sub>4</sub>. Recently, CuInS<sub>2</sub> quantum dots have drawn attention as its suitability for visible light-driven PHE applications [34]. Although there are several reports on PHE such as

CuInS<sub>2</sub>/ZnS quantum dots [35,36] and CuInS<sub>2</sub> quantum dots hybridized polymeric carbon nitride, nevertheless, there is no report on CuInS<sub>2</sub> quantum dots decorated ZnIn<sub>2</sub>S<sub>4</sub> semiconductor for PHE application. To the best of our knowledge, only studies regarding ZnIn<sub>2</sub>S<sub>4</sub>/CuInS<sub>2</sub> system have been reported by Guan et al. and Guo et al. which have been based on 2D-2D structure [37] and core-shell structure [38], respectively.

Herein, ZnIn<sub>2</sub>S<sub>4</sub> microspheres (ZIS) in the presence of different amount of CuInS<sub>2</sub> quantum dots (CIS) were synthesized to obtain CIS decorated ZIS heterostructures (ZIS/CIS) for PHE under visible light irradiation using simple hydrothermal method for the first time. Fixed amount of Pt metal co-catalyst was deposited on the obtained ZIS/CIS samples with different CIS amounts using photodeposition method for photocatalytic hydrogen evolution experiments under visible light irradiation. We find that optimum amount pre-prepared CIS introduced to ZIS hydrothermal reaction medium enhance the photocatalytic hydrogen generation activity of ZIS.

## Experimental

### Materials

Cetyltrimethylammonium bromide (CTAB, 95%) (Aldrich), indium (III) nitrate hydrate (99.99%) (Alfa Aesar), thioacetamide (J.T. Baker, Avantar performance materials), copper (I) iodide (99.99%) and indium (III) acetate (99.99%) (Acros Organics), zinc sulfate heptahydrate (CHEMPUR), chloroplatinic acid hexahydrate (Sigma-Aldrich). All chemicals were used without any further purification.

### Synthesis of CuInS<sub>2</sub> quantum dots

CuInS<sub>2</sub> quantum dots (CIS) synthesis method has been adopted from Booth [39]. The solid mixture of indium acetate, copper iodide, thiourea and mercaptoundecanoic acid (MUA) with 1:1:2:4 M ratio was added into a 50 ml 3-necked round bottom flask. The flask was connected to the basic reflux system with tap water cooling and placed into an oil bath and the temperature was controlled by the immersing thermocouple into the oil bath (the temperature of the oil bath was about 10 °C higher than the reaction mixture). The solid mixture was mixed gently by a magnetic stirrer bar and temperature of the oil bath was increased to 120 °C slowly. Meanwhile, a yellow-red opaque thick liquid has been observed between 90 and 100 °C (Fig. S1b). Then, the blocker on the light neck was replaced with glass nozzle to purge the reaction mixture with nitrogen gas for 30 min while the temperature of the oil bath was slowly increased to 150 °C. After that, the blocker was reset and the oil bath temperature was heated to 190 °C and the color changing was observed that followed in order of yellow/red and dark red (Fig. S1b, c, d) as indicated by Booth. As reaching the dark red product, the flask was immediately placed into an ice bath. Following the temperature drop, approximately 40 ml of isopropanol have been added into the flask with as formed CIS and the flask were sonicated for 15 min. Finally, the CIS-isopropanol mixture was centrifuged and washed with isopropanol several times and dried at 60 °C under atmospheric pressure for 12 h. The



product was grinded using an agate mortar and the obtained red powder was kept in a cool and dry place in a glass container.

#### Solubility test for $\text{CuInS}_2$ quantum dots under alkaline conditions

Due to the poor solubility of MUA capped CIS in water (pH 7) and in ZIS microspheres precursor environment (pH 2), the solubility and PL property of MUA capped CIS quantum dots was also tested in an alkaline solution with different pH levels whether their solubility is higher in alkaline conditions. For that purpose, 20 ml water-CIS quantum dots mixture (1 mg/ml) was prepared (pH = 7). The mixture was mixed for 30 min using magnetic stirrer. As expected, CIS aggregated and could not be dissolved in the water. Later, 25% ammonia water was added dropwise to adjust pH. At each pH level, a sample was collected with a Pasteur pipette and PL intensity was measured swiftly (excitation wavelength: 330 nm). The pH level was controlled using both pH meter and pH-indicator paper.

#### Synthesis of $\text{CuInS}_2$ quantum dots decorated $\text{ZnIn}_2\text{S}_4$ microspheres

CIS decorated  $\text{ZnIn}_2\text{S}_4$  microspheres (ZIS) were synthesized using hydrothermal method. ZIS preparation was adopted from Shen et al. [17]. 6.1 mmol (1.75 g)  $\text{ZnSO}_4 \cdot 7\text{H}_2\text{O}$ , 12.08 mmol (3.85 g)  $\text{In}(\text{NO}_3)_3 \cdot \text{H}_2\text{O}$ , 4.25 mmol (1.55 g) cetrimonium bromide and 41.26 mmol (3.10 g) thioacetamide were added to 120 ml deionized water (Mixture A) in a glass beaker and mixed with a magnetic stirrer bar. The mixture A was left for stirring while pre-prepared CIS–water mixture (Mixture B) were prepared by adding 50, 100, 150 or 200 mg CIS to 10 ml water in a beaker and sonicated for 30 min. Later, the mixture B was added to mixture A and remaining CIS in the beaker were rinsed 10 ml of water and transferred to mixture A. The final mixture (140 ml) was stirred for 10 min vigorously and finally transferred quickly to Teflon-lined stainless-steel autoclave reactor with 200 ml volume for the hydrothermal reaction. The weight ratios of CIS to ZIS precursors plus CIS in the hydrothermal reaction were 0.57 wt%, 1.13 wt%, 1.69 wt% and 2.24 wt% CIS for 50, 100, 150 or 200 mg CIS addition and products were abbreviated as ZIS/CIS\_50, ZIS/CIS\_100, ZIS/CIS\_150 and ZIS/CIS\_200, respectively. The reaction was carried out at 160 °C for 12 h and the reactor was cooled under room temperature. The obtained product was washed with excess amount of ethanol and centrifuged several times for 10 min at 6000 rpm. Later, the product was dried at 60 °C under atmospheric pressure. ZIS without CIS decoration was synthesized by the as mentioned method above, except without any CIS in the hydrothermal reaction medium. Finally, the Pt deposition (0.75 wt%) on ZIS and ZIS/CIS samples were carried out using photodeposition technique.

#### Photodeposition of Pt

Pt was selected as a cocatalyst for ZIS and ZIS/CIS photocatalysts. To obtain Pt deposited ZIS/CIS, photodeposition technique was used. 500 mg ZIS or ZIS/CIS was mixed with 17.5 ml ethanol in a glass beaker and ultrasonicated for

10 min. The mixture was transferred to quartz glass photo-reactor with 25 ml volume. Then,  $\text{H}_2\text{PtCl}_6 \cdot 6\text{H}_2\text{O}$  aqueous solution was added to ethanol-photocatalyst (0.75 wt % of Pt) mixture. The final mixture was mixed in the dark for 2 h and the headspace of the reactor degasified with nitrogen for 1 h. Finally, the reactor was irradiated using Xenon lamp (Oriental, 66,021, 1000 W) at 25 °C for 1 h. The dark yellow product was washed with excess amount of ethanol and centrifuged at 6000 rpm. Later, the product was dried at 60 °C under atmospheric pressure.

#### Characterization

The particle size, shape, and morphology of samples have been analyzed by high-resolution transmission electron microscopy images and EDS maps were recorded in a double aberration-corrected Themis Z microscope (Thermo Fisher Scientific Electron Microscopy Solutions, Hillsboro, USA) equipped with a high-brightness FEG at an accelerating voltage of 200 kV. HAADF scanning TEM images were recorded with a Fischione Model 3000 detector (E.A. Fischione Instruments Inc., Export, PA, USA) with a semi-convergence angle of 30 mrad, a probe current of 50 pA and scanning electron microscopy (JEOL JSM-7001F and JEOL JSM-7610F operating at 15 kV). Transmission electron microscopy (TEM) was performed using bright-field (BF) to analyze ZIS/CIS\_100 and ZIS/CIS\_100-Pt samples with a Hitachi H-800 microscope (Hitachi High-Technologies), operating at 150 kV. The TEM samples were prepared by dry transfer of powder to carbon on copper grid (Agar Scientific), and imaged with dose rate not exceeding 20,000  $\text{e}^-/\text{nm}^2/\text{s}$ . Dose rate above 40,000  $\text{e}^-/\text{nm}^2/\text{s}$  led to the remodeling of the substrate and the coagulation of Pt species into larger nanocomplexes. X-ray diffractometer (XRD, Rigaku MiniFlex 600) equipped with  $\text{Cu K}\alpha$  irradiation in the  $2\theta$  range of 20–80° was used to identify the crystalline structure. The Pt and Cu content were analyzed by inductively coupled plasma optical emission spectroscopy (ICP-OES) using Agilent 5100 spectrometer, according to PN-EN ISO 11885:2009 standard. The mineralization was performed before the samples' analysis. The high-resolution (HR) XPS spectra were recorded by a PHI 5000 VersaProbe - Scanning ESCA Microprobe (ULVAC-PHI, Japan/USA) using monochromatic Al-K $\alpha$  radiation ( $h\nu = 1486.6$  eV) with the energy step size of 0.1 eV at the pass energy of 23.5 eV and the X-ray source operating under the following conditions: 15 kV, 25 W, 100  $\mu\text{m}$  spot. The analyzed area was 250  $\mu\text{m} \times 250 \mu\text{m}$ . The binding energy (BE) scale was referenced to the C 1s peak with BE = 284.8 eV. The UV–vis spectra of samples were recorded in the scan range 200–800 nm using UV–vis spectrophotometer (Evolution 220, Thermo Scientific) equipped with an integrating sphere and  $\text{BaSO}_4$  as the reference (Labsphere certified reflectance standard). The photoluminescence spectra (PL) were recorded using a PerkinElmer Luminescence Spectrometer LS-50B equipped with Xenon discharge lamp as an excitation source. The samples were excited with 330 nm at room temperature and the emission was scanned between 300 and 800 nm. Fourier-transform infrared spectroscopy (FTIR) (Bruker, IFS66) was used to identify the surface characteristics of CIS in the scan range of 500–5000  $\text{cm}^{-1}$  in the diffuse reflectance mode with a resolution of 0.12  $\text{cm}^{-1}$  at room

temperature. KBr was used as a reference material. Surface area and pore volume were analyzed by Gemini V200 Surface Area Analyzer (Micrometrics) equipped in degassing unit. The apparatus was checked with Carbon Black reference material with specific surface area of 30.6 m<sup>2</sup>/g.

#### Photogenerated hydrogen evolution and stability

The photocatalytic hydrogen evolution performance (PHE) test of obtained ZIS/CIS–Pt photocatalysts were carried out using the procedure as follows. 100 mg photocatalyst powder was mixed with 80 ml of 0.35 M Na<sub>2</sub>S/0.25 M Na<sub>2</sub>SO<sub>3</sub> aqueous solution of sacrificial agent. The mixture was ultrasonicated for 10 min and transferred to a quartz glass photoreactor (V = 110 ml) with a cooling jacket. The mixture was then irradiated using a 1000 W Xenon lamp (Oriel, 66,021) which emitted both UV and visible irradiation. UV light was removed by a cut-off filter GG420 ( $\lambda > 420$  nm). The temperature of the reactor was kept at 10 °C by a thermostat. Before PHE, the headspace of the reactor was purged with nitrogen gas with 10–12 dm<sup>3</sup>/h velocity for 30 min under dark while the mixture was mixed with a magnetic stirrer bar. 200  $\mu$ l of gas sample were collected within every hour from the headspace of the photoreactor using an air-tight syringe (Hamilton) and injected to the gas chromatograph (Thermo Scientific TRACE 1300-GC), coupled with thermal conductivity detector (TCD). No hydrogen generated by the irradiation of sacrificial agent solution with the same conditions. Photostability cycle runs were conducted under same conditions but using cut-off filter GG455 ( $\lambda > 455$  nm). The calibration experiments for the calculations to detect amount hydrogen evolution was followed by introducing different volume of pure hydrogen gas to the quartz glass photoreactor with the same conditions as mentioned above and plus a digital manometer was connected to the reactor to monitor the pressure change in the headspace of the photoreactor. Ideal gas equation has been used to calculate the amount of hydrogen in moles.

#### Action spectra analysis for photocatalytic hydrogen evolution reaction

Action spectra analysis was performed in the presence of sample with the highest hydrogen evolution rate, namely ZIS/CIS\_100-Pt, using the procedure as follows. 12.5 mg ZIS/CIS\_100-Pt sample was mixed with 10 ml of 0.35 M Na<sub>2</sub>S/0.25 M Na<sub>2</sub>SO<sub>3</sub> aqueous solution of sacrificial agent and ultrasonicated for 5 min and transferred to a Teflon photoreactor (V = 15 ml) with a quartz window and cooling jacket. The photoreactor was connected to a measuring system consisting of a tunable monochromatic light sources (1000 W Xe lamp – LSH602 and monochromator – MSW306, LOT-Quantum Design), GC-BID (BID-2010 Plus, Shimadzu) and FTIR (not used in this study). Then, the headspace of the photoreactor was purged with helium gas for 30 min under dark while the suspension was mixed with a magnetic stirrer bar. The temperature of the reactor was kept at ambient temperature. The sample was irradiated with the following wavelengths: 420, 440, 460, 480, 500, 540 and 600 nm. Irradiation intensity (W) was measured for individual wavelengths with optical meter (ILT2400, International Light technologies). No hydrogen

generated by the irradiation of sacrificial agent solution with the same conditions. The calibration experiments for the calculations to detect amount hydrogen evolution was followed by introducing different volume of pure hydrogen gas to the quartz glass photoreactor with the same conditions as mentioned above and plus a digital manometer was connected to the reactor to monitor the pressure change in the headspace of the photoreactor. Ideal gas equation has been used to calculate the amount of hydrogen in moles.

The apparent quantum efficiency as a function of wavelength was calculated based on the ratio of rate of hydrogen generation to the flux of incident photons, assuming that two photons are required according to the reaction stoichiometry, starting calculations from Eq. (1).

$$AQE(\%) = \frac{2 \times \text{number of evolved H}_2 \text{ molecules}}{\text{number of incident photons}} \quad (1)$$

## Results and discussion

The characteristics of CIS were investigated by their particle shape, size distribution, PL emission and FTIR spectra HAADF-STEM image of CIS (Fig. S2a) revealed that the size range of dots ranged between 1.8 and 2.4 nm. Two peaks around 420 and 660 nm can be seen from PL spectra of CIS. The first broad peak located around 420 nm can be attributed to nonradiative transition of excited electrons on conduction band bottom to sub-bands due to the surface defects or sulfur vacancies on CIS whereas the second red shifted peak (660 nm) can be based on the radiative transition of those electrons to the valence band of CIS [40]. The presence of MUA on the CIS can be confirmed by comparing the FTIR spectra of CIS and MUA. The disappearance of small region around 2680 cm<sup>-1</sup> which corresponds to S–H stretching in the spectra of CIS confirms the bonding between MUA and CIS surface. Moreover, O–H stretch (broad region around 3000 cm<sup>-1</sup>) and C/O stretch (sharp peak around 1720 cm<sup>-1</sup>) in MUA [41] were cleaved in CIS. Therefore, it can be suggested that MUA capping ligand bonded to CIS surface not only by –SH group but also –COOH group interacted with CIS surface. Finally, C–H stretch (sharp peak around 2900 cm<sup>-1</sup>) due to the alkene chain in MUA can be seen in both samples. The results have revealed that the increase in pH has led to improved solubility of MUA capped CIS quantum dots. The PL characteristic peak from radiative transmission signal was the highest at pH 9 which confirms the uniformly dispersed MUA capped CIS QDs. However, after pH 9, the PL signal decreased gradually and finally no characteristic peak was observed at pH 12.5–13 (Fig. S3). This will be discussed further.

The scanning electron microscopy (SEM) analysis showed that all obtained ZIS and ZIS/CIS photocatalysts are in microsphere shape which consists of many petals that results in microporous or mesoporous structure (Fig. 2a–e) as previously reported which is characteristic morphology for ZIS microspheres [13,17,32]. The size of all ZIS and ZIS/CIS range between 3 and 5  $\mu$ m whereas thickness of the petals that form the microspheres are between 20 and 50 nm (Fig. 2a, b). The presence of CIS can be observed on all ZIS/CIS as aggregated form (Fig. 2b–e) probably due to the mercaptododecanoic acid

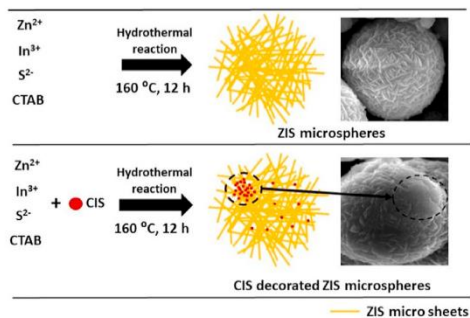


**Fig. 1** – The synthesis route for ZIS and CIS decorated ZIS microspheres. Inset: SEM images of ZIS and ZIS/CIS.

anchored on CIS surface through not only thiol but also acid group (Fig. S2d) [42]. In addition to that, the acidic of reaction medium might cause decrease in electrostatic repulsion between MUA capped CIS which results in aggregation and

nonuniformly distribution of CIS on ZIS surface [43]. On the other hand it was suggested that the better solubility of MUA capped CIS in water can be achieved at basic pH level in which the surface charge on MUA capped CIS increases due to the dissociation of carboxylic groups (Fig. S3) [44]. The increase in CIS on ZIS surface can be seen from the SEM images as in ZIS/CIS\_200 (Fig. 2d), CIS covers most of the surface of ZIS while ZIS/CIS\_50 (Fig. 2b) has lesser covered by CIS compared to ZIS/CIS\_200. The scanning transmission electron microscope with high angle annular dark field (STEM-HAADF) imaging analysis showed the presence of CIS in ZIS which agrees with SEM results. Moreover, presence of CIS ranging between 1.8 and 2.4 nm (Fig. S2a, b) in accordance to comparison of STEM-HAADF images of ZIS/CIS\_50 and ZIS/CIS\_200. ZIS/CIS\_50 has many gaps inside the between the layers of ZIS microspheres whereas these gaps diminishes in ZIS/CIS\_200 which can be clearly seen by recognizable color change in the images due to the more situated CIS between the porous of ZIS/CIS\_200 (Fig. 2j, t). In addition to STEM-HAADF, energy dispersive X-ray spectrometry (EDS) mapping approves the presence of CIS by measuring Cu element on ZIS/CIS photocatalyst and clearly reveals that CIS can be found in ZIS/CIS photocatalysts not only nonuniformly but also uniformly (Fig. 2n, s, x). The TEM images of the most active sample ZIS/CIS\_100-Pt and without

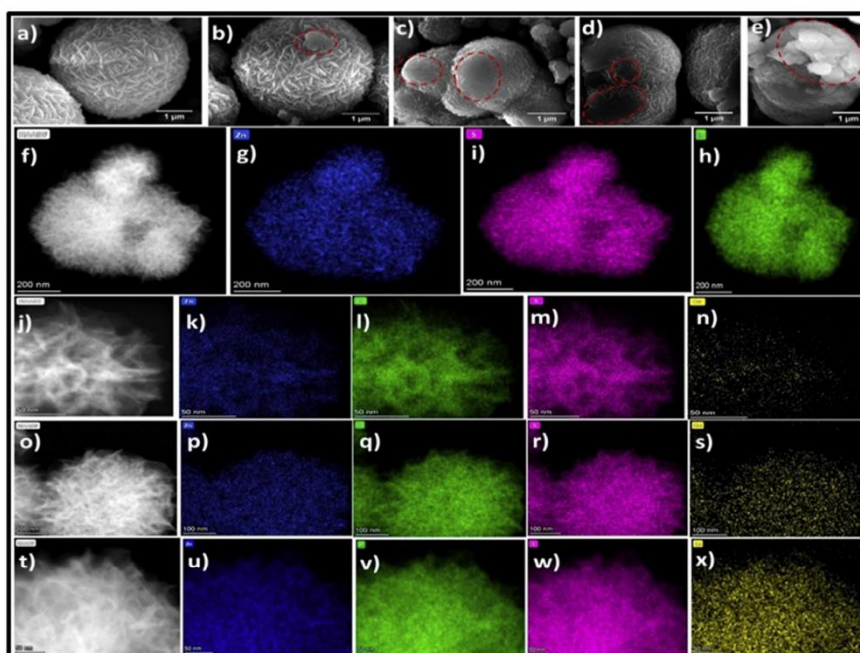


**Fig. 2** – SEM images of a) ZIS, b) ZIS/CIS\_50, c) ZIS/CIS\_100, d) ZIS/CIS\_150, e) ZIS/CIS\_200 (dashed red circles show the aggregated CIS covering the ZIS surface), STEM-HAADF images of j) ZIS/CIS\_50, o) ZIS/CIS\_150, t) ZIS/CIS\_200 with their EDS mapping of k), l), m), n) ZIS/CIS\_50, p), q), r), s) ZIS/CIS\_150, u), v), w), x) ZIS/CIS\_200 (blue, green, purple and yellow colors represent Zn, In, S and Cu elements, respectively). (For interpretation of the references to color in this figure legend, the reader is referred to the Web version of this article.)



Pt deposition ZIS/CIS\_100 was also compared (Fig. 3). The aggregated CIS with excess amount of MUA can be observed both in ZIS/CIS\_100-Pt and ZIS/CIS\_100 (Fig. 3a–c,e,f). Besides, the Pt based nanoparticles in forms of dark dots in the images with particle range around 13 nm can be observed in ZIS/CIS\_100-Pt (Fig. 3d–f) sample differently from ZIS/CIS\_100 (Fig. 3a–c) as expected. The X-ray diffraction (XRD) patterns of bare ZIS and ZIS/CIS exhibit same profile and any phase related with CIS were not detected due to the low crystallinity of CIS comparing to ZIS (Fig. S5a). XRD pattern of all ZIS/CIS, ZIS and CIS whereas Fig. S5b shows the detailed XRD spectra of CIS. All diffraction peaks of ZIS 20.65°, 28.1°, 28.5°, 47.4°, 51.8°, 56.3°, 69.2°, 76.5° and 88.4° were indexed to hexagonal crystal system in a sphalerite phase which are agreement with the literature [45,46] whereas peaks of CIS 27.5°, 46.6°, 54.8° and 74.4° were indexed to tetragonal crystal system in a roquesite phase [39]. Moreover, the change in crystallography of ZIS-Pt and ZIS/CIS\_100-Pt samples after four cycle of PHE performance experiment was also investigated by XRD (Fig. S6) and the newly formed 23.5°, 32.80°, 34.35°, 35.95°, 48.20°, 59.60° and 59.60° peaks which are indexed to trigonal structure of Na<sub>2</sub>SO<sub>3</sub> [47] in the XRD spectra of both samples can be observed.

X-ray photoelectron spectroscopy (XPS) analysis identified all elements originated from ZIS and CIS (Fig. 4) and ZIS/CIS–Pt and evaluated the elemental surface composition of these heterostructures (Table S1). Different amount of CIS decorating ZIS were well controlled by atomic ratio Cu/Zn (Table S.1). The chemical nature of elements detected in ZIS/CIS–Pt (Zn, In, Cu, S and Pt) were determined by analysis of the high-resolution (HR) XPS spectra of Zn 2p, In 3d, Cu 2p, S 2p and Pt 4f, respectively (Tables S2 and S3). As a result, the oxidation states of Zn, In, Cu, and Pt was identified as Zn<sup>2+</sup>, In<sup>3+</sup>, Cu<sup>1+</sup>, and Pt<sup>2+</sup>/Pt<sup>4+</sup>, respectively (Tables S2 and S3). The resulted data are presented in Tables S2 and S3 and Fig. 2(a–e). The high-resolution (HR) XPS spectra of Zn 2p (a), In 3d(b), Cu 2p(c) and S 2p (d) agree well with the corresponding spectra

reported in literature for ZIS/CIS nanocomposites [48–52]. The Zn 2p<sub>3/2</sub> and In 3d<sub>5/2</sub> peaks (BE of 1022.1 and 445.1 eV, respectively, Table S2) confirm the oxidation states of Zn<sup>2+</sup> and In<sup>3+</sup> in ZIS and CIS decorated ZIS heterostructures. The Cu 2p spectra features of MUA-capped CIS (c) identify Cu as Cu<sup>2+</sup> state (Cu 2p<sub>3/2</sub> signal at 932.7 eV accompanied by shakeup satellites at BE higher than 945.4 eV [53]). However, the Cu 2p spectra of all ZIS/CIS nanomaterials (Fig. 4c) exhibit the Cu 2p<sub>3/2</sub> signals at 932.3 eV, what indicates the oxidation states of Cu to be closer to Cu<sup>+</sup> [53]. The S 2p spectra of ZIS (d) are not affected by different amount of doped CIS (the main S 2p<sub>3/2</sub> signals at BE of 161.9 eV). Moreover, for all ZIS/CIS specimens we found a similar atomic ratio S/In close to 2 (2.16 ± 0.19, Table S1). The surface area of Pt deposited ZIS/CIS photocatalyst is also well characterized by the same set of Zn 2p, In 3d, Cu 2p and S 2p spectra (Fig. S7a–c, e). Additionally, the successful doping of Pt was confirmed by the Pt 4f spectrum (Fig. S7d). Unfortunately, the Pt 4f spectrum is overlapped with the Cu 3p and In 4p signals. Thus, deconvolution of this spectrum was necessary to separate the Pt signals and evaluate the Pt contents (Table S1). As a result, two Pt states, represented by Pt 4f<sub>7/2</sub> signals at 72.7 eV and 74.9.9 eV, were distinguished. First, can be assigned to Pt<sup>2+</sup> surface species (PtS, Pt-O<sub>x</sub>) and second one to Pt<sup>4+</sup> compounds (PtS<sub>2</sub>, PtO<sub>2</sub>) [54]. Also, the amount of the Pt in all photocatalysts were confirmed by ICP-OES that proves all the ZIS/CIS–Pt have about 1.26 wt% Pt (Table S.4).

Optical properties of ZIS/CIS, ZIS, CIS and ZIS/CIS–Pt were determined by UV–Vis diffusive reflectance spectroscopy (DRS) (Fig. S4a, b). The direct band gap value of ZIS [55] and CIS [26] were calculated by Kubelka-Munk method (Fig. S9)). CIS (1.87 eV) is more visible light responsive compare to all obtained ZIS (2.5 eV) and ZIS/CIS photocatalysts which has photoabsorption with the edge around more than 800 nm whereas ZIS, ZIS/CIS\_50, ZIS/CIS\_150 and ZIS/CIS\_100, ZIS/CIS\_200 are active with the edge about 630 nm and 660 nm, respectively (Fig. S4a). The color change in ZIS powder from

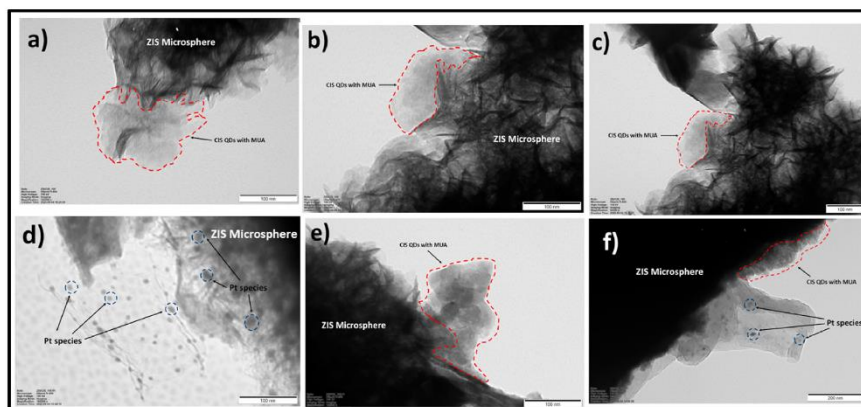


**Fig. 3** – TEM images of a, b, c) ZIS/CIS\_100 and d, e, f) ZIS/CIS\_100-Pt. Red and blue dashed lines represents CIS QDs and Pt based particles, respectively. (For interpretation of the references to color in this figure legend, the reader is referred to the Web version of this article.)

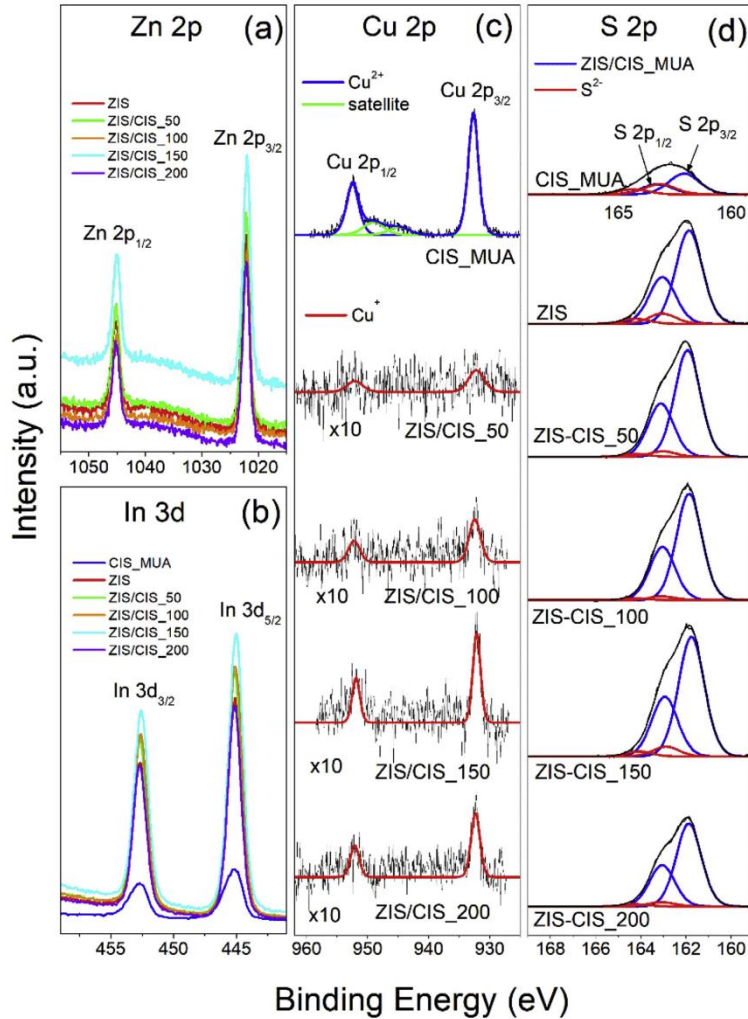
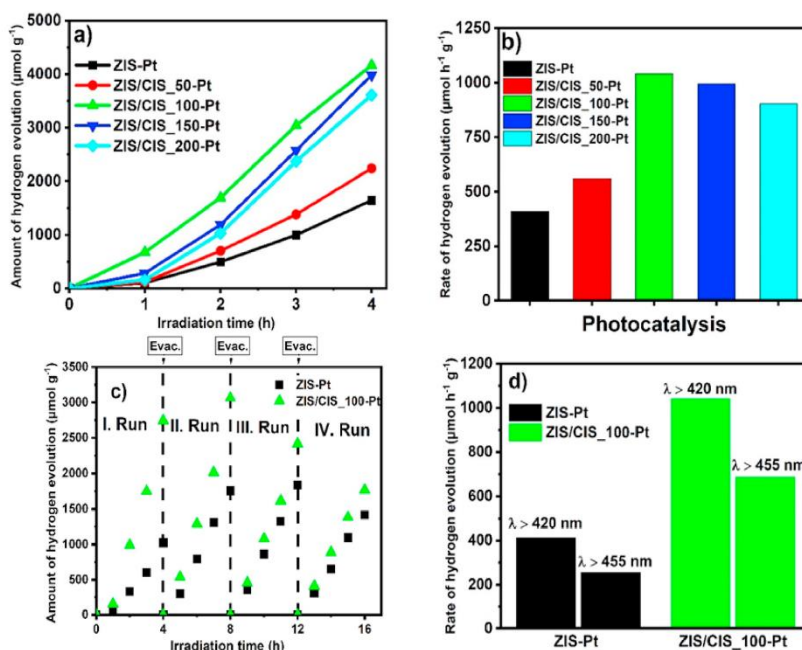


Fig. 4 – XPS spectra of a) Zn 2p, b) In 3d, c) Cu 2p, d) S 2p for ZIS/CIS and CIS with MUA samples.

yellow to reddish-yellow ZIS/CIS powders also confirms the slight increase of visible light absorption between 400 and 600 nm of ZIS/CIS compare to ZIS (Fig. S4a). After the Pt photodeposition on ZIS and ZIS/CIS surface, the significant increase in the absorption edge can be easily identified in all obtained photocatalysts which is much higher than of all ZIS/CIS (Fig. S4b). This enhancement can be explained by the increase in localized energy levels and surface plasmon resonance effect created by Pt nanoparticles on ZIS and ZIS-CIS surface [13,56,57]. Among ZIS/CIS–Pt photocatalysts, ZIS/CIS\_100-Pt has the highest absorption while the lowest absorption can be observed in ZIS/CIS\_50-Pt and ZIS/CIS\_200-

Pt. In order to investigate the recombination of photo-generated electron-hole on the surface of ZIS, ZIS/CIS and ZIS/CIS–Pt, photoluminescence (PL) spectra were studied by fluorescence spectrometry (FS) [32,58]. The lowest PL intensity detected in ZIS/CIS\_100-Pt in comparison to all photocatalysts with and without Pt deposition which proves the lowest electron-hole recombination takes place in that photocatalyst. Meanwhile, ZIS/CIS\_200 and ZIS/CIS\_200-Pt exhibit highest PL (Fig. S4c, d) which reveals that ZIS/CIS\_200-Pt (2.24 wt%) increases the recombination of hole-electrons. This increase might be explained due to the excessive amount of CIS on the ZIS surface leading to



**Fig. 5** – a) Amount and b) rate of hydrogen evolution under visible light irradiation ( $\lambda > 420$  nm) in the presence of ZIS-Pt and ZIS/CIS-Pt samples, c) cycling hydrogen evolution on ZIS-Pt and ZIS/CIS\_100-Pt under visible light irradiation ( $\lambda > 455$  nm) and d) comparison of rate of hydrogen evolution of ZIS-Pt and ZIS/CIS\_100-Pt in the presence of GG420 ( $\lambda > 420$  nm) and GG455 ( $\lambda > 455$  nm) cut-off filters.

formation of recombination centers in connection with the narrow energy gap of CIS [59].

The amount of H<sub>2</sub> generated under visible light irradiation ( $\lambda > 420$  nm) from Na<sub>2</sub>S/Na<sub>2</sub>SO<sub>3</sub> sacrificial agent solution by each ZIS/CIS-Pt after 4 h can be seen in Fig. 3a. All the ZIS/CIS-Pt photocatalysts have higher rate of H<sub>2</sub> than ZIS-Pt (Fig. 5b). The highest H<sub>2</sub> evolution rate of 1041  $\mu\text{mol h}^{-1} \text{g}^{-1}$  is exhibited by ZIS/CIS\_100-Pt which is about 2.5 times higher than that of ZIS-Pt (411.17  $\mu\text{mol h}^{-1} \text{g}^{-1}$ ). Thus, for the best PHE performance by ZIS/CIS can be reached with the ratio of 1.13 wt% of CIS. This hydrogen evolution rate is around 3.4 times lower compare to the 2D ZIS/CIS system with higher optimum amount of CIS (5 wt%) and Pt deposition (2 wt%) but also around 1.3 times higher than Cu doped ZIS with lower amount of Cu doping (0.5 wt%) and higher Pt deposition (1 wt%) (Table S5). Moreover, among ZIS/CIS-Pt, ZIS/CIS\_50-Pt exhibits the lowest H<sub>2</sub> generation rate of 559.88  $\mu\text{mol h}^{-1} \text{g}^{-1}$ . Above 1.13 wt% CIS, the PHE rate gradually decreases as is seen from the H<sub>2</sub> evolution rate of 995.27 and 902.07  $\mu\text{mol h}^{-1} \text{g}^{-1}$  by ZIS/CIS\_150-Pt (1.6 wt%) and ZIS/CIS\_200-Pt (2.24 wt%), respectively (Fig. 5b). On the other hand, the photostability of ZIS/CIS\_100-Pt and ZIS-Pt were investigated (Fig. 5c) under visible light irradiation ( $\lambda > 455$  nm). ZIS/CIS\_100-Pt and ZIS-Pt exhibit considerable H<sub>2</sub> evolution performance even at longer wavelength in the 1st run, 1025.26

and 2745.32  $\mu\text{mol g}^{-1}$ . In the 2nd run, both samples show an increase in H<sub>2</sub> evolution, more particularly ZIS-Pt produced around 1.7 times higher H<sub>2</sub> (1760  $\mu\text{mol g}^{-1}$ ) than in 1st run. After the 2nd run, both samples show a gradual decrease in the amount of H<sub>2</sub> evolution. However, it is worth to mention that the amount of hydrogen evolution by ZIS-Pt after 4th run (1415.66  $\mu\text{mol g}^{-1}$ ) is still higher than that of its evolution amount in the end of 1st run while around 25% decrease can be observed from ZIS/CIS\_100-Pt (1765.46  $\mu\text{mol g}^{-1}$ ) (Fig. 5c). Moreover, around 35% decrease in the rate of hydrogen evolution can be seen in the both ZIS-Pt and ZIS/CIS\_100-Pt as the cut-off filter is changed from GG420 ( $\lambda > 420$  nm) to GG455 ( $\lambda > 455$  nm) (Fig. 5d).

The mechanism of PHE of ZIS/CIS-Pt under visible light can be estimated firstly by approximating band structure of ZIS and CIS in accordance to valence band (VB) XPS spectra and calculated bandgap values from DRS. Based on this, the conduction band potential ( $E_{CB}$ ) of CIS and ZIS can be determined [33,60,61]. Based on this, the valence band maximum values of ZIS and CIS are 1.5 eV and 0.6 eV (V vs NHE) (Fig. S8), whereas the direct band gap ( $E_g$ ) of ZIS and CIS were estimated by Kubelka-Munk function [62–65] using Eq. (2):

$$F(R) \cdot h\nu = k(h\nu - E_g)^{1/n} \quad (2)$$



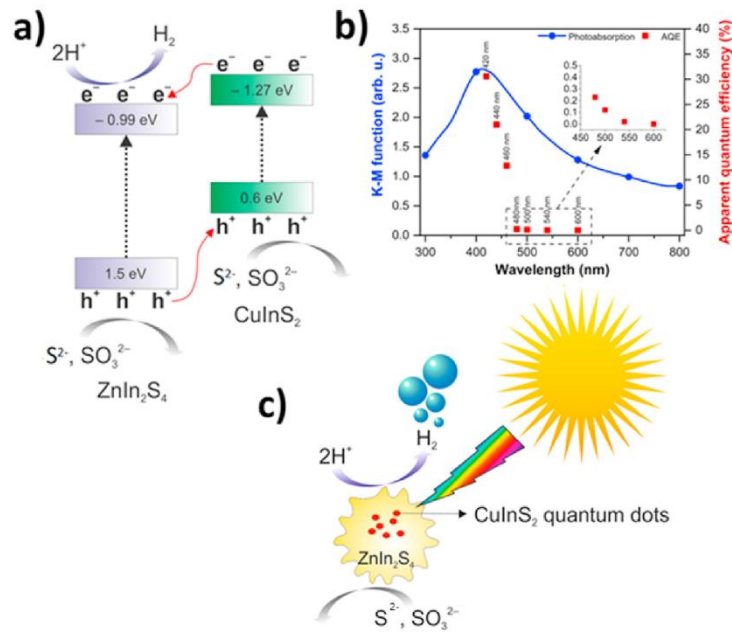


**Fig. 6 – a) Charge transfer mechanism and band alignment in the ZIS/CIS–Pt (V vs NHE) b) action spectra analysis of photogenerated hydrogen evolution over ZIS/CIS\_100-Pt sample c) schematic representation of photogenerated hydrogen evolution.**

where  $F(R)$  is Kubelka-Munk function,  $R$  is the reflectance (Fig. S9) and  $n$  is the exponent depending on the type of transition which is  $n = 2$  for both ZIS and CIS. By using the plot of  $(F(R) \cdot hv)^2$  vs.  $hv$ ,  $E_g$  of CIS and ZIS are about  $E_g = 1.87$  and  $2.49$  eV, respectively. Finally, by considering the  $E_g$  and  $E_{VB}$ , the conduction band (CB) of ZIS and CIS was estimated around  $-0.99$  and  $-1.27$  eV (V vs NHE), respectively. Thus, the CB potentials of both ZIS and CIS are thermodynamically suitable for PHE by considering the  $H^+/H_2$  reduction potential  $0$  eV (V vs NHE) [32]. During the visible light irradiation, ZIS and CIS are photoexcited and produce photogenerated electrons ( $e^-$ ) and holes ( $h^+$ ). The photogenerated electrons on the CIS surface move to lower CB potential of ZIS and are captured by active sites of ZIS/CIS–Pt where Pt nanoparticles act as an electron sink for  $H_2$  generation by capturing the photogenerated electrons and prevent the recombination [66,67]. Meanwhile, photogenerated holes in ZIS are captured by the VB of CIS that results in inhibition of recombination of holes and electrons on ZIS and the holes on CIS surface are scavenged by  $SO_3^{2-}$  and  $S^{2-}$  ions to form  $SO_4^{2-}$  and  $S_2^{2-}$ , respectively. So that the charge separation over ZIS/CIS–Pt surface is facilitated [68,69] (Fig. 6a, c). Moreover, it is worth to mention that the rise in PHE rate of ZIS/CIS\_100-Pt might be associated with the adsorption mechanism on the photocatalysis surface [70]. In more detail, the photogenerated electrons and holes-initiated reactions

are given below on the photocatalysis surface in the case of  $Na_2S/Na_2SO_3$  sacrificial agent solution [71].



After charge carrier generation, photogenerated holes-initiated reactions occur and  $SO_3^{2-}$  and  $S^{2-}$  ions form  $SO_4^{2-}$  and  $S_2^{2-}$  ions, respectively. However, initial condition for these surface reactions is competitive adsorption of  $Na_2SO_3$  and  $Na_2S$  on photocatalysis surface which follows Langmuir-Hinshelwood model [72]. Therefore, the higher surface area in ZIS/CIS\_100-Pt ( $32.5$  m<sup>2</sup>/g) comparing to ZIS-Pt ( $24$  m<sup>2</sup>/g) might lead to more  $Na_2SO_3$  consumption on its surface thus higher PHE rate. Consequently, the optimum amount of CIS (1.13 wt%) in ZIS/CIS photocatalyst increases the charge separation efficiently by forming a heterojunction that leads to enhancement of the PHE rate comparing to bare ZIS. To gain

insight into the mechanism of photocatalytic hydrogen evolution, the action spectra analysis was performed with ZIS/CIS\_100-Pt and apparent quantum efficiency (AQE) was calculated as a function of the irradiation light (420, 440, 460, 480, 500, 540 and 600 nm). Indeed, the ZIS/CIS\_100-Pt sample had high ability to generate H<sub>2</sub> in the visible light range up to a wavelength of 540 nm, which correlates well with its photoabsorption properties – less light absorption capacity led to less H<sub>2</sub> evolution and lower AQE values (Fig. 6b). For the longer wavelength than 540 nm (600 nm), AQE reached the values of 0%. In addition, two regions can be distinguished, namely with extremely high (up to 480 nm) and moderate (from 480 to 540 nm) power to evaluate H<sub>2</sub>. The highest AQE was observed at 420 nm (30.6%). To the best of our knowledge this value is second the highest results among the ZnIn<sub>2</sub>S<sub>4</sub>-based photocatalysts in the literature (Table S5) and the widest region with observable H<sub>2</sub> evolution photoactivity. Thus, photocatalytic H<sub>2</sub> evolution was mainly dependent on the photoabsorption properties of the ZIS/CIS photocatalyst. As very low activity was exhibited by both ZIS and CIS without Pt deposition (Fig. S10), the effect of the Pt species on photogenerated hydrogen evolution rate can be expected. In consideration of Pt oxides, Pt-Ox and PtO<sub>2</sub>, it was suggested that maximization of Pt<sup>4+</sup> sites are more efficient than that of Pt<sup>2+</sup> species in electrochemical hydrogen evolution [73]. However, in the case of Pt sulfides, PtS and PtS<sub>2</sub>, this might be different. During photodeposition process, excessive amount of sulfur in ZnIn<sub>2</sub>S<sub>4</sub> promotes more likely the formation of PtS semiconductor on ZnIn<sub>2</sub>S<sub>4</sub> due to the adsorption of Pt<sup>2+</sup> on ZnIn<sub>2</sub>S<sub>4</sub> [74]. The same phenomena might occur in ZIS/CIS\_100-Pt and ZIS/CIS–Pt samples as is seen from previously mentioned XPS results that Pt<sup>2+</sup> state can be detected in ZIS/CIS\_100-Pt and ZIS/CIS–Pt surface. However, Pt<sup>4+</sup> was also detected which corresponds according to PtO<sub>2</sub> or PtS<sub>2</sub> species in ZIS/CIS\_100-Pt and ZIS/CIS–Pt samples according to the XPS results. The increased Pt(II) component contribution by reduction of PtS<sub>2</sub> resulted in induced the hydrogen evolution rate in PtS<sub>2</sub> [75]. Moreover it was also reported that PtS<sub>2</sub> worked more efficiently than the metallic Pt particles in case of Z-scheme employing metal sulfide photocatalysis [76]. As a result, one can suggest that different species of Pt have different activity: in case of Pt oxides, PtO<sub>2</sub> > Pt-Ox whereas for Pt sulfides PtS > PtS<sub>2</sub> among Pt sulfides. However detailed studies are crucial to reveal which form of those species exist dominantly in ZIS/CIS\_100-Pt and ZIS/CIS–Pt samples. On the other hand, the decrease in H<sub>2</sub> generation rate above the optimum amount of CIS can be also highlighted. Above the optimum value of CIS, as clearly seen in Fig. 1e, the ZIS surface is covered by CIS in which the photons required for photoexcitation of ZIS might be blocked. Therefore, photoexcitation of ZIS diminishes due to the insufficient number of photons reaching ZIS surface. Thereby, induced the number of photoexcited electrons and holes results in a drop of PHE rate. Also, in higher amounts, CIS may locate the active sites in ZIS for H<sub>2</sub> generation [77] and creates recombination centers competing with the active sites for H<sub>2</sub> evolution and increases the recombination rate (Fig. S4d). Moreover, over CIS decoration than the optimum might narrow the space charge region in ZIS/CIS heterojunction system, and the penetration depth of ZIS surpasses the space charge layer in which photogenerated holes and electrons recombine easier [78]. In

addition, the rapid decline in photocatalytic activity in both ZIS-Pt and ZIS/CIS\_100-Pt samples after the 2nd run can be linked to the self-oxidation of S<sup>2-</sup> in ZIS by photo-generated holes in the valence band of ZIS [52]. That is supported by XPS results of both ZIS-Pt and ZIS/CIS\_100-Pt samples before and after cycling experiments in which remarkable drop can be seen in fraction of S<sup>2-</sup> state (Table S3). Furthermore, that decline can be also correlated to the notable decrease in Zn and In contents in ZIS-Pt and ZIS/CIS\_100-Pt samples (Fig. S7 and Table S1 and S3). However, the XPS peak related with Cu 3p orbital decreased also in ZIS/CIS\_100-Pt sample after photostability cycle runs, but this decrease is not significant as in Zn and In contents (Fig. S7).

## Conclusions

ZnIn<sub>2</sub>S<sub>4</sub> microspheres decorated with pre-prepared CuInS<sub>2</sub> quantum dots were prepared successfully by simple hydrothermal reaction and modified by Pt photodeposition for the first time. Introducing optimum amount of 1.13 wt% CuInS<sub>2</sub> quantum dots to the hydrothermal reaction medium for ZnIn<sub>2</sub>S<sub>4</sub> microspheres increased rate of bare ZIS about 2.5 times under visible light irradiation. This enhancement is related with the improved light harvesting ability of ZnIn<sub>2</sub>S<sub>4</sub> microspheres/CuInS<sub>2</sub> quantum dots system in consequence of the formed heterojunction between CuInS<sub>2</sub> quantum dots and ZnIn<sub>2</sub>S<sub>4</sub> matrix. The broad visible range photoactivity up to 540 nm was observed with remarkable AQE at 420 nm (30.6%). Further investigations are required to understand the fate of the quantum dots during hydrothermal reaction, the effect of the different reaction conditions on configuration of quantum dots on ZnIn<sub>2</sub>S<sub>4</sub> matrixes and impact on photocatalytic activity. Moreover, the optimum amount of Pt deposition on ZnIn<sub>2</sub>S<sub>4</sub> microspheres/CuInS<sub>2</sub> quantum dots heterojunction system must be investigated for the further studies. We suggest that using CuInS<sub>2</sub> quantum dots as a reactant in a hydrothermal synthesis can be an alternative approach to obtain heterojunction to improve the photocatalytic activity of ZnIn<sub>2</sub>S<sub>4</sub> for photogenerated hydrogen evolution applications.

## Declaration of competing interest

The authors declare that they have no known competing financial interests or personal relationships that could have appeared to influence the work reported in this paper.

## Acknowledgement

This research was financially supported by National Science Centre, Poland (Grant No. 2016/23/D/ST8/02682). Action spectra set-up was financially support by National Science Centre, Poland (Grant No. 2016/23/B/ST8/03336). We would like to thank Lothar Houben from Weizmann Institute of Science for STEM-HAADF images and Andrzej Żak from Wrocław University of Science and Technology for TEM images of ZIS/CIS\_100 and ZIS/CIS\_100-Pt samples.



## Appendix A. Supplementary data

Supplementary data to this article can be found online at <https://doi.org/10.1016/j.ijhydene.2020.09.212>.

## REFERENCES

- [1] Dutta S. A review on production, storage of hydrogen and its utilization as an energy resource. *J Ind Eng Chem* 2014;20:1148–56. <https://doi.org/10.1016/j.jiec.2013.07.037>.
- [2] Edwards PP, Kuznetsov VL, David WIF, Brandon NP. Hydrogen and fuel cells: towards a sustainable energy future. *Energy Pol* 2008;36:4356–62. <https://doi.org/10.1016/j.enpol.2008.09.036>.
- [3] Dincer I, Acar C. Review and evaluation of hydrogen production methods for better sustainability. *Int J Hydrogen Energy* 2014;40:11094–111. <https://doi.org/10.1016/j.ijhydene.2014.12.035>.
- [4] Fujishima A, Honda K. Electrochemical photolysis of water at a semiconductor electrode. *Nature* 1972;238:37–8. <https://doi.org/10.1038/238037a0>.
- [5] Yang X, Xue H, Xu J, Huang X, Zhang J, Tang YB, Ng TW, Kwong HL, Meng XM, Lee CS. Synthesis of porous ZnS:Ag2S nanosheets by ion exchange for photocatalytic H<sub>2</sub> generation. *ACS Appl Mater Interfaces* 2014;6:9078–84. <https://doi.org/10.1021/am5020953>.
- [6] Liu Z, Bai H, Xu S, Sun DD. Hierarchical CuO/ZnO “corn-like” architecture for photocatalytic hydrogen generation. *Int J Hydrogen Energy* 2011;36:13473–80. <https://doi.org/10.1016/j.ijhydene.2011.07.137>.
- [7] Bai H, Juay J, Liu Z, Song X, Lee SS, Sun DD. Hierarchical SrTiO<sub>3</sub>/TiO<sub>2</sub> nanofibers heterostructures with high efficiency in photocatalytic H<sub>2</sub> generation. *Appl Catal B Environ* 2012;125:367–74. <https://doi.org/10.1016/j.apcatb.2012.06.007>.
- [8] Gasparotto A, Barreca D, Bekermann D, Devi A, Fischer RA, Fornasiero P, Gombac V, Lebedev OI, MacCato C, Montini T, Van Tendeloo G, Tondello E. F-doped Co<sub>3</sub>O<sub>4</sub> photocatalysts for sustainable H<sub>2</sub> generation from water/ethanol. *J Am Chem Soc* 2011;133:19362–5. <https://doi.org/10.1021/ja210078d>.
- [9] Tijare SN, Joshi MV, Padole PS, Mangrulkar PA, Rayalu SS, Labhsetwar NK. Photocatalytic hydrogen generation through water splitting on nano-crystalline LaFeO<sub>3</sub> perovskite. *Int J Hydrogen Energy* 2012;37:10451–6. <https://doi.org/10.1016/j.ijhydene.2012.01.120>.
- [10] Marschall R, Soldat J, Wark M. Enhanced photocatalytic hydrogen generation from barium tantalate composites. *Photochem Photobiol Sci* 2013;12:671–7. <https://doi.org/10.1039/c2pp25200g>.
- [11] Khan Z, Qureshi M. Tantalum doped BaZrO<sub>3</sub> for efficient photocatalytic hydrogen generation by water splitting. *Catal Commun* 2012;28:82–5. <https://doi.org/10.1016/j.catcom.2012.08.002>.
- [12] Lozano-Sánchez LM, Méndez-Medrano MG, Colbeau-Justin C, Rodríguez-López JL, Hernández-Uresti DB, Obregón S. Long-lived photoinduced charge-carriers in Er<sup>3+</sup>-doped CaTiO<sub>3</sub> for photocatalytic H<sub>2</sub> production under UV irradiation. *Catal Commun* 2016;84:36–9. <https://doi.org/10.1016/j.catcom.2016.06.002>.
- [13] Li Q, Cui C, Meng H, Yu J. Visible-light photocatalytic hydrogen production activity of ZnIn<sub>2</sub>S<sub>4</sub> microspheres using carbon quantum dots and platinum as dual co-catalysts. *Chem - An Asian J* 2014;9:1766–70. <https://doi.org/10.1002/asia.201402128>.
- [14] Lei Z, You W, Liu M, Zhou G, Takata T, Hara M, Domen K, Li C. Photocatalytic water reduction under visible light on a novel ZnIn<sub>2</sub>S<sub>4</sub> catalyst synthesized by hydrothermal method. *Chem Commun* 2003;3:2142–3. <https://doi.org/10.1039/b306813g>.
- [15] Zhang S, Liu X, Liu C, Luo S, Wang L, Cai T, Zeng Y, Yuan J, Dong W, Pei Y, Liu Y. MoS<sub>2</sub> quantum dot growth induced by S vacancies in a ZnIn<sub>2</sub>S<sub>4</sub> monolayer: atomic-level heterostructure for photocatalytic hydrogen production. *ACS Nano* 2018;12:751–8. <https://doi.org/10.1021/acsnano.7b07974>.
- [16] Gou X, Cheng F, Shi Y, Zhang L, Peng S, Chen J, Shen P. Shape-controlled synthesis of ternary chalcogenide ZnIn<sub>2</sub>S<sub>4</sub> and CuIn(S,Se)<sub>2</sub> nano-/microstructures via facile solution route. *J Am Chem Soc* 2006;128:7222–9. <https://doi.org/10.1021/ja0580845>.
- [17] Shen S, Zhao L, Zhou Z, Guo L. Enhanced photocatalytic hydrogen evolution over Cu-doped ZnIn<sub>2</sub>S<sub>4</sub> under visible light irradiation. *J Phys Chem C* 2008;112:16148–55. <https://doi.org/10.1021/jp804525q>.
- [18] Xia Y, Li Q, Lv K, Tang D, Li M. Superiority of graphene over carbon analogs for enhanced photocatalytic H<sub>2</sub>-production activity of ZnIn<sub>2</sub>S<sub>4</sub>. *Appl Catal B Environ* 2017;206:344–52. <https://doi.org/10.1016/j.apcatb.2017.01.060>.
- [19] Zhu R, Tian F, Yang R, He J, Zhong J, Chen B. Z scheme system ZnIn<sub>2</sub>S<sub>4</sub>/RGO/BiVO<sub>4</sub> for hydrogen generation from water splitting and simultaneous degradation of organic pollutants under visible light. *Renew Energy* 2019;139:22–7. <https://doi.org/10.1016/j.renene.2019.02.049>.
- [20] Zeng D, Xiao L, Ong WJ, Wu P, Zheng H, Chen Y, Peng DL. Hierarchical ZnIn<sub>2</sub>S<sub>4</sub>/MoSe<sub>2</sub> nanoarchitectures for efficient noble-metal-free photocatalytic hydrogen evolution under visible light. *ChemSusChem* 2017;10:4624–31. <https://doi.org/10.1002/cssc.201701345>.
- [21] Liu H, Jin Z, Xu Z, Zhang Z, Ao D. Fabrication of ZnIn<sub>2</sub>S<sub>4</sub>-g-C<sub>3</sub>N<sub>4</sub> sheet-on-sheet nanocomposites for efficient visible-light photocatalytic H<sub>2</sub>-evolution and degradation of organic pollutants. *RSC Adv* 2015;5:97951–61. <https://doi.org/10.1039/c5ra17028a>.
- [22] Ye L, Wen Z. ZnIn<sub>2</sub>S<sub>4</sub> nanosheets decorating WO<sub>3</sub> nanorods core-shell hybrids for boosting visible-light photocatalysis hydrogen generation. *Int J Hydrogen Energy* 2019;44:3751–9. <https://doi.org/10.1016/j.ijhydene.2018.12.093>.
- [23] Bozetine H, Wang Q, Barras A, Li M, Hadjersi T, Szunerits S, Boukherrouf R. Green chemistry approach for the synthesis of ZnO-carbon dots nanocomposites with good photocatalytic properties under visible light. *J Colloid Interface Sci* 2016;465:286–94. <https://doi.org/10.1016/j.jcis.2015.12.001>.
- [24] Kumar S, Dhiman A, Sudhagar P, Krishnan V. ZnO-graphene quantum dots heterojunctions for natural sunlight-driven photocatalytic environmental remediation. *Appl Surf Sci* 2018;447:802–15. <https://doi.org/10.1016/j.apsusc.2018.04.045>.
- [25] Li Y, Lv K, Ho W, Dong F, Wu X, Xia Y. Hybridization of rutile TiO<sub>2</sub> (rTiO<sub>2</sub>) with g-C<sub>3</sub>N<sub>4</sub> quantum dots (CN QDs): an efficient visible-light-driven Z-scheme hybridized photocatalyst. *Appl Catal B Environ* 2017;202:611–9. <https://doi.org/10.1016/j.apcatb.2016.09.055>.
- [26] Shen F, Que W, Liao Y, Yin X. Photocatalytic activity of TiO<sub>2</sub> nanoparticles sensitized by CuInS<sub>2</sub> quantum dots. *Ind Eng Chem Res* 2011;50:9131–7. <https://doi.org/10.1021/ie2007467>.
- [27] Wang K, Zhang G, Li J, Li Y, Wu X. 0D/2D Z-scheme heterojunctions of bismuth tantalate quantum dots/ultrathin g-C<sub>3</sub>N<sub>4</sub> nanosheets for highly efficient visible light photocatalytic degradation of antibiotics. *ACS Appl Mater Interfaces* 2017;9:43704–15. <https://doi.org/10.1021/acsnano.7b14275>.

- [28] Ge L, Zuo F, Liu J, Ma Q, Wang C, Sun D, Bartels L, Feng P. Synthesis and efficient visible light photocatalytic hydrogen evolution of Polymeric g-C 3N 4 coupled with CdS quantum dots. *J Phys Chem C* 2012;116:13708–14. <https://doi.org/10.1021/jp3041692>.
- [29] Bera D, Qian L, Tseng TK, Holloway PH. Quantum dots and their multimodal applications: a review. *Materials* 2010;3:2260–345. <https://doi.org/10.3390/ma3042260> (Basel).
- [30] Frigerio C, Ribeiro DSM, Rodrigues SSM, Abreu VLRG, Barbosa JAC, Prior JAV, Marques KL, Santos JLM. Application of quantum dots as analytical tools in automated chemical analysis: a review. *Anal Chim Acta* 2012;735:9–22. <https://doi.org/10.1016/j.aca.2012.04.042>.
- [31] Bajorowicz B, Kobylański MP, Gołębiewska A, Nadolna J, Zaleska-Medynska A, Malankowska A. Quantum dot-decorated semiconductor micro- and nanoparticles: a review of their synthesis, characterization and application in photocatalysis. *Adv Colloid Interface Sci* 2018;256:352–72. <https://doi.org/10.1016/j.cis.2018.02.003>.
- [32] Hou J, Yang C, Cheng H, Wang Z, Jiao S, Zhu H. Ternary 3D architectures of CdS QDs/graphene/ZnIn2S4 heterostructures for efficient photocatalytic H<sub>2</sub> production. *Phys Chem Chem Phys* 2013;15:15660–8. <https://doi.org/10.1039/c3cp51857d>.
- [33] Zhang S, Wang L, Liu C, Luo J, Crittenden J, Liu X, Cai T, Yuan J, Pei Y, Liu Y. Photocatalytic wastewater purification with simultaneous hydrogen production using MoS<sub>2</sub> QD-decorated hierarchical assembly of ZnIn<sub>2</sub>S<sub>4</sub> on reduced graphene oxide photocatalyst. *Water Res* 2017;121:11–9. <https://doi.org/10.1016/j.watres.2017.05.013>.
- [34] Sandroni M, Gueret R, Wegner KD, Reiss P, Fortage J, Aldakov D, Collomb MN. Cadmium-free CuInS<sub>2</sub>/ZnS quantum dots as efficient and robust photosensitizers in combination with a molecular catalyst for visible light-driven H<sub>2</sub> production in water. *Energy Environ Sci* 2018;11:1752–61. <https://doi.org/10.1039/c8ee00120k>.
- [35] Hu W, Yang S, Huang J. Composition effect on the carrier dynamics and catalytic performance of CuInS<sub>2</sub>/ZnS quantum dots for light driven hydrogen generation. *J Chem Phys* 2019;151. <https://doi.org/10.1063/1.5125024>.
- [36] Nie C, Ni W, Gong L, Jiang J, Wang J, Wang M. Charge transfer dynamics and catalytic performance of a covalently linked hybrid assembly comprising a functionalized cobalt tetraazamacrocyclic catalyst and CuInS<sub>2</sub>/ZnS quantum dots for photochemical hydrogen production. *J Mater Chem A* 2019;7:27432–40. <https://doi.org/10.1039/c9ta10479h>.
- [37] Guan Z, Pan J, Li Q, Li G, Yang J. Boosting visible-light photocatalytic hydrogen evolution with an efficient CuInS<sub>2</sub>/ZnIn<sub>2</sub>S<sub>4</sub> 2D/2D heterojunction. *ACS Sustain Chem Eng* 2019;7:7736–42. <https://doi.org/10.1021/acssuschemeng.8b06587>.
- [38] Guo X, Peng Y, Liu G, Xie G, Guo Y, Zhang Y, Yu J. An efficient ZnIn<sub>2</sub>S<sub>4</sub>@CuInS<sub>2</sub> core-shell p-n heterojunction to boost visible-light photocatalytic hydrogen evolution. *J Phys Chem C* 2020;124:5934–43. <https://doi.org/10.1021/acs.jpcc.9b11623>.
- [39] Booth M. Synthesis and characterisation of CuInS<sub>2</sub> quantum dots. *The University of Leeds School of Physics & Astronomy*; 2014. <https://doi.org/uk.bl.ethos.640628>.
- [40] Lim J, Bae WK, Kwak J, Lee S, Lee C, Char K. Perspective on synthesis, device structures, and printing processes for quantum dot displays. *Opt Mater Express* 2012;2:594. <https://doi.org/10.1364/ome.2.000594>.
- [41] Simsikova M, Antalík M, Kaňuchová M, Škvarla J. Anionic 11-mercaptoundecanoic acid capped ZnO nanoparticles. *Appl Surf Sci* 2013;282:342–7. <https://doi.org/10.1016/j.apsusc.2013.05.130>.
- [42] Kim H, Suh M, Kwon BH, Jang DS, Kim SW, Jeon DY. In situ ligand exchange of thiol-capped CuInS<sub>2</sub>/ZnS quantum dots at growth stage without affecting luminescent characteristics. *J Colloid Interface Sci* 2011;363:703–6. <https://doi.org/10.1016/j.jcis.2011.06.087>.
- [43] Algar WR, Krull UJ. Luminescence and stability of aqueous thioalkyl acid capped CdSe/ZnS quantum dots correlated to ligand ionization. *ChemPhysChem* 2007;8:561–8. <https://doi.org/10.1002/cphc.200600686>.
- [44] Hardzei M, Artemyev M. Influence of pH on luminescence from water-soluble colloidal Mn-doped ZnSe quantum dots capped with different mercaptoacids. *J Lumin* 2012;132:425–8. <https://doi.org/10.1016/j.jlumin.2011.09.018>.
- [45] Shen S, Zhao L, Guo L, Crystallite. Optical and photocatalytic properties of visible-light-driven ZnIn<sub>2</sub>S<sub>4</sub> photocatalysts synthesized via a surfactant-assisted hydrothermal method. *Mater Res Bull* 2009;44:100–5. <https://doi.org/10.1016/j.materresbull.2008.03.027>.
- [46] Tian F, Zhu R, Song K, Niu M, Ouyang F, Cao G. The effects of hydrothermal temperature on the photocatalytic performance of ZnIn<sub>2</sub>S<sub>4</sub> for hydrogen generation under visible light irradiation. *Mater Res Bull* 2015;70:645–50. <https://doi.org/10.1016/j.materresbull.2015.05.033>.
- [47] Jain A, Ong SP, Hautier G, Chen W, Richards WD, Dacek S, Cholia S, Gunter D, Skinner D, Ceder G, Persson KA. Commentary: the materials project: a materials genome approach to accelerating materials innovation. *Apl Mater* 2013;1. <https://doi.org/10.1063/1.4812323>.
- [48] De Trizio L, Prato M, Genovese A, Casu A, Povia M, Simonutti R, Alcocer MJP, D'Andrea C, Tassone F, Manna L. Strongly fluorescent quaternary Cu-In-Zn-S nanocrystals prepared from Cu 1-xInS 2 nanocrystals by partial cation exchange. *Chem Mater* 2012;24:2400–6. <https://doi.org/10.1021/cm301211e>.
- [49] Tang X, Tay Q, Chen Z, Chen Y, Goh GKL, Xue J. CuInZnS-decorated graphene nanosheets for highly efficient visible-light-driven photocatalytic hydrogen production. *J Mater Chem A* 2013;1:6359–65. <https://doi.org/10.1039/c3ta01602a>.
- [50] Gabka G, Bujak P, Giedyk K, Kotwica K, Ostrowski A, Malinowska K, Lisowski W, Sobczak JW, Pron A. Ligand exchange in quaternary alloyed nanocrystals - a spectroscopic study. *Phys Chem Chem Phys* 2014;16:23082–8. <https://doi.org/10.1039/c4cp03850a>.
- [51] Courtel FM, Paynter RW, Marsan B, Morin M. Synthesis, characterization, and growth mechanism of n-Type CuInS<sub>2</sub> colloidal particles. *Chem Mater* 2009;21:3752–62. <https://doi.org/10.1021/cm900601k>.
- [52] Do JY, Choi S, Nahm K, Kim SK, Kang M. Reliable hydrogen production from methanol photolysis in aqueous solution by a harmony between in and Zn in bimetallic zinc indium sulfide. *Mater Res Bull* 2018;100:234–42. <https://doi.org/10.1016/j.materresbull.2017.12.034>.
- [53] Biesinger MC, Lau LWM, Gerson AR, Smart RSC. Resolving surface chemical states in XPS analysis of first row transition metals, oxides and hydroxides: Sc, Ti, V, Cu and Zn. *Appl Surf Sci* 2010;257:887–98. <https://doi.org/10.1016/j.apsusc.2010.07.086>.
- [54] Naumkin AV, Kraut-Vass A, Gaarenstroom SW, Powell CJ. NIST X-ray photoelectron spectroscopy database, NIST standard reference database 20. Natl. Inst. Stand. Technol.; 2012. <https://doi.org/10.18434/T4T88K>, Version 4.1.
- [55] Wang G, Chen G, Yu Y, Zhou X, Teng Y. Mixed solvothermal synthesis of hierarchical ZnIn<sub>2</sub>S<sub>4</sub> spheres: specific facet-induced photocatalytic activity enhancement and a DFT elucidation. *RSC Adv* 2013;3:18579–86. <https://doi.org/10.1039/c3ra42245c>.
- [56] Sakhthivel S, Shankar MV, Palanichamy M, Arabindoo B, Bahnemann DW, Murugesan V. Enhancement of photocatalytic activity by metal deposition: characterisation and photonic efficiency of Pt, Au and Pd deposited on TiO<sub>2</sub>



- catalyst. *Water Res* 2004;38:3001–8. <https://doi.org/10.1016/j.watres.2004.04.046>.
- [57] Vamvasakis I, Liu B, Armatas GS. Size effects of platinum nanoparticles in the photocatalytic hydrogen production over 3D mesoporous networks of CdS and Pt nanojunctions. *Adv Funct Mater* 2016;26:8062–71. <https://doi.org/10.1002/adfm.201603292>.
- [58] Wang Z, Hou J, Jiao S, Huang K, Zhu H. In situ chemical reduction of the Ta 3N 5 quantum dots coupled TaON hollow spheres heterojunction photocatalyst for water oxidation. *J Mater Chem* 2012;22:21972–8. <https://doi.org/10.1039/c2jm35374a>.
- [59] Li X, Wang J, Men Y, Bian Z. TiO<sub>2</sub> mesocrystal with exposed (001) facets and CdS quantum dots as an active visible photocatalyst for selective oxidation reactions. *Appl Catal B Environ* 2016;187:115–21. <https://doi.org/10.1016/j.apcatb.2016.01.034>.
- [60] Zhou X, Wierzbicka E, Liu N, Schmuki P. Black and white anatase, rutile and mixed forms: band-edges and photocatalytic activity. *Chem Commun* 2019;55:533–6. <https://doi.org/10.1039/c8cc07665k>.
- [61] Xu J, Teng Y, Teng F. Effect of surface defect states on valence band and charge separation and transfer efficiency. *Sci Rep* 2016;6:1–9. <https://doi.org/10.1038/srep32457>.
- [62] Köferstein R, Jäger L, Ebbinghaus SG. Magnetic and optical investigations on LaFeO<sub>3</sub> powders with different particle sizes and corresponding ceramics. *Solid State Ionics* 2013;249–250:1–5. <https://doi.org/10.1016/j.ssi.2013.07.001>.
- [63] Köferstein R, Ebbinghaus SG. Investigations of BaFe<sub>0.5</sub>Nb<sub>0.5</sub>O<sub>3</sub> nano powders prepared by a low temperature aqueous synthesis and resulting ceramics. *J Eur Ceram Soc* 2017;37:1509–16. <https://doi.org/10.1016/j.jeurceramsoc.2016.12.014>.
- [64] López R, Gómez R. Band-gap energy estimation from diffuse reflectance measurements on sol-gel and commercial TiO<sub>2</sub>: a comparative study. *J Sol-Gel Sci Technol* 2012;61:1–7. <https://doi.org/10.1007/s10971-011-2582-9>.
- [65] Nowak M, Kauch B, Szperlich P. Determination of energy band gap of nanocrystalline SbSI using diffuse reflectance spectroscopy. *Rev Sci Instrum* 2009;80:21–4. <https://doi.org/10.1063/1.3103603>.
- [66] Shen J, Zai J, Yuan Y, Qian X. 3D hierarchical ZnIn 2S 4: the preparation and photocatalytic properties on water splitting. *Int J Hydrogen Energy* 2012;37:16986–93. <https://doi.org/10.1016/j.ijhydene.2012.08.038>.
- [67] Malankowska A, Kobylański MP, Mikolajczyk A, Cavdar O, Nowaczyk G, Jarek M, Lisowski W, Michalska M, Kowalska E, Ohtani B, Zaleska-Medynska A. TiO<sub>2</sub> and NaTaO<sub>3</sub> decorated by trimetallic Au/Pd/Pt core-shell nanoparticles as efficient photocatalysts: experimental and computational studies. *ACS Sustain Chem Eng* 2018;6:16665–82. <https://doi.org/10.1021/acssuschemeng.8b03919>.
- [68] Wang L, Wang W, Shang M, Yin W, Sun S, Zhang L. Enhanced photocatalytic hydrogen evolution under visible light over Cd<sub>1-x</sub>Zn<sub>x</sub>S solid solution with cubic zinc blend phase. *Int J Hydrogen Energy* 2010;35:19–25. <https://doi.org/10.1016/j.ijhydene.2009.10.084>.
- [69] Mahadik MA, Shinde PS, Cho M, Jang JS. Fabrication of a ternary CdS/ZnIn<sub>2</sub>S<sub>4</sub>/TiO<sub>2</sub> heterojunction for enhancing photoelectrochemical performance: effect of cascading electron-hole transfer. *J Mater Chem A* 2015;3:23597–606. <https://doi.org/10.1039/c5ta07454a>.
- [70] Tambago HMG, de Leon RL. Intrinsic kinetic modeling of hydrogen production by photocatalytic water splitting using cadmium zinc sulfide catalyst. *Int. J. Chem. Eng. Appl.* 2015;6:220–7. <https://doi.org/10.7763/ijcea.2015.v6.485>.
- [71] Bao N, Shen L, Takata T, Domen K. Self-templated synthesis of nanoporous CdS nanostructures for highly efficient photocatalytic hydrogen production under visible light. *Chem Mater* 2008;20:110–7. <https://doi.org/10.1021/cm7029344>.
- [72] Markovskaya DV, Cherepanova SV, Saraev AA, Gerasimov EY, Kozlova EA. Photocatalytic hydrogen evolution from aqueous solutions of Na<sub>2</sub>S/Na<sub>2</sub>SO<sub>3</sub> under visible light irradiation on CuS/Cd<sub>0.3</sub>Zn<sub>0.7</sub>S and Ni<sub>3</sub>Cd<sub>0.3</sub>Zn<sub>0.7</sub>S<sub>1+z</sub>. *Chem Eng J* 2015;262:146–55. <https://doi.org/10.1016/j.cej.2014.09.090>.
- [73] Nichols F, Lu JE, Mercado R, Dudschus R, Bridges F, Chen S. Platinum oxide nanoparticles for electrochemical hydrogen evolution: influence of platinum valence state. *Chem - A Eur J* 2019;41:36–42. <https://doi.org/10.1002/chem.201904559>.
- [74] Wan S, Ou M, Zhong Q, Zhang S, Song F. Construction of Z-scheme photocatalytic systems using ZnIn<sub>2</sub>S<sub>4</sub>, CoOx-loaded Bi<sub>2</sub>MoO<sub>6</sub> and reduced graphene oxide electron mediator and its efficient nonsacrificial water splitting under visible light. *Chem Eng J* 2017;325:690–9. <https://doi.org/10.1016/j.cej.2017.05.047>.
- [75] Chia X, Adriano A, Lazar P, Sofer Z, Luxa J, Pumera M. Layered platinum dichalcogenides (PtS<sub>2</sub>, PtSe<sub>2</sub>, and PtTe<sub>2</sub>) electrocatalysis: monotonic dependence on the chalcogen size. *Adv Funct Mater* 2016;26:4306–18. <https://doi.org/10.1002/adfm.201505402>.
- [76] Iwashina K, Iwase A, Ng YH, Amal R, Kudo A. Z-schematic water splitting into H<sub>2</sub> and O<sub>2</sub> using metal sulfide as a hydrogen-evolving photocatalyst and reduced graphene oxide as a solid-state electron mediator. *J Am Chem Soc* 2015;137:604–7. <https://doi.org/10.1021/ja511615s>.
- [77] Qu A, Xie H, Xu X, Zhang Y, Wen S, Cui Y. High quantum yield graphene quantum dots decorated TiO<sub>2</sub> nanotubes for enhancing photocatalytic activity. *Appl Surf Sci* 2016;375:230–41. <https://doi.org/10.1016/j.apsusc.2016.03.077>.
- [78] Wang D, Guo L, Zhen Y, Yue L, Xue G, Fu F. AgBr quantum dots decorated mesoporous Bi<sub>2</sub>WO<sub>6</sub> architectures with enhanced photocatalytic activities for methylene blue. *J Mater Chem A* 2014;2:11716–27. <https://doi.org/10.1039/c4ta01444h>.

## **Supplementary information for P1**

---

## SUPPORTING INFORMATION

### **Remarkable visible-light induced hydrogen generation with ZnIn<sub>2</sub>S<sub>4</sub> microspheres/CuInS<sub>2</sub> quantum dots photocatalytic system**

**Onur Cavdar<sup>a)</sup>, Anna Malankowska<sup>a)</sup>, Daniel Amgar<sup>b)</sup>, Paweł Mazierski<sup>a)</sup>, Justyna Łuczak<sup>c)</sup>, Wojciech Lisowski<sup>d)</sup> and Adriana Zaleska-Medynska<sup>a)</sup>**

<sup>a)</sup> Department of Environmental Technology, Faculty of Chemistry, University of Gdansk, Wita Stwosza str. 63, Gdansk 80-308, Poland

<sup>b)</sup> Department of Physics of Complex Systems, Faculty of Physics, Weizmann Institute of Science, Rehovot 761000, Israel

<sup>c)</sup> Department of Process Engineering and Chemical Technology, Faculty of Chemistry, Gdansk University of Technology, Gdansk 80-233, Poland

<sup>d)</sup> Institute of Physical Chemistry, Polish Academy of Sciences, Kasprzaka str. 44/52, Warsaw 01-224, Poland

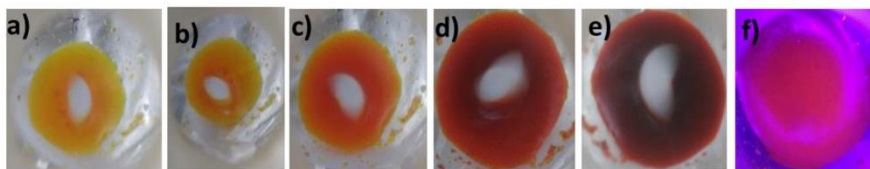


**Fig. S1** Step-by-step color change during CIS synthesis using heating up method at **a)** 60 °C **b)** 90-100 °C **c)** 120 °C **d)** 160 °C **e)** 190 °C and **f)** irradiation of just synthesized CIS by UV light

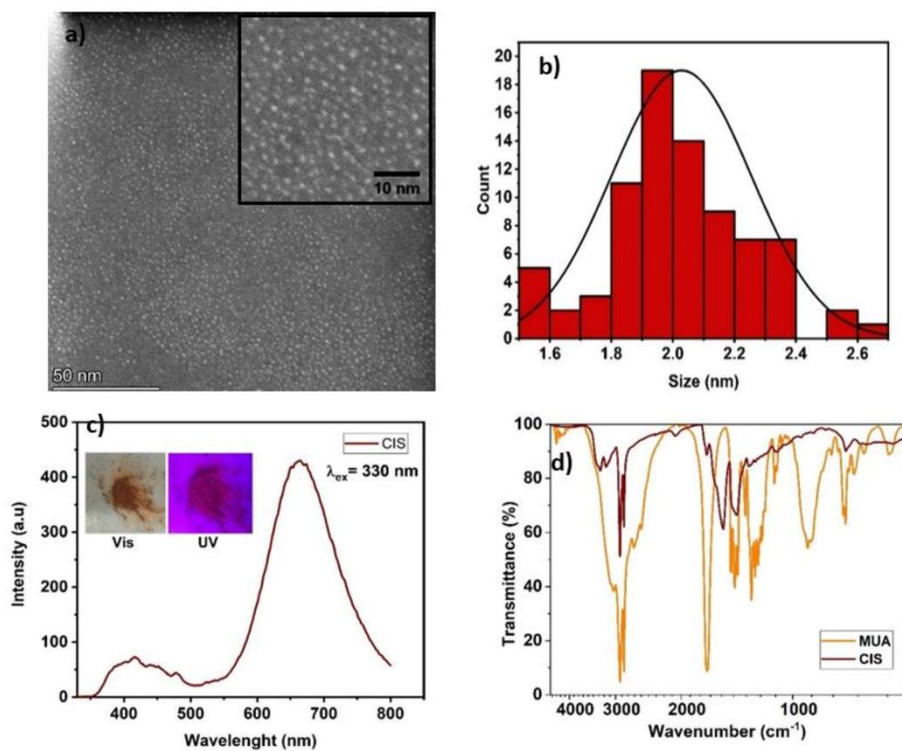


**Fig. S2 a)** HAADF-TEM image of CIS **b)** particles size distribution **c)** PL spectra of CIS and **d)** FTIR spectra of CIS and MUA

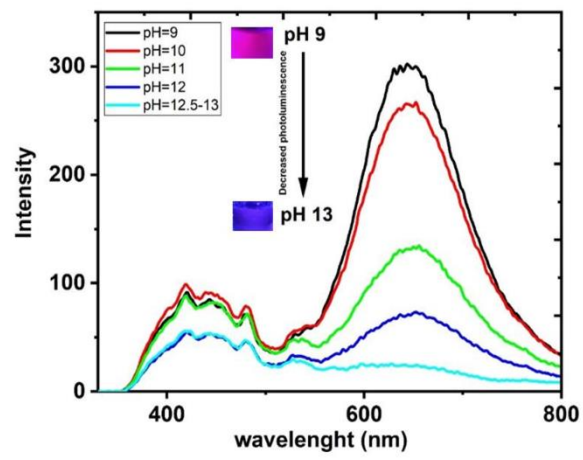


**Fig. S3** Photoluminescence of MUA capped CIS QDs under different alkalinity levels



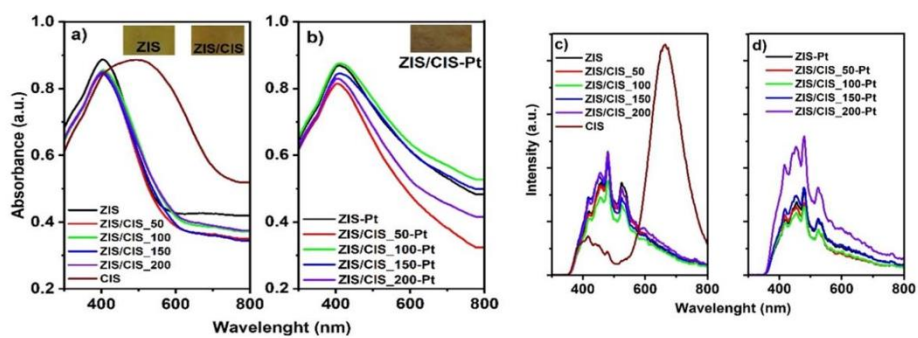


**Fig. S4** UV-vis absorption spectra of ZIS/CIS, ZIS, CIS Pt **a)** before, **b)** after Pt photodeposition and PL spectra of ZIS/CIS, ZIS, CIS **c)** before and **d)** after Pt photodeposition. Inset images: color change from pale yellow to dark yellow in a) ZIS, ZIS/CIS and b) ZIS/CIS-Pt, respectively

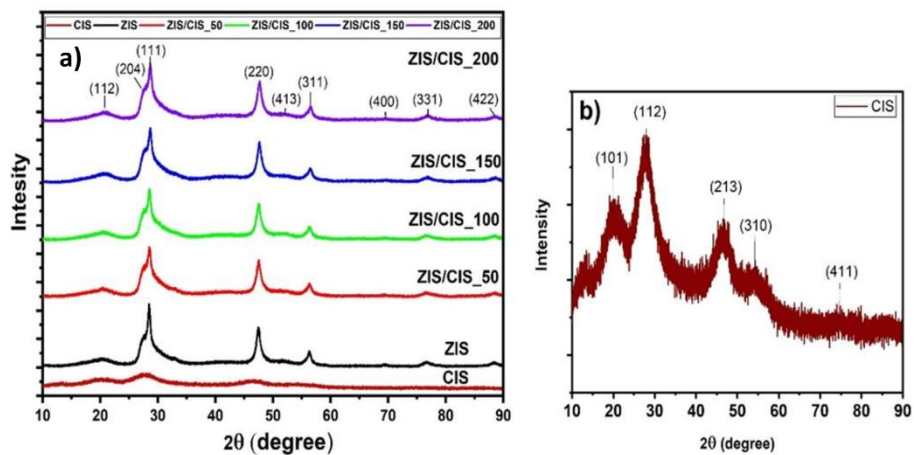


Fig. S5 a) Comparison of XRD patterns of ZIS, ZIS/CIS and b) the detailed XRD spectra of CIS

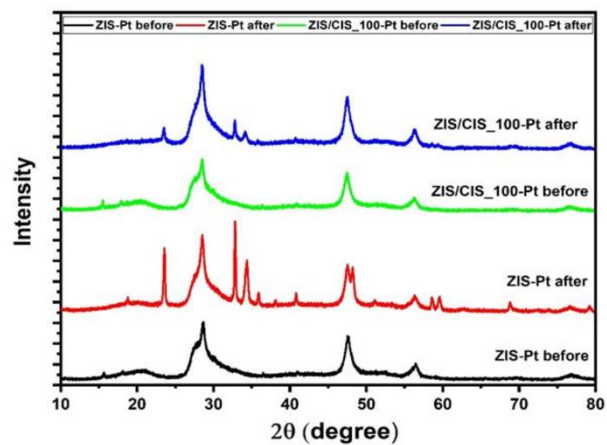
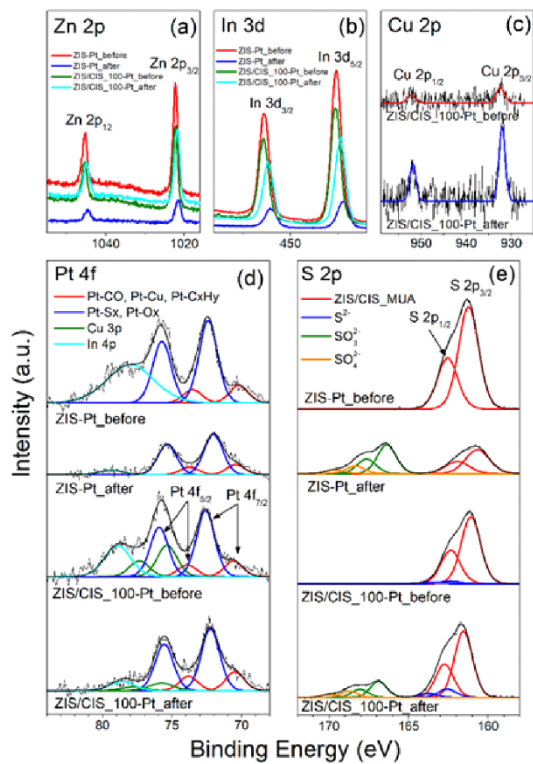


Fig. S6 XRD spectra of ZIS-Pt and ZIS/CIS\_100-Pt before and after 4 runs of photostability experiment



**Fig. S7** XPS spectra of **a)** Zn 2p, **b)** In 3d, **c)** Cu 2p, **d)** Pt 4f, and **e)** S 2p for ZIS-Pt and ZIS/CIS\_100-Pt before and after 4 runs of photostability experiment

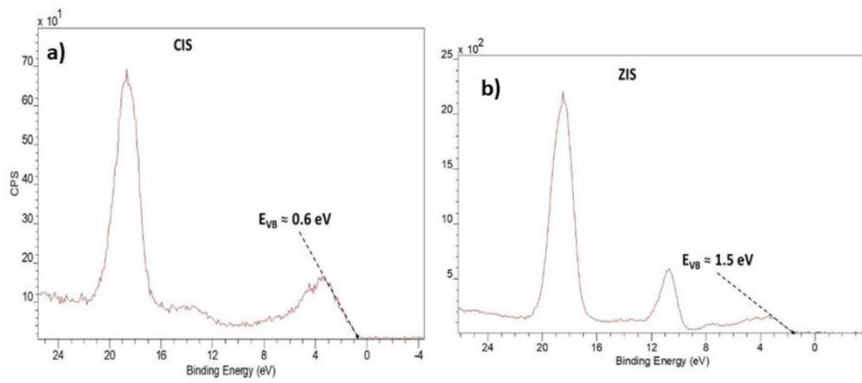


Fig. S8 XPS valence band spectra of a) CIS and b) ZIS and approximated valence band values

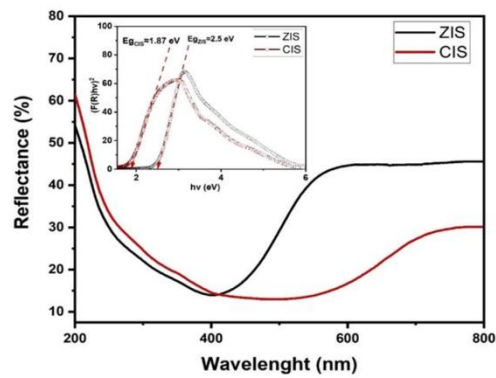
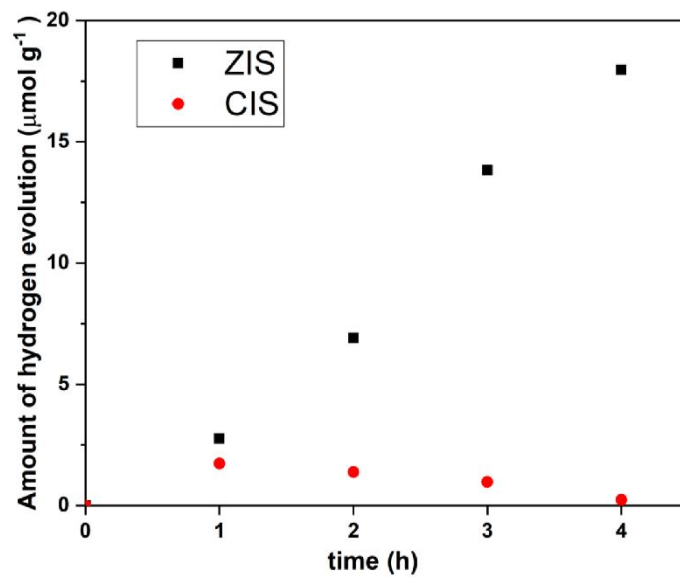


Fig. S9 Reflectance spectra of ZIS (black) and CIS (red). Inset: plots of  $(F(R)hv)^2$



**Fig. S10** Amount of hydrogen evolution under visible light irradiation ( $\lambda > 420$  nm) in the presence of pure ZIS and CIS samples

**Table S.1** Elemental contents in the surface layer of bare ZnIn<sub>2</sub>S<sub>4</sub> (ZIS), CuInS<sub>2</sub> (CIS) with 11-Mercaptoundecanoic acid (MUA) ligand and ZIS QDs decorated by CIS. Below the corresponding data of ZIS-Pt and ZIS/CIS-Pt samples before and after 4 runs of photostability

Sample label	Elements content (at.%)								S/In	Cu/Zn
	Zn	Cu	In	Pt	S	C	O	Na		
CIS_MUA	0	1.87	3.24	-	8.09	75.81	10.99	0	2.50	-
ZIS	6.11	0	14.65	-	32.57	45.79	0.88	0	2.22	-
ZIS/CIS_50	6.85	0.09	16.92	-	35.24	39.79	1.11	0	2.08	0.013
ZIS/CIS_100	5.58	0.13	17.47	-	33.82	41.29	1.71	0	1.94	0.023
ZIS/CIS_150	5.88	0.16	15.62	-	31.27	45.52	1.55	0	2.00	0.027
ZIS/CIS_200	6.43	0.17	16.37	-	33.99	41.91	1.13	0	2.08	0.027
ZIS/CIS_100-Pt_before	8.05	0.24	16.98	0.37	38.95	34.72	0.69	0	2.29	0.030
ZIS/CIS_100-Pt_after	4.75	0.24	8.49	0.24	28.25	17.34	18.78	21.91	3.33	0.050
ZIS-Pt_before	7.53	0	16.27	0.35	36.11	38.72	1.03	0	2.22	-
ZIS-Pt_after	1.55	0	2.84	0.11	18.84	20.05	27.05	29.56	6.63	-

**Table S.2** Chemical Character of Zn, In, Cu, and S atoms detected in the surface layer of ZnIn<sub>2</sub>S<sub>4</sub> (ZIS), ZIS/CIS and CIS with MUA linker samples

Sample label	Zn 2p <sub>3/2</sub>	In 3d <sub>5/2</sub>	Cu 2p <sub>3/2</sub>		S 2p <sub>3/2</sub>	
	Zn <sup>2+</sup> (%)	In <sup>3+</sup> (%)	Cu <sup>2+</sup> (%)	Cu <sup>+</sup> (%)	S <sup>2-</sup> (ZIS/CIS) (%)	S <sup>2-</sup> (sulfide) (%)
	1022.1±0.1 eV	445.1±0.1 eV	932.7 eV	932.3±0.1 eV	161.9±0.1 eV	163.0±0.1 eV
CIS_MUA	-	100	100	0	66.9	33.1
ZIS	100	100	-	-	90.1	9.9
ZIS/CIS_50	100	100	0	100	95.0	5.0
ZIS/CIS_100	100	100	0	100	96.6	3.4
ZIS/CIS_150	100	100	0	100	92.3	7.7
ZIS/CIS_200	100	100	0	100	95.0	5.0

**Table S.3** Chemical character of Pt and S atoms detected in the surface layer of ZIS-Pt and ZIS/CIS\_100-Pt samples before and after 4 runs of photocatalytic experiment

Sample label	Pt 4f <sub>7/2</sub>		S 2p <sub>3/2</sub>			
	Pt-CO, Pt-Cu Pt-C <sub>x</sub> H <sub>y</sub> (%)	Pt-S <sub>x</sub> , Pt-O <sub>x</sub> (%)	S <sup>2-</sup> (ZIS/CIS) (%)	S <sup>2-</sup> (sulfide) (%)	SO <sub>3</sub> <sup>2-</sup> sulfite (%)	SO <sub>4</sub> <sup>2-</sup> sulfate (%)
	70.3-70.6 eV	72.1-72.6 eV	161.6- 162.0 eV	162.6- 163.1 eV	166.8 eV	168.7 eV
ZIS/CIS_100-Pt_before	19.34	80.66	92.84	7.16	0	0
ZIS/CIS_100-Pt_after	23.65	76.35	69.53	8.69	15.58	6.19
ZIS-Pt_before	17.69	82.31	100	0	0	0
ZIS-Pt_after	20.21	79.79	45.69	0	43.15	11.16



**Table S.4** Amount of Pt and Cu elements detected in ZIS/CIS-Pt samples by ICP-OES

<b>Sample label</b>	<b>Pt (wt%)</b>	<b>Cu (wt%)</b>
ZIS/CIS_50-Pt	1.23	0.17
ZIS/CIS_100-Pt	1.25	0.22
ZIS/CIS_150-Pt	1.31	0.43
ZIS/CIS_200-Pt	1.25	0.65

**Table S.5** Comparison of the ZnIn<sub>2</sub>S<sub>4</sub> based photocatalysts in the literature

Photocatalysts	Co-catalyst	Light source	H <sub>2</sub> evolution rate mmol g <sup>-1</sup> h <sup>-1</sup>	Quantum efficiency %	Sacrificial agent
2D/2D CuInS <sub>2</sub> /ZnIn <sub>2</sub> S <sub>4</sub> <sup>16</sup>	2 wt% Pt	300 W Xe lamp, λ > 420 nm	3.43	12.4@420 nm	0.35 M Na <sub>2</sub> S and 0.25 M Na <sub>2</sub> SO <sub>3</sub>
Cu-doped ZnIn <sub>2</sub> S <sub>4</sub> <sup>1</sup>	1 wt% Pt	300 W Xe lamp, λ > 430 nm	0.75	14.2@420 nm	0.35 M Na <sub>2</sub> S and 0.25 M Na <sub>2</sub> SO <sub>3</sub>
WO <sub>3</sub> @ ZnIn <sub>2</sub> S <sub>4</sub> <sup>18</sup>	Co-catalysts free	300 W Xe lamp, λ > 420 nm	3.9	n/a	15v% triethanolamine
CdS/ZnIn <sub>2</sub> S <sub>4</sub> /graphene <sup>20</sup>	0.4 wt% Pt	300 W Xe lamp, λ > 420 nm	2.7	56@420 nm	0.1 M Na <sub>2</sub> S and 0.04 M Na <sub>2</sub> SO <sub>3</sub>
2D/2D g-C <sub>3</sub> N <sub>4</sub> @ZnIn <sub>2</sub> S <sub>4</sub> <sup>21</sup>	Co-catalysts free	300 W Xe lamp, λ > 420 nm	2.78	7.05@420 nm	20 v% triethanolamine
CuInS <sub>2</sub> QDs/ZnIn <sub>2</sub> S <sub>4</sub> <sup>*</sup>	0.75wt% Pt	1000 W Xe lamp, λ > 420 nm	1.04	30.6@420 nm	0.35 M Na <sub>2</sub> S and 0.25 M Na <sub>2</sub> SO <sub>3</sub>

\* This work



---

**P2. Capping ligand initiated CuInS<sub>2</sub> quantum dots decoration on, ZnIn<sub>2</sub>S<sub>4</sub> microspheres surface under different alkalinity levels resulting in different hydrogen evolution performance**

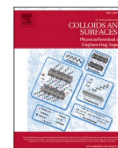
---



ELSEVIER

Contents lists available at ScienceDirect

# Colloids and Surfaces A: Physicochemical and Engineering Aspects

journal homepage: [www.elsevier.com/locate/colsurfa](http://www.elsevier.com/locate/colsurfa)

## Capping ligand initiated CuInS<sub>2</sub> quantum dots decoration on, ZnIn<sub>2</sub>S<sub>4</sub> microspheres surface under different alkalinity levels resulting in different hydrogen evolution performance

Onur Cavdar<sup>a</sup>, Anna Malankowska<sup>a,\*</sup>, Justyna Łuczak<sup>b</sup>, Andrzej Żak<sup>c</sup>, Wojciech Lisowski<sup>d</sup>, Tomasz Klimczuk<sup>e,f</sup>, Adriana Zaleska-Medynska<sup>a</sup>

<sup>a</sup> Department of Environmental Technology, Faculty of Chemistry, University of Gdansk, Gdansk, Poland

<sup>b</sup> Department of Process Engineering and Chemical Technology, Faculty of Chemistry, Gdansk University of Technology, Gdansk, Poland

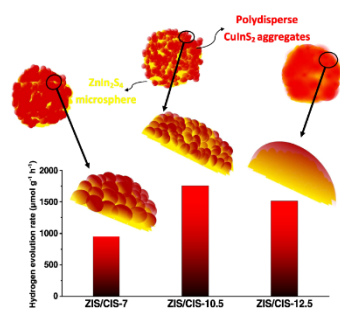
<sup>c</sup> Electron Microscopy Laboratory, Faculty of Mechanical Engineering, Wrocław University of Science and Technology, Gdansk, Poland

<sup>d</sup> Institute of Physical Chemistry, Polish Academy of Science, Warsaw, Poland

<sup>e</sup> Faculty of Applied Physics and Mathematics, Gdansk University of Technology, Narutowicza, Gdansk, Poland

<sup>f</sup> Advanced Materials Center, Gdansk University of Technology, Narutowicza, Gdansk, Poland

### GRAPHICAL ABSTRACT



### ARTICLE INFO

#### Keywords:

CuInS<sub>2</sub>  
ZnIn<sub>2</sub>S<sub>4</sub>  
Quantum dots  
Visible light photoactivity  
Hydrogen  
Aggregates

### ABSTRACT

Surface distribution of quantum dots (QDs) at the semiconductor matrix caused by synthesis condition (e.g. pH of solution during coupling) could lead to different photocatalytic activity. Thus, achieving an optimal covering of semiconductor matrix by QDs has been challenging. Herein, the influence of the alkalinity level of aqueous decoration medium for the coupling of mercaptoundecanoic acid (MUA) capped CuInS<sub>2</sub> quantum dots (CIS) and ZnIn<sub>2</sub>S<sub>4</sub> microspheres (ZIS) on photocatalytic hydrogen evolution (PHE) performance was investigated. Aqueous decoration medium with different alkalinity levels for the formation of ZIS/CIS photocatalytic system resulted in significantly different PHE performances in the presence of (0.5 wt%) Pt co-catalyst deposition without any change in crystal structure of ZIS matrix up to pH 12.5. The photocatalytic system obtained at pH 10.5 possessed the highest performance followed by the decrease at pH 11.5 and again the remarkable increase was detected at

\* Corresponding author.

<https://doi.org/10.1016/j.colsurfa.2022.129760>

Received 9 May 2022; Received in revised form 7 July 2022; Accepted 18 July 2022

Available online 20 July 2022

0927-7757/© 2022 The Authors. Published by Elsevier B.V. This is an open access article under the CC BY-NC-ND license (<http://creativecommons.org/licenses/by-nc-nd/4.0/>).

pH 12.5 that was the pH level for uniform dispersion of CIS in aqueous medium. This work remarks the importance of the nanoparticle's aggregates on PHE performance over non-toxic ZnIn<sub>2</sub>S<sub>4</sub>/CuInS<sub>2</sub> photocatalytic system.

## 1. Introduction

H<sub>2</sub> fuel has a great potential to reduce reliance on fossil fuels [1]. As one of the solar conversion technology, photocatalytic water splitting has been drawing intensive attention to produce green H<sub>2</sub> [2]. For that purpose, metal sulfide based photocatalysts have been widely investigated due to relatively high conduction band edge that is thermodynamically suitable for H<sub>2</sub>O reduction in the presence of sacrificial agents [3].

Among the various type of photocatalytic metal sulfide semiconductors [4–8], n-type ZnIn<sub>2</sub>S<sub>4</sub> semiconductor based photocatalytic systems became prominent because ZnIn<sub>2</sub>S<sub>4</sub> is easy to prepare, and has adjustable bandgap through doping and wide absorption range [9]. Several type of ZnIn<sub>2</sub>S<sub>4</sub> based photocatalytic systems have been studied to overcome its low photocatalytic activity due to the rapid recombination of photogenerated charge carriers [10–16]. One of the other alternative method to induce the performance of ZnIn<sub>2</sub>S<sub>4</sub> is to incorporate it with other metal sulfide-based nanomaterials such Ag<sub>2</sub>S [17], Cu<sub>2</sub>S [18], CdS [19], MoS<sub>2</sub> [20], WS<sub>2</sub> [21]. Besides, ZnIn<sub>2</sub>S<sub>4</sub>/CuInS<sub>2</sub> based photocatalytic system also have been attracted attention [22–24] owing to a large absorption coefficient of a typical p-type semiconductor CuInS<sub>2</sub> [25]. In our previous report, we obtained ZnIn<sub>2</sub>S<sub>4</sub> microspheres (ZIS) decorated with pre-prepared CuInS<sub>2</sub> quantum dots (CIS QDs) capped with mercaptoundecanoic acid (MUA) by simply introducing CIS into ZIS precursors for hydrothermal treatment medium [26]. This approach resulted in significant increase in photocatalytic hydrogen evolution activity of pristine ZIS in the presence of Pt deposition. However, the formation of aggregates of CIS during the synthesis that resulted in an uneven distribution of CIS on ZIS surface. This has led to the question whether the different formation of those aggregates can affect the photocatalytic activity of ZIS/CIS photocatalytic system or not.

The pH dependent aggregation of mercaptocarboxylic acid capping ligand, such as thioglycolic acid and mercaptopropionic acid, capped quantum dots and its effect on their optoelectronic properties have been reported generally with the purpose of bioimaging applications [27–29]. Beyond the aggregation effect, Xu et al. reported that there are several reasons leading different optoelectronic properties of mercaptocarboxylic acid ligand capped quantum dots including thiol group effect, counter ions effect, and terminal group effect in which their contributions differ at different pH values [30]. However, to best of our knowledge, there are very limited reports on the effect of aggregation phenomenon on photocatalytic hydrogen evolution performance by controlling the decoration medium of mercaptocarboxylic acid ligand capped quantum dots on a surface of larger matrix. Yu et al. have studied the assembly of MPA-regulated CdSe QDs on commercial photocatalysis TiO<sub>2</sub> (P25) by adjusting the pH level of the interaction medium to alkaline level in order to avoid the aggregates of quantum dots in acidic conditions to be furtherly coupled with in-situ formed Ni(OH)<sub>2</sub> deposition [31]. On the other hand, PHE performances depending on the aggregation of single or double nanoparticle photocatalytic systems were investigated by several groups. For instance, Chang et al. reported that aggregates of CdS QDs were more favorable than that of CdS with aggregation preventing mercaptopropionic acid capping due to efficient charge separation with reduced charge carrier recombination [32] which was corroborative Park's work [33]. Moreover, Gao et al. suggested that the interparticle hole transfer which was accelerated by the formation of CdSe QDs-ZnSe QDs aggregation was the crucial factor for boosting the photocatalytic hydrogen evolution performance of the system [34]. Additionally, Sawaguchi-Sato et al. investigated the

aggregation induced photocatalytic hydrogen evolution from Pt colloidal catalysts CdTe quantum dots photocatalytic system by means of the type of mercaptocarboxylic acid capping ligand on quantum dots surface that changed the formation of aggregation [35]. Considering above-referred works, aggregation can have an important role on photocatalytic hydrogen evolution.

In this study, we investigated the effect of the aggregation formation of mercaptoundecanoic acid capped (MUA) CIS by adjusting the alkalinity of aqueous decoration medium for the formation of ZIS/CIS photocatalytic system. Despite all obtained photocatalytic systems contained the same amount of CIS, the treatment of sample under different alkalinity levels resulted in significantly different photocatalytic hydrogen evolution performances in the presence of same amount of Pt cocatalyst under visible light irradiation. The possible reasons behind that were discussed in terms of information on the morphology, optoelectronic and surface chemistry properties.

## 2. Experimental

### 2.1. Materials

Cetyltrimethylammonium bromide (CTAB, 95 %) (Aldrich), indium (III) nitrate hydrate (99.99 %) (Alfa Aesar), thioacetamide (J.T. Baker, Avantor performance materials), copper (I) iodide (99.99 %) (Sigma-Aldrich), indium (III) acetate (99.99 %) (Acros Organics), thiourea (99.99 %) (CHEMPUR), 11-mercaptoundecanoic acid (95 %) (Sigma-Aldrich), zinc sulfate heptahydrate (99.99 %) (CHEMPUR), potassium tetrachloroplatinate (II), (99.9 %) (Alfa Aesar), methyl viologen dichloride hydrate (98 %) (Sigma-Aldrich). All chemicals were used without any further purification.

### 2.2. Synthesis of ZIS/CIS photocatalytic system

ZIS and CIS QDs were synthesized as mentioned in a previous report [26]. To obtain ZIS/CIS photocatalytic system, the ratio of CIS was fixed to 5 wt%. The pH level of aqueous medium (deionized water) for the decoration was adjusted to 7, 9.5, 10.5, 11.5, 12.5 and 12.9 by adding 0.1 M KOH or H<sub>2</sub>SO<sub>4</sub> aqueous solution and the concentration of CIS quantum dots were always kept 2 mg/ml. After adding CIS to the aqueous decoration medium with desired pH level, the mixture was sonicated for 10 min and vigorously stirred for 30 min. Finally, ZIS powder was added, and all mixture was stirred for 24 h. The products were washed with ethanol and water and separated using centrifuge (6000 RPM) and dried at 60 °C. The products were abbreviated according to the pH level of aqueous decoration medium as ZIS/CIS-7, ZIS/CIS-9.5, ZIS/CIS-10.5, ZIS/CIS-11.5, ZIS/CIS-12.5 and ZIS/CIS-12.9. Samples during and after Pt in-situ deposition assisted PHE tests were abbreviated as ZIS/CIS-7/Pt, ZIS/CIS-9.5/Pt, ZIS/CIS-10.5/Pt, ZIS/CIS-11.5/Pt, ZIS/CIS-12.5/Pt and ZIS/CIS-12.9/Pt.

### 2.3. Characterization

To prove all the samples, have the same amount Pt or CIS, Pt and Cu content were analyzed by inductively coupled plasma optical emission spectroscopy (ICP-OES) using Agilent 5100 spectrometer, according to PN-EN ISO 11885:2009 standard. X-ray diffraction (XRD) technique was used to determine the crystalline structure of the samples and detect whether any changes has occurred in ZIS matrix during the preparation of ZIS/CIS samples. Powder X-ray diffraction experiments were

conducted at 20 °C on powdered samples with a Bruker D8 Focus diffractometer with Cu K $\alpha$  ( $\lambda = 1.54 \text{ \AA}$ ) radiation and a LynxEye XE-T detector. Data were collected from 5° to 70° 2 $\theta$  over a scan time of 30 min. LeBail refinement of the pXRD pattern was performed to determine the crystal structure type of the tested samples, using HighScore Plus ver. 3.0e software. The chemical composition of samples surface (ZIS/CIS-7, ZIS/CIS-10.5 and ZIS-CIS-12.5) areas was analyzed by X-ray photoelectron spectroscopy (XPS) using a PHI 5000 VersaProbeTM spectrometer (ULVAC-PHI, Chigasaki, Japan) with monochromatic Al K $\alpha$  irradiation ( $h\nu = 1486.6 \text{ eV}$ ) to highlight the reduction of Pt precursor over the samples during PHE leading to formation of Pt species. The high-resolution (HR) XPS spectra were recorded with the hemispherical analyzer at the pass energy of 23.5 eV and the energy step size of 0.1 eV. The morphology of samples (ZIS/CIS-7, ZIS/CIS-10.5 and ZIS-CIS-12.5) was observed using scanning electron microscope (SEM, JEOL JSM-7610F) and transmission electron microscope (TEM, Hitachi H-800 microscope, Hitachi High-Technologies) operating at 150 kV. The UV-vis spectra of samples were recorded using UV-vis spectrophotometer (Evolution 220, Thermo Scientific). The photoluminescence spectra (PL) were recorded using a PerkinElmer Luminescence Spectrometer LS-50B equipped with Xenon discharge lamp as an excitation source. The samples were excited with 330 nm at room temperature and the emission was scanned between 300 and 800 nm. Fourier-transform infrared spectroscopy (FTIR) (Bruker, IFS66) was used to identify the surface characteristics of CIS QDs and ZIS/CIS photocatalytic system in the scan range of 500–5000  $\text{cm}^{-1}$  in the diffuse reflectance mode with a resolution of 0.12  $\text{cm}^{-1}$  at room temperature and KBr was used as a reference material. Malvern Zetasizer Nano ZS or Mastersizer 3000 were used to measure CIS aggregates size under different alkalinity levels by dynamic light scattering (DLS) technique, the zeta potential of ZIS samples in the aqueous decoration medium and ZIS/CIS samples in photocatalytic hydrogen evolution reaction solution.

#### 2.4. Photocatalytic hydrogen evolution experiments

50 mg photocatalyst was added into 50 ml 0.35 M Na<sub>2</sub>S/0.25 M Na<sub>2</sub>SO<sub>3</sub> aqueous solution in a beaker and the mixture was sonicated using ultrasonic bath for 5 min. The mixture was transferred to a photoreactor equipped with a quartz glass with 110 ml volume and 50 mM K<sub>2</sub>PtCl<sub>4</sub> aqueous solution was dripped to deposit 0.5 wt% Pt on ZIS/CIS photocatalytic system's surface. After sealing the reactor with a plastic septum, the mixture was purged with N<sub>2</sub> gas with 12 dm<sup>3</sup>/h flow rate for 30 min in dark. Finally, the mixture was irradiated by 1000 W Xenon lamp external light source (Quantum Design, LSH 602) equipped with a cut-off filter GG420 (Optel,  $\lambda > 420 \text{ nm}$ ). The temperature of the PHE process was always kept at 10 °C using a thermostat. The amount of hydrogen gas was monitored by adding 200  $\mu\text{l}$  of gas sample collected from the headspace of the photoreactor within every using an air-tight syringe (Hamilton) to the gas chromatograph (Thermo Scientific TRACE 1300-GC, N<sub>2</sub> carrier) No hydrogen was evolved in the absence of ZIS/CIS photocatalyst under the same condition. The amount of hydrogen was calculated using calibration curve which was based on a collected data from GC-TCD and pressure value from a digital manometer (SIKA) attached to the photoreactor following addition of different volume of hydrogen (99.99 %) using an air-tight syringe (HAMILTON). Later, the amount of hydrogen in moles was calculated using the ideal gas equation [36]. The recycling performance tests were carried out under the same experimental conditions. After each cycle, the sample was collected and washed with deionized water by a centrifuge. The fresh 0.35 M Na<sub>2</sub>S/0.25 M Na<sub>2</sub>SO<sub>3</sub> aqueous solution was added in a centrifuge tube with the sample and then the mixture was poured into the photoreactor for the next cycle test. The pH of photocatalytic hydrogen evolution solution after one cycle was around 12.

### 3. Results and discussion

To reveal the different optical characteristics of CIS aggregates under different alkalinity levels, UV-vis and PL spectrum of samples was compared (Fig. 1). To conduct those measurements, the samples were dispersed in water with the pre-adjusted alkalinity level using 0.1 M H<sub>2</sub>SO<sub>4</sub> or KOH solution and stirred vigorously following for 30 min following 10 min sonication. Particle concentration during all measurements was 0.5 mg/ml. From pH = 7 to pH = 11.5, the red-shifted absorption edge was observed that was followed by the drastic change in UV-vis spectra at pH = 12.5, and the specific absorption shoulder appeared at around 250 nm at pH = 12.5. Also, to check the spectrum only originating from MUA, MUA has been dispersed in aqueous solution with pH = 7, 10.5, and 12.5 and their absorbance spectra were recorded. The same peak at 250 nm can be observed from the absorption spectra only from MUA in pH 12.5 which has shown the spectrum with the similar trend as in MUA capped CIS (Fig. S1). However, considerable red-shifting was exhibited by MUA-capped CIS compared to that of only MUA. Likewise, the same red shifting is observed from the spectrum originating from MUA capped CIS under pH = 7 and 10.5 attributing to the coupling between the MUA and CIS [37]. Moreover, the aggregation induced emission was proven comparing the PL spectra of CIS aggregates under different alkalinity levels, as the emission intensity was the highest at pH = 7 and significantly dropped at pH = 11.5 and finally quenched at pH = 12.5 where the clear, red-colored dispersion of CIS were achieved (inset in Fig. 1b). The change in the optical properties of CIS aggregates which was mediated by alkalinity level can be explained by the degree of the aggregation considering the aggregation induced emission. To this respect, DLS was measured to show how the size of aggregates were distributed depending on the level of the alkalinity of aqueous medium. As seen from Fig. 2, all CIS aggregates displayed high polydispersity with macro-sized aggregates around 100  $\mu\text{m}$  at pH = 9.5 and 10.5. At pH = 11.5, the aggregate size decreased noticeably along with the new peak formed corresponding 1  $\mu\text{m}$  particle size. After reaching pH = 12, the size of aggregates was shifted to remarkably lower size and two significant peaks formed around 5 nm and 100 nm at pH = 12.5 and 12.9. The reason behind the macro-sized aggregation between the alkalinity level pH = 9.5–11.5 was due to the non-ionized carboxylic acid end group in MUA ligand on CIS surface [38–40]. Thus, inter-nanoparticle H-bonds through the hydrophilic groups on nanoparticle surface resulted in aggregation in a weak basic aqueous solution [38]. On the other hand, after high pH = 12, the carboxylic groups in MUA on CIS surface was deprotonated and stabilized CIS aggregates were achieved via electrostatic repulsion [41], so that the aggregation was reduced [42].

Accordingly, as the aggregate sizes of CIS under different alkalinity levels, it can be proposed that each CIS aggregates in aqueous medium under different alkalinity behaves different that led to different morphology of ZIS/CIS photocatalytic system. The SEM images (Fig. 3a–c) indicated that, at the pH = 12.5, ZIS microparticles surface were lesser overwhelmed by CIS and coating-like CIS on ZIS formed smooth surface on ZIS/CIS photocatalytic system. While, at pH 7, non-uniform shape of ZIS/CIS with rough surface formed. On the other hand, at pH 10.5 both smooth and rigid surface can be observed in ZIS/CIS photocatalytic system. Same observation can be seen also from TEM images (Fig. 3d–f). Even in ZIS/CIS-12.5 sample, the presence of CIS is distinguishable in the form of single dots on the ZIS surface (please refer to Fig. S2 for the SEM image of pristine ZIS) and around the ZIS particles (Fig. 3f). Additionally, layers in ZIS/CIS-7 (Fig. 3d) can be selected easily, while the layers in ZIS/CIS-12.5 were almost covered by CIS uniformly so that the layers were not noticeable easily.

Moreover, the obtained powder's optoelectronic characteristics also proved the differences between ZIS/CIS photocatalytic system. Fig. 4a shows, UV-vis absorption spectra of pristine ZIS and all other ZIS/CIS photocatalytic samples. As expected, all the ZIS/CIS samples showed red-shifted absorption edge as similar to the previous report on ZIS/CIS



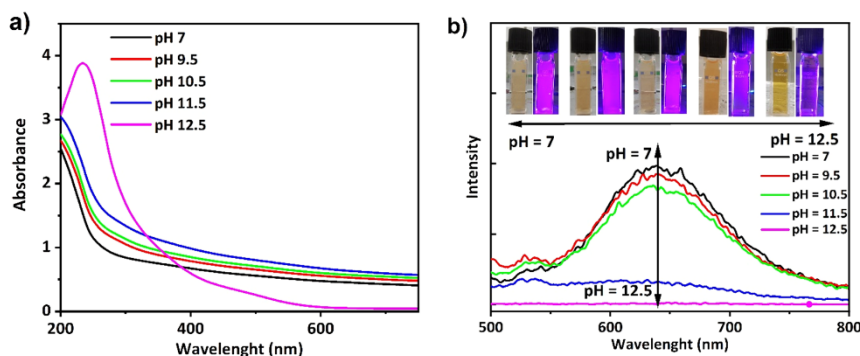


Fig. 1. a) UV-vis absorption spectrum of MUA capped CIS aggregates under different alkalinity levels (inset: The comparison of UV-vis absorption spectrum of MUA capped CIS and only MUA under pH = 7, 10.5 and 12.5. The dashed line represents UV-vis absorption spectrum of only MUA) and b) PL spectrum of CIS aggregates ( $\lambda$  excitation = 330 nm) at different alkalinity levels (inset: luminescence images of CIS aggregates under different alkalinity levels).

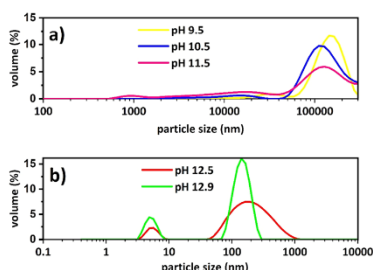


Fig. 2. CIS aggregates size distribution by DLS measurement under different alkaline levels a) pH 9.5–11.5 b) 12.5–12.9.

photocatalytic system [26]. However considerable red-shifting can be seen especially in ZIS/CIS-12.5 and ZIS/CIS-12.9 samples probably because of the uniform distribution of CIS on ZIS surface initiating the higher light harvesting due to the increase in surface-to-volume ratio. This is even observable from the significant color difference in obtained ZIS/CIS photocatalyst powder (Fig. S3). On the other hand, all samples' PL spectrum (Fig. 4b) have two characteristic peaks around 400–450 nm and 500–550 nm band which can be attributed to defects (sulfur and zinc vacancy) and band-to-band transition, respectively [43–45]. It is worth to mention that in all series of ZIS/CIS samples CIS decreased the electron-hole recombination efficiency in all ZIS/CIS samples as the lower PL intensity indicates lower recombination of photogenerated charge carriers [46].

Powder x-ray diffraction patterns (Fig. 5) for ZIS/CIS-7, ZIS/CIS-10.5, ZIS/CIS-12.5 and ZIS/CIS-12.9 shows the characteristic broad reflections were indexed by  $\text{ZnIn}_2\text{S}_4$  that forms in a hexagonal crystal structure P63mc with reported lattice constants  $a = 3.871 \text{ \AA}$  and  $c = 26.121 \text{ \AA}$ . Expected positions for  $\text{ZnIn}_2\text{S}_4$  phase are marked by the vertical bars. A XRD pattern for pristine  $\text{CuInS}_2$  with tetragonal crystal structure in roquesite phase is presented in supplementary information (Fig. S4). The strongest broad reflections appear at  $2\theta = 27.7, 46.3^\circ$  and  $19.9^\circ$  and except the second one ( $2\theta = 46.3^\circ$ ) they overlap with the ZIS reflections and hence cannot be observed. The only impurity phase –  $\text{In}(\text{OH})_3$  marked by stars - appears for ZIS/CIS-12.9 sample.

In addition to this, more insight regarding samples' surface chemistry was also checked with FTIR (Fig. S5). All samples exhibited the same pattern. C-H stretch vibration peaks located at  $2844$  and  $2921 \text{ cm}^{-1}$

indicates the alkyl chain originated from the presence of CTAB molecule over ZIS/CIS and ZIS samples [47,48]. The peaks around  $3415, 1620$  and  $1385 \text{ cm}^{-1}$  corresponded to the hydroxyl and surface-absorbed water molecules, while the absorption peak related with the absorbed  $\text{CO}_2$  molecules around  $1100 \text{ cm}^{-1}$  only can be seen in ZIS [49]. Interestingly In-S stretching vibration originated peak at around  $640 \text{ cm}^{-1}$  [49,50] can be seen all samples except ZIS/CIS-7. This may be related with rough surface topology due to the overwhelmingly distributed CIS over ZIS surface as ZIS/CIS-10 and ZIS/CIS-12.5 with relatively more uniform CIS obtained that peak intensity is almost as high as in only ZIS especially in the case for ZIS/CIS-12.5.

PHE rates and the amount of hydrogen evolved from ZIS/CIS samples under visible light irradiation for 3 h in the presence of  $0.35 \text{ M}/0.25 \text{ M}$   $\text{Na}_2\text{S}/\text{Na}_2\text{SO}_3$  as the sacrificial reagent can be seen in Fig. 6a and b, respectively. In Fig. 6a, black bars represent the PHE performances without in-situ Pt deposition, while red bars demonstrate with Pt. In case of the comparison of the samples' PHE rate without Pt, the highest rate was exhibited by ZIS/CIS-12.9 with  $105.31 \mu\text{mol g}^{-1} \text{ h}^{-1}$ . That result is reasonable as ZIS/CIS-12.9 was the only sample among all ZIS/CIS in which  $\text{In}(\text{OH})_3$  was formed during the preparation due to the high alkaline decoration medium (Fig. 5). Therefore, the presence of  $\text{In}(\text{OH})_3$  induced PHE performance of ZIS/CIS-12.9 remarkably as it has acted as a cocatalyst [11,51]. ZIS/CIS-7 and ZIS/CIS-9.5 showed very close PHE rate around  $21.41$  and  $13.10 \mu\text{mol g}^{-1} \text{ h}^{-1}$ , respectively. Around two folder PHE rate than ZIS/CIS-7 were achieved by ZIS/CIS-10.5 ( $55.65 \mu\text{mol g}^{-1} \text{ h}^{-1}$ ) and ZIS/CIS-11.5 ( $59.25 \mu\text{mol g}^{-1} \text{ h}^{-1}$ ). Interestingly, a notable decline was displayed in PHE rate from ZIS/CIS-12.5 ( $21.39 \mu\text{mol g}^{-1} \text{ h}^{-1}$ ). On the other hand, as the main scope of this study, the remarkable effect of the in-situ Pt deposition on PHE is readily observable in all ZIS/CIS/Pt samples. The lowest PHE rate was shown by ZIS/CIS-7/Pt ( $1180.46 \mu\text{mol g}^{-1} \text{ h}^{-1}$ ) and then ZIS/CIS-9.5/Pt ( $1300.46 \mu\text{mol g}^{-1} \text{ h}^{-1}$ ) whereas ZIS/CIS-10.5/Pt generated the highest amount of hydrogen with the rate of  $1753.79 \mu\text{mol g}^{-1} \text{ h}^{-1}$  which implies that the pH = 10.5 is the optimum pH level for the ZIS/CIS synthesis aqueous decoration medium that leading most efficient photocatalytic system for PHE. However, after reaching the optimum pH level for the decoration medium, PHE rate of the sample prepared in pH = 11.5 decreased to  $1450.76 \mu\text{mol g}^{-1} \text{ h}^{-1}$ . The significant rise can be seen from ZIS/CIS-12.5/Pt with the PHE rate of  $1670.16 \mu\text{mol g}^{-1} \text{ h}^{-1}$ . It seems that the optimum pH = 10.5 of the decoration of ZIS microspheres with CIS was the best for the hydrogen evolution from ZIS/CIS photocatalytic system in the presence of in-situ Pt deposition. Besides, the treatment of pristine ZIS or CIS sample in pH = 10.5 had no effect on PHE performance as almost the same amount of hydrogen was evolved from ZIS/Pt



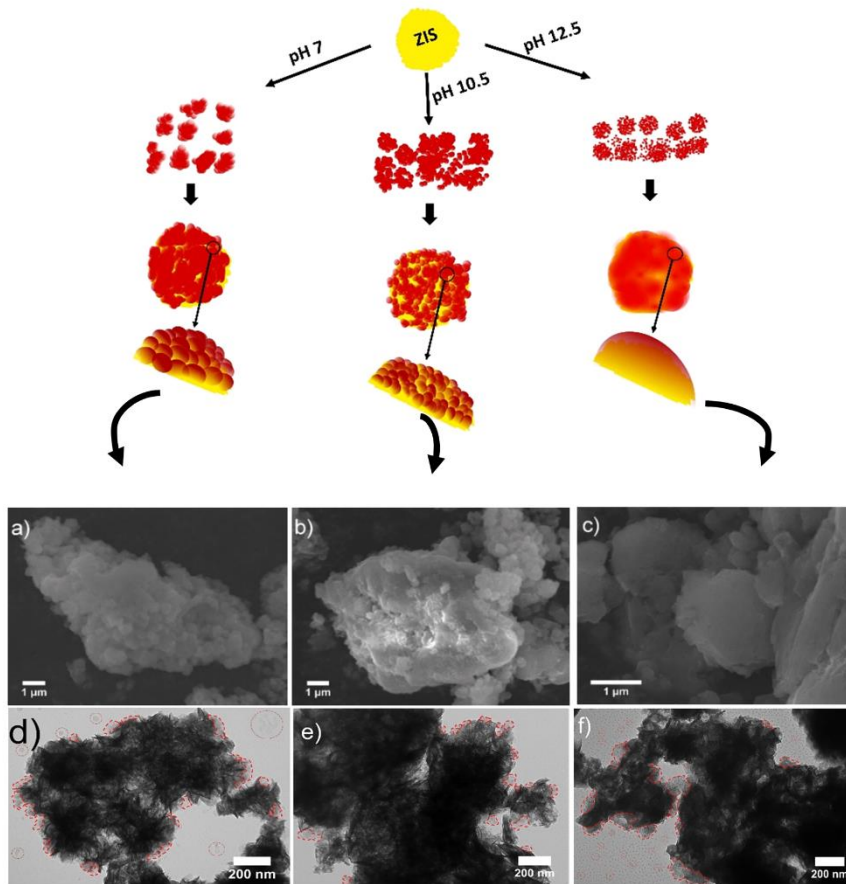


Fig. 3. Schematic description of controlled aggregation induced CIS (red spheres) decoration of ZIS microsphere (yellow sphere) based on SEM and TEM images of a, d) ZIS/CIS-7, b, e) ZIS/CIS-10.5 and c, f) ZIS/CIS-12.5. Red dashed circles in TEM images indicates CIS aggregates on and around the ZIS surface.

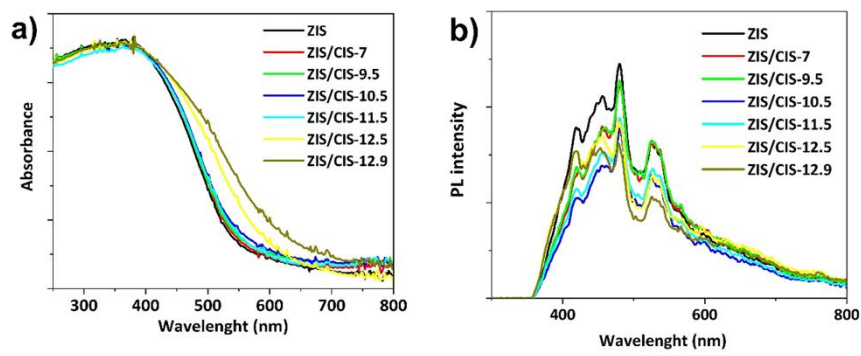


Fig. 4. a) UV-vis and b) PL spectrum of ZIS/CIS and pristine ZIS samples.

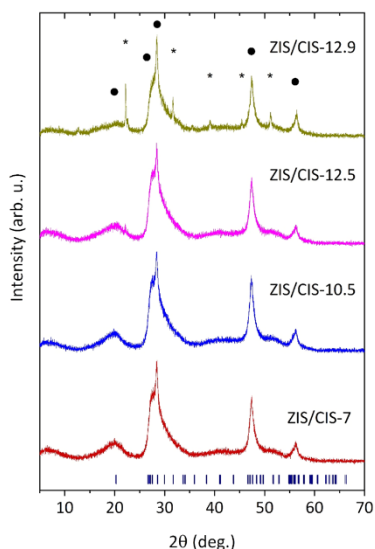


Fig. 5. XRD patterns of ZIS/CIS-7, 10.5, 12.5 and 12.9 samples. Dots and stars indicates the characteristic peaks in diffraction patterns originated from ZIS and  $\text{In}(\text{OH})_3$ , respectively.

with and without the treatment (Fig. S6). It is also worth to mention that ZIS/CIS-12.9/Pt exhibited PHE rate of  $1512.58 \mu\text{mol g}^{-1} \text{h}^{-1}$  but the competition between the electron transfer from ZIS/CIS to two cocatalyst Pt species and  $\text{In}(\text{OH})_3$  could inhibit the performance of ZIS/CIS-12.9/Pt in comparison to ZIS/CIS-12.5/Pt [52]. Fig. 6c. shows the recycling performance experiments of three selected samples: ZIS/CIS-7/Pt, ZIS/CIS-10.5/Pt and ZIS/CIS-12.5/Pt (The reason of that selection will be discussed further). The samples were not stable after 3 cycles as a drop about 60 % in PHE for ZIS/CIS-10.5/Pt and ZIS/CIS-12.5/Pt was observed while around 30 % for ZIS/CIS-7. Particularly, around 50 % rapid decline was observed from ZIS/CIS-10.5/Pt at the end of 2nd cycle. Higher stability in ZIS/CIS-7/Pt comparing to ZIS/CIS-10.5/Pt might be attributed to the relatively larger CIS aggregates in ZIS/CIS-7 which are somehow lesser prone to photocorrosion in ZIS/CIS photocatalytic system. On the other hand, the core-shell like structure in ZIS/CIS-12.5 exhibited higher photostability than that of ZIS/CIS-10.5 which indicates the stronger interaction

between ZIS and CIS in ZIS/CIS-12.5 can be more beneficial for the stability of ZIS/CIS photocatalytic system. Lastly, additional second PHE tests were carried out over those selected samples (Fig. S7) to affirm the above-mentioned PHE results. Very close PHE evolution performance was proven from ZIS/CIS-10.5/Pt and ZIS/CIS-12.5/Pt whereas ZIS/CIS-7/Pt exhibited lowest performance among the selected samples.

To acquire more insight to reveal the reason behind PHE activity, the three key samples ZIS/CIS-7, 10.5 and 12.5 was highlighted. This is because of the above-mentioned characteristic of CIS under different decoration medium resulting in different aggregation properties of CIS. The decoration under  $\text{pH} = 7$  and  $10.5$  led to CIS aggregates with aggregation induced emission property and CIS under  $\text{pH} = 12.5$  was relatively more uniformly dispersed with quenched emission while keeping the polydispersity. To further verify photocatalytic reducing power ability of selected ZIS/CIS samples, photocatalytic methyl viologen ( $\text{MV}^{2+}$ ) reduction to radical ( $\text{MV}^{+}$ ) was carried out (Fig. 7) to investigate the difference in reducing power ability ( $E(\text{MV}^{2+}/\text{MV}^{+}) = -0.44 \text{ V vs. NHE, pH } 7$ ) [53,54]. After 9 min the irradiation under  $\lambda = 420 \text{ nm}$ , a change in color from yellow to dark blue as an indication of  $\text{MV}^{+}$  generation [55–57] was observed from all samples proving that all samples' photogenerated electrons are sufficient for  $\text{MV}^{2+}$  reduction [58]. Moreover, UV–vis absorption spectra of all samples displayed a characteristic peak at  $605 \text{ nm}$  corresponding to  $\text{MV}^{+}$  [59]. The highest radical generation was observed from ZIS/CIS-10.5 that similar result as in PHE activity. However, ZIS/CIS-7 produced higher  $\text{MV}^{+}$  than that of ZIS/CIS-12.5 that is incompatible with the trend as in PHE result. This could be related with the adsorption of  $\text{MV}^{2+}$  which is more favorable on S-terminated surfaces with electron rich sulfur ions due to the positively charged nitrogens on  $\text{MV}^{2+}$  with poor electron [60]. Consequently, the uniform coating like coupling of MUA capped CIS over ZIS surface in ZIS/CIS-12.5 could block sulfur rich S-terminated surface in ZIS microspheres resulting in the poorest adsorption of  $\text{MV}^{2+}$  in comparison with ZIS/CIS-7 and ZIS/CIS-10.5. Therefore, it would be sensible to make comparison between only ZIS/CIS-7 and ZIS/CIS-10.5 in which ZIS/CIS-10.5 has higher reducing power ability than that of ZIS/CIS-7.

Optimization of the amount of Pt over photocatalytic systems is required to achieve the highest PHE rate [61,62]. However, the type of Pt species formed during in-situ deposition are very crucial as well as the amount and the formation of the Pt species [63]. Besides, the content of Pt species in ZIS/CIS can give an insight about PHE performances of selected samples. To confirm this supposition, firstly the percentage of weight loading of Pt in collected three selected samples after PHE tests were confirmed by ICP-OES technique (Table 1). Then the XPS technique was used to analyze the chemical composition of the selected samples (Table 1 and Table S1).

Indeed, the recorded Pt 4f and O 1s HR spectra confirm the presence of  $\text{Pt}(\text{OH})_x$ , Pt-Ox and Pt-Sx species [26,64] over ZIS/CIS-7/Pt,

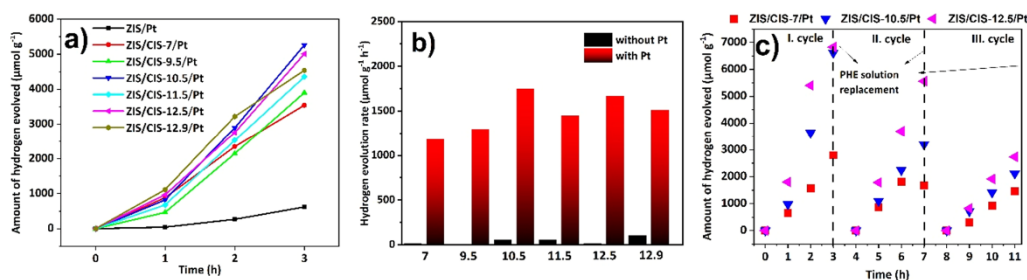


Fig. 6. a) Amount of evolved hydrogen with Pt deposition and b) hydrogen evolution rate by ZIS and ZIS/CIS samples with and without in-situ Pt deposition (7, 9.5, 10.5, 11.5, 12.5 and 12.9 represent ZIS/CIS-7, ZIS/CIS-9.5, ZIS/CIS-10.5, ZIS/CIS-11.5, ZIS/CIS-12.5 and ZIS/CIS-12.9, respectively) c) Recycling performance of three selected samples ZIS/CIS-7, ZIS/CIS-10.5 and ZIS/CIS-12.5.

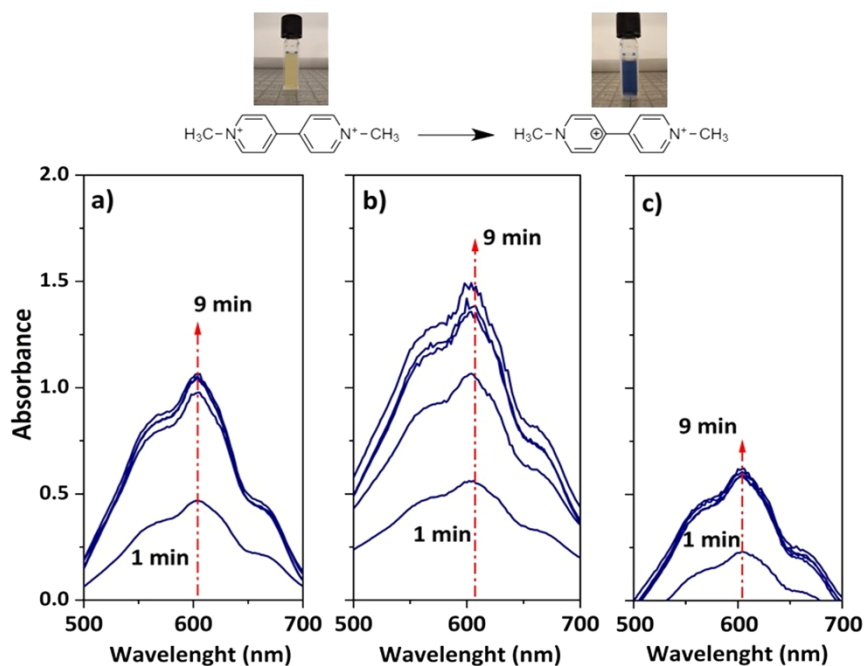


Fig. 7. Normalized UV-vis spectra originated from photoreduction of methyl viologen ( $MV^{2+}$ ) over a 3 ml mixture composed of a) ZIS/CIS-7, b) ZIS/CIS-10.5 and c) ZIS/CIS-12.5 samples (0.5 mg/ml), methyl viologen dichloride,  $[MV^{2+}] = 1.8$  mM and sacrificial reagent  $Na_2S/Na_2SO_3$  (0.35 M/0.25 M). Prior to the monochromatic light irradiation  $\lambda = 420$  nm, the mixture was purged with  $N_2$  gas with 4 dm<sup>3</sup>/h flow rate for 4 min to remove the  $O_2$  from the system to prevent the reoxidation of  $MV^{•+}$ . Inset image shows the color change of mixture from yellow to dark blue as an indication of  $MV^{•+}$ .

**Table 1**  
ICP-OES, XPS analysis of ZIS/CIS-7/Pt, 10.5/Pt and 12.5/Pt samples and their PHE rate.

Sample	ICP-OES		XPS			PHE rate ( $\mu\text{mol g}^{-1}$ $\text{h}^{-1}$ )
	Cu (wt%)	Pt (wt %)	Pt-CO,Pt- CxHy (%)	Pt- OH, Pt- Ox, Pt-Sx (%)	Pt content (at %)	
ZIS/CIS-7/ Pt	0.36	0.36	30.40	69.60	0.21	1180.46
ZIS/CIS- 10.5/Pt	0.39	0.20	27.14	72.86	0.26	1753.79
ZIS/CIS- 12.5/Pt	0.39	0.25	30.72	69.28	0.18	1670.16

ZIS/CIS-10.5/Pt and ZIS/CIS-12.5/Pt samples (Fig. 8) and highly likely originated from  $Pt(OH)_2$  that will be explained later. Moreover, the highest content of those Pt species was identified for the ZIS/CIS-10.5/Pt sample (Table 1) that is around more than 3 % higher than that of ZIS/CIS-7/Pt and ZIS/CIS-12.5/Pt samples. Similar minor difference in oxidative species was also reported elsewhere where 2 % higher oxidative species resulted in significantly higher electrocatalytic hydrogen evolution performance in alkaline media [65].

It is known that, highly alkaline aqueous solution in PHE solution can be formed (pH = 13) because of the formation of bisulfide ion  $HS^-$  and  $HSO_3^-$  from  $Na_2S/Na_2SO_3$  through the hydrolysis [66] (Eqs. (1) and (2)):



Therefore, displacement of  $Cl^-$  from  $PtCl_4^{2-}$  by  $OH^-$  takes place resulted in  $Pt(OH)_2$  by the adsorption of  $PtCl_4^{2-}$  on  $OH^-$  on ZIS/CIS surface leading the formation of  $Pt(OH)_2$  taking place before the light irradiation during the nitrogen purging (Eq. (3)):



As acidic conditions are suitable for the formation of Pt-Sx, the formation of Pt-Sx species are unlikely under high pH of PHE solution (pH = 13) [67]. On the other hand, Pt-C<sub>x</sub>H<sub>x</sub> and Pt-CO species might reveal the simultaneous formation of metallic  $Pt^0$  on ZIS/CIS surface during the visible light irradiation induced PHE [68] (Eqs. (4) and (5)).



However, it is worth to note that the proximity in binding energies (BE) of  $Pt^0$  and Pt with the Cu, CO and C<sub>x</sub>H<sub>x</sub> chemical environment make difficult to predict the exact oxidation state whether is zero or close the zero.

Supposedly, PHE evolution over ZIS/CIS sample were initiated by  $Pt(OH)_2$  species, and taking into consideration that the formation of  $Pt(OH)_2$  occurs before the light irradiation as above-mentioned,  $PtCl_4^{2-}$  complex ion interaction with ZIS/CIS surface before the light irradiation should be pointed out. For that purpose,  $\zeta$ -potentials of the selected samples was investigated in the PHE solution. Expectedly, the surfaces of

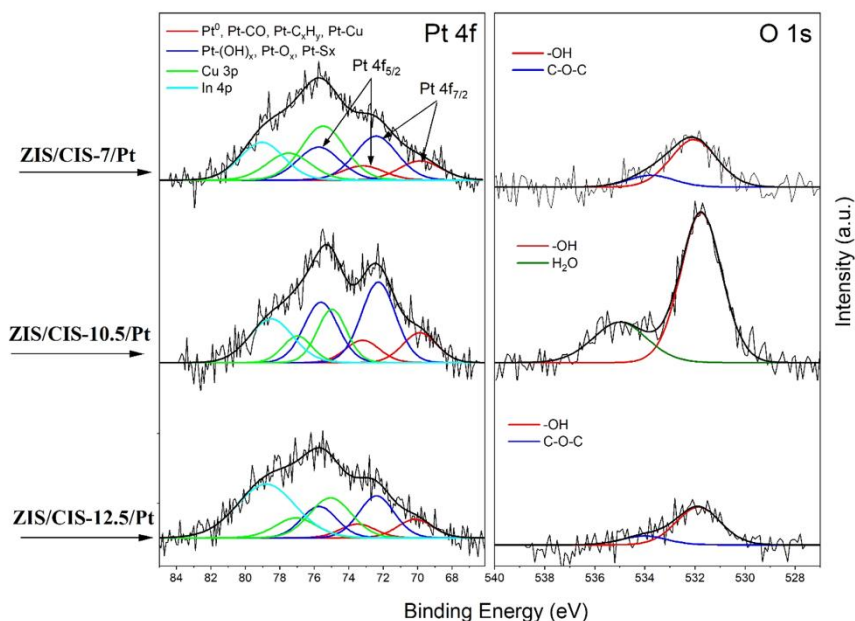


Fig. 8. XPS High resolution Pt 4f and O 1s XPS spectra recorded on ZIS/CIS-7/Pt, ZIS/CIS-10.5/Pt and ZIS/CIS-12.5/Pt photocatalytic systems after PHE tests. Deconvoluted peaks of Pt species are overlapped by Cu 3p and In 4p signals.

ZIS/CIS-7, 10.5 and 12.5 were negatively charged with a  $\zeta$ -potential of  $-18.3 \pm 0.60$ ,  $15.56 \pm 0.58$  and  $-14.46 \pm 0.43$  mV, respectively (Fig. S8).  $\zeta$ -potential of the samples decreases as their decoration medium pH increase. Comparing with ZIS/CIS-7,  $Pt^{2+}$  cations from  $PtCl_4^{2-}$  complex ion can be adsorbed relatively harder over ZIS/CIS-10.5 surface than that of ZIS/CIS-7 by electrostatic interactions. Yet, the difference in  $\zeta$ -potential is little, thereby it might have no decisive role in the difference between PHE performances.

Consequently, the overall mechanism from before light irradiation to PHE process can be proposed as follows (Fig. 9); (1) hydrolysis of  $Na_2S/Na_2SO_3$  sacrificial reagent results in formation of OH<sup>-</sup> (2) which is

adsorbed by the ZIS/CIS surface and displace the chloride ligands in  $PtCl_4^{2-}$  complex ion. Upon the visible light irradiation, (3) photo-generated electrons and holes over ZIS/CIS transferring across p-n junction mechanism similar to the reports elsewhere [23,26] in accordance to the conduction (CB) and valance band (VB) alignment in ZIS ( $CB_{ZIS} = -0.99$  eV,  $VB_{ZIS} = 1.5$  eV) and CIS ( $CB_{CIS} = -1.27$  eV,  $VB_{CIS} = 0.6$  eV) [26] leading to (4) three different simultaneous reaction including reduction of Pt(II) to Pt(0), PHE hydrogen evolution over Pt(OH)<sub>2</sub> and simultaneously formed metallic Pt, and oxidation of sacrificial reagent by photogenerated holes. In addition, it is worth clarifying the effect of the morphology of CIS in ZIS/CIS photocatalytic systems on

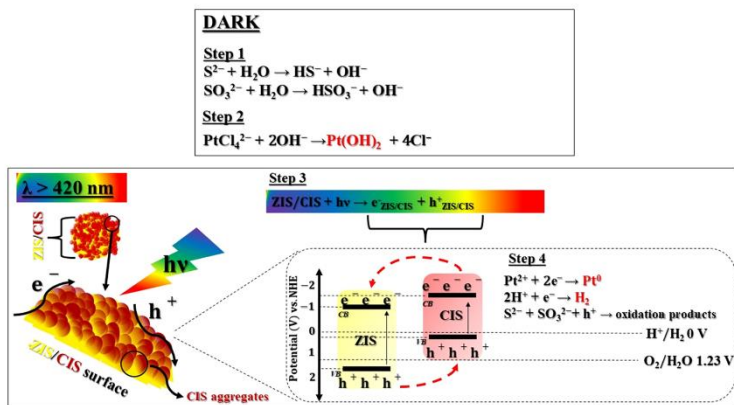


Fig. 9. Overall PHE mechanism before and after the light irradiation illustrated step-by-step.



PHE performance. Based on UV-vis spectra (Fig. 4), the significantly improved light harvesting property in ZIS/CIS-12.5 might be responsible for the sudden increased trend in PHE performance in ZIS/CIS-12.5/Pt (Fig. 6b). However, as PL spectra is a useful tool to explore the charge separation of the photogenerated electron-hole carriers [69–71], the lower recombination was observed in ZIS/CIS-10.5 compared to ZIS/CIS-12.5 (Fig. 4). That can be interpreted in terms of the presence of CIS in a form of single quantum size in core-shell like ZIS/CIS-12.5 photocatalytic system [72]. At this amount (5 wt%) of CIS in this photocatalytic system might act as a recombination center that inhibits the electron transfer reducing the PHE performance. On the other hand, it was not the case for ZIS/CIS-10.5 in which core-shell structure was not obtained and the contact between ZIS and CIS was poorer. Thus, lower recombination of charge carriers was observed in ZIS/CIS-10.5. Therefore, although the light harvesting property is lower in ZIS/CIS-10.5 than that of ZIS/CIS-12.5, the recombination is higher in ZIS/CIS-12.5. As a result, taken together with the Pt species factor and the optimum balance between light harvesting and charge recombination property, the most suitable condition for PHE was achieved in ZIS/CIS-10.5/Pt among other prepared ZIS/CIS photocatalytic systems.

#### 4. Conclusion

The controlled aggregation of the photoluminescent CIS QDs over hydrothermally obtained ZIS surface in aqueous media was initiated by the mercaptocarboxylic acid capping ligand by adjusting the alkalinity level of aqueous decoration medium. Despite the same amount of CIS decoration (5 wt%) and in-situ Pt deposition (0.5 wt%) in prepared ZIS/CIS photocatalytic samples, their photocatalytic hydrogen evolution performances after 3 h of visible light irradiation ( $\lambda > 420$  nm) differed significantly. Optimum aggregation control for the highest amount of hydrogen evolution rate from ZIS/CIS-10.5/Pt was higher than that of ZIS/CIS-7/Pt and ZIS/CIS-12.5/Pt where CIS formed uniform surface topology over ZIS surface. Those results remark the importance of the surface chemical states of most popular cocatalyst Pt noble metal which was supported by the XPS analysis revealing that ZIS/CIS-10.5 exhibited the highest content of Pt-Ox and Pt-(OH)<sub>x</sub> species in comparison with ZIS/CIS-7 and ZIS/CIS-12.5. Moreover, a similar trend was also confirmed by the monochromatic light irradiation ( $\lambda = 420$  nm) induced methyl viologen (MV<sup>2+</sup>) photoreduction to radical (MV<sup>•+</sup>) over samples in Na<sub>2</sub>S/Na<sub>2</sub>SO<sub>3</sub> (0.35 M/0.25 M) aqueous solution confirming that ZIS/CIS-10.5 reduced highest amount of MV<sup>2+</sup> to MV<sup>•+</sup> implying the reducing power is the highest in ZIS/CIS-10.5.

This work indicates the importance of the surface chemistry and the topology in photocatalytic system's hydrogen evolution performances that requires Pt cocatalyst that is essential for the sustainable hydrogen economy.

#### CRedit authorship contribution statement

**Onur Cavdar:** Conceptualization, Methodology, Investigation, Validation, Visualization, Writing – original draft. **Anna Malankowska:** Funding acquisition, Supervision, Conceptualization, Resources, Writing – review & editing. **Justyna Łuczak:** Methodology. **Andrzej Żak:** Investigation. **Wojciech Lisowski:** Investigation, Writing – original draft. **Tomasz Klimeczuk:** Investigation, Writing – original draft. **Adriana Zaleska-Medynska:** Resources, Writing – review & editing.

#### Declaration of Competing Interest

The authors declare that they have no known competing financial interests or personal relationships that could have appeared to influence the work reported in this paper.

#### Data Availability

Data will be made available on request.

#### Acknowledgements

This research was financially supported by National Science Centre, Poland (Grant No. 2016/23/D/ST8/02682).

#### Appendix A. Supporting information

Supplementary data associated with this article can be found in the online version at doi:10.1016/j.colsurfa.2022.129760.

#### References

- [1] J.O. Abe, A.P.I. Popoola, E. Ajenifuja, O.M. Popoola, Hydrogen energy, economy and storage: review and recommendation, *Int. J. Hydrogen Energy* 44 (2019) 15072–15086, <https://doi.org/10.1016/j.ijhydene.2019.04.068>.
- [2] J. Qi, W. Zhang, R. Cao, Solar-to-hydrogen energy conversion based on water splitting, *Adv. Energy Mater.* 8 (2018) 1–16, <https://doi.org/10.1002/aenm.201701620>.
- [3] K. Zhang, L. Guo, Metal sulphide semiconductors for photocatalytic hydrogen production, *Catal. Sci. Technol.* 3 (2013) 1672–1690, <https://doi.org/10.1039/c3cy00018d>.
- [4] A. Amedeo, N. Yifat, A. Lilac, B. Giacomo, Photosynthetic H<sub>2</sub> generation and organic transformations with CdSe@CdS-Pt nanorods for highly efficient solar-to-chemical energy conversion, *Nano Energy* 70 (2020), 104510, <https://doi.org/10.1016/j.nanoen.2020.104510>.
- [5] S. Bojja, U. Pal, T.P. Yendrapati, J. Soumya, Robust Co<sub>9</sub>S<sub>8</sub>@CdIn<sub>2</sub>S<sub>4</sub> cage for efficient photocatalytic H<sub>2</sub> evolution, *J. Phys. Chem. C* 125 (2021) 5099–5109, <https://doi.org/10.1021/acs.jpcc.0c11554>.
- [6] R. Bariki, D. Majhi, K. Das, A. Behera, B.G. Mishra, Facile synthesis and photocatalytic efficacy of UiO-66/CdIn<sub>2</sub>S<sub>4</sub> nanocomposites with flowerlike 3D-microspheres towards aqueous phase decontamination of triclosan and H<sub>2</sub> evolution, *Appl. Catal. B Environ.* 270 (2020), 118882, <https://doi.org/10.1016/j.apcatb.2020.118882>.
- [7] Y. Li, J. Wang, S. Peng, G. Lu, S. Li, Photocatalytic hydrogen generation in the presence of glucose over ZnS-coated ZnIn<sub>2</sub>S<sub>4</sub> under visible light irradiation, *Int. J. Hydrogen Energy* 35 (2010) 7116–7126, <https://doi.org/10.1016/j.ijhydene.2010.02.017>.
- [8] M. Tabata, K. Maeda, T. Ishihara, T. Minegishi, T. Takata, K. Domen, Photocatalytic hydrogen evolution from water using copper gallium sulfide under visible-light irradiation, *J. Phys. Chem. C* 114 (2010) 11215–11220, <https://doi.org/10.1021/jp103158f>.
- [9] J. Wang, S. Sun, R. Zhou, Y. Li, Z. He, H. Ding, et al., A review: synthesis, modification and photocatalytic applications of ZnIn<sub>2</sub>S<sub>4</sub>, *J. Mater. Sci. Technol.* 78 (2021) 1–19, <https://doi.org/10.1016/j.jmst.2020.09.045>.
- [10] H. Liu, J. Zhang, D. Ao, Construction of heterostructured ZnIn<sub>2</sub>S<sub>4</sub>@NH<sub>2</sub>-MIL-125 (Ti) nanocomposites for visible-light-driven H<sub>2</sub> production, *Appl. Catal. B Environ.* 221 (2018) 433–442, <https://doi.org/10.1016/j.apcatb.2017.09.043>.
- [11] M. Geng, Y. Peng, Y. Zhang, X. Guo, F. Yu, X. Yang, et al., Hierarchical ZnIn<sub>2</sub>S<sub>4</sub>: a promising cocatalyst to boost visible-light-driven photocatalytic hydrogen evolution of In(OH)<sub>3</sub>, *Int. J. Hydrogen Energy* 44 (2019) 5787–5798, <https://doi.org/10.1016/j.ijhydene.2019.01.094>.
- [12] C. Zhao, Y. Zhang, H. Jiang, J. Chen, Y. Liu, Q. Liang, et al., Combined effects of octahedron NH<sub>2</sub>-UiO-66 and Flowerlike ZnIn<sub>2</sub>S<sub>4</sub> microspheres for photocatalytic dye degradation and hydrogen evolution under visible light, *J. Phys. Chem. C* 123 (2019) 18037–18049, <https://doi.org/10.1021/acs.jpcc.9b03807>.
- [13] D. Kong, H. Fan, D. Yin, D. Zhang, X. Pu, S. Yao, et al., AgFeO<sub>2</sub> nanoparticle/ZnIn<sub>2</sub>S<sub>4</sub> microsphere p-n heterojunctions with hierarchical nanostructures for efficient visible-light-driven H<sub>2</sub> evolution, *ACS Sustain. Chem. Eng.* 9 (2021) 2673–2683, <https://doi.org/10.1021/acssuschemeng.0c07638>.
- [14] G. Zuo, Y. Wang, W.L. Teo, A. Xie, Y. Guo, Y. Dai, et al., Ultrathin ZnIn<sub>2</sub>S<sub>4</sub> nanosheets anchored on Ti<sub>3</sub>C<sub>2</sub>TX MXene for photocatalytic H<sub>2</sub> evolution, *Angew. Chem.* 132 (2020) 11383–11388, <https://doi.org/10.1002/ange.202002136>.
- [15] Z. Li, X. Wang, W. Tian, A. Meng, L. Yang, CoNi bimetal cocatalyst modifying a hierarchical ZnIn<sub>2</sub>S<sub>4</sub> nanosheet-based microsphere noble-metal-free photocatalyst for efficient visible-light-driven photocatalytic hydrogen production, *ACS Sustain. Chem. Eng.* 7 (2019), <https://doi.org/10.1021/acssuschemeng.9b06430>, 20190–201.
- [16] Z. Gao, K. Chen, L. Wang, B. Bai, H. Liu, Q. Wang, Aminated flower-like ZnIn<sub>2</sub>S<sub>4</sub> coupled with benzoic acid modified g-C<sub>3</sub>N<sub>4</sub> nanosheets via covalent bonds for ameliorated photocatalytic hydrogen generation, *Appl. Catal. B Environ.* 268 (2020), 118462, <https://doi.org/10.1016/j.apcatb.2019.118462>.
- [17] J. Liu, G. Chen, J. Sun, Ag<sub>2</sub>S-modified ZnIn<sub>2</sub>S<sub>4</sub> nanosheets for photocatalytic H<sub>2</sub> generation, *ACS Appl. Nano Mater.* 3 (2020) 11017–11024, <https://doi.org/10.1021/acsnano.0c02240>.
- [18] Y. Chen, Z. Qin, X. Wang, X. Guo, L. Guo, Noble-metal-free Cu<sub>2</sub>S-modified photocatalysts for enhanced photocatalytic hydrogen production by forming

- nanoscale p-n junction structure, *RSC Adv.* 5 (2015) 18159–18166, <https://doi.org/10.1039/c5ra00091b>.
- [19] E. Zhang, Q. Zhu, J. Huang, J. Liu, G. Tan, C. Sun, et al., Visually resolving the direct Z-scheme heterojunction in CdS@ ZnIn<sub>2</sub>S<sub>4</sub> hollow cubes for photocatalytic evolution of H<sub>2</sub> and H<sub>2</sub>O<sub>2</sub> from pure water, *Appl. Catal. B Environ.* 293 (2021), 120213, <https://doi.org/10.1016/j.apcatb.2021.120213>.
- [20] W. Li, Z. Lin, G. Yang, A 2D self-assembled MoS<sub>2</sub>/ZnIn<sub>2</sub>S<sub>4</sub> heterostructure for efficient photocatalytic hydrogen evolution, *Nanoscale* 9 (2017) 18290–18298, <https://doi.org/10.1039/c7nr06755k>.
- [21] W. Pudkon, S. Kaowphong, S. Pattison, P.J. Miedziak, H. Bahruji, T.E. Davies, et al., Microwave synthesis of ZnIn<sub>2</sub>S<sub>4</sub>/WS<sub>2</sub> composites for photocatalytic hydrogen production and hexavalent chromium reduction, *Catal. Sci. Technol.* 9 (2019) 5698–5711, <https://doi.org/10.1039/c9cy01553a>.
- [22] X. Guo, Y. Peng, G. Liu, G. Xie, Y. Guo, Y. Zhang, et al., An efficient ZnIn<sub>2</sub>S<sub>4</sub>@ CuInS<sub>2</sub> core-shell p-n heterojunction to boost visible-light photocatalytic hydrogen evolution, *J. Phys. Chem. C* 124 (2020) 5934–5943, <https://doi.org/10.1021/acs.jpcc.9b11623>.
- [23] Z. Guan, J. Pan, Q. Li, G. Li, J. Yang, Boosting visible-light photocatalytic hydrogen evolution with an efficient CuInS<sub>2</sub>/ZnIn<sub>2</sub>S<sub>4</sub> 2D/2D heterojunction, *ACS Sustain. Chem. Eng.* 7 (2019) 7736–7742, <https://doi.org/10.1021/acscuschemeng.8b06587>.
- [24] A. Raja, N. Son, M. Swaminathan, M. Kang, Facile synthesis of sphere-like structured ZnIn<sub>2</sub>S<sub>4</sub>-rGO-CuInS<sub>2</sub> ternary heterojunction catalyst for efficient visible-active photocatalytic hydrogen evolution, *J. Colloid Interface Sci.* 602 (2021) 669–679, <https://doi.org/10.1016/j.jcis.2021.06.034>.
- [25] Z. Long, W. Zhang, J. Tian, G. Chen, Y. Liu, R. Liu, Recent research on the luminous mechanism, synthetic strategies, and applications of CuInS<sub>2</sub> quantum dots, *Inorg. Chem. Front.* 8 (2021) 880–897, <https://doi.org/10.1039/D0QI01228A>.
- [26] O. Cavdar, A. Malankowska, D. Amgar, P. Mazierski, J. Luczak, W. Lisowski, et al., Remarkable visible-light induced hydrogen generation with ZnIn<sub>2</sub>S<sub>4</sub> microspheres/CuInS<sub>2</sub> quantum dots photocatalytic system, *Int. J. Hydrogen Energy* 46 (2020) 486–498, <https://doi.org/10.1016/j.ijhydene.2020.09.212>.
- [27] M. Mou, Y. Wu, Q. Niu, Y. Wang, Z. Yan, S. Liao, Aggregation-induced emission properties of hydrothermally synthesized Cu-In-S quantum dots, *Chem. Commun.* 53 (2017) 3357–3360, <https://doi.org/10.1039/c7cc00170c>.
- [28] Y. Zhang, L. Mi, P.N. Wang, J. Ma, J.Y. Chen, pH-dependent aggregation and photoluminescence behavior of thiol-capped CdTe quantum dots in aqueous solutions, *J. Lumin* 128 (2008) 1948–1951, <https://doi.org/10.1016/j.jlumin.2008.06.004>.
- [29] V. Swayambunathan, D. Hayes, K.H. Schmidt, Y.X. Liao, D. Meisel, Thiol surface complexation on growing CdS clusters, *J. Am. Chem. Soc.* 112 (1990) 3831–3837, <https://doi.org/10.1021/ja00166a017>.
- [30] S. Xu, C. Wang, H. Zhang, Z. Wang, B. Yang, Y. Cui, PH-sensitive photoluminescence for aqueous thiol-capped CdTe nanocrystals, *Nanotechnology* (2011) 22, <https://doi.org/10.1088/0957-4484/22/31/315703>.
- [31] S. Yu, Z.J. Li, X.B. Fan, J.K. Li, F. Zhan, X.B. Li, et al., Vectorial electron transfer for improved hydrogen evolution by mercaptopropionic-acid-regulated CdSe quantum-dots-TiO<sub>2</sub>-Ni(OH)<sub>2</sub> assembly, *ChemSusChem* 8 (2015) 642–649, <https://doi.org/10.1002/cssc.201402885>.
- [32] C.M. Chang, K.L. Orchard, B.C.M. Martindale, E. Reisner, Ligand removal from CdS quantum dots for enhanced photocatalytic H<sub>2</sub> generation in pH neutral water, *J. Mater. Chem. A* 4 (2016) 2856–2862, <https://doi.org/10.1039/c5ta04136h>.
- [33] Y. Park, W. Kim, D. Monlor-Satoaca, T. Tachikawa, T. Majima, W. Choi, Role of interparticle charge transfers in agglomerated photocatalyst nanoparticles: demonstration in aqueous suspension of dye-sensitized TiO<sub>2</sub>, *J. Phys. Chem. Lett.* 4 (2013) 189–194, <https://doi.org/10.1021/jz301881d>.
- [34] Y.J. Gao, Y. Yang, X.B. Li, H.L. Wu, S.L. Meng, Y. Wang, et al., Self-assembled inorganic clusters of semiconducting quantum dots for effective solar hydrogen evolution, *Chem. Commun.* 54 (2018) 4858–4861, <https://doi.org/10.1039/c8cc02091d>.
- [35] K. Sawaguchi-Sato, A. Kobayashi, M. Yoshida, M. Kato, Aggregation-enhanced photocatalytic H<sub>2</sub> evolution activity of photosensitizing cadmium selenide quantum dots and platinum colloidal catalysts, *J. Photochem. Photobiol. A Chem.* 335 (2017) 182–189, <https://doi.org/10.1016/j.jphotochem.2016.11.028>.
- [36] M.C. Nevárez Martínez, O. Cavdar, Haliński Ł.P., M. Miodyńska, P. Parnicka, B. Bajorowicz, et al., Hydrogen detection during photocatalytic water splitting: a tutorial, *Int. J. Hydrogen Energy* (2022), <https://doi.org/10.1016/j.ijhydene.2022.03.050>.
- [37] Y. Liang, J.E. Thorne, B.A. Parkinson, Controlling the electronic coupling between CdSe quantum dots and thiol capping ligands via pH and ligand selection, *Langmuir* 28 (2012) 11072–11077, <https://doi.org/10.1021/la301237p>.
- [38] J. Moon, K. Choi, B. Kim, K. Yoon, T. Seong, K. Woo, Aggregation-free process for functional CdSe/CdS core/shell quantum dots, *J. Phys. Chem. C* (2009) 7114–7119.
- [39] W. Jiang, S. Mardiyani, H. Fischer, W.C.W. Chan, Design and characterization of lysine cross-linked mercapto-acid biocompatible quantum dots, *Chem. Mater.* 18 (2006) 872–878, <https://doi.org/10.1021/cm051393>.
- [40] H.T. Uyeda, I.L. Medintz, J.K. Jaiswal, S.M. Simon, H. Mattoussi, Synthesis of compact multidentate ligands to prepare stable hydrophilic quantum dot fluorophores, *J. Am. Chem. Soc.* 127 (2005) 3870–3878, <https://doi.org/10.1021/ja044031v>.
- [41] T. Laaksonen, P. Ahonen, C. Johans, K. Kontturi, Stability and electrostatics of mercaptoundecanoic acid-capped gold nanoparticles with varying counterion size, *ChemPhysChem* 7 (2006) 2143–2149, <https://doi.org/10.1002/cphc.200600307>.
- [42] C. Wei, X. Wei, Z. Hu, D. Yang, S. Mei, G. Zhang, et al., A fluorescent probe for Cd<sup>2+</sup> detection based on the aggregation-induced emission enhancement of aqueous Zn-Ag-In-S quantum dots, *Anal. Methods* 11 (2019) 2559–2564, <https://doi.org/10.1039/c9ay00716d>.
- [43] S. Shen, P. Guo, L. Zhao, Y. Du, L. Guo, Insights into photoluminescence property and photocatalytic activity of cubic and rhombohedral ZnIn<sub>2</sub>S<sub>4</sub>, *J. Solid State Chem.* 184 (2011) 2250–2256, <https://doi.org/10.1016/j.jssc.2011.06.033>.
- [44] J. Ding, C. Zheng, L. Wang, C. Lu, B. Zhang, Y. Chen, et al., Viologen-inspired functional materials: Synthetic strategies and applications, *J. Mater. Chem. A* 7 (2019) 23337–23360, <https://doi.org/10.1039/c9ta01724k>.
- [45] S. Shen, L. Zhao, X. Guan, L. Guo, Improving visible-light photocatalytic activity for hydrogen evolution over ZnIn<sub>2</sub>S<sub>4</sub>: a case study of alkaline-earth metal doping, *J. Phys. Chem. Solids* 73 (2012) 79–83, <https://doi.org/10.1016/j.jpcs.2011.09.027>.
- [46] C. Liu, Y. Zhang, J. Wu, H. Dai, C. Ma, Q. Zhang, et al., Ag-Pd alloy decorated ZnIn<sub>2</sub>S<sub>4</sub> microspheres with optimal Schottky barrier height for boosting visible-light-driven hydrogen evolution, *J. Mater. Sci. Technol.* 114 (2022) 81–89, <https://doi.org/10.1016/j.jmst.2021.12.003>.
- [47] Y. Jiang, Z.Y. Peng, S. Zhang, F. Li, Z. Liu, J. Zhang, et al., Facile in-situ Solvothermal Method to synthesize double shell ZnIn<sub>2</sub>S<sub>4</sub> nanosheets/TiO<sub>2</sub> hollow nanosphere with enhanced photocatalytic activities, *Ceram. Int.* 44 (2018) 6115–6126, <https://doi.org/10.1016/j.ceramint.2017.12.244>.
- [48] H. Xu, Y. Jiang, X. Yang, F. Li, A. Li, Y. Liu, et al., Fabricating carbon quantum dots doped ZnIn<sub>2</sub>S<sub>4</sub> nanoflower composites with broad spectrum and enhanced photocatalytic Tetracycline hydrochloride degradation, *Mater. Res. Bull.* 97 (2018) 158–168, <https://doi.org/10.1016/j.materresbull.2017.09.004>.
- [49] X. Pan, C. Shang, Z. Chen, M. Jin, Y. Zhang, Z. Zhang, et al., Enhanced photocatalytic H<sub>2</sub> evolution over ZnIn<sub>2</sub>S<sub>4</sub> flower-like microspheres doped with black phosphorus quantum dots, *Nanomaterials* (2019) 9, <https://doi.org/10.3390/nano9091266>.
- [50] J. Wang, D. Wang, X. Zhang, C. Zhao, M. Zhang, Z. Zhang, et al., An anti-symmetric dual (ASD) Z-scheme photocatalytic system: (ZnIn<sub>2</sub>S<sub>4</sub>/Er<sup>3+</sup>:Y<sub>3</sub>Al<sub>5</sub>O<sub>12</sub>@ZnTiO<sub>3</sub>/CaIn<sub>2</sub>S<sub>4</sub>) for organic pollutants degradation with simultaneous hydrogen evolution, *Int. J. Hydrogen Energy* 44 (2019) 6592–6607, <https://doi.org/10.1016/j.ijhydene.2019.01.214>.
- [51] J. Zhao, X. Yan, N. Zhao, X. Li, B. Lu, X. Zhang, et al., Cocatalyst designing: a binary noble-metal-free cocatalyst system consisting of ZnIn<sub>2</sub>S<sub>4</sub> and In(OH)<sub>3</sub> for efficient visible-light photocatalytic water splitting†, *RSC Adv.* 8 (2018) 4979–4986, <https://doi.org/10.1039/c7ra12586k>.
- [52] Q. Gu, J. Long, H. Zhuang, C. Zhang, Y. Zhou, X. Wang, Ternary Pt/SnO<sub>2</sub>/TiO<sub>2</sub> photocatalysts for hydrogen production: consequence of Pt sites for synergy of dual co-catalysts, *Phys. Chem. Phys.* 16 (2014) 12521–12534, <https://doi.org/10.1039/c4cp01496k>.
- [53] W. Chen, R.Q. Yan, J.Q. Zhu, G.B. Huang, Z. Chen, Highly efficient visible-light-driven photocatalytic hydrogen evolution by all-solid-state Z-scheme CdS/QDs/ZnIn<sub>2</sub>S<sub>4</sub> architectures with MoS<sub>2</sub> quantum dots as solid-state electron mediator, *Appl. Surf. Sci.* 504 (2020), 144406, <https://doi.org/10.1016/j.apsusc.2019.144406>.
- [54] Y. Honda, M. Watanabe, H. Hagiwara, S. Ida, T. Ishihara, Inorganic/whole-cell biohybrid photocatalyst for highly efficient hydrogen production from water, *Appl. Catal. B Environ.* 210 (2017) 400–406, <https://doi.org/10.1016/j.apcatb.2017.04.015>.
- [55] C.A. Caputo, L. Wang, R. Beranek, E. Reisner, Carbon nitride-TiO<sub>2</sub> hybrid modified with hydrogenase for visible light driven hydrogen production, *Chem. Sci.* 6 (2015) 5690–5694, <https://doi.org/10.1039/c5sc02017d>.
- [56] S. Krishnamurthy, I.V. Lightcap, P.V. Kamat, Electron transfer between methyl viologen radicals and graphene oxide: Reduction, electron storage and discharge, *J. Photochem. Photobiol. A Chem.* 221 (2011) 214–219, <https://doi.org/10.1016/j.jphotochem.2011.02.024>.
- [57] C. Kong, L. Qin, J. Liu, X. Zhong, L. Zhu, Y.T. Long, Determination of dissolved oxygen based on photoinduced electron transfer from quantum dots to methyl viologen, *Anal. Methods* 2 (2010) 1056–1062, <https://doi.org/10.1039/c9ay00201a>.
- [58] H. Lu, R. Hu, H. Bai, H. Chen, F. Lv, L. Liu, et al., Efficient conjugated polymer-methyl viologen electron transfer system for controlled photo-driven hydrogen evolution, *ACS Appl. Mater. Interfaces* 9 (2017) 10355–10359, <https://doi.org/10.1021/acsmami.7b00069>.
- [59] A. Iagatti, L. Tarpani, E. Fiacchi, L. Bussotti, L. Latterini, P. Foggi, Charge transfer dynamics between MPA capped CdTe quantum dots and methyl viologen, *J. Photochem. Photobiol. A Chem.* 346 (2017) 382–389, <https://doi.org/10.1016/j.jphotochem.2017.06.022>.
- [60] M.D. Peterson, S.C. Jensen, D.J. Weinberg, E.A. Weiss, Mechanisms for adsorption of methyl viologen on cds quantum dots, *ACS Nano* 8 (2014) 2826–2837, <https://doi.org/10.1021/nn406651a>.
- [61] F. Gao, Y. Zhao, L. Zhang, B. Wang, Y. Wang, X. Huang, et al., Well dispersed MoC quantum dots in ultrathin carbon films as efficient co-catalysts for photocatalytic H<sub>2</sub> evolution, *J. Mater. Chem. A* 6 (2018) 18979–18986, <https://doi.org/10.1039/c8ta06029k>.
- [62] B. Mei, K. Han, G. Mul, Driving surface redox reactions in heterogeneous photocatalysis: the active state of illuminated semiconductor-supported nanoparticles during overall water-splitting, *ACS Catal.* 8 (2018) 9154–9164, <https://doi.org/10.1021/acscatal.8b02215>.
- [63] K. Wenderich, G. Mul, Methods, mechanism, and applications of photodeposition in photocatalysis: a review, *Chem. Rev.* 116 (2016) 14587–14619, <https://doi.org/10.1021/acs.chemrev.6b00327>.
- [64] V. Naumkin, A. Kraut-Vass, A.W. Gaarenstroom S.J., Powell C. NIST X-ray Photoelectron Spectroscopy Database, NIST Standard Reference Database 20, Version 4.1. Natl Inst Stand Technol 2012. <https://doi.org/10.18434/T4T88K>.

- [65] L. Zeng, J. Luo, G. Mao, D. Wu, R. Li, L. Huang, et al., Boosted hydrogen evolution in alkaline media enabled by a facile oxidation-involving surface modification, *Electro Acta* 398 (2021), 139337, <https://doi.org/10.1016/j.electacta.2021.139337>.
- [66] C. Li, P. Hu, H. Meng, Z. Jiang, Role of sulfites in the water splitting reaction, *J. Solut. Chem.* 45 (2016) 67–80, <https://doi.org/10.1007/s10953-015-0422-1>.
- [67] Q. Li, Z. Chen, X. Zheng, Z. Jin, Study of photoreduction of  $\text{PtCl}_6^{2-}$  on CdS, *J. Phys. Chem.* 96 (1992) 5959–5962, <https://doi.org/10.1021/j100193a057>.
- [68] Y. Wang, Y. Wang, R. Xu, Photochemical deposition of Pt on CdS for  $\text{H}_2$  evolution from water: Markedly enhanced activity by controlling Pt reduction environment, *J. Phys. Chem. C* 117 (2013) 783–790, <https://doi.org/10.1021/jp309603c>.
- [69] Z. Shen, G. Chen, Y. Yu, Q. Wang, C. Zhou, L. Hao, et al., Sonochemistry synthesis of nanocrystals embedded in a  $\text{MoO}_3$ -CdS core-shell photocatalyst with enhanced hydrogen production and photodegradation, *J. Mater. Chem.* 22 (2012) 19646–19651, <https://doi.org/10.1039/c2jm33432a>.
- [70] J.G. Yu, H.G. Yu, B. Cheng, X.J. Zhao, J.C. Yu, W.K. Ho, The effect of calcination temperature on the surface microstructure and photocatalytic activity of  $\text{TiO}_2$  thin films prepared by liquid phase deposition, *J. Phys. Chem. B* 107 (2003) 13871–13879, <https://doi.org/10.1021/jp036158y>.
- [71] F.B. Li, X.Z. Li, Photocatalytic properties of gold/gold ion-modified titanium dioxide for wastewater treatment, *Appl. Catal. A Gen.* 228 (2002) 15–27, [https://doi.org/10.1016/S0926-860X\(01\)00953-X](https://doi.org/10.1016/S0926-860X(01)00953-X).
- [72] M. Guo, Z. Xing, T. Zhao, Z. Li, S. Yang, W. Zhou,  $\text{WS}_2$  quantum dots/ $\text{MoS}_2$ @ $\text{WO}_3-x$  core-shell hierarchical dual Z-scheme tandem heterojunctions with wide-spectrum response and enhanced photocatalytic performance, *Appl. Catal. B Environ.* 257 (2019), 117913, <https://doi.org/10.1016/j.apcatb.2019.117913>.

## **Supplementary information for P2**

---



## Capping ligand initiated CuInS<sub>2</sub> quantum dots decoration on ZnIn<sub>2</sub>S<sub>4</sub> microspheres surface under different alkalinity levels resulting in different hydrogen evolution performance

Onur Cavdar <sup>a</sup>, Anna Malankowska <sup>a,\*</sup>, Justyna Łuczak <sup>b</sup>, Andrzej Żak <sup>c</sup>, Wojciech Lisowski <sup>d</sup>,  
Tomasz Klimeczuk <sup>e,f</sup>, Adriana Zaleska-Medynska <sup>a</sup>

<sup>a</sup> Department of Environmental Technology, Faculty of Chemistry, University of Gdansk, Gdansk, Poland

<sup>b</sup> Department of Process Engineering and Chemical Technology, Faculty of Chemistry, Gdansk University of Technology, Gdansk, Poland.

<sup>c</sup> Electron Microscopy Laboratory, Faculty of Mechanical Engineering, Wrocław University of Science and Technology, Gdansk, Poland

<sup>d</sup> Institute of Physical Chemistry, Polish Academy of Science, Warsaw, Poland

<sup>e</sup> Faculty of Applied Physics and Mathematics, Gdansk University of Technology, Narutowicza, Gdansk, Poland

<sup>f</sup> Advanced Materials Center, Gdansk University of Technology, Narutowicza, Gdansk, Poland

### Supporting information

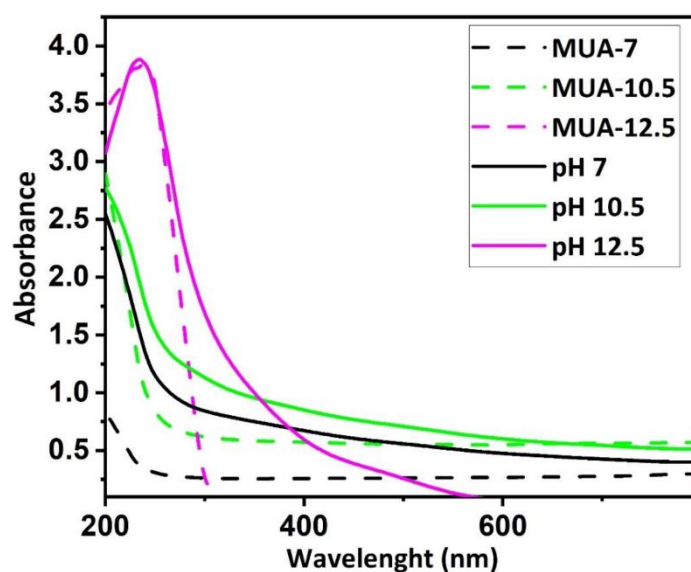


Fig. S1 The comparison of UV-vis absorption spectrum of MUA capped CIS and only MUA under pH = 7, 10.5 and 12.5. The dashed line represents UV-vis absorption spectrum of only MUA)

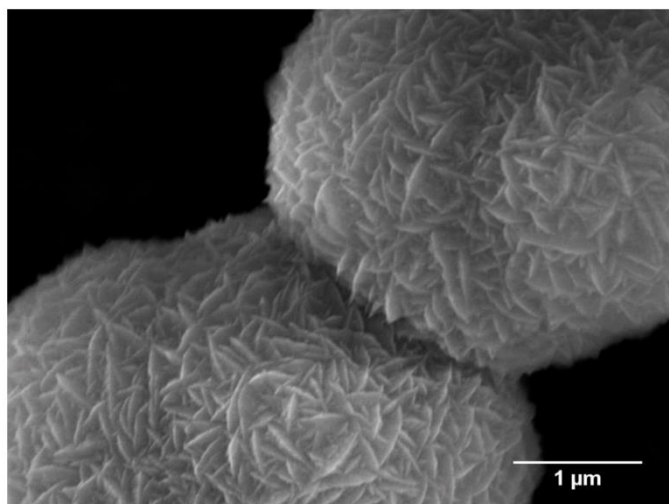


Fig. S2 SEM image of ZnIn<sub>2</sub>S<sub>4</sub> (ZIS)



**Fig. S3** Distinguishable color change of prepared ZIS/CIS-7, ZIS/CIS-10.5 and ZIS/CIS-12.5 samples from left to right

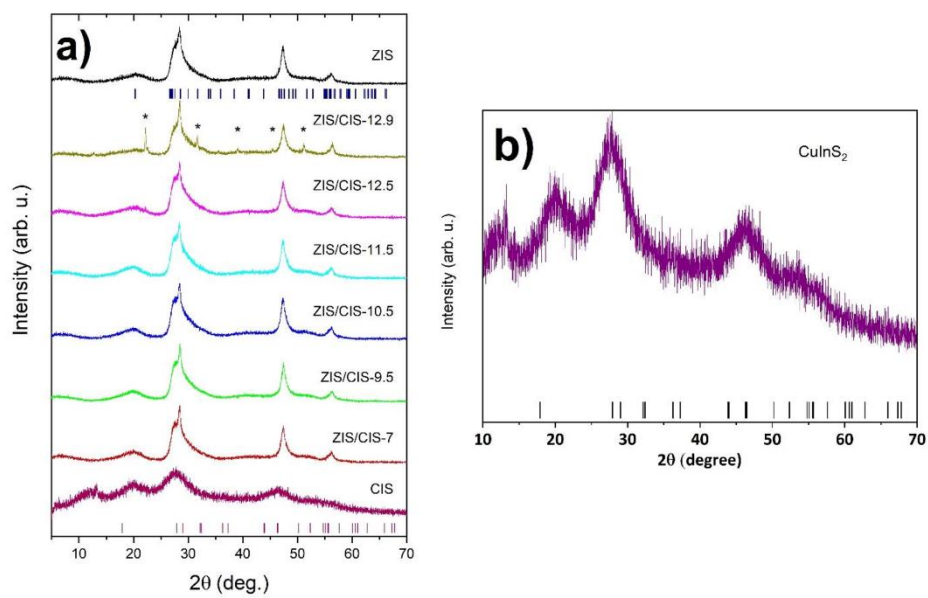


Fig. S4 XRD patterns of a) ZIS, ZIS/CIS and CIS samples and b) only CIS

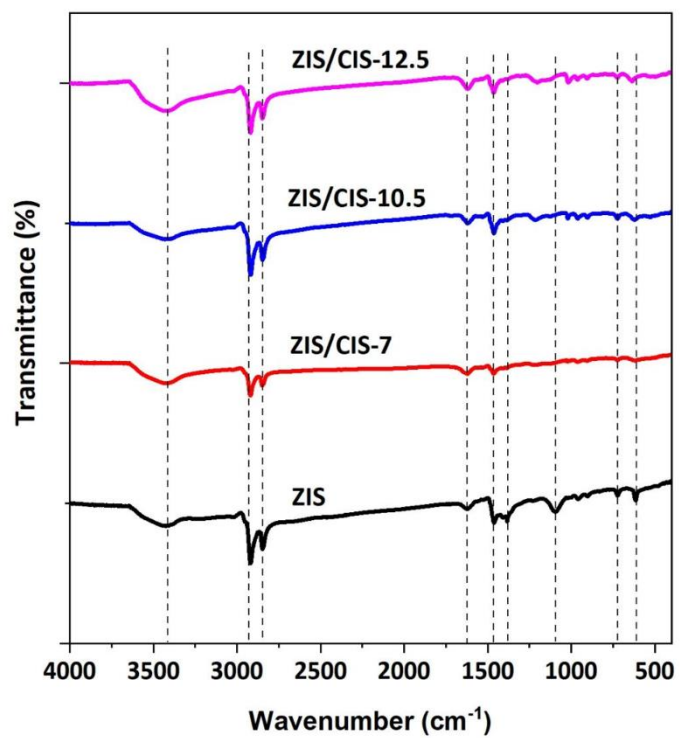


Fig. S5 FT-IR spectra of ZIS/CIS-7, 10.5 and 12.5

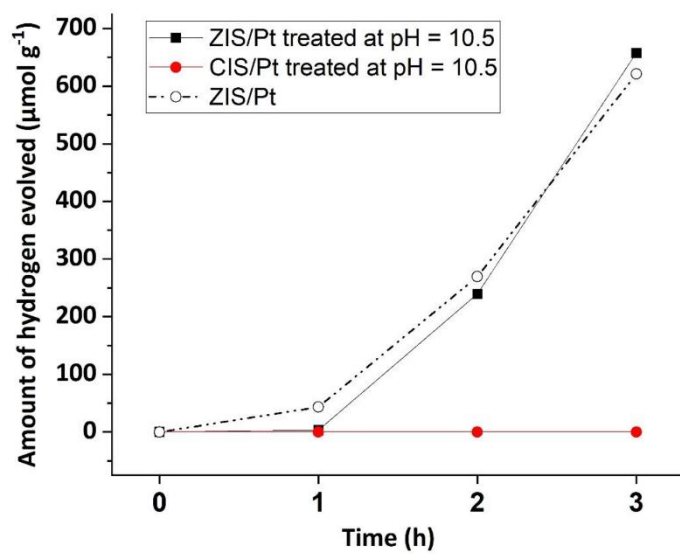


Fig. S6 Amount of evolved hydrogen with Pt deposition from ZIS and CIS treated under pH 10.5. Dashed line represents the data from ZIS/Pt without any treatment as a comparison

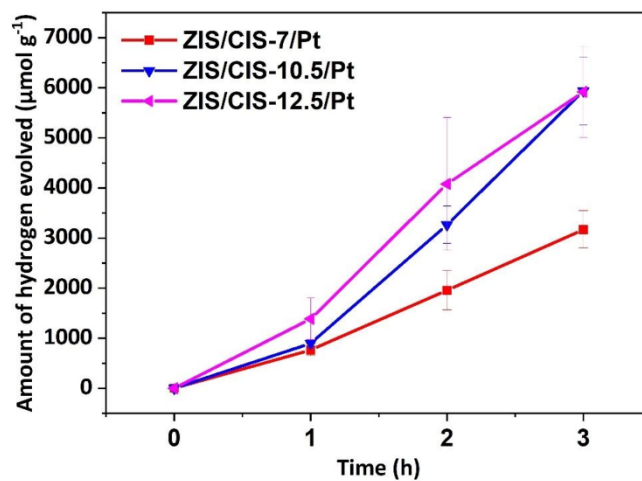


Fig. S7 Repetition experiments for evolved hydrogen with Pt deposition from selected three samples ZIS/CIS-7/Pt, ZIS/CIS-10.5/Pt and ZIS/CIS-12.5/Pt

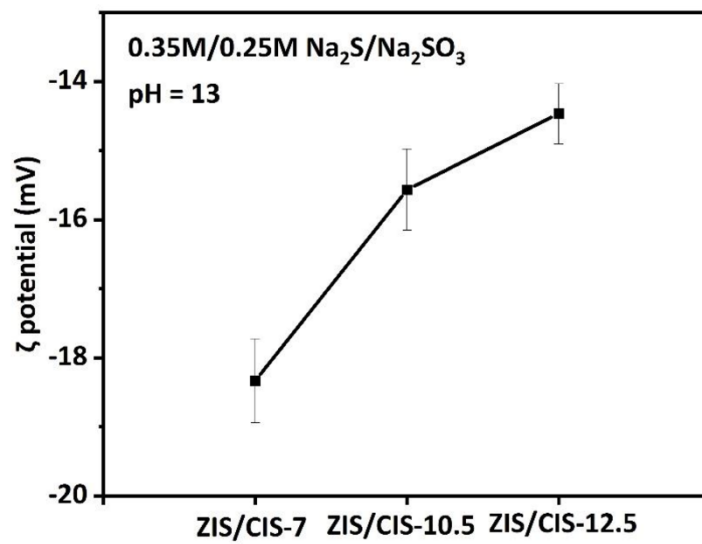


Fig. S8 ζ potential of the selected ZIS/CIS-7, 10.5 and 12.5 samples in photocatalytic hydrogen evolution solution



Table S1 The elements content at the surface layer of bare ZnIn<sub>2</sub>S<sub>4</sub> (ZIS) and ZIS composites decorated by CuInS<sub>2</sub> (CIS) after

Elements' content (at. %)									
Sample label	Zn	Cu	In	S	C	Pt	O	C/(Zn+In+S)	O/Pt
ZIS	6.11	0	14.65	32.57	45.79	0	0.88	0.86	0
ZIS/CIS-7/Pt	8.42	0.51	12.44	33.01	42.38	0.21	3.03	0.79	14.4
ZIS/CIS-10.5/Pt	9.50	0.55	13.70	36.43	31.63	0.26	7.94	0.53	30.5
ZIS/CIS-12.5/Pt	8.58	0.40	12.43	31.57	44.39	0.18	2.46	0.84	13.7

## Capping ligand initiated CuInS<sub>2</sub> quantum dots decoration on ZnIn<sub>2</sub>S<sub>4</sub> microspheres surface under different alkalinity levels resulting in different hydrogen evolution performance

Onur Cavdar <sup>a</sup>, Anna Malankowska <sup>a,\*</sup>, Justyna Łuczak <sup>b</sup>, Andrzej Żak <sup>c</sup>, Wojciech Lisowski <sup>d</sup>,  
Tomasz Klimeczuk <sup>e,f</sup>, Adriana Zaleska-Medynska <sup>a</sup>

<sup>a</sup> Department of Environmental Technology, Faculty of Chemistry, University of Gdansk, Gdansk, Poland

<sup>b</sup> Department of Process Engineering and Chemical Technology, Faculty of Chemistry, Gdansk University of Technology, Gdansk, Poland.

<sup>c</sup> Electron Microscopy Laboratory, Faculty of Mechanical Engineering, Wrocław University of Science and Technology, Gdansk, Poland

<sup>d</sup> Institute of Physical Chemistry, Polish Academy of Science, Warsaw, Poland

<sup>e</sup> Faculty of Applied Physics and Mathematics, Gdansk University of Technology, Narutowicza, Gdansk, Poland

<sup>f</sup> Advanced Materials Center, Gdansk University of Technology, Narutowicza, Gdansk, Poland

### Supporting information

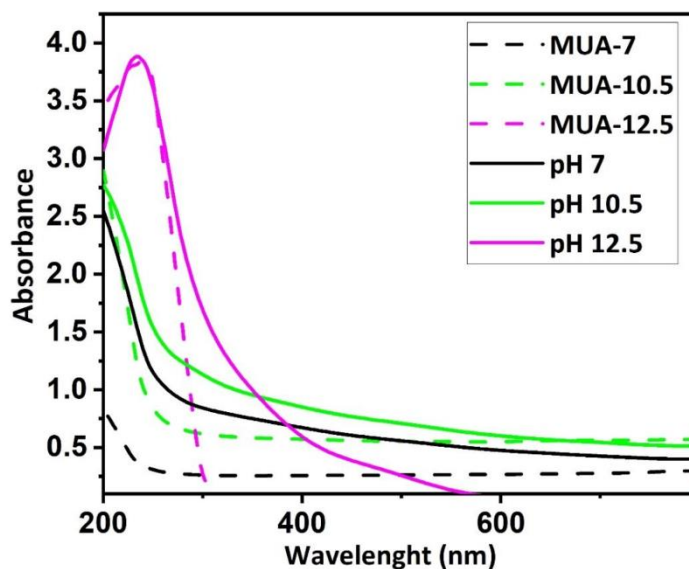


Fig. S1 The comparison of UV-vis absorption spectrum of MUA capped CIS and only MUA under pH = 7, 10.5 and 12.5. The dashed line represents UV-vis absorption spectrum of only MUA)

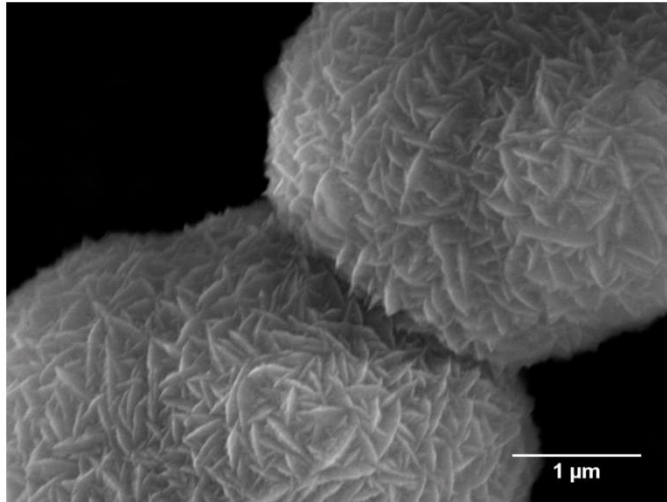


Fig. S2 SEM image of ZnIn<sub>2</sub>S<sub>4</sub> (ZIS)



**Fig. S3** Distinguishable color change of prepared ZIS/CIS-7, ZIS/CIS-10.5 and ZIS/CIS-12.5 samples from left to right

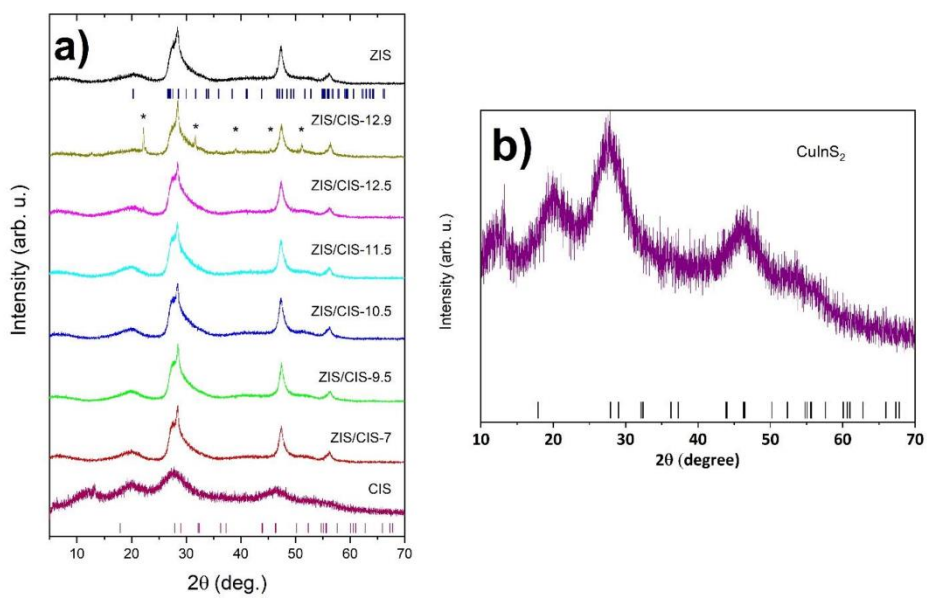


Fig. S4 XRD patterns of a) ZIS, ZIS/CIS and CIS samples and b) only CIS

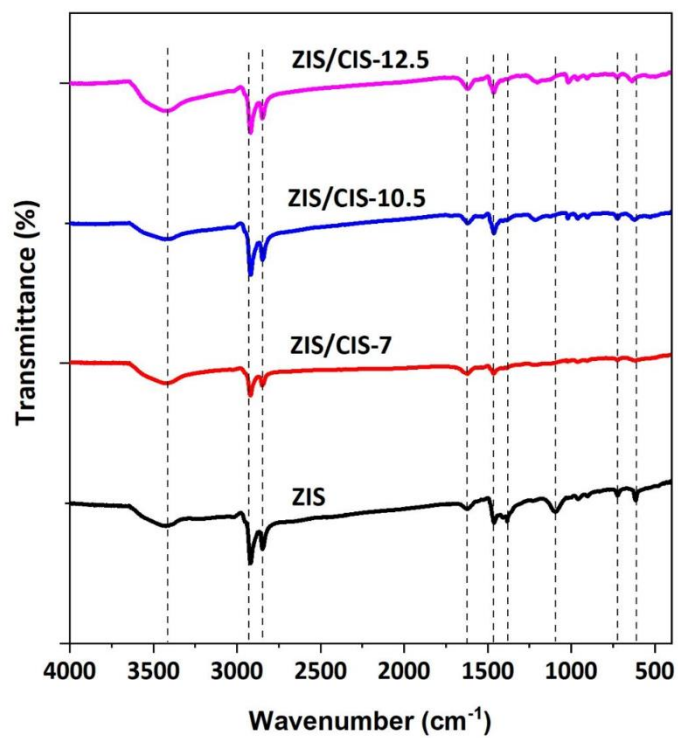


Fig. S5 FT-IR spectra of ZIS/CIS-7, 10.5 and 12.5

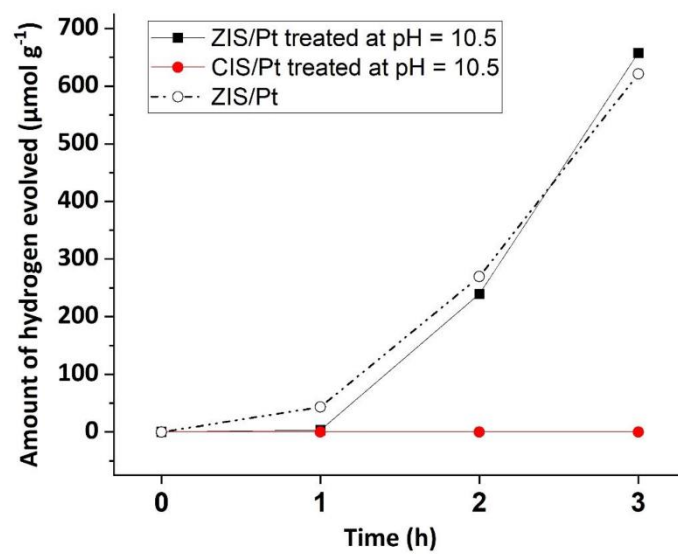


Fig. S6 Amount of evolved hydrogen with Pt deposition from ZIS and CIS treated under pH 10.5. Dashed line represents the data from ZIS/Pt without any treatment as a comparison

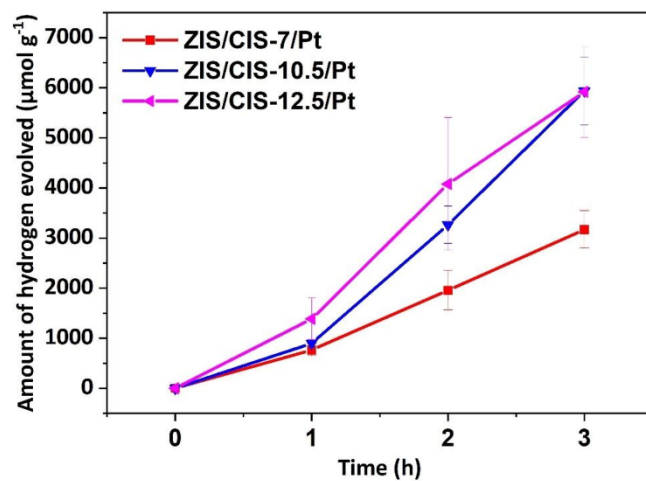


Fig. S7 Repetition experiments for evolved hydrogen with Pt deposition from selected three samples ZIS/CIS-7/Pt, ZIS/CIS-10.5/Pt and ZIS/CIS-12.5/Pt



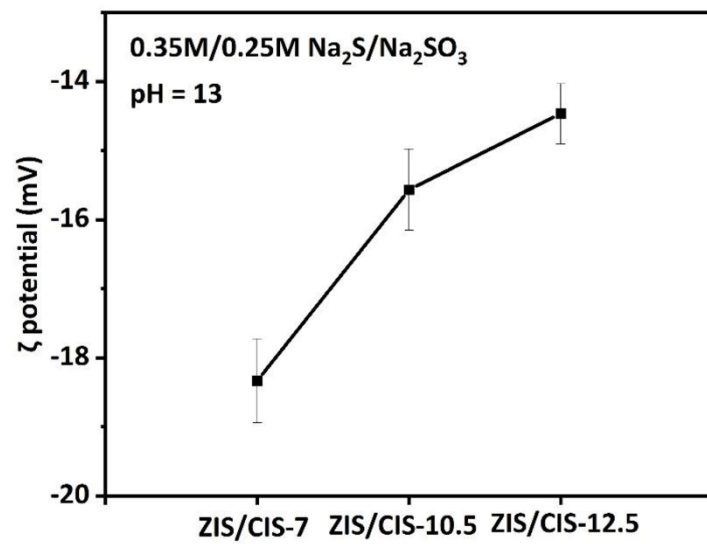


Fig. S8 ζ potential of the selected ZIS/CIS-7, 10.5 and 12.5 samples in photocatalytic hydrogen evolution solution

Table S1 The elements content at the surface layer of bare ZnIn<sub>2</sub>S<sub>4</sub> (ZIS) and ZIS composites decorated by CuInS<sub>2</sub> (CIS) after

Elements' content (at. %)									
Sample label	Zn	Cu	In	S	C	Pt	O	C/(Zn+In+S)	O/Pt
ZIS	6.11	0	14.65	32.57	45.79	0	0.88	0.86	0
ZIS/CIS-7/Pt	8.42	0.51	12.44	33.01	42.38	0.21	3.03	0.79	14.4
ZIS/CIS-10.5/Pt	9.50	0.55	13.70	36.43	31.63	0.26	7.94	0.53	30.5
ZIS/CIS-12.5/Pt	8.58	0.40	12.43	31.57	44.39	0.18	2.46	0.84	13.7

---

---

**P3. Photocatalytic hydrogen evolution from glycerol-water mixture under visible light over zinc indium sulfide ( $\text{ZnIn}_2\text{S}_4$ ) nanosheets grown on bismuth oxychloride ( $\text{BiOCl}$ ) microplates**

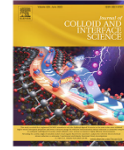
---

---



Contents lists available at ScienceDirect

Journal of Colloid and Interface Science

journal homepage: [www.elsevier.com/locate/jcis](http://www.elsevier.com/locate/jcis)

## Photocatalytic hydrogen evolution from glycerol-water mixture under visible light over zinc indium sulfide ( $\text{ZnIn}_2\text{S}_4$ ) nanosheets grown on bismuth oxychloride ( $\text{BiOCl}$ ) microplates



Onur Cavdar<sup>a,\*</sup>, Mateusz Baluk<sup>a</sup>, Anna Malankowska<sup>a</sup>, Andrzej Żak<sup>b</sup>, Wojciech Lisowski<sup>c</sup>, Tomasz Klimczuk<sup>d,e</sup>, Adriana Zaleska-Medynska<sup>a</sup>

<sup>a</sup> Department of Environmental Technology, Faculty of Chemistry, University of Gdansk, Gdansk, Poland

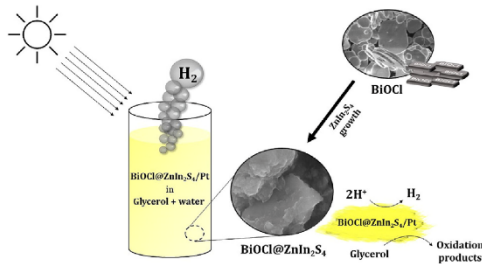
<sup>b</sup> Electron Microscopy Laboratory, Faculty of Mechanical Engineering, Wrocław University of Science and Technology, Gdansk, Poland

<sup>c</sup> Institute of Physical Chemistry, Polish Academy of Science, Warsaw, Poland

<sup>d</sup> Faculty of Applied Physics and Mathematics, Gdansk University of Technology, Narutowicza, Gdansk, Poland

<sup>e</sup> Advanced Materials Center, Gdansk University of Technology, Narutowicza, Gdansk, Poland

### GRAPHICAL ABSTRACT



### ARTICLE INFO

Article history:  
Received 3 November 2022  
Revised 26 January 2023  
Accepted 25 February 2023  
Available online 2 March 2023

Keywords:  
Photocatalysis  
Photocatalytic hydrogen evolution  
Photocatalytic glycerol reforming  
Z-scheme  
 $\text{ZnIn}_2\text{S}_4$   
 $\text{BiOCl}$

### ABSTRACT

$\text{ZnIn}_2\text{S}_4$  (ZIS) is one of the widely studied photocatalyst for photocatalytic hydrogen evolution applications due to its prominent visible light response and strong reduction ability. However, its photocatalytic glycerol reforming performance for hydrogen evolution has never been reported. Herein, the visible light driven  $\text{BiOCl}@ZnIn_2\text{S}_4$  ( $\text{BiOCl}@ZIS$ ) composite was synthesized by growth of ZIS nanosheets on a template-like hydrothermally pre-prepared wide-band-gap  $\text{BiOCl}$  microplates using simple oil-bath method to be used for the first time for photocatalytic glycerol reforming for photocatalytic hydrogen evolution (PHE) under visible light irradiation ( $\lambda > 420 \text{ nm}$ ). The optimum amount of  $\text{BiOCl}$  microplates in the composite was found 4 wt% (4%  $\text{BiOCl}@ZIS$ ) in the presence of in-situ 1 wt% Pt deposition. Then, the in-situ Pt photodeposition optimization studies over 4%  $\text{BiOCl}@ZIS$  composite showed the highest PHE rate of  $674 \mu\text{mol g}^{-1}\text{h}^{-1}$  with the ultra-low platinum amount (0.0625 wt%). The possible mechanisms behind this improvement can be ascribed to the formation of  $\text{Bi}_2\text{S}_3$  low-band-gap semiconductor during  $\text{BiOCl}@ZIS$  composite synthesis resulting in Z-scheme charge transfer mechanism between ZIS and  $\text{Bi}_2\text{S}_3$  upon visible light irradiation. This work expresses not only the photocatalytic glycerol reforming over ZIS photocatalyst but also a solid proof of the contribution of wide-band-gap  $\text{BiOCl}$  photocatalysts to enhancement of ZIS PHE performance under visible light.

© 2023 Elsevier Inc. All rights reserved.

\* Corresponding author.  
E-mail address: [onur.cavdar@phdstud.ug.edu.pl](mailto:onur.cavdar@phdstud.ug.edu.pl) (O. Cavdar).

<https://doi.org/10.1016/j.jcis.2023.02.129>  
0021-9797/© 2023 Elsevier Inc. All rights reserved.

## 1. Introduction

Glycerol is the major byproduct of biodiesel production, and its utilization methods for hydrogen production have been widely investigated topic [1–3]. The most common methods for overall glycerol reforming, such as steam reforming, autothermal reforming, supercritical water reforming, partial oxidation reforming, liquid phase reforming and gasification require temperature in the range of 300–900 °C [1]. On the other hand, photocatalytic glycerol reforming enables the glycerol reforming process under ambient conditions thus relatively lower energy input is expected for photocatalytic hydrogen evolution (PHE) [4]. For this purpose, TiO<sub>2</sub>, as one of the most studied semiconductors in PHE applications [5], was studied by many groups for glycerol photoreforming [6–10]. Despite its thermodynamically suitable band alignment for PHE, the implementation of PHE from glycerol using TiO<sub>2</sub> is challenging under visible light spectrum due to its large band gap. Photogenerated charge carriers over TiO<sub>2</sub> can be produced only via UV irradiation with wavelengths shorter than 400 nm that makes 3–5% of solar light harvestable to proceed chemical reactions [11,12]. Accordingly, visible light harvesting photocatalysts design is crucial step towards sustainable PHE from glycerol reforming. To achieve this goal, various approaches have been explored from modification of TiO<sub>2</sub> such as non-metal doping [13,14] and noble metal doping [15] or loading [9,16–19] to design of other metal oxide photocatalysts beyond TiO<sub>2</sub> including Bi<sub>2</sub>WO<sub>6</sub> [20,21], Fe<sub>2</sub>O<sub>3</sub> [22], ZnO [23], WO<sub>3</sub> [24]. Another remarkable alternative to metal oxides is metal sulfide photocatalysts as their more responsive nature to visible light and relatively higher conduction band position [25,26]. However, reports on photocatalytic glycerol reforming for hydrogen production from metal sulfide based photocatalysts are very limited. ZnO@ZnS–Bi<sub>2</sub>S<sub>3</sub> core–shell nanorod grown on reduced graphene oxide [27], Cd-doped SnO<sub>2</sub>/CdS heterostructures [28], ZnO/ZnS heterostructured nanorods [29], hexagonal CdS [30], ZnO–ZnS/graphene photocatalysts [31] and hybrid Pt–CdS–TiO<sub>2</sub> [32] have been reported so far. Interestingly, IIB–IIIA–VIA sulfide semiconductor, ZIS has been never reported for glycerol reforming despite its nontoxicity, easy preparation method, uncomplicated modification and coupling methods with other semiconductors to develop better photocatalytic systems [33–36]. To the best of our knowledge, only glucose photoreforming from ZIS was investigated for PHE by Liu et al. [37].

Recently, using 2D layered wide-band-gap photocatalyst BiOCl as a template for ZIS growth has gained attention to develop novel heterostructure for N<sub>2</sub> fixation [38], Cr(VI) reduction [39], rhodamine B [40] and antibiotics degradation such as tetracycline, ciprofloxacin and oxytetracycline [41]. Hence, the aim of this work was to study ZIS growth on BiOCl microplates surface creating visible light driven BiOCl@ZIS composite seeking to overcome obstacle of recombination in single ZIS to improve its photocatalytic performance [38] for PHE from glycerol–water mixture under visible light ( $\lambda > 420$  nm) for the first time. The amount of BiOCl microplates in BiOCl@ZIS composite was optimized for the best PHE performance in the presence of 1 wt% Pt deposition. Over the optimized BiOCl@ZIS composite, the effect of the type of Pt precursor (Pt<sup>2+</sup> and Pt<sup>4+</sup>) and then the amount of the Pt deposition on PHE have been assessed. Our results can be an important contribution for designing of efficient photocatalysts based on BiOCl@ZIS for the green energy production using visible light irradiation.

## 2. Experimental

### 2.1. Materials

Indium (III) acetate (In(Ac)<sub>3</sub>, 99.99%) (Acros Organics), thioacetamide (99.99%) (Chemat), bismuth nitrate pentahydrate (Bi(NO<sub>3</sub>)<sub>3</sub>·5H<sub>2</sub>O, 99.99%) (STANLAB), zinc chloride (ZnCl<sub>2</sub>, 98%) (EURO-CHEM BGD), potassium chloride (KCl, 99.5%) (STANLAB), potassium tetrachloroplatinate (II) (K<sub>2</sub>PtCl<sub>4</sub>, 99.9%) (Alfa Aesar), hydrogen hexachloroplatinate (IV) hexahydrate (H<sub>2</sub>PtCl<sub>6</sub>·6H<sub>2</sub>O 99.99%) (Sigma-Aldrich), methyl viologen dichloride hydrate (98%) (Sigma-Aldrich), glycerol (99.5%) (STANLAB). All chemicals were used without any further purification.

### 2.2. Preparation of BiOCl microplates

2 mmol KCl and 2 mmol Bi(NO<sub>3</sub>)<sub>3</sub>·5H<sub>2</sub>O were mixed in 30 ml water for 1 h. Later, mixture was transferred to the autoclave with 50 ml volume and treated for 24 h at 160 °C [42]. The product was cleaned with water and isopropanol using a centrifugation and dried at 60 °C for 24 h.

### 2.3. Preparation of BiOCl@ZIS composite

Different amounts of pre-prepared BiOCl (12.5, 25 and 50 mg) were dispersed in 60 ml DI water with pH 2.5 (adjusted with 0.1 M H<sub>2</sub>SO<sub>4</sub>) and sonicated about 5 min. Later, a certain amount of ZIS precursors, 272 mg of ZnCl<sub>2</sub>, 602 mg of In(Ac)<sub>3</sub> and 300 mg of thioacetamide were dissolved in BiOCl dispersion. After 5 min sonication, the mixture was transferred to a 100 ml three-necked round-bottom flask with a condenser placed in an oil bath and treated at 80 °C for 2 h under magnetic stirring [43]. The products were cleaned with water and isopropanol using a centrifugation and dried at 60 °C for 24 h. The amount of BiOCl added were equivalent to theoretical mass ratio of BiOCl 2%, 4% and 8% in BiOCl@ZIS composites which were abbreviated 2% BiOCl@ZIS, 4% BiOCl@ZIS, 8% BiOCl@ZIS, respectively. Pristine ZIS was prepared as mentioned above without the addition of BiOCl. The schematic representation of the synthesis route can be seen in Fig. 1.

### 2.4. Characterization

The crystalline structure was determined with X-ray diffraction (XRD) technique. Powder X-ray diffraction experiments were conducted at 20 °C on powdered samples with a Bruker D8

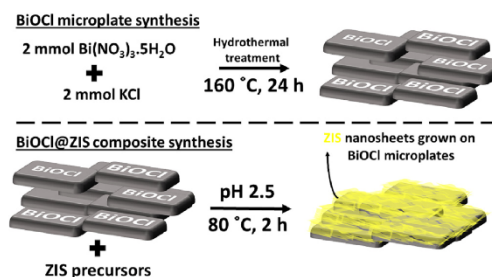


Fig. 1. Schematic representation of the synthesis route for BiOCl@ZIS composite.

Focus diffractometer with Cu K $\alpha$  ( $\lambda = 1.54 \text{ \AA}$ ) radiation and a LynxEye XE-T detector. Data were collected from  $5^\circ$  to  $70^\circ$   $2\theta$  over a scan time of 30 min. LeBail refinement of the pXRD pattern was performed to determine the crystal structure type of the tested samples, using HighScore Plus ver. 3.0e software. The chemical composition of samples surface areas was analyzed by X-ray photoelectron spectroscopy (XPS) using a PHI 5000 VersaProbeTM spectrometer (ULVAC-PHI, Chigasaki, Japan) with monochromatic Al K $\alpha$  irradiation ( $h\nu = 1486.6 \text{ eV}$ ). The high-resolution (HR) XPS spectra were recorded with the hemispherical analyzer at the pass energy of 23.5 eV and the energy step size of 0.1 eV. The binding energy (BE) scale was referenced to the C 1s peak with BE = 284.8 eV. The morphology was observed using scanning electron microscope (SEM, JEOL JSM-7610F) and transmission electron microscope (TEM, Hitachi H-800 microscope, Hitachi High-Technologies) operating at 150 kV. The UV–vis spectra of samples were recorded using UV–vis spectrophotometer (Evolution 220, Thermo Scientific).

### 2.5. Photocatalytic hydrogen evolution tests

15 mg photocatalyst was dispersed in 10 ml 5% (v/v) glycerol: water mixture and sonicated for 3 min and all the mixture was transferred to a quartz made tube reactor with 12.5 ml volume and 1.5 mm thickness. Then a Pt precursor solution ( $\text{K}_2\text{PtCl}_4$  or  $\text{H}_2\text{PtCl}_6$ ) with calculated amounts dripped to the PHE mixture. After the reactor was sealed with a plastic septum,  $\text{N}_2$  purging with  $4 \text{ dm}^3/\text{h}$  flow rate was applied to the mixture in the reactor for 10 min in the dark. Finally, the mixture was irradiated by 1000 W Xenon lamp external light source (Quantum Design, LSH 602) equipped with a cut-off filter GG420 (Optel,  $\lambda > 420 \text{ nm}$ ). The temperature of the PHE reaction medium during all experiments was around  $40 \text{ }^\circ\text{C}$  (the laboratory temperature was kept always around  $17\text{--}18 \text{ }^\circ\text{C}$ ). The amount of hydrogen gas was monitored by adding 200  $\mu\text{l}$  of gas sample collected from the headspace of the photoreactor within every using an air-tight syringe (Hamilton) to the gas chromatograph (Thermo Scientific TRACE 1300-GC,  $\text{N}_2$  carrier). No hydrogen was evolved in the absence of photocatalyst under the same condition. The recycling performance tests were carried out under the same experimental conditions. The sample was collected using centrifugation and washed with deionized water and isopropanol. After drying the sample at  $60 \text{ }^\circ\text{C}$ , a fresh glycerol-water mixture was added to the centrifuge tube containing the sample and the PHE mixture with the sample was transferred to the reactor for the next cycle. Qualitative analysis of the liquid phase was conducted using GC–MS (Schimadzu, GCMS-QP2010 SE). The column (Schimadzu, 30 m, 0.25 mm ID, 0.5  $\mu\text{m}$  df) is connected to the ionization source. For this purpose, the derivatization [44] was made as follows: 2.5 ml liquid phase was mixed with 3.5 g  $\text{NaHSO}_4$  and 0.5 ml anhydrous ethanol and transferred to the vial for the autosampling (Schimadzu, AOC-6000). After 30 min incubation at  $80^\circ\text{C}$ , headspace was sampled and injected into GC–MS system.

### 3. Results and discussion

SEM images of BiOCl, ZIS and 4% BiOCl@ZIS demonstrating the morphology of the sample can be seen in Fig. 2. BiOCl microplates' diameter was estimated around  $1\text{--}5 \mu\text{m}$  (Fig. S1) and the thickness of  $100 \text{ nm}$  (Fig. 2a) while the pristine ZIS suffered from the aggregation but the nanosheet formation is observable (Fig. 2b). Apparently, BiOCl@ZIS composite synthesis was accomplished as the ZIS nanosheets grown on BiOCl is clear from Fig. 2c which was also confirmed by TEM images of the 4%BiOCl@ZIS composite (Fig. 2e). ZIS nanosheets formed overwhelmingly on BiOCl are visible with additional formation of clusters over the composite

located on BiOCl in the 4%BiOCl@ZIS composite (Fig. 2f and 2g) suggesting the  $\text{Bi}_2\text{S}_3$  formation during the composite synthesis which was detected by XPS analysis that will be discussed further.

Crystal structure of the samples were analyzed using XRD technique (Fig. 3). Diffraction peaks of the ZIS can be indexed to hexagonal ZIS structure (PDF No. 01–089–3962) [45,46] represented by pink bars while BiOCl microplates exhibited tetragonal structure with high crystallinity (PDF No. 00–006–0249) [42]. All obtained composites exhibited the diffraction patterns originated from the ZIS and BiOCl confirming that BiOCl structure was unchanged during the ZIS growth.

The chemical composition of samples surface region was investigated by XPS. The high-resolution (HR) XPS spectra recorded on ZIS, BiOCl and 4% BiOCl@ZIS identified all elements originated from these composites (Fig. 4). The Zn  $2p_{3/2}$ , In  $3d_{5/2}$ , S  $2p_{3/2}$  and S  $2s$  peaks (BE of 1021.9, 445.2, 161.8 and 226.1 eV, respectively,) confirm the oxidation states of  $\text{Zn}^{2+}$ ,  $\text{In}^{3+}$  and  $\text{S}^{2-}$  in ZIS heterostructures [47,48]. The Bi4f spectrum of BiOCl consists of two states, Bi(+3) and Bi(+3-x), representing by Bi  $4f_{7/2}$  signals at 159.5 and 157.6 eV, respectively [47,49], whereas the Bi 4f spectra recorded on BiOCl@ZIS samples show the main Bi  $4f_{7/2}$  signals shifted to lower BE (158.0–158.9 eV) what can indicate the Bi-S bond formation due to BiOCl interaction with ZIS material [50] indicating the existence of  $\text{Bi}_2\text{S}_3$ . The O 1s spectrum of the pristine BiOCl is characterized by the main oxygen peak at 530.3 eV [47,49] whereas the O 1s spectra recorded on all BiOCl@ZIS samples exhibit the main signal located at  $531.6 \pm 0.2 \text{ eV}$ , which indicates formation of –OH groups [47,51]. The Pt 4f spectra recorded on both 4%BiOCl@ZIS/0.0625 wt % Pt samples, used for PHE test, are overlapped with the In 4p signals. However, after deconvolution, the Pt  $4f_{7/2}$  signal at 71.1 eV was well identified. This peak can be assigned to metallic  $\text{Pt}^0$  surface species, but similar BE were also reported for Pt–CxHy and PtOx bonds [47]. The Pt 4f spectrum recorded on the sample after 16 h of PHE test (4% BiOCl@ZIS/0.0625 wt% Pt\_16h), exhibits in addition the small Pt  $4f_{7/2}$  signal at 75.2 eV, which can be assigned to  $\text{PtO}_2$  surface species [47]. It is important to note that the oxygen contents in the surface layer of 4%BiOCl@ZIS samples is close to that, detected for pre-prepared ZIS composite (Table S1) and becomes only slightly lower for samples after 4 and 16 h photocatalytic test (see the atomic ratios In/O in Table S1). Moreover, the atomic ratio In/Zn = 5.86 for pre-prepared ZIS is much higher than corresponding stoichiometric ratio of ZIS (In/Zn = 2) and increase for all 4%BiOCl@ZIS samples (In/Zn = 6.85–16.28, Table S.1). That indicates segregation of In and formation of  $\text{InO}_x$  or  $\text{In}(\text{OH})_x$  surface species. The presence of the last species is well supported by the O 1s spectra (Fig. 4).

DRS patterns of the samples indicating the BiOCl sample has absorption edge around 375 nm thus cannot be activated by visible light irradiation while 550 nm edge can be seen from ZIS (Fig. 5). Clearly all the composites' absorption edge shifted slightly to UV region (i.e. blueshift), showing that even the small amount of BiOCl content in the composites affected the optical property. This could be related the wide-band-gap nature of BiOCl prompting the blueshifted spectra which is similar to the previously reported ZIS/BiOCl photocatalytic system by Zou et al. [40]. Moreover, an elevation around 550 nm in the DRS line of 4%BiOCl@ZIS and 8% BiOCl@ZIS was observed that can be attributed to the formation of narrow bandgap  $\text{Bi}_2\text{S}_3$  semiconductor during the synthesis of the composite as was confirmed previously by XPS. This elevation was the highest in 8%BiOCl@ZIS in comparison to the 2%BiOCl@ZIS and 4%BiOCl@ZIS composites where the highest amount of BiOCl exists among all BiOCl@ZIS composites forming more  $\text{Bi}_2\text{S}_3$  content in the composite.

PHE performances of the composites under visible light ( $\lambda > 420 \text{ nm}$ ) have been assessed in the presence of 1 wt% Pt deposition (precursor:  $\text{K}_2\text{PtCl}_4$ ) to find the best performing composite (Fig. 6a). 4%BiOCl@ZIS/1 wt% Pt exhibited the best ( $1992.2 \mu\text{mol g}^{-1}$ ) among the all composites while 2%



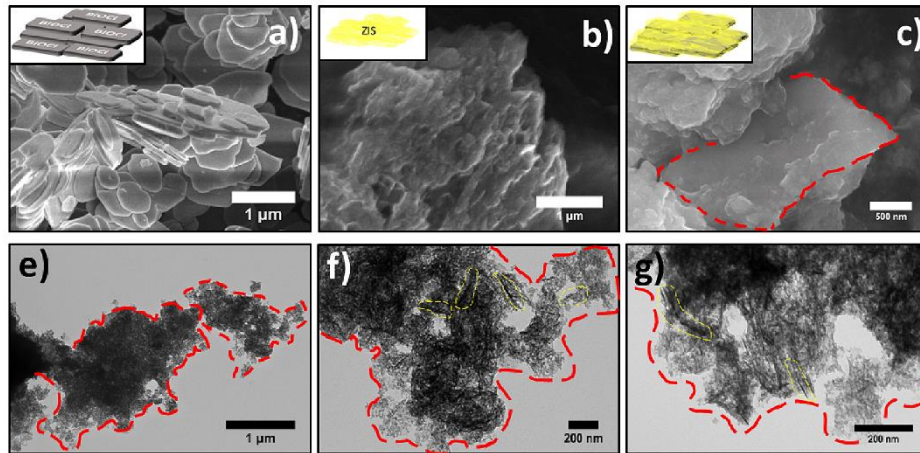


**Fig. 2.** SEM images of a) BiOCl microplates, b) ZIS nanosheets and c) 4% BiOCl@ZIS composite (inset: the schematic representation of BiOCl, ZIS and BiOCl@ZIS composite, respectively) and (e-g) TEM images of 4%BiOCl@ZIS. Red and yellow dashed lines microplates in c) and e-g) show BiOCl microplates and some of ZIS nanosheets in 4% BiOCl@ZIS composite, respectively. (For interpretation of the references to colour in this figure legend, the reader is referred to the web version of this article.)

BiOCl@ZIS/1 wt% Pt and 8%BiOCl@ZIS/1 wt% Pt produced  $1469.9 \mu\text{mol g}^{-1}$  and  $1179.6 \mu\text{mol g}^{-1}$ , respectively. However,

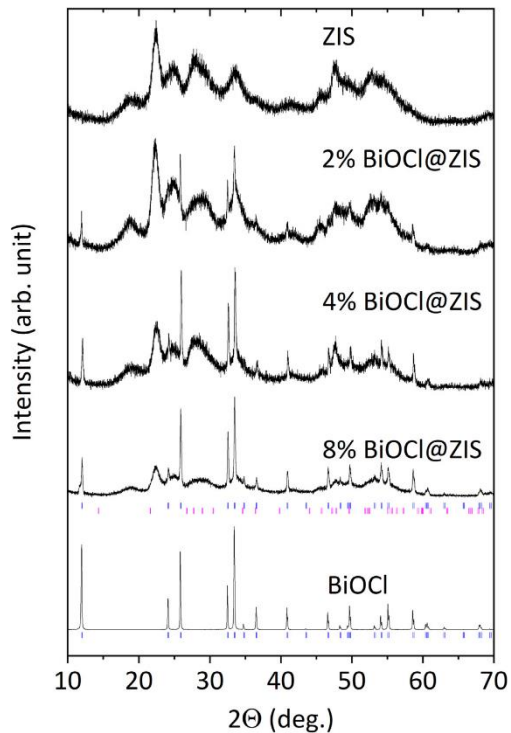


**Fig. 3.** XRD patterns of ZIS, BiOCl and BiOCl@ZIS composites in the range of 10–70.

the amount of hydrogen evolved from the ZIS/1 wt% Pt was close ( $1945.4 \mu\text{mol g}^{-1}$ ) to 4%BiOCl@ZIS/1 wt% Pt indicating that no considerable synergistic effect was achieved from this composite. The composites' PHE performances without any Pt deposition were compared as well and very close PHE performance was obtained from ZIS ( $260 \mu\text{mol g}^{-1}$ ) and 4%BiOCl@ZIS ( $165 \mu\text{mol g}^{-1}$ ) composites (Fig. S3). Nevertheless, the Pt amount was investigated from the 0.0625 wt% to 3 wt% over 4%BiOCl@ZIS composite (Fig. 6b). There was no notable change in PHE performance within the Pt amount, in the range from 0.5 wt% ( $2013.4 \mu\text{mol g}^{-1}$ ) to 2 wt% ( $2046.6 \mu\text{mol g}^{-1}$ ) over the composite while drastic decrease can be seen in 4%BiOCl@ZIS/3 wt% Pt ( $696.4 \mu\text{mol g}^{-1}$ ). Interestingly, lower Pt amount range, 0.0625 wt%, 0.125 wt% and 0.25 wt%, resulted in significant increase in the performance producing  $2696.8 \mu\text{mol g}^{-1}$ ,  $2502.5 \mu\text{mol g}^{-1}$  and  $2548.2 \mu\text{mol g}^{-1}$  hydrogen under visible light ( $\lambda > 420 \text{ nm}$ ), respectively. Yet again, whether the same effect of synergistic effect was achievable in the presence of the same amount of 0.0625 wt% Pt, PHE performance test of ZIS/0.0625 wt% Pt sample was evaluated (Fig. S2). Based on that, around 1.75-fold enhancement was observed from 4%BiOCl@ZIS 0.0625 wt% confirming the synergistic effect originating from the presence of BiOCl as a template for the ZIS growth. As a result, the best PHE rate was achieved with 4%BiOCl@ZIS/0.0625 wt% Pt sample around  $674 \mu\text{mol g}^{-1}\text{h}^{-1}$  then followed by around 1.3-fold drop as the lower in-situ deposited Pt amount from 0.5 wt% ( $503 \mu\text{mol g}^{-1}\text{h}^{-1}$ ), 1 wt% ( $498 \mu\text{mol g}^{-1}\text{h}^{-1}$ ) and 2 wt% ( $511 \mu\text{mol g}^{-1}\text{h}^{-1}$ ) and finally ending up with a sharp drop in 3 wt% ( $174 \mu\text{mol g}^{-1}\text{h}^{-1}$ ). Meanwhile, the highest PHE rate from in-situ deposited ZIS sample was detected from ZIS/0.25 wt% Pt ( $513 \mu\text{mol g}^{-1}\text{h}^{-1}$ ) and 0.0625 wt% Pt in-situ deposition was poor for the pristine ZIS as PHE rate was around  $384 \mu\text{mol g}^{-1}\text{h}^{-1}$  (Fig. 6c) under visible light irradiation. Lastly, as shown in Fig. 6e, the mean evolved hydrogen from the produced ZIS and 4%BiOCl@ZIS composites exhibited small standard errors under the same testing conditions, proving the good reproducibility.

Based on the above results, the performance of the 4% BiOCl@ZIS/0.0625 wt% Pt sample ( $674 \mu\text{mol g}^{-1}\text{h}^{-1}$ ) was remarkable comparing to the other reported metal-sulfide based photocatalytic systems in the literature for the photocatalytic glycerol

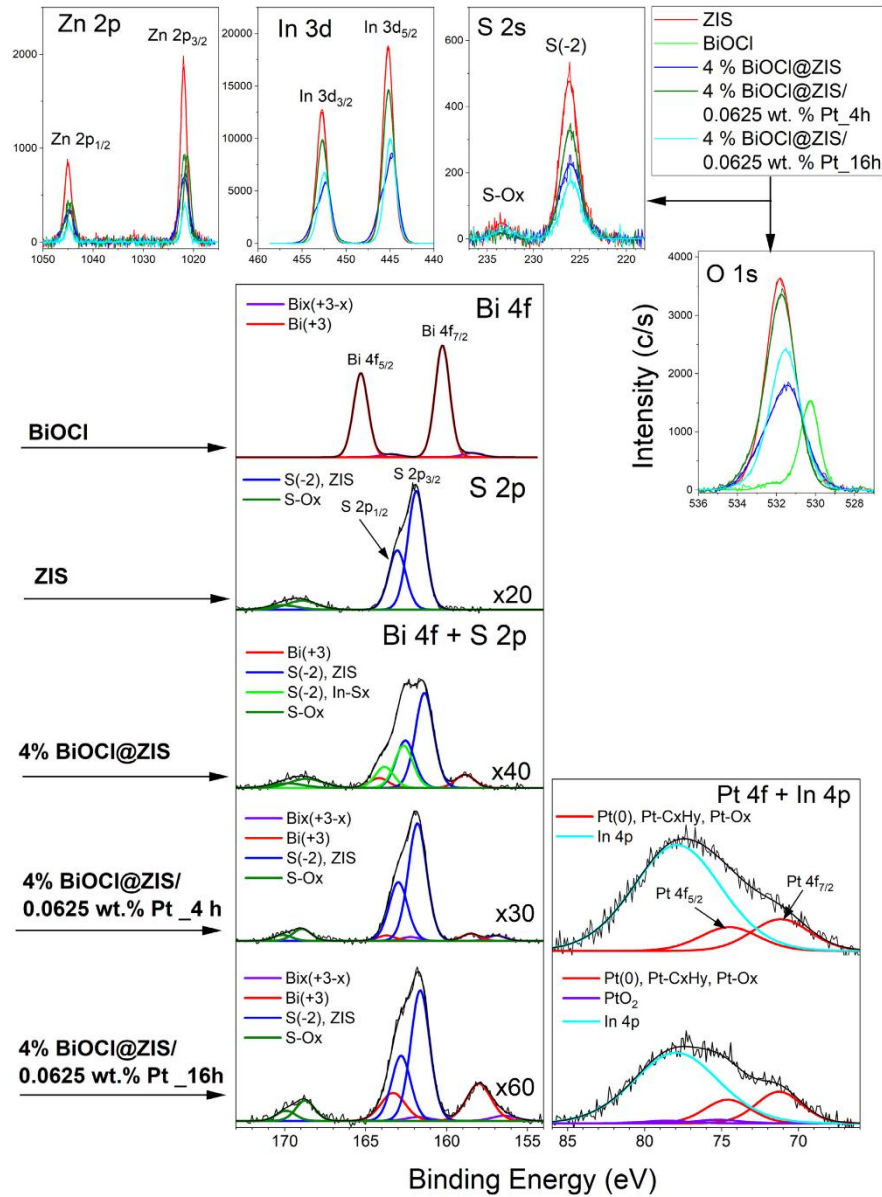


Fig. 4. XPS spectra of ZIS, BiOCl, 4% BiOCl@ZIS, 4% BiOCl@ZIS\_4h and 4% BiOCl@ZIS\_16h.

reforming for PHE especially taking into consideration the visible light induced ( $\lambda > 420$  nm) PHE (Table S2). This PHE performance might look poor and needs to be improved considering the noteworthy report by Wang et al. on noble metal free CdS-Ni photocatalytic system where PHE rate of  $74600 \mu\text{mol g}^{-1}\text{h}^{-1}$  was achieved under visible light ( $\lambda > 400$  nm) [52]. Also, it is worth to mention

that the amount of the glycerol percentages reported in the literature significantly vary from low (5% (v/v)) [27,29,53] to very high (90% (v/v)) [54]. In the view of this factor, our reported composite in this study exhibited the highest when it is compared to the 5% (v/v) glycerol concentration.



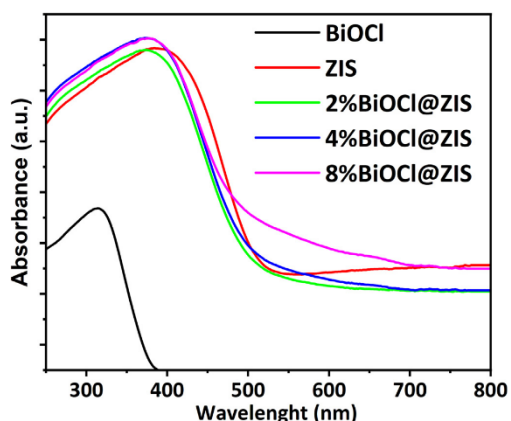


Fig. 5. UV-vis DRS of BiOCl, ZIS 2%BiOCl@ZIS, 4%BiOCl@ZIS and 8%BiOCl@ZIS samples.

The stability tests of the best performing composite, 4% BiOCl@ZIS in the presence of the optimum amount of 0.0625 wt% Pt in-situ deposition under visible light ( $\lambda > 420$  nm) was given in Fig. 6d. During 8 h continuous PHE test, two distinguishable slopes can be seen in the first cycle as a quick PHE kinetic was noticeable in the first 4 h later decelerating and almost stable at the end of 8 h. In the 2nd cycle, the rate dropped vastly around 4-fold ( $677 \mu\text{mol g}^{-1}$ ) and around same amount of hydrogen as in the 2nd cycle was evolved at the end of the 3rd cycle suggesting that 4%BiOCl@ZIS composite was not quite stable for photocatalytic glycerol reforming for hydrogen production as it is well accepted that metal sulfide photocatalysts suffer from photocorrosion effect [55]. However, to explore the reason behind the instability more, XPS, XRD and TEM analysis of 4% BiOCl@ZIS/ 0.0625 wt% Pt were performed. Although no significant change was observed in morphology and the crystal structure of the sample after 16 h of PHE test (Fig. S4) two emerging peaks were attributed to Bi  $4f_{7/2}$  and Bi  $4f_{5/2}$  in the XPS spectra of 4% BiOCl@ZIS/ 0.0625 wt% Pt sample after 16 h PHE test (4% BiOCl@ZIS/ 0.0625 wt% Pt\_16h) (Fig. 4) which corresponds to Bi<sup>(+3-x)</sup> imply the photoreduction of BiOCl [27]. However, this photoreduction should be induced by not the self-reduction of BiOCl but the photoexcited electrons over ZIS transferred to BiOCl as BiOCl is a wide-band-gap semiconductor. This has been proven by also the predicted band alignment of the two components of the composite. The photoreduction of BiOCl was thermodynamically suitable that was induced by the photoexcited electrons from the conduction band of ZIS to BiOCl as the conduction band level is located higher level than that of BiOCl (this will be discussed in detail further). Also, the acidification during the photocatalytic reaction from pH = 7 to 5 proving the intermediate formation during the photoreforming process that can be another factor influencing the stability of the photocatalytic system [56].

Moreover, insight into the mechanism was investigated by the qualitative analysis of the by-products arising from the photocatalytic reforming of the glycerol. GC chromatogram of PHE media before the photocatalytic test shows that there were no generation of by-products (Fig. S6). Only diethyl ether formation occurred due to the dehydration of ethanol through derivatization before the photocatalytic test. After 8 h of PHE test, the mass spectra analysis of 5 peaks arising from the GC chromatogram revealed that photoreforming of the glycerol leading to formation of by-products

such as acetaldehyde, propanal, formic acid, acrolein and acetic acid (Fig. S6). Therefore, it can be concluded that the involvement of the hole mediating mechanism generating H<sup>+</sup> ions to be reduced by the photogenerated electrons could be source of the hydrogen evolution [4,57].

Direct [58] and indirect [59] band gaps of ZIS ( $E_g \approx 2.20$  eV) and BiOCl ( $E_g \approx 3.35$  eV) were predicted using Tauc plot derived from the UV-vis absorption spectra of the samples (Fig. S5) while the valence band values were approximated from the XPS spectra ( $V_{\text{BiOCl}} \approx 1.3$  eV and  $V_{\text{BiOCl}} \approx 2.5$  eV) (Fig. S5). Thus, on the basis of the equation:  $E_{\text{CB}} = E_{\text{VB}} - E_g$  the conduction band level of the samples was estimated for ZIS and BiOCl around  $-0.90$  eV and  $-0.85$  eV, respectively [60,61]. Besides, thermodynamically suitable CB levels for PHE were further confirmed by methyl viologen ( $\text{MV}^{2+}$ ) reduction experiments [51,62] under monochromatic light irradiation over BiOCl, ZIS and 4%BiOCl@ZIS composites as all of them were able to reduce  $\text{MV}^{2+}$  to methyl viologen radical ( $\text{MV}^{\bullet+}$ ) in 5% (v/v) glycerol-water mixture with UV-vis spectra absorption peak appearing at 603 nm [51,62] (Fig. S7). Additionally, the comparison of reducing power between the ZIS and 4%BiOCl@ZIS can be seen, as the more methyl viologen radical was generated over 4%BiOCl@ZIS than that of ZIS which is accord with the PHE performance results (Fig. S6).

Considering all above, the photocatalytic mechanism under visible light can be proposed as follows (Fig. 7).

The photogenerated charge carriers produced only over ZIS since all experiments were conducted under visible light irradiation ( $\lambda > 420$  nm). However, the noteworthy effect of  $\text{Bi}_2\text{S}_3$  that was formed during BiOCl@ZIS synthesis cannot be ignored in the photocatalytic mechanism considering its proven existence by XPS where Bi-S bonds were revealed (Fig. 4) and similar reports on BiOCl@ZIS photocatalytic systems in the literature [38,39]. Thus, photoexcited electrons in the composite originating from ZIS follows two different paths. H<sup>+</sup> ions are reduced to hydrogen gas thanks to the presence of the Pt in-situ deposition forming simultaneously Pt nanoparticles (Route I). It is also worth to mention that the Pt oxidation state in the precursor was crucial. Pt<sup>4+</sup> oxidation state acted lesser active than Pt<sup>2+</sup> (Fig. S8), which was the reason why all the experiments were conducted with Pt<sup>2+</sup> precursor ( $\text{K}_2\text{PtCl}_4$ ) in this work. This might be related with more time required for the disassociation of Cl<sup>-</sup> from  $\text{H}_2\text{PtCl}_6$  than that of  $\text{K}_2\text{PtCl}_4$  that leads quicker formation of Pt nanoparticles [63] for the photocatalytic glycerol reforming. However, there was no morphological evidence of the presence of the Pt nanoparticles as the amount of Pt used was ultralow. In the meantime, the migration of the electrons to electron capturing BiOCl took place and reduced BiOCl in the composite (Route II). Meanwhile, the photogenerated electrons over  $\text{Bi}_2\text{S}_3$  surface migrated to the CB of ZIS via the Z-scheme mechanism that was previously reported by Chachvalvutikul et al. [64] and Li et al. [65]. On the contrary, the photogenerated holes from ZIS and  $\text{Bi}_2\text{S}_3$  caused the oxidation of the water molecule that generated the hydroxyl radical or self-reacted hydroxyl radicals producing hydrogen peroxide leading the formation of the byproducts and H<sup>+</sup> ions from glycerol to be reduced by the CB of ZIS to hydrogen fuel (Route III).

#### 4. Conclusion

The visible light driven BiOCl@ZIS composite was obtained successfully using a simple oil bath method for ZIS nanosheets growth on the template-like BiOCl microplates. 4%BiOCl@ZIS was chosen as a most promising among other composite for detailed Pt optimization study for photocatalytic glycerol reforming for PHE under visible light ( $\lambda > 420$  nm). 0.0625 wt% Pt in-situ deposition over 4% BiOCl@ZIS exhibited highest PHE rate ( $674 \mu\text{mol g}^{-1}\text{h}^{-1}$ ) that is

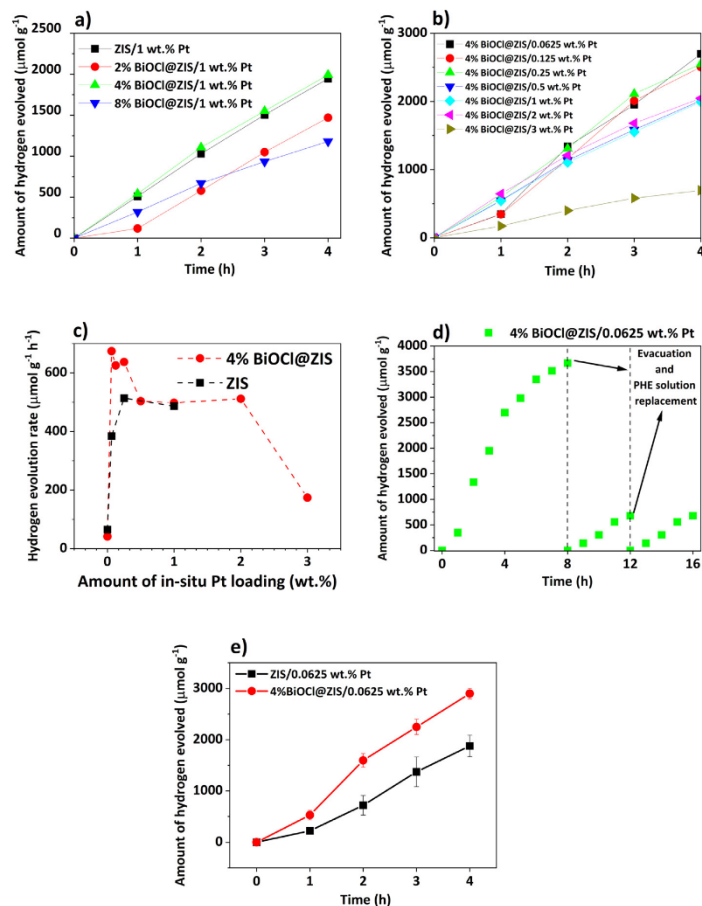


**Fig. 6.** A) amount of biocl optimization for the best phe performance in the presence of *in-situ* deposited 1 wt% Pt (precursor:  $\text{K}_2\text{PtCl}_4$ ) over ZIS, 2% BiOCl@ZIS/1 wt% Pt, 4% BiOCl@ZIS/1 wt% Pt, 8% BiOCl@ZIS/1 wt% Pt, b) Pt optimization test over 4%BiOCl@ZIS composite, c) comparison of PHE rate of 4%BiOCl@ZIS composite and ZIS with different amount of in-situ deposited Pt and d) stability tests for 4%BiOCl@ZIS/0.0625 wt% Pt under visible light ( $\lambda > 420 \text{ nm}$ ) and e) repetition of ZIS/0.0625 wt% Pt and 4%BiOCl@ZIS/0.0625 wt% Pt (The experimental error was estimated to be the standard deviation of three replicates).

around 1.75-fold higher than that of ZIS with the same amount of Pt ( $384 \mu\text{mol g}^{-1}\text{h}^{-1}$ ) which is a remarkable performance comparing other metal-sulfide based photocatalytic system for photocatalytic glycerol reforming in the literature (Table S2). The improved performance with ultra-low amount of Pt can be attributed to formation of low band gap  $\text{Bi}_2\text{S}_3$  semiconductor during the preparation of the BiOCl@ZIS composite promoting the effective charge separation through Z-scheme mechanism and the electron scavenging effect of BiOCl capturing photoexcited electrons from ZIS and inhibiting the recombination rate over ZIS. Moreover, owing to this simultaneous  $\text{Bi}_2\text{S}_3$  growth originated from the template-like BiOCl microplates, the strong interface contact between  $\text{Bi}_2\text{S}_3$  and ZIS was achievable which is considered as one of the determining factors for PHE activity of composites [66]. In comparison to the reported PHE performances from 5% (v/v) glycerol aqueous solution over other metal-sulfide based photocatalytic systems such as  $\text{ZnO}/\text{ZnS}-\text{PdS}$  [53] ( $238 \mu\text{mol g}^{-1}\text{h}^{-1}$ ),

$\text{ZnO}/\text{ZnS}-\text{Bi}_2\text{S}_3$  [27] ( $310 \mu\text{mol g}^{-1}\text{h}^{-1}$ ) and  $\text{ZnO}/\text{ZnS}$  [29] ( $384 \mu\text{mol g}^{-1}\text{h}^{-1}$ ), the sample 4%BiOCl@ZIS/0.0625 wt% Pt composite in our work showed the highest performance ( $674 \mu\text{mol g}^{-1}\text{h}^{-1}$ ) even under visible light. However, the photocatalytic system was not stable due to the several above-mentioned factors such as photocorrosion effect over ZIS, indirect BiOCl reduction and acidification of the PHE reaction conditions. Therefore, more research is required to focus on stability problem in that kind photocatalytic system.

In summary, our work paves the way toward designing BiOCl@ZIS composites photocatalyst for solar energy driven hydrogen production via photocatalytic glycerol reforming. The optimized 4% BiOCl@ZIS composite requires only 0.0625 wt% Pt cocatalyst loading for the boosted PHE performance which is highly effective way to lower the cost. Also, this study confirms the ZIS semiconductor photocatalyst as a remarkable candidate for photocatalytic glycerol reforming under visible light irradiation at neutral pH conditions.

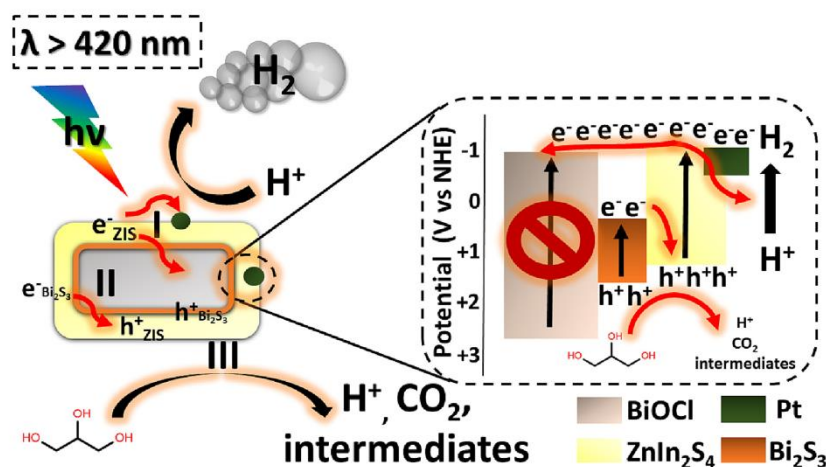


Fig. 7. The overall mechanism of PHE over BiOCl@ZIS/Pt composite under visible light irradiation.

#### CRedit authorship contribution statement

**Onur Cavdar:** Funding acquisition, Conceptualization, Methodology, Investigation, Validation, Visualization, Writing – original draft. **Mateusz Baluk:** Methodology, Investigation. **Anna Malankowska:** Conceptualization, Resources, Writing – review & editing. **Andrzej Zak:** Investigation. **Wojciech Lisowski:** Investigation, Writing – original draft. **Tomasz Klimczuk:** Investigation, Writing – original draft. **Adriana Zaleska-Medynska:** Resources, Writing – review & editing.

#### Data availability

Data will be made available on request.

#### Declaration of Competing Interest

The authors declare that they have no known competing financial interests or personal relationships that could have appeared to influence the work reported in this paper.

#### Acknowledgements

This work was financially supported by National Science Centre, Poland (Grant no. PRELUDIUM UMO-2018/31/N/ST5/00607).

#### Appendix A. Supplementary data

Supplementary data to this article can be found online at <https://doi.org/10.1016/j.jcis.2023.02.129>

#### References

- [1] C.A. Schwengber, H.J. Alves, R.A. Schaffner, F.A. Da Silva, R. Sequinel, V.R. Bach, R.J. Ferracin, Overview of glycerol reforming for hydrogen production, *Renew. Sustain. Energy Rev.* 58 (2016) 259–266, <https://doi.org/10.1016/j.rser.2015.12.279>.
- [2] P.D. Vaidya, A.E. Rodrigues, Glycerol reforming for hydrogen production: A review, *Chem. Eng. Technol.* 32 (2009) 1463–1469, <https://doi.org/10.1002/ceat.200900120>.
- [3] F. Qureshi, M. Yusuf, A.A. Pasha, H.W. Khan, B. Imteyaz, K. Irshad, Sustainable and energy efficient hydrogen production via glycerol reforming techniques: A review, *Int. J. Hydrogen Energy.* (2022), <https://doi.org/10.1016/j.ijhydene.2022.04.010>.
- [4] M.R. Karimi Estahbanati, M. Feilizadeh, F. Attar, M.C. Iliuta, Current developments and future trends in photocatalytic glycerol valorization: Process analysis, *React. Chem. Eng.* 6 (2021) 197–219, <https://doi.org/10.1039/d0re00382d>.
- [5] A. Ozawa, M. Yamamoto, T. Tanabe, T. Yoshida, TiO<sub>x</sub>N<sub>y</sub>/TiO<sub>2</sub> Photocatalyst for Hydrogen Evolution under Visible-Light Irradiation. I: Characterization of N in TiO<sub>x</sub>N<sub>y</sub>/TiO<sub>2</sub> Photocatalyst, *ACS Omega* 4 (2019) 20424–20429, <https://doi.org/10.1021/acsomega.9b02977>.
- [6] R. Liu, H. Yoshida, S. ichiro Fujita, M. Arai, Photocatalytic hydrogen production from glycerol and water with NiOx/TiO<sub>2</sub> catalysts, *Appl. Catal. B Environ.* 144 (2014) 47–45, <https://doi.org/10.1016/j.apcatb.2013.06.024>.
- [7] A. Petala, E. Ioannidou, A. Georgaka, K. Bourikas, D.I. Kondarides, Hysteresis phenomena and rate fluctuations under conditions of glycerol photo-reforming reaction over CuOx/TiO<sub>2</sub> catalysts, *Appl. Catal. B Environ.* 178 (2015) 201–209, <https://doi.org/10.1016/j.apcatb.2014.09.021>.
- [8] F.J. López-Tenllado, J. Hidalgo-Carrillo, V. Montes-Jiménez, E. Sánchez-López, F. J. Urbano, A. Marinas, Photocatalytic production of hydrogen from binary mixtures of C-3 alcohols on Pt/TiO<sub>2</sub>: Influence of alcohol structure, *Catal. Today.* 328 (2019) 2–7, <https://doi.org/10.1016/j.cattod.2018.10.001>.
- [9] N. Lakshmana Reddy, K.K. Cheralathan, V. Durga Kumari, B. Neppolian, S. Muthukonda Venkatakrishnan, Photocatalytic Reforming of Biomass Derived Crude Glycerol in Water: A Sustainable Approach for Improved Hydrogen Generation Using Ni(OH)<sub>2</sub> Decorated TiO<sub>2</sub> Nanotubes under Solar Light Irradiation, *ACS Sustain. Chem. Eng.* 6 (2018) 3754–3764, <https://doi.org/10.1021/acssuschemeng.7b04118>.
- [10] T.W.P. Seadira, C.M. Masuku, M.S. Scurrill, Solar photocatalytic glycerol reforming for hydrogen production over Ternary Cu/THS/graphene photocatalyst: Effect of Cu and graphene loading, *Renew. Energy.* 156 (2020) 84–97, <https://doi.org/10.1016/j.renene.2020.04.020>.
- [11] E. Kowalska, O.O.P. Mahaney, R. Abe, B. Ohtani, Visible-light-induced photocatalysis through surface plasmon excitation of gold on titania surfaces, *Phys. Chem. Chem. Phys.* 12 (2010) 2344–2355, <https://doi.org/10.1039/b917399d>.
- [12] B. Ohtani, Preparing Articles on Photocatalysis—Beyond the Illusions, Misconceptions, and Speculation, *Chem. Lett.* 37 (2008) 216–229, <https://doi.org/10.1246/cl.2008.216>.
- [13] J. Payormhorm, R. Idem, Synthesis of C-doped TiO<sub>2</sub> by sol-microwave method for photocatalytic conversion of glycerol to value-added chemicals under visible light, *Appl. Catal. A Gen.* 590 (2020) 117362, <https://doi.org/10.1016/j.apcata.2019.117362>.
- [14] D.A. Slamet, T. Agriyafani, M. Elysabeth, M. Ibadurrohman, Nurdin, Synthesis of Ni- and N-doped titania nanotube arrays for photocatalytic hydrogen production from glycerol–water solutions, *Catalysts.* 10 (2020) 1–17, <https://doi.org/10.3390/catal10111234>.
- [15] V. Kumaravel, S. Mathew, J. Bartlett, S.C. Pillai, Photocatalytic hydrogen production using metal doped TiO<sub>2</sub>: A review of recent advances, *Appl. Catal. B Environ.* 244 (2019) 1021–1064, <https://doi.org/10.1016/j.apcatb.2018.11.080>.
- [16] T.W.P. Seadira, G. Sadanandam, T. Ntho, C.M. Masuku, M.S. Scurrill, Preparation and characterization of metals supported on nanostructured TiO<sub>2</sub> hollow spheres for production of hydrogen via photocatalytic reforming of glycerol, *Appl. Catal. B Environ.* 222 (2018) 133–145, <https://doi.org/10.1016/j.apcatb.2017.09.072>.



- [17] K. Lalitha, G. Sadanandam, V.D. Kumari, M. Subrahmanyam, B. Sreedhar, N.Y. Hebalkar, Highly stabilized and finely dispersed Cu<sub>2</sub>O/TiO<sub>2</sub>: A promising visible sensitive photocatalyst for continuous production of hydrogen from glycerol: water mixtures, *J. Phys. Chem. C* 114 (2010) 22181–22189, <https://doi.org/10.1021/jp107405u>.
- [18] G. Sadanandam, D.K. Valluri, M.S. Scurrell, Highly stabilized Ag<sub>2</sub>O-loaded nano TiO<sub>2</sub> for hydrogen production from glycerol: Water mixtures under solar light irradiation, *Int. J. Hydrogen Energy* 42 (2017) 807–820, <https://doi.org/10.1016/j.ijhydene.2016.10.131>.
- [19] S. Mohan P, M.K. Purkait, C.T. Chang, Experimental evaluation of Pt/TiO<sub>2</sub>/rGO as an efficient HER catalyst via artificial photosynthesis under UVB & visible irradiation, *Int. J. Hydrogen Energy* 45 (2020) 17174–17190, <https://doi.org/10.1016/j.ijhydene.2020.04.072>.
- [20] J.Z. Marinho, L.L. Nascimento, A.L.R. Santos, A.M. Faria, A.E.H. Machado, A.O.T. Patrocínio, On the influence of hydrothermal treatment pH on the performance of Bi<sub>2</sub>WO<sub>6</sub> as photocatalyst in the glycerol photoreforming, *Photochem. Photobiol. Sci.* (2022), <https://doi.org/10.1007/s43630-022-00249-5>.
- [21] R.P. Panmand, Y.A. Sethi, S.R. Kadam, M.S. Tamboli, L.K. Nikam, J.D. Ambekar, C. J. Park, B.B. Kale, Self-assembled hierarchical nanostructures of Bi<sub>2</sub>WO<sub>6</sub> for hydrogen production and dye degradation under solar light, *CrystEngComm* 17 (2015) 107–115, <https://doi.org/10.1039/c4ce01968g>.
- [22] G. Carraro, C. MacCato, A. Gasparotto, T. Montini, S. Turner, O.I. Lebedev, V. Combari, G. Adami, G. Van Tendeloo, D. Barreca, P. Fornasiero, Enhanced hydrogen production by photoreforming of renewable oxygenates through nanostructured Fe<sub>2</sub>O<sub>3</sub> polymorphs, *Adv. Funct. Mater.* 24 (2014) 372–378, <https://doi.org/10.1002/adfm.201302043>.
- [23] V. Vaiano, G. Iervolino, Photocatalytic hydrogen production from glycerol aqueous solution using Cu-doped ZnO under visible light irradiation, *Appl. Sci.* 9 (2019), <https://doi.org/10.3390/app9132741>.
- [24] A. Tanaka, K. Hashimoto, H. Kominami, Visible-light-induced hydrogen and oxygen formation over Pt/Au/WO<sub>3</sub> photocatalyst utilizing two types of photoabsorption due to surface plasmon resonance and band-gap excitation, *J. Am. Chem. Soc.* 136 (2014) 586–589, <https://doi.org/10.1021/ja410230u>.
- [25] A. Kudo, Y. Miseki, Heterogeneous photocatalyst materials for water splitting, *Chem. Soc. Rev.* 38 (2009) 253–278, <https://doi.org/10.1039/b800489g>.
- [26] K. Zhang, L. Guo, Metal sulphide semiconductors for photocatalytic hydrogen production, *Catal. Sci. Technol.* 3 (2013) 1672–1690, <https://doi.org/10.1039/c3cy00018d>.
- [27] W. Xiaot, L. Rong, W. Kang, Synthesis of ZnO@ZnS-Bi<sub>2</sub>S<sub>3</sub> core-shell nanorod grown on reduced graphene oxide sheets and its enhanced photocatalytic performance, *J. Mater. Chem. A* 2 (2014) 8304–8313, <https://doi.org/10.1039/c4ta00696h>.
- [28] T.N.S. Trindade, L.A. Silva, Cd-doped SnO<sub>2</sub>/CdS heterostructures for efficient application in photocatalytic reforming of glycerol to produce hydrogen under visible light irradiation, *J. Alloys Compd.* 735 (2018) 400–408, <https://doi.org/10.1016/j.jallcom.2017.11.134>.
- [29] D. Bao, P. Gao, X. Zhu, S. Sun, Y. Wang, X. Li, Y. Chen, H. Zhou, Y. Wang, P. Yang, ZnO/ZnS Heterostructured Nanorod Arrays and Their Efficient Photocatalytic Hydrogen Evolution, *Chem. - Eur. J.* 21 (2015) 12728–12734, <https://doi.org/10.1002/chem.201501595>.
- [30] S.A.L. Bastos, P.A.L. Lopes, F.N. Santos, L.A. Silva, Experimental design as a tool to study the reaction parameters in hydrogen production from photoinduced reforming of glycerol over CdS photocatalyst, *Int. J. Hydrogen Energy* 39 (2014) 14588–14595, <https://doi.org/10.1016/j.ijhydene.2014.07.073>.
- [31] C.J. Chang, Y.G. Lin, H.T. Weng, Y.H. Wei, Photocatalytic hydrogen production from glycerol solution at room temperature by ZnO-ZnS/graphene photocatalysts, *Appl. Surf. Sci.* 451 (2018) 198–206, <https://doi.org/10.1016/j.apsusc.2018.05.004>.
- [32] M. De Oliveira Melo, L.A. Silva, Visible light-induced hydrogen production from glycerol aqueous solution on hybrid Pt-CdS-TiO<sub>2</sub> photocatalysts, *J. Photochem. Photobiol. A Chem.* 226 (2011) 36–41, <https://doi.org/10.1016/j.jphotochem.2011.10.012>.
- [33] J. Wang, S. Sun, R. Zhou, Y. Li, Z. He, H. Ding, D. Chen, W. Ao, A review: Synthesis, modification and photocatalytic applications of ZnIn<sub>2</sub>S<sub>4</sub>, *J. Mater. Sci. Technol.* 78 (2021) 1–19, <https://doi.org/10.1016/j.jmst.2020.09.045>.
- [34] G. Zhang, H. Wu, D. Chen, N. Li, Q. Xu, H. Li, J. He, J. Lu, A mini-review on ZnIn<sub>2</sub>S<sub>4</sub>-Based photocatalysts for energy and environmental application, *Green. Energy Environ.* 7 (2022) 176–204, <https://doi.org/10.1016/j.gee.2020.12.015>.
- [35] R. Janani, V. Raja Preethi, S. Singh, A. Rani, C.T. Chang, Hierarchical ternary sulfides as effective photocatalyst for hydrogen generation through water splitting: A review on the performance of znin<sub>2</sub>s<sub>4</sub>, *Catalysts* 11 (2021) 1–19, <https://doi.org/10.3390/catal11102077>.
- [36] Y. Song, J. Zhang, X. Dong, H. Li, A Review and Recent Developments in Full-Spectrum Photocatalysis using ZnIn<sub>2</sub>S<sub>4</sub>-Based Photocatalysts, *Energy Technol.* 9 (2021) 1–29, <https://doi.org/10.1002/ente.202100033>.
- [37] Y. Li, J. Wang, S. Peng, G. Lu, S. Li, Photocatalytic hydrogen generation in the presence of glucose over ZnS-coated ZnIn<sub>2</sub>S<sub>4</sub> under visible light irradiation, *Int. J. Hydrogen Energy* 35 (2010) 7116–7126, <https://doi.org/10.1016/j.ijhydene.2010.02.017>.
- [38] L. Guo, X. Han, K. Zhang, Y. Zhang, Q. Zhao, D. Wang, F. Fu, In-situ construction of 2D/2D znin<sub>2</sub>s<sub>4</sub>/BiOCl heterostructure with enhanced photocatalytic activity for N<sub>2</sub> fixation and phenol degradation, *Catalysts* 9 (2019), <https://doi.org/10.3390/catal9090729>.
- [39] J. Qiu, M. Li, J. Xu, X.-F. Zhang, J. Yao, Bismuth sulfide bridged hierarchical Bi<sub>2</sub>S<sub>3</sub>/BiOCl@ZnIn<sub>2</sub>S<sub>4</sub> for efficient photocatalytic Cr(VI) reduction, *J. Hazard. Mater.* 389 (2020) 121858, <https://doi.org/10.1016/j.jhazmat.2019.121858>.
- [40] P. Zou, G. Su, Z. Li, Y. Li, T. Zhou, Y. Kang, Oxalic acid modified hexagonal ZnIn<sub>2</sub>S<sub>4</sub> combined with bismuth oxychloride to fabricate a hierarchical dual Z-scheme heterojunction: Accelerating charge transfer to improve photocatalytic activity, *Colloids Surf. A Physicochem. Eng. Asp.* 633 (2022) 127835, <https://doi.org/10.1016/j.colsurfa.2021.127835>.
- [41] R. Jiang, D. Wu, G. Lu, Z. Yan, J. Liu, Modified 2D–2D ZnIn<sub>2</sub>S<sub>4</sub>/BiOCl van der Waals heterojunctions with CQDs: Accelerated charge transfer and enhanced photocatalytic activity under vis- and NIR-light, *Chemosphere* 227 (2019) 82–92, <https://doi.org/10.1016/j.chemosphere.2019.04.038>.
- [42] L. Zhang, W. Wang, S. Sun, D. Jiang, E. Gao, Selective transport of electron and hole among 001 and 110 facets of BiOCl for pure water splitting, *Appl. Catal. B Environ.* 162 (2015) 470–474, <https://doi.org/10.1016/j.apcatb.2014.07.024>.
- [43] B. Shao, J. Wang, Y. Zhang, X. Tan, W. Zhou, Y. Chen, T. Xie, T. Yu, Construction of a 3D/2D g-C<sub>3</sub>N<sub>4</sub>/ZnIn<sub>2</sub>S<sub>4</sub> hollow spherical heterostructure for efficient CO<sub>2</sub> photoreduction under visible light, *Catal. Sci. Technol.* 11 (2021) 1282–1291, <https://doi.org/10.1039/d0cy01890b>.
- [44] D. Zhou, Q. Hou, W. Liu, X. Ren, Rapid determination of formic and acetic acids in biomass hydrolysate by headspace gas chromatography, *J. Ind. Eng. Chem.* 47 (2017) 281–287, <https://doi.org/10.1016/j.jiec.2016.11.044>.
- [45] C. Li, H. Li, L. Han, C. Li, S. Zhang, Ionothermal/hydrothermal synthesis of the ternary metal chalcogenide ZnIn<sub>2</sub>S<sub>4</sub>, *Mater. Lett.* 65 (2011) 2537–2540, <https://doi.org/10.1016/j.matlet.2011.05.052>.
- [46] J. Chen, S.J. Wu, W.J. Cui, Y.H. Guo, T.W. Wang, Z.W. Yao, Y. Shi, H. Zhao, J. Liu, Z. Y. Hu, Y. Li, Nickel clusters accelerating hierarchical zinc indium sulfide nanoflowers for unprecedented visible-light hydrogen production, *J. Colloid Interface Sci.* 608 (2022) 504–512, <https://doi.org/10.1016/j.jcis.2021.09.156>.
- [47] A. V. Naumkin, A. Kraut-Vass, S. W. Gaarenrood, C. J. Powell, NIST X-ray Photoelectron Spectroscopy Database, NIST Standard Reference Database Number 20, Version 4.1, Natl. Inst. Stand. Technol. Gaithersburg, MD, 20899, (2012). 10.18434/T4T88K.
- [48] O. Cavdar, A. Malankowska, D. Amgar, P. Mazierski, J. Luczak, W. Lisowski, A. Zaleska-Medynska, Remarkable visible-light induced hydrogen generation with ZnIn<sub>2</sub>S<sub>4</sub> microspheres/CuInS<sub>2</sub> quantum dots photocatalytic system, *Int. J. Hydrogen Energy* 46 (2020) 486–498, <https://doi.org/10.1016/j.ijhydene.2020.09.212>.
- [49] S. Kang, R.C. Pawar, Y. Pyo, V. Khare, C.S. Lee, Size-controlled BiOCl–RGO composites having enhanced photodegradative properties, *J. Exp. Nanosci.* 11 (2016) 259–275, <https://doi.org/10.1080/17458080.2015.1047420>.
- [50] J. Zhou, G. Tian, Y. Chen, Y. Shi, C. Tian, K. Pan, H. Fu, Growth rate controlled synthesis of hierarchical Bi<sub>2</sub>S<sub>3</sub>/In<sub>2</sub>S<sub>3</sub> core/shell microspheres with enhanced photocatalytic activity, *Sci. Rep.* 4 (2014), <https://doi.org/10.1038/srep04027>.
- [51] O. Cavdar, A. Malankowska, J. Łuczak, A. Zak, W. Lisowski, T. Klimczuk, A. Zaleska-medynska, Capping ligand initiated CuInS<sub>2</sub> quantum dots decoration on ZnIn<sub>2</sub>S<sub>4</sub> microspheres surface under different alkalinity levels resulting in different hydrogen evolution performance, *652* (2022), <https://doi.org/10.1016/j.colsurfa.2022.129760>.
- [52] J.J. Wang, Z.J. Li, X.B. Li, X.B. Fan, Q.Y. Meng, S. Yu, C.B. Li, J.X. Li, C.H. Tung, L.Z. Wu, Photocatalytic hydrogen evolution from glycerol and water over nickel-hybrid cadmium sulfide quantum dots under visible-light irradiation, *ChemSusChem* 7 (2014) 1468–1475, <https://doi.org/10.1002/cssc.201400028>.
- [53] S. Liu, X. Wang, K. Wang, R. Lv, Y. Xu, ZnO/ZnS-PdS core/shell nanorods: Synthesis, characterization and application for photocatalytic hydrogen production from a glycerol/water solution, *Appl. Surf. Sci.* 283 (2013) 732–739, <https://doi.org/10.1016/j.apsusc.2013.07.009>.
- [54] Z. Zhang, M. Wang, H. Zhou, F. Wang, Surface Sulfate Ion on CdS Catalyst Enhances Syngas Generation from Biopolysols, *J. Am. Chem. Soc.* 143 (2021) 6533–6541, <https://doi.org/10.1021/jacs.1c00830>.
- [55] X. Guo, Y. Peng, G. Liu, G. Xie, Y. Guo, Y. Zhang, J. Yu, An Efficient ZnIn<sub>2</sub>S<sub>4</sub>@CuInS<sub>2</sub> Core-Shell p-n Heterojunction to Boost Visible-Light Photocatalytic Hydrogen Evolution, *J. Phys. Chem. C* 124 (2020) 5934–5943, <https://doi.org/10.1021/acs.jpcc.9b11623>.
- [56] X. Jiang, X. Fu, L. Zhang, S. Meng, S. Chen, Photocatalytic reforming of glycerol for H<sub>2</sub> evolution on Pt/TiO<sub>2</sub>: Fundamental understanding the effect of co-catalyst Pt and the Pt deposition route, *J. Mater. Chem. A* 3 (2015) 2271–2282, <https://doi.org/10.1039/c4ta06052k>.
- [57] M. Tahir, M. Siraj, B. Tahir, M. Umer, H. Alias, N. Othman, Au-NPs embedded Z-scheme WO<sub>3</sub>/TiO<sub>2</sub> nanocomposite for plasmon-assisted photocatalytic glycerol-water reforming towards enhanced H<sub>2</sub> evolution, *Appl. Surf. Sci.* 503 (2020) 144344, <https://doi.org/10.1016/j.apsusc.2019.144344>.
- [58] A. Sabbah, I. Shown, M. Qorbani, F.Y. Fu, T.Y. Lin, H.L. Wu, P.W. Chung, C.I. Wu, S.R.M. Santiago, J.L. Shen, K.H. Chen, L.C. Chen, Boosting photocatalytic CO<sub>2</sub> reduction in a ZnS/ZnIn<sub>2</sub>S<sub>4</sub> heterostructure through strain-induced direct Z-scheme and a mechanistic study of molecular CO<sub>2</sub> interaction thereon, *Nano Energy* 93 (2022) 106809, <https://doi.org/10.1016/j.nanoen.2021.106809>.
- [59] J. Lu, W. Zhou, X. Zhang, G. Xiang, Electronic Structures and Lattice Dynamics of Layered BiOCl Single Crystals, *J. Phys. Chem. Lett.* 11 (2020) 1038–1044, <https://doi.org/10.1021/acs.jpclett.9b03575>.
- [60] H. Zhao, X. Liu, Y. Dong, Y. Xia, H. Wang, A special synthesis of BiOCl photocatalyst for efficient pollutants removal: New insight into the band structure regulation and molecular oxygen activation, *Appl. Catal. B Environ.* 256 (2019) 117872, <https://doi.org/10.1016/j.apcatb.2019.117872>.
- [61] S. Zhang, L. Wang, C. Liu, J. Luo, J. Crittenden, X. Liu, T. Cai, J. Yuan, Y. Pei, Y. Liu, Photocatalytic wastewater purification with simultaneous hydrogen

- production using MoS<sub>2</sub> QD-decorated hierarchical assembly of ZnIn<sub>2</sub>S<sub>4</sub> on reduced graphene oxide photocatalyst, *Water Res.* 121 (2017) 11–19, <https://doi.org/10.1016/j.watres.2017.05.013>.
- [62] W. Chen, R.Q. Yan, J.Q. Zhu, G.B. Huang, Z. Chen, Highly efficient visible-light-driven photocatalytic hydrogen evolution by all-solid-state Z-scheme CdS/QDs/ZnIn<sub>2</sub>S<sub>4</sub> architectures with MoS<sub>2</sub> quantum dots as solid-state electron mediator, *Appl. Surf. Sci.* 504 (2020) 144406, <https://doi.org/10.1016/j.apsusc.2019.144406>.
- [63] K. Wenderich, G. Mul, Methods, Mechanism, and Applications of Photodeposition in Photocatalysis: A Review, *Chem. Rev.* 116 (2016) 14587–14619, <https://doi.org/10.1021/acs.chemrev.6b00327>.
- [64] A. Chachvalvutikul, W. Pudkon, T. Luangwanta, T. Thongtem, S. Thongtem, S. Kittiwachana, S. Kaowphong, Enhanced photocatalytic degradation of methylene blue by a direct Z-scheme Bi<sub>2</sub>S<sub>3</sub>/ZnIn<sub>2</sub>S<sub>4</sub> photocatalyst, *Mater. Res. Bull.* 111 (2019) 53–60, <https://doi.org/10.1016/j.materresbull.2018.10.034>.
- [65] J. Li, F. Meng, H. Wu, H. Zhang, Construction of Ag: ZnIn<sub>2</sub>S<sub>4</sub>/Bi<sub>2</sub>S<sub>3</sub> Z-scheme heterojunctions for boosting interfacial charge separation and photocatalytic degradation of TC, *Appl. Surf. Sci.* 605 (2022), <https://doi.org/10.1016/j.apsusc.2022.154763> 154763.
- [66] H. Zhu, Y. Yang, Y. Kang, P. Niu, X. Kang, Z. Yang, H. Ye, G. Liu, Strong interface contact between NaYF<sub>4</sub>:Yb, Er and CdS promoting photocatalytic hydrogen evolution of NaYF<sub>4</sub>:Yb, Er/CdS composites, *J. Mater. Sci. Technol.* 102 (2022) 1–7, <https://doi.org/10.1016/j.jmst.2021.05.069>.

## **Supplementary information for P3**

---

**Photocatalytic hydrogen evolution from glycerol-water mixture under visible light over zinc indium sulfide ( $ZnIn_2S_4$ ) nanosheets grown on bismuth oxychloride (BiOCl) microplates**

Onur Cavdar<sup>a,\*</sup>, Mateusz Baluk<sup>a</sup>, Anna Malankowska<sup>a</sup>, Andrzej Żak<sup>b</sup>,

Wojciech Lisowski<sup>c</sup>, Tomasz Klimczuk<sup>d,e</sup>, Adriana Zaleska-Medynska<sup>a</sup>

<sup>a</sup> Department of Environmental Technology, Faculty of Chemistry, University of Gdansk, Gdansk, Poland

<sup>b</sup> Electron Microscopy Laboratory, Faculty of Mechanical Engineering, Wrocław University of Science and Technology, Gdansk, Poland

<sup>c</sup> Institute of Physical Chemistry, Polish Academy of Science, Warsaw, Poland

<sup>d</sup> Faculty of Applied Physics and Mathematics, Gdansk University of Technology, Narutowicza, Gdansk, Poland

<sup>e</sup> Advanced Materials Center, Gdansk University of Technology, Narutowicza, Gdansk, Poland

\* Corresponding author. E-mail: [onur.cavdar@phdstud.ug.edu.pl](mailto:onur.cavdar@phdstud.ug.edu.pl) Tel: +48 58 523 52 21

**Supplementary information**

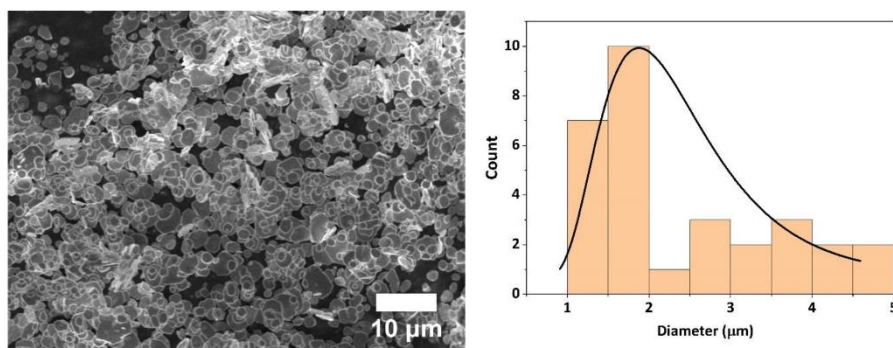


Fig. S1 SEM images of BiOCl microplates with the particle size distribution profile

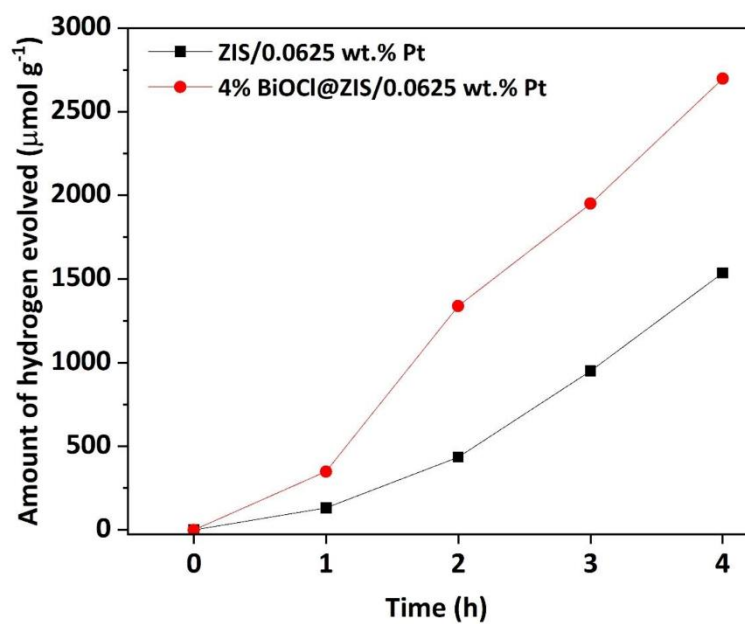


Fig. S2 Photocatalytic hydrogen evolution tests from ZIS/0.0625 wt.% and 4%BiOCl@ZIS/0.0625 wt.% Pt

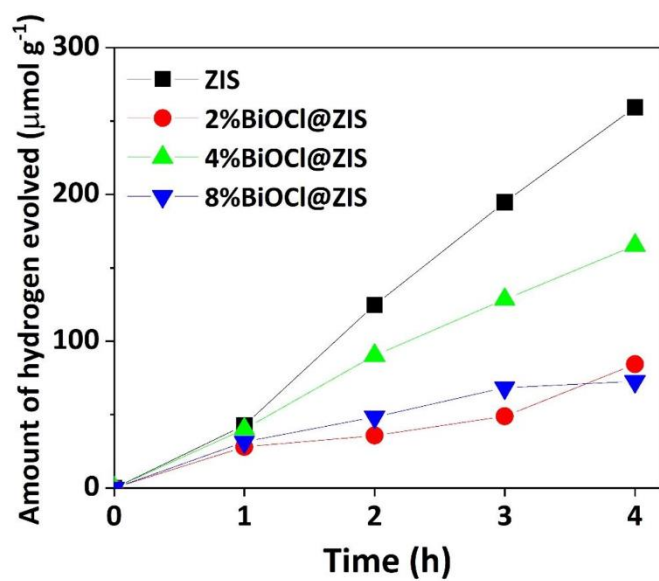
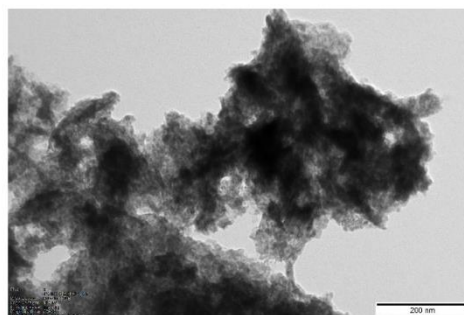
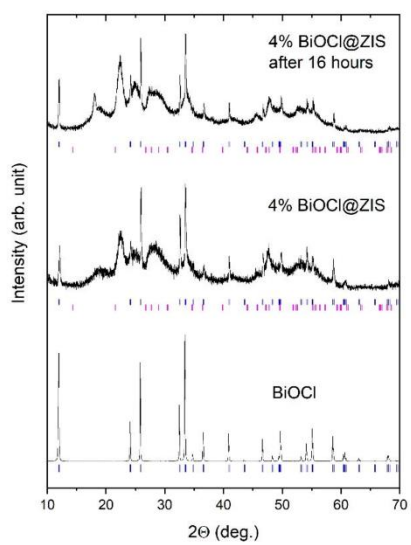


Fig. S3 Photocatalytic hydrogen evolution tests from ZIS, 2%BiOCl@ZIS, 4%BiOCl@ZIS and 8%BiOCl@ZIS without any Pt deposition





**Fig. S4** Left: Comparison of XRD patterns of 4%BiOCl@ZIS composite before and after 16 hours of photocatalytic test in the presence of 0.0625 wt.% in-situ Pt deposition. Right: TEM image of 4%BiOCl@ZIS/0.0625 wt.% Pt after 16 h

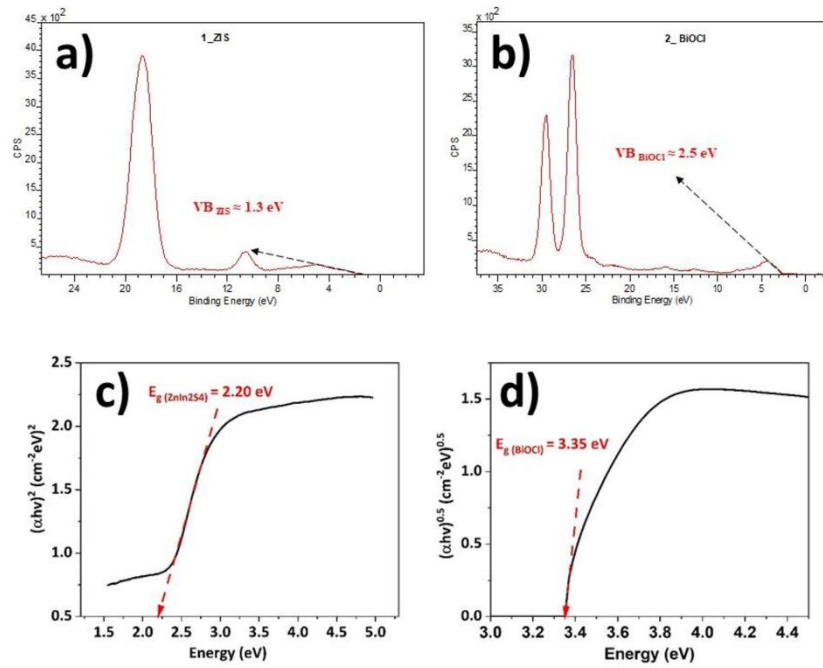
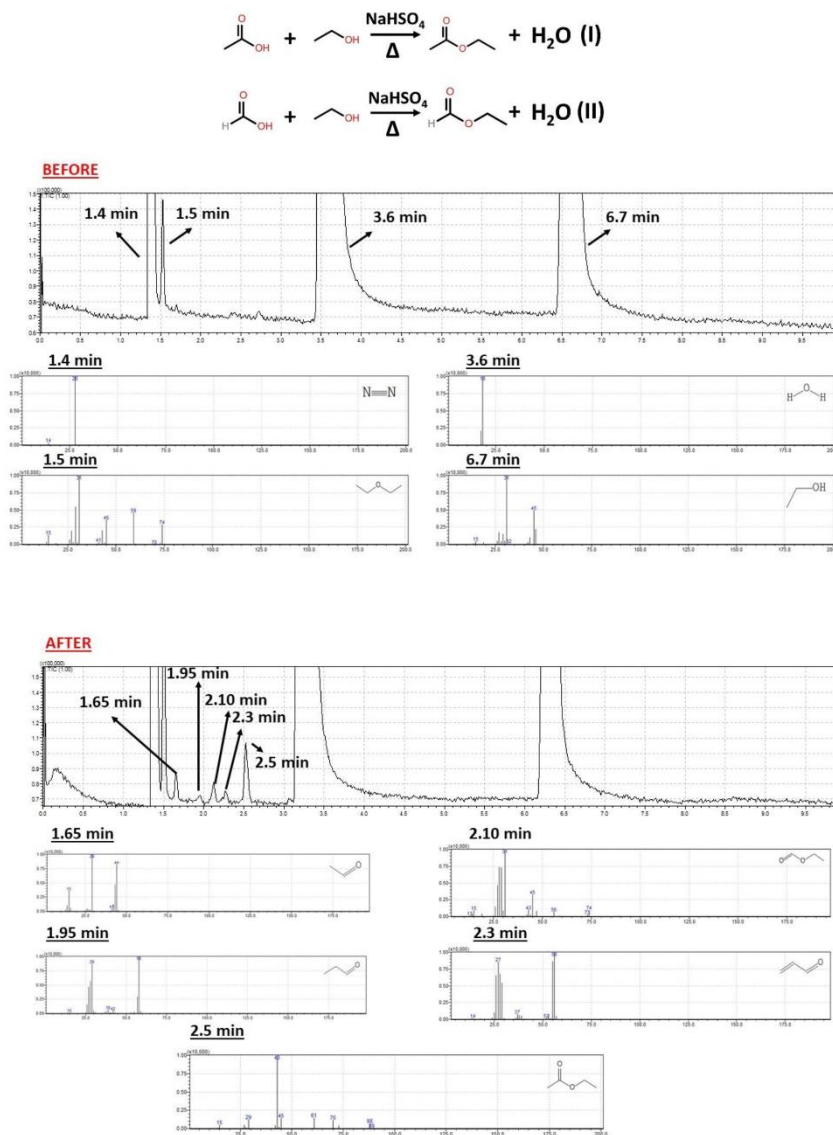
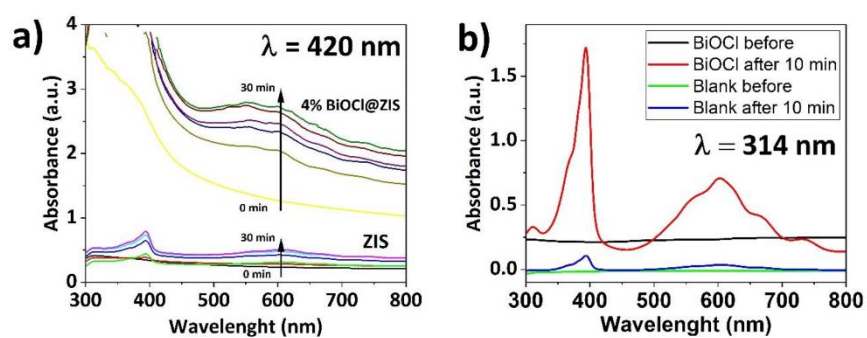


Fig. S5 Valence band spectra of a) BiOCl and b) ZIS and Tauc plots to estimate valence band level and the band gap of the c) ZIS and d) BiOCl.

Thanks to the derivatization, the esterification products in the presence of ethanol under acidic condition, ethyl formate (2.1 min) and ethyl acetate (2.5 min) were detected in accordance with the reaction (I) and (II) which is a proof of formic acid (I) and acetic acid (II) formation. Other detectable products also can be seen such as acetaldehyde (1.65 min), propanal (1.91 min), acrolein (2-propenal) (2.3 min) by-products that are formed directly from the photocatalytic reforming of glycerol without need of derivatization for the GC-MS analysis.



**Fig. S6** Qualificative analysis of by-products before (up) and after (down) 8 hours of photocatalytic hydrogen evolution test over 4%BiOCl@ZIS/0.0625 wt.% Pt



**Fig. S7** UV-vis spectra of 5% (v/v) glycerol-water mixture solution with a) 4%BiOCl@ZIS and ZIS under monochromatic irradiation ( $\lambda > 420 \text{ nm}$ ) and b) BiOCl ( $\lambda > 314 \text{ nm}$ ). Each 3 ml mixture contains [photocatalyst] = 1.5 mg/ml and  $[\text{MV}^{2+}] = 1 \text{ mM}$ . Prior to the mono-chromatic light irradiation, the mixtures were purged with  $\text{N}_2$  gas with  $4 \text{ dm}^3/\text{h}$  flow rate for 4 min to remove the  $\text{O}_2$  from the system to prevent the reoxidation of  $\text{MV}^{+}$ .

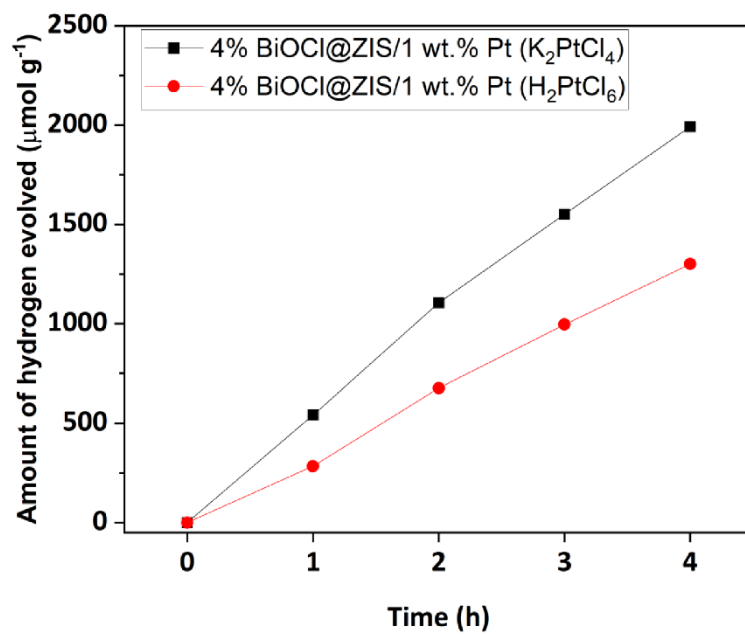


Fig. S8 Photocatalytic hydrogen evolution tests from 4%BiOCl@ZIS/1 wt.% Pt using  $\text{K}_2\text{PtCl}_4$  or  $\text{H}_2\text{PtCl}_6$  as a Pt precursor

Table S1 Elemental contents in the surface layer of pre-prepared ZIS, BiOCl and 4% BiOCl@ZIS composites modified by Pt, evaluated by XPS

Sample label	Elemental composition (atomic %)								In/O	Bi/O	In/Zn
	Zn	In	S	O	C	Bi	Cl	Pt			
ZIS	4.38	25.65	14.08	44.15	11.74	-	-	-	0.581	-	5.86
BiOCl	-	-	-	18.88	35.20	25.48	20.45	-	-	1.35	-
4% BiOCl@ZIS	4.05	27.79	13.30	47.63	6.38	0.10	0.75	-	0.583	0.0021	6.85
4% BiOCl@ZIS/ 0.0625 wt.% Pt (K <sub>2</sub> PtCl <sub>4</sub> ) 4 h	2.28	22.00	9.60	42.63	23.04	0.08	0.16	0.22	0.516	0.0019	9.65
4% BiOCl@ZIS/ 0.0625 wt.% Pt (K <sub>2</sub> PtCl <sub>4</sub> ) 16 h	1.05	17.08	6.86	35.95	38.59	0.20	0.06	0.22	0.480	0.0056	16.28

Table S2 Reported works in the literature on photocatalytic glycerol reforming over metal-sulfide based photocatalytic system

Material	Pt co-catalysts	Amount of glycerol (%v/v)	Rate of Photocatalytic hydrogen evolution ( $\mu\text{mol g}^{-1} \text{h}^{-1}$ )	Light source	Source
ZnO/ZnS	-	5	384	450 W Xe arc lamp	[1]
Pt-CdS-TiO <sub>2</sub>	0.3 wt.% Pt, (Precursor: H <sub>2</sub> PtCl <sub>6</sub> )	30	106.5	500 W Hg-Xe arc lamp, $\lambda > 418 \text{ nm}$	[2]
ZnO@ZnS-Bi <sub>2</sub> S <sub>3</sub>	-	5	310	300 W Xe lamp	[3]
ZnO-ZnS/graphene	-	40	1070	300 W high pressure mercury lamp	[4]
Cd-doped SnO <sub>2</sub> /CdS	0.3 wt.% Pt, (Precursor: H <sub>2</sub> PtCl <sub>6</sub> )	50	290	500 W Hg-Xe arc lamp, $\lambda > 400 \text{ nm}$	[5]
Cd <sub>1-x</sub> Zn <sub>x</sub> S	0.3 wt.% Pt, (Precursor: H <sub>2</sub> PtCl <sub>6</sub> )	50	239	500 W Hg-Xe arc lamp	[6]
CdS	-	90	50	60 W blue LEDs (455 ± 5 nm)	[7]
ZnO/ZnS-PdS	-	5	238	500 W Xe lamp	[8]
CuS-NiO	-	25	400	300 W Xe lamp	[9]
Bi <sub>2</sub> S <sub>3</sub> -CdS	-	50	4380	300 W visible light source, $\lambda > 420 \text{ nm}$	[10]
Ni-CdS	-	32	74600	500 W mercury lamp, $\lambda > 400 \text{ nm}$	[11]
ZnO/ZnS	-	7	384.4	A solar simulated light source (Xe lamp, 500 W)	[12]
ZnS/NiO	-	10	9300	Simulated solar light	[13]
Cd <sub>0.5</sub> Zn <sub>0.5</sub> S	0.5 wt.% (Precursor: H <sub>2</sub> PtCl <sub>6</sub> )	7.3	590	250 W high pressure mercury lamp, $\lambda > 420 \text{ nm}$	[14]
<b>BiOCl@ZnIn<sub>2</sub>S<sub>4</sub></b>	<b>0.0625 wt.%</b> (Precursor: K <sub>2</sub> PtCl <sub>6</sub> )	<b>5</b>	<b>674</b>	<b>1000 W Xe lamp, <math>\lambda &gt; 420 \text{ nm}</math></b>	<b>This work</b>

## References

- [1] Bao D, Gao P, Zhu X, Sun S, Wang Y, Li X, et al. ZnO/ZnS Heterostructured Nanorod Arrays and Their Efficient Photocatalytic Hydrogen Evolution. *Chem - A Eur J* 2015;21:12728–34. <https://doi.org/10.1002/chem.201501595>.
- [2] De Oliveira Melo M, Silva LA. Visible light-induced hydrogen production from glycerol aqueous solution on hybrid Pt-CdS-TiO<sub>2</sub> photocatalysts. *J Photochem Photobiol A Chem* 2011;226:36–41. <https://doi.org/10.1016/j.jphotochem.2011.10.012>.
- [3] Xitao W, Rong L, Kang W. Synthesis of ZnO@ZnS-Bi<sub>2</sub>S<sub>3</sub> core-shell nanorod grown on reduced graphene oxide sheets and its enhanced photocatalytic performance. *J Mater Chem A* 2014;2:8304–13. <https://doi.org/10.1039/c4ta00696h>.
- [4] Chang CJ, Lin YG, Weng HT, Wei YH. Photocatalytic hydrogen production from glycerol solution at room temperature by ZnO-ZnS/graphene photocatalysts. *Appl Surf Sci* 2018;451:198–206. <https://doi.org/10.1016/j.apsusc.2018.05.004>.
- [5] Trindade TNS, Silva LA. Cd-doped SnO<sub>2</sub>/CdS heterostructures for efficient application in photocatalytic reforming of glycerol to produce hydrogen under visible light irradiation. *J Alloys Compd* 2018;735:400–8. <https://doi.org/10.1016/j.jallcom.2017.11.134>.
- [6] Lopes PAL, Mascarenhas AJS, Silva LA. Sonochemical synthesis of Cd<sub>1-x</sub>Zn<sub>x</sub>S solid solutions for application in photocatalytic reforming of glycerol to produce hydrogen. *J Alloys Compd* 2015;649:332–6. <https://doi.org/10.1016/j.jallcom.2015.07.123>.
- [7] Zhang Z, Wang M, Zhou H, Wang F. Surface Sulfate Ion on CdS Catalyst Enhances Syngas Generation from Biopolyols. *J Am Chem Soc* 2021;143:6533–41. <https://doi.org/10.1021/jacs.1c00830>.
- [8] Liu S, Wang X, Wang K, Lv R, Xu Y. ZnO/ZnS-PdS core/shell nanorods: Synthesis, characterization and application for photocatalytic hydrogen production from a glycerol/water solution. *Appl Surf Sci* 2013;283:732–9. <https://doi.org/10.1016/j.apsusc.2013.07.009>.
- [9] Vempuluru NR, Kanakkampalayam Krishnan C, Parnapalli R, Velusamy J, Marappan S, Pitchaimuthu S, et al. Solar hydrogen generation from organic substance using earth abundant CuS–NiO heterojunction semiconductor photocatalyst. *Ceram Int* 2021;47:10206–15. <https://doi.org/10.1016/j.ceramint.2020.12.062>.
- [10] Panmand RP, Sethi YA, Deokar RS, Late DJ, Gholap HM, Baeg JO, et al. In situ fabrication of highly crystalline CdS decorated Bi<sub>2</sub>S<sub>3</sub> nanowires (nano-heterostructure) for visible light photocatalyst application. *RSC Adv* 2016;6:23508–17. <https://doi.org/10.1039/c6ra01488g>.



- [11] Wang JJ, Li ZJ, Li XB, Fan XB, Meng QY, Yu S, et al. Photocatalytic hydrogen evolution from glycerol and water over nickel-hybrid cadmium sulfide quantum dots under visible-light irradiation. *ChemSusChem* 2014;7:1468–75. <https://doi.org/10.1002/cssc.201400028>.
- [12] Sang HX, Wang XT, Fan CC, Wang F. Enhanced photocatalytic H<sub>2</sub> production from glycerol solution over ZnO/ZnS core/shell nanorods prepared by a low temperature route. *Int J Hydrogen Energy* 2012;37:1348–55. <https://doi.org/10.1016/j.ijhydene.2011.09.129>.
- [13] Navakoteswara Rao V, Preethi V, Bhargav U, Ravi P, Kumar A, Sathish M, et al. Gram-scale synthesis of ZnS/NiO core-shell hierarchical nanostructures and their enhanced H<sub>2</sub> production in crude glycerol and sulphide wastewater. *Environ Res* 2021;199:111323. <https://doi.org/10.1016/j.envres.2021.111323>.
- [14] Peng S, Min D, Ting Y, Zhikang Z, Yuexiang L. Photocatalytic Hydrogen Evolution and Decomposition of Glycerol over Cd<sub>0.5</sub>Zn<sub>0.5</sub>S Solid Solution Under Visible Light Irradiation. *Environ Prog Sustain Energy* 2016;35:141–8. <https://doi.org/10.1002/ep>.

## 6 Scientific Achievements

### Publications

**Cavdar, O.**, Baluk, M., Malankowska, A., Żak, A., Lisowski, W., Klimczuk, T., Zaleska-Medynska, Photocatalytic hydrogen evolution from glycerol-water mixture under visible light over zinc indium sulfide ( $\text{ZnIn}_2\text{S}_4$ ) nanosheets grown on bismuth oxychloride ( $\text{BiOCl}$ ) microplates (2023), *Journal of Colloid and Interface Science*, 640, 15 June 2023, Pages 578-587, DOI: 10.1016/j.jcis.2023.02.129

**IF:** 9.965

**Cavdar, O.**, Malankowska, A., Łuczak, J., Żak, A., Lisowski, W., Klimczuk, T., Zaleska-Medynska, A. Capping ligand initiated  $\text{CuInS}_2$  quantum dots decoration on,  $\text{ZnIn}_2\text{S}_4$  microspheres surface under different alkalinity levels resulting in different hydrogen evolution performance (2022), *Colloids and Surfaces A: Physicochemical and Engineering Aspects*, 652, art. no. 129760, DOI: 10.1016/j.colsurfa.2022.129760

**IF:** 5.518

Sowik, J., Grzyb, T., Trykowski, G., Klimczuk, T., Nikiforow, K., **Cavdar, O.**, Zaleska-Medynska, A., Malankowska, A., Lanthanide-organic-frameworks modified  $\text{ZnIn}_2\text{S}_4$  for boosting hydrogen generation under UV–Vis and visible light (2022), *International Journal of Hydrogen Energy*, 47 (36), pp. 16065-16079, DOI: 10.1016/j.ijhydene.2022.03.111

**IF:** 7.139

Nevárez Martínez, M.C., **Cavdar, O.**, Haliński, Ł.P., Miodyńska, M., Parnicka, P., Bajorowicz, B., Kobylański, M., Lewandowski, Zaleska-Medynska, A. Hydrogen detection during photocatalytic water splitting: A tutorial (2022) *International Journal of Hydrogen Energy*, 47 (35), pp. 15783-15788, DOI: 10.1016/j.ijhydene.2022.03.050

**IF:** 7.139

**Cavdar, O.**, Malankowska, A., Amgar, D., Mazierski, P., Łuczak, J., Lisowski, W., Zaleska-Medynska, A., Remarkable visible-light induced hydrogen generation with ZnIn<sub>2</sub>S<sub>4</sub> microspheres/CuInS<sub>2</sub> quantum dots photocatalytic system (2021), International Journal of Hydrogen Energy, 46 (1), pp. 486-498, DOI: 10.1016/j.ijhydene.2020.09.212

**IF:** 7.139

Malankowska, A., Kulesza, D., Sowik, J., **Cavdar, O.**, Klimczuk, T., Trykowski, G., Zaleska-Medynska, A., The Effect of AgInS<sub>2</sub>, SnS, CuS<sub>2</sub>, Bi<sub>2</sub>S<sub>3</sub> Quantum Dots on the Surface Properties and Photocatalytic Activity of QDs-Sensitized TiO<sub>2</sub> Composite (2020), Catalysts, 10 (4), art. no. 403, DOI: 10.3390/catal10040403

**IF:** 4.146

Malankowska, A., Kobylański, M.P., Mikolajczyk, A., **Cavdar, O.**, Nowaczyk, G., Jarek, M., Lisowski, W., Michalska, M., Kowalska, E., Ohtani, B., Zaleska-Medynska, A. TiO<sub>2</sub> and NaTaO<sub>3</sub> Decorated by Trimetallic Au/Pd/Pt Core-Shell Nanoparticles as Efficient Photocatalysts: Experimental and Computational Studies (2018) ACS Sustainable Chemistry and Engineering, 6 (12), pp. 16665-16682, DOI:10.1021/acssuschemeng.8b03919

**IF:** 9.224

### **Scientific conferences**

**O. Cavdar**, M. Baluk, A. Malankowska, A. Żak, W. Lisowski, T. Klimczuk, A. Zaleska-Medynska, Photocatalytic hydrogen evolution from glycerol-water mixture over ZnIn<sub>2</sub>S<sub>4</sub> obtained on Bi-based semiconductor as a template, **SPASEC-25/AOTs-26, 29.08-01.09.2022**, Rostock (Germany), University of Rostock

Note: Poster presentation

**O. Cavdar**, A. Malankowska, D. Amgar, A. Żak, M. Witkowska, P. Mazierski, J. Łuczak, W. Lisowski, T. Klimczuk, A. Zaleska-Medynska, pH-dependent CuInS<sub>2</sub> quantum dots decoration on ZnIn<sub>2</sub>S<sub>4</sub> microsphere for photocatalytic H<sub>2</sub> evolution under visible light, **11<sup>th</sup> European Conference on Solar Chemistry and Photocatalysis: Environmental Applications (SPEA11), 06-10.06.2022**, Turin (Italy), Palazzo Citta Metropolitana, Corso Inghilterra 7

Note: Flash talk (5 minutes speech + poster presentation)

**O. Cavdar**, A. Malankowska, D. Amgar, A. Żak, M. Witkowska, P. Mazierski, J. Łuczak, W. Lisowski, T. Klimczuk, A. Zaleska-Medynska, Synthesis and applications of ZnIn<sub>2</sub>S<sub>4</sub>/CuInS<sub>2</sub> photocatalytic system for visible light induced photocatalytic hydrogen evolution, **NanoTech Poland 2022, 01-03.06.2022**, Poznań, Centrum Nanobiomedyczne Uniwersytet im. Adama Mickiewicza w Poznaniu

Note: Speech (15 minutes)

**O. Cavdar**, M. Baluk, A. Malankowska, A. Żak, W. Lisowski, T. Klimczuk, A. Zaleska-Medynska, Photocatalytic hydrogen evolution from glycerol-water mixture over BiOCl@ZnIn<sub>2</sub>S<sub>4</sub> composite with ultra-low in-situ Pt loading, **NanoTech Poland 2022, 01-03.06.2022**, Poznań, Centrum Nanobiomedyczne Uniwersytet im. Adama Mickiewicza w Poznaniu

Note: Poster presentation

**O. Cavdar**, A. Malankowska, A. Zaleska-Medynska, Preparation, optical properties, and photocatalytic activity of CuInS<sub>2</sub> Quantum Dots for H<sub>2</sub> generation, **CNM 2019, 6th Conference on Nano- and Micromechanics, 03-05.07.2019**, Poland, Rzeszów, Politechnika Rzeszowska

Note: Poster presentation

**O. Cavdar**, M. Jarek, A. Malankowska, A. Zaleska-Medynska, Preparation, optical properties, and photocatalytic activity of CuInS<sub>2</sub> Quantum Dots for H<sub>2</sub> generation, **PANIC 2019, PhoBIA Annual Nanophotonics International Conference, 15-17.05.2019**, Poland, Wrocław, Politechnika Wroclawska

Note: Speech (15 minutes)

### **Scientific projects and grants**

1. 2016/23/D/ST8/02682, SONATA (Narodowe Centrum Nauki), Photo-Bio Production of hydrogen by [NiFe] hydrogenase-MNPs/SiO<sub>2</sub>/M<sub>a</sub>S<sub>b</sub> hybrids under visible light, 2016-2019, **as the contractor**
2. 2018/31/N/ST5/00607, PRELUDIUM (Narodowe Centrum Nauki), Bismuth oxyhalides assisted with silver sulfide based asymmetric or multimeric nanoparticles, 2019-2022, **as the head of the project**

### **Scientific internships**

I completed a 3-month scientific internship in the field of heterogeneous photocatalysis at the University of Milan (Italian: Università degli Studi di Milano) in the period from September 30, 2022 to December 30, 2022.

## **Author Statements**

---

Onur Cavdar  
Wita Stwosza 63, 80-952, Gdańsk  
58 523 52 21 / onur.cavdar@phdstud.ug.edu.pl

Gdańsk, dnia 06/03/2023

### OŚWIADCZENIE

Mój wkład w powstanie publikacji pt:” **Remarkable visible-light induced hydrogen generation with ZnIn<sub>2</sub>S<sub>4</sub> microspheres/CuInS<sub>2</sub> quantum dots photocatalytic system**” jest następujący:

- Konceptualizacja,
- Optymalizacja i wykonywanie syntez (ZnIn<sub>2</sub>S<sub>4</sub> mikrosfery, CuInS<sub>2</sub> kropki kwantowe, wytwarzanie kompozytów ZnIn<sub>2</sub>S<sub>4</sub>/CuInS<sub>2</sub>, fotoosadzanie Pt),
- Opracowanie i wykonywanie analiz (GC-TCD, UV-vis DRS, PL),
- Wykonanie krzywej kalibracyjnej do ilościowego oznaczania wodoru w fazie gazowej,
- Wykonywanie procesów fotokatalicznego generowania wodoru,
- Tworzenie oryginalnego manuskryptu (pisanie tekstu manuskryptu, interpretacja uzyskanych wyników, tworzenie wykresów i rysunków).

Wzrost  
Ciężar ciała  
Ciężar ciała  
Ciężar ciała  
Ciężar ciała  
Ciężar ciała  
Ciężar ciała  
Ciężar ciała  
Ciężar ciała  
Ciężar ciała

Podpis



KIEROWNIK KATEDRY  
Katedra Technologii Środowiska

prof. dr hab. inż. Adriana Zaleska-Medynska



Prof. dr hab. inż. Adriana Zaleska-Medynska

Z 4

Gdańsk, dnia 6.03.2023

.....  
imię/imiona i nazwisko

Katedra Technologii Środowiska  
Wydział Chemii, Uniwersytet Gdański  
Ul. Wita Stwosza 63, 80-308 Gdańsk

.....  
adres korespondencyjny  
604 189 143/ adriana.zaleska-medynska@ug.edu.pl

.....  
nr telefonu / adres e-mail

#### OŚWIADCZENIE

Mój wkład w powstanie publikacji pt: " **Remarkable visible-light induced hydrogen generation with ZnIn<sub>2</sub>S<sub>4</sub> microspheres/CuInS<sub>2</sub> quantum dots photocatalytic system**" jest następujący:

1. krytyczna dyskusja stosowanych metod badawczych
2. krytyczna dyskusja wyników badań
3. korekta manuskryptu artykułu

Podpis

*Adriana Zaleska-Medynska*



Paweł Marzec

Gdańsk, dnia 05.08.2023

imię/imiona i nazwisko

Katedra Technologii Środowiska, Wita Stwosza 63, 80-308  
Gdańsk

adres korespondencyjny

58 523 5230 / pawel.marzec@ug.edu.pl

nr telefonu / adres e-mail

## OŚWIADCZENIE

Mój wkład w powstanie publikacji pt: "Remarkable visible-light induced hydrogen generation with  $ZnIn_2S_4$  microspheres/ $CuInS_2$  quantum dots photocatalytic system" jest następujący:

1. Wykonanie pomiarów widm akcji (Action Spectra analysis)

Podpis Paweł Marzec

**ANNA MALANKOWSKA**

imię/imiona i nazwisko

Gdańsk, dnia 06.03.2023

**ul. Wita Stwosza 63, 80-308 Gdańsk**

adres korespondencyjny

**(+48 58) 523 52 22, [anna.malankowska@ug.edu.pl](mailto:anna.malankowska@ug.edu.pl)**

nr telefonu / adres e-mail

### OŚWIADCZENIE

Mój wkład w powstanie publikacji pt:” **Remarkable visible-light induced hydrogen generation with ZnIn<sub>2</sub>S<sub>4</sub> microspheres/CuInS<sub>2</sub> quantum dots photocatalytic system**” jest następujący:

1. Koncepcja badań: zaproponowanie tematu badawczego, zaplanowanie doświadczeń, nadzór merytoryczny nad prowadzonymi badaniami.
2. Analiza danych, dyskusja i interpretacja wyników.
3. Recenzja i korekta publikacji.
4. Finansowanie badań z grantu SONATA.



Podpis

Justyna Łuczak  
imię/imiona i nazwisko

Gdańsk, dnia 03.03.2023

Politechnika Gdańska  
Wydział Chemiczny  
Katedra Inżynierii Procesowej i Technologii Chemicznej  
Narutowicza 11/12  
80-233 Gdańsk  
adres korespondencyjny

justyna.luczak@pg.edu.pl  
nr telefonu / adres e-mail

#### OŚWIADCZENIE

Mój wkład w powstanie publikacji pt:” **Remarkable visible-light induced hydrogen generation with ZnIn<sub>2</sub>S<sub>4</sub> microspheres/CuInS<sub>2</sub> quantum dots photocatalytic system**” jest następujący:

1. analiza próbek metodą XRD
2. pomoc w analizie powierzchni właściwej (BET)



Podpis

Onur Cavdar  
Wita Stwosza 63, 80-952, Gdańsk  
58 523 52 21 / onur.cavdar@phdstud.ug.edu.pl

Gdańsk, dnia 06/03/2023

## OŚWIADCZENIE

Mój wkład w powstanie publikacji pt:” **Capping ligand initiated CuInS<sub>2</sub> quantum dots decoration on, ZnIn<sub>2</sub>S<sub>4</sub> microspheres surface under different alkalinity levels resulting in different hydrogen evolution performance**” jest następujący:

- Konceptualizacja,
- Optymalizacja i wykonywanie syntez (ZnIn<sub>2</sub>S<sub>4</sub> mikrosfery, CuInS<sub>2</sub> kropki kwantowe, wytwarzanie kompozytów ZnIn<sub>2</sub>S<sub>4</sub>/CuInS<sub>2</sub>, fotoosadzanie Pt),
- Wykonanie analiz zdolności redukcyjnych opratyh na kompozytów ZnIn<sub>2</sub>S<sub>4</sub>/CuInS<sub>2</sub>
- Opracowanie i wykonywanie analiz (GC-TCD, UV-vis DRS, PL),
- Wykonanie analiz: rozkładu wielkości cząstek (CuInS<sub>2</sub> kropki kwantowe) i potencjału zeta,
- Wykonanie krzywej kalibracyjnej do ilościowego oznaczania wodoru w fazie gazowej,
- Wykonywanie procesów fotokatalicznego generowania wodoru,
- Tworzenie oryginalnego manuskryptu (pisanie tekstu manuskryptu, interpretacja uzyskanych wyników, tworzenie wykresów i rysunków).

Podpis



KIEROWNIK KATEDRY  
Katedra Technologii Środowiska

prof. dr hab. inż. Adriana Zaleska-Medynska



Prof. dr hab. inż. Adriana Zaleska-Medynska

Z 4

Gdańsk, dnia 6.03.2023

.....  
imię/imiona i nazwisko

Katedra Technologii Środowiska  
Wydział Chemii, Uniwersytet Gdański  
Ul. Wita Stwosza 63, 80-308 Gdańsk

.....  
adres korespondencyjny  
604 189 143/ adriana.zaleska-medynska@ug.edu.pl

.....  
nr telefonu / adres e-mail

### OŚWIADCZENIE

Mój wkład w powstanie publikacji pt: " **Capping ligand initiated CuInS<sub>2</sub> quantum dots decoration on, ZnIn<sub>2</sub>S<sub>4</sub> microspheres surface under different alkalinity levels resulting in different hydrogen evolution performance**" jest następujący:

1. krytyczna dyskusja stosowanych metod badawczych
2. krytyczna dyskusja wyników badań
3. korekta manuskryptu artykułu

Podpis

*Adriana Zaleska - Medynska*

**ANNA MALANKOWSKA**  
imię/imiona i nazwisko

Gdańsk, dnia 06.03.2023

**ul. Wita Stwosza 63, 80-308 Gdańsk**  
adres korespondencyjny

**(+48 58) 523 52 22, [anna.malankowska@ug.edu.pl](mailto:anna.malankowska@ug.edu.pl)**  
nr telefonu / adres e-mail

### OŚWIADCZENIE

Mój wkład w powstanie publikacji pt: " **Capping ligand initiated CuInS<sub>2</sub> quantum dots decoration on, ZnIn<sub>2</sub>S<sub>4</sub> microspheres surface under different alkalinity levels resulting in different hydrogen evolution performance**" jest następujący:

1. Koncepcja badań, nadzór merytoryczny nad prowadzonymi badaniami.
2. Analiza danych, dyskusja i interpretacja wyników.
3. Recenzja i korekta publikacji.
4. Finansowanie badań z grantu SONATA.



Podpis



Justyna Łuczak  
imię/imiona i nazwisko

Gdańsk, dnia 03.03.2023

Politechnika Gdańska  
Wydział Chemiczny  
Katedra Inżynierii Procesowej i Technologii Chemicznej  
Narutowicza 11/12  
80-233 Gdańsk  
adres korespondencyjny

justyna.luczak@pg.edu.pl  
nr telefonu / adres e-mail

#### OŚWIADCZENIE

Mój wkład w powstanie publikacji pt:” **Capping ligand initiated CuInS<sub>2</sub> quantum dots decoration on, ZnIn<sub>2</sub>S<sub>4</sub> microspheres surface under different alkalinity levels resulting in different hydrogen evolution performance**” jest następujący:

1. pomoc w analizie rozkładu wielkości cząstek oraz potencjału Zeta



Podpis



**GDAŃSK UNIVERSITY  
OF TECHNOLOGY**

FACULTY OF APPLIED PHYSICS AND MATHEMATICS

Prof. Tomasz Klimczuk  
Zakład Silnie Skorelowanych Układów Elektronowych  
Instytut Nanotechnologii i Inżynierii Materiałowej  
Wydział Fizyki Technicznej i Matematyki Stosowanej  
Politechnika Gdańska

Gdańsk, 03.03.2023

## OŚWIADCZENIE

Mój wkład w powstanie publikacji pt: **“Capping ligand initiated CuInS<sub>2</sub> quantum dots decoration on, ZnIn<sub>2</sub>S<sub>4</sub> microspheres surface under different alkalinity levels resulting in different hydrogen evolution performance”** polegał na przygotowaniu, wykonaniu a następnie badań metodą dyfrakcji rentgenowskiej. Przygotowałem rysunki i opis dyfraktogramów.

Z wyrazami szacunku

Prof. Tomasz Klimczuk



Onur Cavdar  
Wita Stwosza 63, 80-952, Gdańsk  
58 523 52 21 / onur.cavdar@phdstud.ug.edu.pl

Gdańsk, dnia 06/03/2023

### OŚWIADCZENIE

Mój wkład w powstanie publikacji pt: " **Photocatalytic hydrogen evolution from glycerol-water mixture under visible light over zinc indium sulfide (ZnIn<sub>2</sub>S<sub>4</sub>) nanosheets grown on bismuth oxychloride (BiOCl) microplates** " jest następujący:

- Pozyskiwanie funduszy (PRELUDIUM),
- Konceptualizacja,
- Optymalizacja i wykonywanie syntez (ZnIn<sub>2</sub>S<sub>4</sub> nanosheets, BiOCl mikroplątka, wytwarzanie kompozytów BiOCl@ZnIn<sub>2</sub>S<sub>4</sub>, fotoosadzanie Pt),
- Opracowanie i wykonywanie analiz (GC-TCD, UV-vis DRS),
- Wykonanie analiz zdolności redukcyjnych opratyh na ZnIn<sub>2</sub>S<sub>4</sub> nanosheets, BiOCl mikroplątka, kompozytów BiOCl@ZnIn<sub>2</sub>S<sub>4</sub>
- Wykonanie krzywej kalibracyjnej do ilościowego oznaczania wodoru w fazie gazowej,
- Wykonywanie procesów fotokatalicznego generowania wodoru,
- Tworzenie oryginalnego manuskryptu (pisanie tekstu manuskryptu, interpretacja uzyskanych wyników, tworzenie wykresów i rysunków).

Podpis



KIEROWNIK KATEDRY  
Katedra Technologii Środowiska

prof. dr hab. inż. Adrianna Zaleska-Medynska

Prof. dr hab. inż. Adriana Zaleska-Medynska

Z 4

Gdańsk, dnia 6.03.2023

.....  
imię/imiona i nazwisko

Katedra Technologii Środowiska  
Wydział Chemii, Uniwersytet Gdański  
Ul. Wita Stwosza 63, 80-308 Gdańsk

.....  
adres korespondencyjny  
604 189 143/ adriana.zaleska-medynska@ug.edu.pl

.....  
nr telefonu / adres e-mail

#### OŚWIADCZENIE

Mój wkład w powstanie publikacji pt: " **Photocatalytic hydrogen evolution from glycerol-water mixture under visible light over zinc indium sulfide (ZnIn<sub>2</sub>S<sub>4</sub>) nanosheets grown on bismuth oxychloride (BiOCl) microplates** " jest następujący:

1. krytyczna dyskusja stosowanych metod badawczych
2. krytyczna dyskusja wyników badań
3. korekta manuskryptu artykułu

Podpis

*Adriana Zaleska, Medynska*

**ANNA MALANKOWSKA**

imię/imiona i nazwisko

Gdańsk, dnia 06.03.2023

**ul. Wita Stwosza 63, 80-308 Gdańsk**

adres korespondencyjny

**(+48 58) 523 52 22, [anna.malankowska@ug.edu.pl](mailto:anna.malankowska@ug.edu.pl)**

nr telefonu / adres e-mail

### OŚWIADCZENIE

Mój wkład w powstanie publikacji pt:” **Photocatalytic hydrogen evolution from glycerol-water mixture under visible light over zinc indium sulfide (ZnIn<sub>2</sub>S<sub>4</sub>) nanosheets grown on bismuth oxychloride (BiOCl) microplates** ” jest następujący:

1. Nadzór merytoryczny nad prowadzonymi badaniami.
2. Analiza danych, dyskusja i interpretacja wyników.
3. Recenzja i korekta publikacji.



Podpis



**GDAŃSK UNIVERSITY  
OF TECHNOLOGY**

FACULTY OF APPLIED PHYSICS AND MATHEMATICS

Prof. Tomasz Klimczuk  
Zakład Silnie Skorelowanych Układów Elektronowych  
Instytut Nanotechnologii i Inżynierii Materiałowej  
Wydział Fizyki Technicznej i Matematyki Stosowanej  
Politechnika Gdańska

Gdańsk, 03.03.2023

#### OŚWIADCZENIE

Mój wkład w powstanie publikacji pt: **“Photocatalytic hydrogen evolution from glycerol-water mixture under visible light over zinc indium sulfide (ZnIn<sub>2</sub>S<sub>4</sub>) nanosheets grown on bismuth oxychloride (BiOCl) microplates”** polegał na przygotowaniu, wykonaniu a następnie badań metodą dyfrakcji rentgenowskiej. Przygotowałem rysunki i opis dyfraktogramów.

Z wyrazami szacunku

Prof. Tomasz Klimczuk

Mateusz Adam Baluk

.....

imię/imiona i nazwisko

Gdańsk, dnia 06.03.2023

80-308 Gdańsk, ul. Wita Stwosza 63

.....

adres korespondencyjny

+48 783 343 995 / mateusz.baluk@phdstud.ug.edu.pl

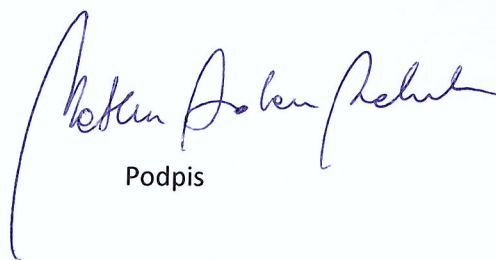
.....

nr telefonu / adres e-mail

#### OŚWIADCZENIE

Mój wkład w powstanie publikacji pt: " **Photocatalytic hydrogen evolution from glycerol-water mixture under visible light over zinc indium sulfide (ZnIn<sub>2</sub>S<sub>4</sub>) nanosheets grown on bismuth oxychloride (BiOCl) microplates** " jest następujący:

1. Opracowanie metody analitycznej analizy produktów rozkładu glicerolu podczas fotoprocusu



Podpis